STUDIES ON THERMOELECTRIC PROPERTIES OF HEAVILY DOPED SEMICONDUCTING ALLOYS FOR THE DEVELOPMENT OF POWER GENERATORS

By

Ranita Basu

(CHEM 01201204002)

Bhabha Atomic Research Centre, Mumbai

A thesis submitted to the

Board of Studies in Chemical Sciences

In partial fulfillment of requirements

For the Degree of

DOCTOR OF PHILOSOPHY

of

HOMI BHABHA NATIONAL INSTITUTE

March, 2015

STATEMENT BY AUTHOR

This dissertation has been submitted in partial fulfillment of requirements for an advanced degree at Homi Bhabha National Institute (HBNI) and is deposited in the Library to be made available to borrowers under rules of the HBNI.

Brief quotations from this dissertation are allowable without special permission, provided that accurate acknowledgement of source is made. Requests for permission for extended quotation from or reproduction of this manuscript in whole or in part may be granted by the Competent Authority of HBNI when in his or her judgment the proposed use of the material is in the interests of scholarship. In all other instances, however, permission must be obtained from the author.

Ranita Basu

DECLARATION

I, hereby declare that the investigation presented in the thesis has been carried out by me. The work is original and has not been submitted earlier as a whole or in part for a degree / diploma at this or any other Institution / University.

Ranita Basu

List of Publications arising from the thesis

Publications in refereed journals

a. Published

1. Improved thermoelectric performance of hot pressed nanostructured n-type SiGe bulk alloys, **Ranita Basu**, Shovit Bhattacharya, Ranu Bhatt, Mainak Roy, Sajid Ahmad, Ajay Singh, M. Navaneethan, Y. Hayakawa, D. K. Aswal, S. K. Gupta, *J. Mater. Chem. A* 2 (2014) 6922.
2. High thermoelectric performance of $(AgCrSe_2)_{0.5}(CuCrSe_2)_{0.5}$ nanocomposites having all scale natural hierarchical architectures, Shovit Bhattacharya, Anil Bohra, **Ranita Basu**, Ranu Bhatt, Sajid Ahmad, K.N. Meshram, A.K. Debnath, Ajay Singh, Shaibal Sarkar, M. Navaneethan, Y. Hayakawa, D. K. Aswal, S. K. Gupta, *J. Mater. Chem. A* 2 (2014) 17122.
3. Improved thermoelectric properties of Se-doped n-type $PbTe_{1-x}Se_x$, **Ranita Basu**, Shovit Bhattacharya, Ranu Bhatt, Ajay Singh, D. K. Aswal, S. K. Gupta, *J. Elect. Mater.* 7 (2013) 2292.
4. $CuCrSe_2$: a high performance phonon glass and electron crystal thermoelectric material, Shovit Bhattacharya, **Ranita Basu**, Ranu Bhatt, S. Pitale, Ajay Singh, D. K. Aswal, S. K. Gupta, M. Navaneethan, Y. Hayakawa, *J. Mater. Chem. A* 1 (2013) 11289.
5. Thermoelectric performance of Cu intercalated layered $TiSe_2$ above 300K, R. Bhatt, S. Bhattacharya, M. Patel, **R. Basu**, A. Singh, C. Surger, M. Navaneethan, Y. Hayakawa, D. K. Aswal and S. K. Gupta, *J. Appl. Phy.* 114 (2013) 114509.
6. Low temperature thermoelectric properties of Cu intercalated $TiSe_2$: a charge density wave material, Ranu Bhatt, **Ranita Basu**, S. Bhattachraya, A. Singh, D. K. Aswal,

S.K. Gupta, G.S. Okram, V. Ganeshan, D. Venkateshwarlu, *Appl. Phys. A* 111 (2013) 465.

7. Development of thermoelectric devices based on n-type PbTe/p-type TAGS-85 ($(AgSbTe_2)_{0.15}(GeTe)_{0.85}$) and n/p-type Si-Ge alloy, **Ranita Basu**, S. Bhattacharya, Ranu Bhatt, K.N. Meshram, A. Singh, D.K. Aswal, S.K. Gupta, *J. Thermoelectricity* 3 (2012) 1607.
8. Effect of Te doping on the thermopower of $PbSe_{1-x}Te_x$, **Ranita Basu**, S. Bhattacharya, R. Bhatt, A.K. Singh, D.K. Aswal and S.K. Gupta, *Emer. Mater. Res.* 1 (2012) 306.

b. Other Publications

1. Enhanced thermoelectric properties of Se deficient layered $TiSe_{2-x}$: a charge density wave material, Ranu Bhatt, Shovit Bhattacharya, **Ranita Basu**, Sajid Ahmad, A. K. Chauhan , G.K. Okram, Pramod Bhatt, Mainak Roy, M. Navaneethan,Y. Hayakawa, Ajay Singh, D. K. Aswal and S. K. Gupta, *Appl. Mater. & Interf.* 6 (2014) 18619.
2. Thermoelectric performance of layered Sr_xTiSe_2 above 300 K, Ranu Bhatt, Miral Patel, Shovit Bhattacharya, **Ranita Basu**, Sajid Ahmad, Pramod Bhatt, A K Chauhan, M Navneethan,Y Hayakawa, Ajay Singh, D K Aswal and S K Gupta, *J. Phys.: Condens. Mat.* 26 (2014) 445002.
3. Growth of Pd_4S, PdS and PdS_2 films by controlled sulfurization of sputtered Pd on native oxide of Si, R. Bhatt, S. Bhattacharya, **R. Basu**, A. Singh, U. Deshpande, C. Surger, S. Basu, D.K. Aswal, S.K. Gupta, *Thin Solid Films* 539 (2013) 41.

Dedicated to my family

Acknowledgements

First of all, I would like to express my deepest appreciation to my guide **Prof. D.K. Aswal**, who has been a source of continual energy and inspiration during the course of this dissertation. The present thesis work would not have been possible without his endless support and astute guidance. His contagious enthusiasm and uninterrupted motivation has driven me to carry out timely submission of this dissertation. I would like to thank **Dr. S.K. Gupta**, Head Technical Physics Division, for encouragement, support and guidance.

I sincerely thank **Dr. Ajay Singh** for valuable advices and consistent encouragement and support in each and every step of this dissertation work. I am thankful to large number of colleagues for extending help in different experiments: **Dr. Mainak Roy** for Raman and Hall measurements, **Dr. Kaustava Bhattacharyya** for band gap measurement using diffuse reflectance spectroscopy, **Mr. Radhakrishnan Nair** for vacuum sealing, **Dr. A.K. Debnath** for XPS measurements. I would also like to thank **Dr. M. Navaneethan** and **Dr. Y. Hayakawa** for TEM analysis.

I am exceptionally grateful to **Dr. Shovit Bhattacharya** and **Dr. Ranu Bhatt** for their help, support, encouragement and most of all their affection that kept me in good spirits and enthusiastic while carrying out the dissertation work. I am thankful to **Dr. K.P. Muthe, Dr. Manmeet Kaur, Shri R. Prasad, Dr. Soumen Samanta, Dr. Anil Chauhan, Dr. Vibha Saxena, Dr. Shankar Koiry, Dr. Purushottam Jha, Dr. N.Ramgir, Dr. P. Veerender, Dr. Niyanta Datta, Mr. Sajid Ahmad, Shri K.N. Meshram, Mrs K. Ganapati** and **the students** for extending support and help at various stages of the thesis work.

Last but not the least, I would like to extend my heartiest gratitude to my husband **Mr. H. Basu,** my son **Master Bhumit Basu** and my parents for their unconditional support, love and patience during this dissertation work. I would also like to thank all my friends for their backing and encouragement during the dissertation work.

Ranita Basu

CONTENTS

Page No.

CHAPTER

SYNOPSIS

Thermoelectric devices convert heat directly into electricity, and therefore, are very useful for tapping the enormous waste heat (~60%) generated in various combustion processes e.g. power plants, industries, automobiles and other heat engines. In a thermoelectric device, n-type and p-type semiconductor legs are connected electrically in series through metallic interconnects so that all legs are thermally in parallel. The conversion efficiency of thermoelectric devices is expressed by: $\eta = \frac{T_2 - T_1}{T_2} . \frac{(M-1)}{(M + T_1/T_2)}$, where $\mathrm{M} = (1 + \mathrm{Z}\bar{\mathrm{T}})^{1/2}$ with $T = (T_1 + T_2)/2$. $\mathrm{Z}\bar{\mathrm{T}}$ is the average figure-of-merit of the thermoelectric material. The *ZT* is expressed by: $ZT = \frac{\alpha^2 \sigma}{\kappa} T$ (where, α is the Seebeck coefficient, σ is the electrical conductivity and κ is thermal conductivity, respectively). Currently, the efficiency of thermoelectric device is ~6-8%, which limits their use in commercial applications. Nevertheless, they are being used in places where cost is not a major issue e.g. radioisotope generators for deep-space satellites and remote power generation for unmanned systems. Current international research on thermoelectric is focussed on enhancing the *ZT*. The methods commonly used for enhancing *ZT* include (i) alloys of heavy and light elements i.e. mass difference results in scattering of low wavelength phonons; (ii) materials having large unit cell and complex crystal structure such as, skutterudites, clathrates and Zintl phases; (iii) synthesizing materials in the nanostructured forms; (iv) incorporation of mesoscale features in the nanostructured bulk, which leads to the scattering of high wavelength phonons; and (v) Slack's proposal of phonon glass and electron crystal (PGEC). In addition the efficiency of the devices is governed by various electrical and thermal contacts.

This thesis aims at: (i) enhancing the ZT of semiconductor alloys by reducing the lattice thermal conductivity through introducing all-scale hierarchical defects i.e. from atomic, nano, meso to micro, (ii) investigation of the formation of metallic-interconnects with legs having low contact resistances, and (iii) fabrication of thermoelectric devices with minimum thermal shunts. The thermoelectric materials investigated in this thesis are: PbTe, $(AgSbTe_2)_{0.15}(GeTe)_{0.85}$(TAGS-85), different selenides and SiGe alloys. These alloys have been synthesized using vacuum-melting, melt-and-quench, and/or high-energy ball milling. The synthesized alloys have been characterized for morphology, structure and temperature dependent thermoelectric properties. The prototype devices have been fabricated and tested for their long term stability. The work done and the obtained results are organised in following six chapters.

Chapter 1: Introduction

In this chapter, we discuss the physics of thermoelectricity, categorization of thermoelectric materials based on the operating temperature and various approaches to enhance the ZT. Various issues involved in the fabrication of thermoelectric devices, including electrical and thermal contacts and the housing of the devices are discussed. Finally the scope of the thesis is presented.

Chapter 2: Experimental Techniques

This chapter describes the details of experimental methods used for the synthesis, and characterization of different types of thermoelectric materials and fabrication of devices. Thermoelectric materials have been synthesized using vacuum melting, melt-and-quench, and/or high-energy ball milling. Details of the equipments used in these synthesis methods (i.e. rocking furnace, induction melting furnace, ball-mill and vacuum hot press) as well as the process of the synthesis are described. Overview of the various characterization techniques used in the thesis work are discussed, which includes X-ray diffraction (XRD), X-ray photoelectron spectroscopy (XPS), diffuse reflectance UV-Vis spectroscopy (DR-UV-Vis), scanning electron microscope (SEM), transmission electron microscope (TEM) and energy dispersive X-ray analysis (EDX). In addition, the details of the setups used for the temperature dependent measurements of Seebeck coefficient (α), electrical resistivity (ρ) and thermal conductivity (κ) are described.

Chapter 3: Thermoelectric Generators based on PbTe and TAGS-85 Alloys

In this Chapter the results on the synthesis of single-phase n-type PbTe and p-type TAGS-85 thermoelectric materials as well as their morphological and structural characterization are discussed. The temperature dependence of α, ρ and κ were measured for both PbTe and TAGS-85 samples. For both the samples, ρ was found to increase with temperature, which is typical of degenerate semiconductors, as scattering of charge carriers with phonons increases with temperature. However, TAGS-85 samples exhibited down-turn at ~625 K, which is attributed to intrinsic excitation due to narrow band gap. The κ, in the temperature 300-600 K, decreases with increasing temperature and follows κ ~1/T behaviour, indicating predominant scattering of acoustic phonons. However at temperatures >600 K, the κ starts increasing, which is attributed to the additional contribution from diffusion of bipolarons. The peak *ZT* values obtained for PbTe and TAGS-85 samples were respectively 0.8 and 1.15.

A new strategy was adopted to fabricate the n- and p-type legs that have metallic shoes with ohmic contacts. In order to minimize the thermal and lattice expansion mismatch between metallic shoe and legs, layer-structured legs i.e. Ag/Fe/PbTe+Fe/ PbTe/ PbTe+Fe/Fe/Ag and Ag/Fe/SnTe/TAGS-85/SnTe/Fe/Ag, were fabricated. The cross-sectional back-scattered electron images of the legs clearly revealed that all the interfaces are chemically sharp i.e. minimal inter-diffusion. The specific contact-resistances estimated were ~7-10 $\mu\,cm^2$. Thermoelectric power generators were fabricated by packing the n- and p-type legs using zircar housing and interconnecting them by silver strips through diffusion bonding. The devices exhibited an efficiency of ~6%. In addition, the devices were stable in air for more than one year.

Chapter 4: *ZT* Enhancement in Selenides

In this Chapter, we describe the thermoelectric properties of the selenides with an emphasis on enhancing their *ZT*. The results obtained on various selenides are summarized below.

1. **$PbTe_{1-x}Se_x$:** The effect of Se substitution has been systematically investigated $PbTe_{1-x}Se_x$. For a particular composition of x =0.5, α is highest ~ 292 μV/K, while κ is lowest ~ 0.75 W/m-K, resulting in the highest *ZT* of ~0.95 at 600K. The increase in α for x=0.5 is attributed to the high distortion in the crystal lattice which leads to the formation of defect states. These defect states scatters the majority charge carriers leading to high α as well as high ρ. The dramatic reduction of κ for x=0.5 is also attributed to the scattering of the phonons by the defect states.

2. **Cu intercalated $TiSe_2$:** High temperature (300–650K) thermoelectric performance of Cu intercalated Cu_xTiSe_2 (x=0-0.11) material show that Cu intercalation transforms the p-type $TiSe_2$ to n-type Cu_xTiSe_2 with α value saturating to ~ -90 µV/K (for $x \geq 0.06$) at 650 K. Spanning the entire range of Cu_xTiSe_2 samples, very low κ has been observed which is attributed to the layered growth structure and rattling effect of weakly bound Cu atoms in the van der Waals gaps of $TiSe_2$ layers. At 650 K, the *ZT* values of 0.1 and 0.15 are achieved for pure $TiSe_2$ and $Cu_{0.11}TiSe_2$, respectively.
3. **$CuCrSe_2$ and $AgCrSe_2$:** Both $CuCrSe_2$ and $AgCrSe_2$ are emerging thermoelectric materials due to their complex layered structure and acts like a phonon liquid electron crystal (PLEC) system. The κ (at 773K) values obtained for $CuCrSe_2$ and $AgCrSe_2$ were found to be ~ 7 and ~4 $mWcm^{-1}K^{-1}$ respectively. The low κ values are attributed to various phonon-scattering sources i.e. superionic Cu/Ag ions between $CrSe_2^-$ layers, nanoscale precipitates and natural grain boundaries. The low κ values yield *ZT* of 1 and 0.8 respectively for $CuCrSe_2$ and $AgCrSe_2$.
4. **$(AgCrSe_2)_{0.5}(CuCrSe_2)_{0.5}$ nanocomposites:** A further improvement of *ZT* has been obtained in the $(AgCrSe_2)_/(CuCrSe_2)$ nanocomposites through hierarchically organized microstructures that significantly lowers the lattice thermal conductivity without any appreciable change in the power factor. $(AgCrSe_2)_{0.5}(CuCrSe_2)_{0.5}$ nanocomposites synthesized via the vacuum hot pressing of a mixture of the constituents consisted of phonon scattering centers in a multiscale hierarchical fashion, i.e. atomic scale disorder, nanoscale amorphous structure, natural grain boundaries due to layered structure and mesoscale grain boundaries/interfaces. XRD results show that in composite samples there is a slight migration of Cu into the Ag site. Nanocomposite samples exhibit

extremely low κ of ~2 mWcm^{-1} K^{-1} at 773 K, which is much lower than that of $AgCrSe_2$ and $CuCrSe_2$. The composite samples exhibit a high *ZT* of 1.4 at 773 K.

Chapter 5: *ZT* Enhancement in SiGe and Thermoelectric Generators

In this Chapter we describe the results on the synthesis of $Si_{80}Ge_{20}$ alloys using ball milling as well as melt-quench methods. We have demonstrated the highest value of *ZT* ~1.84 at 1073 K for ball-milled n-type SiGe nanostructured alloys, which is 34% higher than the reported value till date. The enhancement of *ZT* is due to the presence of atomic size defects, dislocations, and grain boundaries that reduces κ to very low values.

In addition, n- and p- type $Si_{80}Ge_{20}$ were synthesized using melt-quench method. The advantage of this method is that $Si_{80}Ge_{20}$ can be prepared in large quantities for device fabrication. However, the *ZT* values for these samples were in the range of 0.1-0.2 (at 1073K) largely due to the phase segregations and grain growth. Prototype devices have been fabricated using Mo as interconnect. The average contact resistance for each element was found to be 6.5 mΩ-cm^2, which is quite higher than the resistance of the legs. These devices were tested at a hot end temperature of 900°C with a temperature difference of 600°C between hot and cold ends. The device exhibited an open circuit voltage of 230 mV with an output power of ~0.2 W (with load voltage of 120mV and current of 1.74A). The working efficiency of the device was calculated to be 1.2%.

Chapter 6: Summary

In this chapter, we summarize the main conclusions of the thesis. It has been conclusively demonstrated that by introducing various types of defects, such as, atomic scale disorder, nanoscale amorphous structure, grain boundaries at meso/microscales in the thermoelectric alloys, their *ZT* can be dramatically enhanced. This is because these defects can scatter phonons of all wavelengths, and therefore, dramatically reduce the lattice thermal conductivity. In this regard, layered nanocomposites $(AgCrSe_2)_{0.5}(CuCrSe_2)_{0.5}$ have yielded *ZT* of 1.4 (at 773 K). Similarly, a record value of *ZT*~1.84 has been obtained in the nanostructured n-type $Si_{80}Ge_{20}$. In addition, we have emphasized that the contact resistance play an important role in governing the overall efficiency of the thermoelectric device. This Chapter is concluded by bringing out the future scope of the work.

LIST OF FIGURES

structures for high performance thermoelectric systems where major contributing factors for reducing the lattice thermal conductivity are indicated. (c) Maximum achievable *ZT* values for the respective length scales: the atomic scale (alloy scattering: red, Te; blue, Pb; green, dopant), the nanoscale (PbTe matrix, grey; SrTe nanocrystals, blue) to the mesoscale (grain-boundary scattering).

Fig.2.1. A photograph showing the material filled graphite bottle enclosed in a vacuum sealed quartz ampoule.

Fig.2.2. A photograph of the in-house built rocking furnace.

Fig.2.3. Photograph of PbTe ingot obtained from the melt growth.

Fig.2.4. (a) Photograph of the melting-casting furnace and (b) Photograph showing the inner view of the chamber with induction coil and water cooled Cu-mould.

Fig.2.5. a) Photograph of the ball mill used in the present work (Fritsch make Pulverisette 5). (b) Schematic showing: (1) rotation of the grinding bowls; (2) centrifugal force; and (3) movement of the support disc.

Fig.2.6. (a) A photograph of the in-house built vacuum hot press. (b) Schematic of uniaxial compaction of material in a die.

Fig. 2.7. (a) Photographs of a stainless steel zig for fabrication of devices. (a) top and bottom plates of the zig. (b) Mounting of p-n themolegs along with strips. (c) Mounted 16 p-n thermolegs device ready for vacuum hot pressing.

Fig.2.8. A photograph of the scanning electron microscope equipped with energy dispersive x-ray analysis system.

Fig. 2.9. Photograph of the x-ray diffractometer used in the present work.

Fig. 2.10. Schematic showing the principle of diffuse reflectance measurements.

region inside white dotted lines shows the presence of nanoscale precipitates with amorphous structure inside a crystalline matrix. For clarity the white dotted region of image (c) is magnified as image (d).

Fig. 4.17. Temperature dependence of the thermoelectric properties of hot pressed $CuCrSe_2$ (a) electrical resistivity (ρ). Inset shows the plot of ln ρ_{ionic} versus $1/T$ for $T > 365$ K. (b) Seebeck coefficient (α). (c) Temperature dependence of the power factor. Parallel (∥) and perpendicular (⊥) symbol represents the measurement of samples sliced from the hot pellet in parallel and perpendicular to the hot press direction (d) Temperature dependence of carrier concentration (n) derived from Hall effect measurement.

Fig. 4.18. Temperature dependence of (a) thermal diffusivity (b) specific heat (c) thermal conductivity for $CuCrSe_2$. In the diffusivity and specific heat plots, the data for sample sliced perpendicular (shown by ⊥) to the hot pressing direction is multiplied by 2 to show them clear.

Fig. 4.19. Temperature dependence of the Raman spectra for $CuCrSe_2$ in the temperature range 300 K – 443 K.

Fig. 4.20. Temperature dependence of dimensionless figure of Merit (ZT) for $CuCrSe_2$.

Fig. 4.21. Electronic absorption spectra for the samples.

Fig.4.22. Powder X-ray diffraction pattern for (a) $AgCrSe_2$, (b) $CuCrSe_2$ (c) $(AgCrSe_2)_{0.5}(CuCrSe_2)_{0.5}$ composites. (d) Magnified view of the highest intensity (*012*) XRD peak for all samples.

Fig. 4.23 XRD pattern for the hot pressed $(AgCrSe_2)_{0.5}(CuCrSe_2)_{0.5}$ pellets.

Fig. 4.24. SEM images of (a) $AgCrSe_2$ (b) $CuCrSe_2$ (c) $(AgCrSe_2)_{0.5}(CuCrSe_2)_{0.5}$ composites.

Fig. 4.25. Transmission electron microscope (TEM) image of (a) $CuCrSe_2$ (b) $AgCrSe_2$, and (c) $(AgCrSe_2)_{0.5}(CuCrSe_2)_{0.5}$. In the images, region inside white dotted lines shows the presence of nanoscale features with amorphous structure.

Fig. 4.26. (a) Survey (b) Se 3d XPS spectra of pure $AgCrSe_2$, $CuCrSe_2$ and $(AgCrSe_2)_{0.5}(CuCrSe_2)_{0.5}$ samples.

Fig. 4.27. Back scattered electron (BSE) image and X-ray elemental mapping of Cu, Cr and Se in the $AgCrSe_2$, $CuCrSe_2$ and $(AgCrSe_2)_{0.5}(CuCrSe_2)_{0.5}$ samples.

Fig. 4.28. Back scattered image of hot pressed $(AgCrSe_2)_{0.5}(CuCrSe_2)_{0.5}$ sample. The EDX spectrum of two different regions of the sample is shown at right.

Fig. 4.29. Thermoelectric properties of all hot pressed samples (a) electrical resistivity (ρ). (b) Seebeck coefficient (α). (c) Power factor (α^2/ρ).

Fig. 4.30. (a) Thermal diffusivity (D) and (b) specific heat (Cp) results for $AgCrSe_2$, $CuCrSe_2$ and $(AgCrSe_2)_{0.5}(CuCrSe_2)_{0.5}$ samples.

Fig. 4.31. Temperature dependence of thermal conductivity (k).

Fig. 4.32. Temperature dependence of the *ZT* for all hot pressed samples. (f) x dependence of *ZT* and k (at 773 K) for $(AgCrSe_2)_{1-x}(CuCrSe_2)_x$.

Fig.4.33. Schematic showing naturally obtained hierarchical architecture of the $(AgCrSe_2)_{0.5}(CuCrSe_2)_{0.5}$ sample. In the composites, the atomic scale (due to the disordered Ag and Cu atoms at high temperature), nanoscale (due to the presence of amorphous phase, dislocations, grain boundaries) and mesoscale ($CuCrSe_2$ precipitates in the uniformly mixed matrix of composite) disorders results in scattering of phonons of all wavelength. The green and purple circles in the middle schematic shows the presence of nanoscale disorder in the pure $CuCrSe_2$ and $AgCrSe_2$ matrix.

LIST OF TABLES

Chapter 1

Introduction

1.1 Physics of thermoelectricity

Thermoelectricity deals with direct conversion of a temperature difference across two ends of a material into electric voltage [1,2]. Conversely, when a voltage is applied to the material, it creates a temperature difference across the two ends [1,2]. At the atomic scale, as schematically shown in Fig. 1.1, an applied temperature gradient across a material causes charge carriers (electron or holes) to diffuse from the hot side to the cold side, resulting in the generation of a voltage across the material. In a metal, according to free electron model, conduction electrons are treated as a free flowing gas, "Fermi Gas"[3,4]. Heating one end of the metal, Fig 1.1, increases the thermodynamic chemical potential of the charge carriers (electron or holes), which allows electrons to diffuse towards cold end [5,6]. Thus a higher density of charge carriers builds up at the cold end, which continues to build up until the force due to the coulomb repulsion balances the force of thermal diffusion. Therefore the net flow of charge carriers towards the cold end of the material results in an electric potential difference between the ends of the material. Hence, a temperature difference, ΔT, in an ideal metal produces an electric potential gradient, ΔV. These two gradients are related by the Seebeck coefficient defined by: $\alpha = \frac{\Delta V}{\Delta \mathrm{T}}$ [1,2]. The sign of Seebeck coefficient or thermopower can be positive or negative, which depends upon the nature of charge carriers (holes or electrons) in the material, as shown in Fig. 1.1. The magnitude of α in a material is physically represented by the entropy per unit charge carried by electrical currents. In metals, since the charge carriers are large in number, rapid thermal equilibrium is obtained and thus the net value of α is very low [7].

Thermoelectricity encompasses three independently identified effects: Seebeck effect, Peltier effect, and Thomson effect. In addition, there is another effect known as Joule heating that is generated whenever a current is passed through a resistive material. Joule heating is though related, but not considered as a part of thermoelectric effect. The Seebeck, Peltier and Thomson effects are thermodynamically reversible, whereas Joule heating is irreversible [1,2].

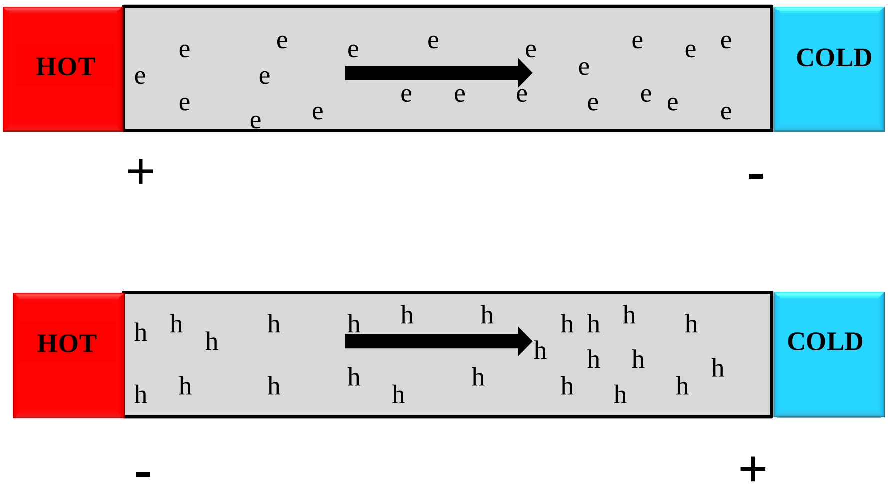

Fig. 1.1 Idealized bar of a metal demonstrating thermoelectric effect.

1.1.1 Seebeck effect

In 1821 Thomas Johann Seebeck found that a circuit made from two dissimilar metals with junctions at different temperatures, as shown in Fig. 1.2, produces an electric potential (voltage) which can drive an electric current in a closed circuit[8]. The Seebeck effect is a classic example of an electromotive force (emf) and leads to measurable currents or voltages in the same way as any other emf. The magnitude of this emf depends on: (i) The nature of materials forming the couple. Metals, such as, selenium, antimony, iron, cadmium, zinc, silver and gold are thermoelectrically negative; while metals, such as, mercury, copper, platinum, nickel and bismuth are thermoelectrically positive. (ii) The temperature difference between the two junctions. This model for metals can be extended to semiconductors or insulators by invoking the electronic distribution as a function of thermal energy. As shown in Fig. 1.3, the band structures are quite different for metals, semiconductors, and insulators. However, under a temperature gradient the higher energy conduction electrons at the hot end will migrate to the cold end that has unoccupied states of lower energies, leading to a Seebeck coefficient.

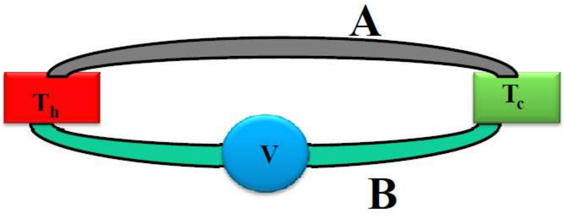

Fig 1.2 Schematic of a Seebeck loop.

At T=0 K, since there are no thermal or other energies for exciting electrons, therefore electron energy states are filled starting from the lowest state, obeying the Pauli's exclusion principle, to a highest occupied energy state known as the Fermi energy (E_F) [3]. At T > 0, electrons can be excited to higher energy states. The concentration of electrons ($n_{\Delta E}$) with energies between E and $E+\Delta E$, can be estimated by integrating the Fermi-distribution function, *f(E)*, and the density of electronic states, *g(E)*:

$$n_{(\Delta E)} = \int_{E}^{E+\Delta E} f(E).g(E).dE \tag{1.1}$$

Where *f (E)* is given by

$$f(E) = \frac{1}{e^{(E-E_F)/k_B T} + 1} \tag{1.2}$$

The number of states per unit energy is given by:

$$g(E) \equiv \frac{dn}{dE} \tag{1.3}$$

At T= 0K, *f (E)* reduces to a step function, with *f (E)*=1 for $E<E_F$ and = 0 for $E>E_F$. For T > 0K the *f (E)* remains an exponential function representing the statistical distribution of electrons. The energy state at *f(E)* = 1/2 represents the state that has the same probability of being occupied as well as unoccupied and is known as the Fermi level (E_F) for semiconductors. E_F must vary with temperature so that the electron concentration, according to Eq.1.2, is constant if integrated over all energies. For metals, electrons within k_BT of E_F contribute to conduction. In a semiconductor, above or below E_F, there exists a region where *g (E)* = 0, see Fig.1.3, which is known as band gap, and its value is of the order of 0.3-3.0 eV at 300K.

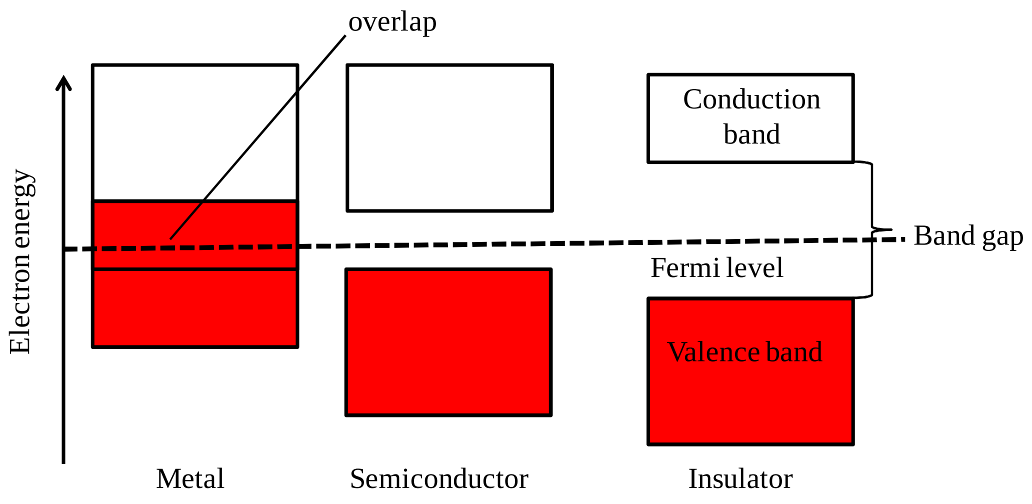

Fig 1.3 Schematic showing the band structure of crystalline metal, semiconductor and insulator at low temperature.

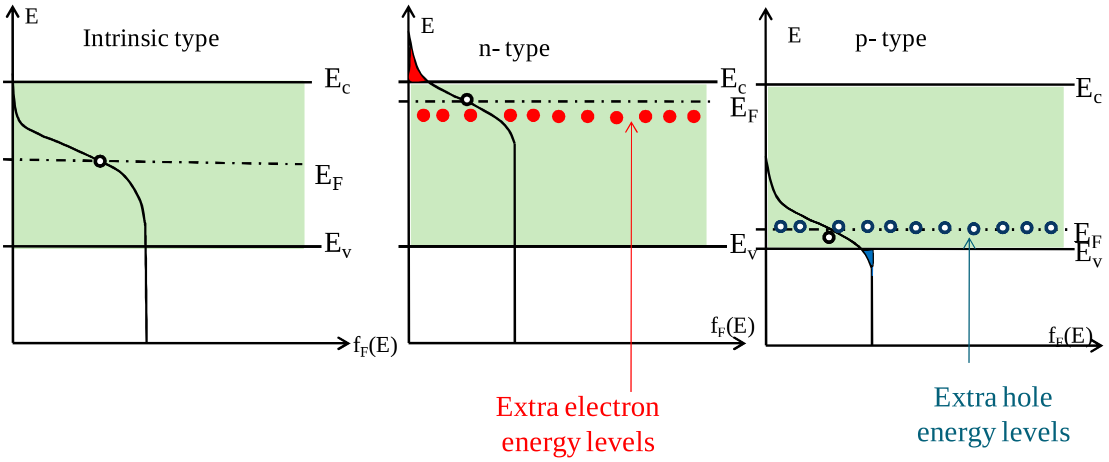

Fig 1.4 Schematic showing a shift of Fermi level (E_F) upon doping a semiconductor with acceptor and donor.

Under high energy approximation i.e. E >> E_F, *f(E)* reduces to Boltzmann distribution function:

$$f(E)=\frac{1}{e^{(E-E_F)/k_BT}} \qquad (1.4)$$

The population of electrons in the conduction band is governed by this distribution, and clearly depends on both the band gap and temperature. As a result, the carrier concentration and electrical conductivity of a semiconductor exhibit strong temperature dependence. For intrinsic semiconductors, the numbers of excited electrons are equal to the number of holes. For extrinsic semiconductors, doping of an impurity determines the electron and hole concentrations at thermal equilibrium. As shown in Fig. 1.4, the doping of semiconductors results in a shift in the Fermi level. Based on the number of valence electrons of the impurity atom, an electron will be donated or accepted from the conduction band, resulting in shifting Fermi level towards conduction band (i.e. n-type semiconductor) or towards valance band (i.e. p-type semiconductor). The sign of the Seebeck coefficient is a strong indication to whether the majority carriers are holes or electrons in a semiconductor i.e. negative Seebeck coefficient indicate electrons as carriers, and a positive indicate holes as the dominate carriers[7].

1.1.2 Peltier Effect

The Peltier effect is viewed as the inverse of the Seebeck effect. In 1834, French physicist Jean-Charles-Athanase Peltier discovered that when electric current is maintained in a circuit consisting of junctions of two dissimilar conductors, one junction gets cooled while other one gets heated[9]. For example, in a circuit consisting of a battery connected by two pieces of copper wire to a length of bismuth wire, a temperature rise occurs at the junction where the current passes from copper to bismuth, and a temperature drop occurs at the junction where the current passes from bismuth to copper. Peltier effect is stronger in circuits containing dissimilar semiconductors. The Peltier heat generated at the junction per unit time, dQ/dt, is given by:

$$\frac{dQ}{dt} = (\pi_A - \pi_B)I \tag{1.5}$$

where π_A ($=\alpha_A.T$) and π_B ($=\alpha_B.T$) are the Peltier coefficients of conductor A and B, respectively and I is the electric current (from A to B). Peltier coefficient is defined as the amount of energy in joules that is absorbed or evolved at a junction when one coulomb of charge flows through it for one second. It may be noted that the total heat generated at the junction may not only be due to Peltier effect but Joule heating may also contribute.

The Peltier heat is a consequence of the difference in the Fermi levels (or chemical potentials) of two dissimilar metals, as shown in Fig. 1.5. When a current passes from the material of lower Fermi level to the material of higher Fermi level, it absorbs heat from the lattice of the lower Fermi level material, causing cooling at the junction. A reversal of the current causes heating at the junction as the charge carriers dump heat back into the lattice as they go from a higher to lower Fermi level. The Peltier effect is also described in terms of entropy, where energy in the form of heat is evolved when the carriers flow from a material with higher entropy to one with lower entropy[10].

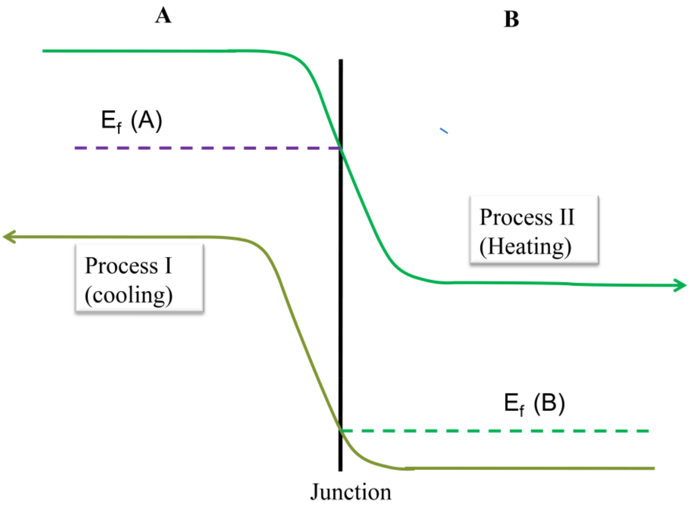

Fig 1.5 Schematic showing the mismatched Fermi levels of two dissimilar metals leading to cooling or heating at the junction depending upon the direction of the current.

1.1.3 Thomson effect

In 1854, British physicist William Thomson discovered that evolution or absorption of heat takes place when electric current passes through a circuit composed of a single material that has a temperature difference along its length[11]. This transfer of heat is superimposed on the common production of heat associated with the electrical resistance to currents in conductors. For example, if a metal wire carrying a steady current is subjected to external heating at a short zone (while the rest remains cooler), heat is absorbed from the metal as the current approaches the hot zone, and heat is transferred to the metal just beyond the hot zone.

If a current density J is passed through a homogeneous conductor, the Thomson effect predicts a heat production rate $\dot{Q}$ per unit volume of

$$\dot{Q} = -KJ.\Delta T \tag{1.6}$$

where ΔT is the temperature gradient and K is the Thomson coefficient, which is defined as the amount of energy in joules that is absorbed or evolved due to one coulomb of electricity flowing between two points in an unequally heated material differing in temperature by 1^{o}C. The K is related to the Seebeck coefficient as: $K = \frac{d\alpha}{dT}$. This equation however neglects Joule heating and ordinary thermal conductivity[12].

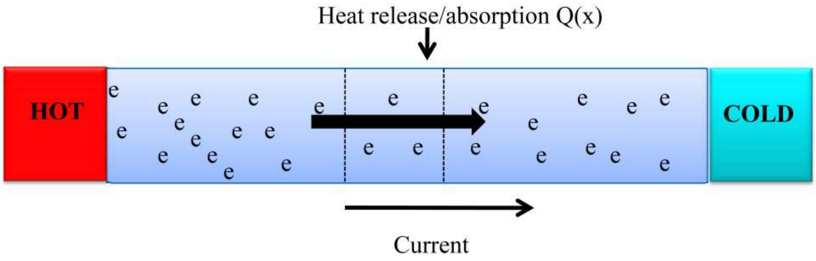

Fig 1.6 Schematic showing the Thomson effect.

1.2 Application of thermoelectricity

The thermoelectric devices based on Peltier and Seebeck effects are used for applications in refrigeration and electrical power generation, respectively [13]. The basic requirements to achieve a significant thermoelectric performance are the same for both generators and coolers. However, in practice both types of devices are usually very different from each other in design and construction, due to the difference in temperature range of operation and the intended application.

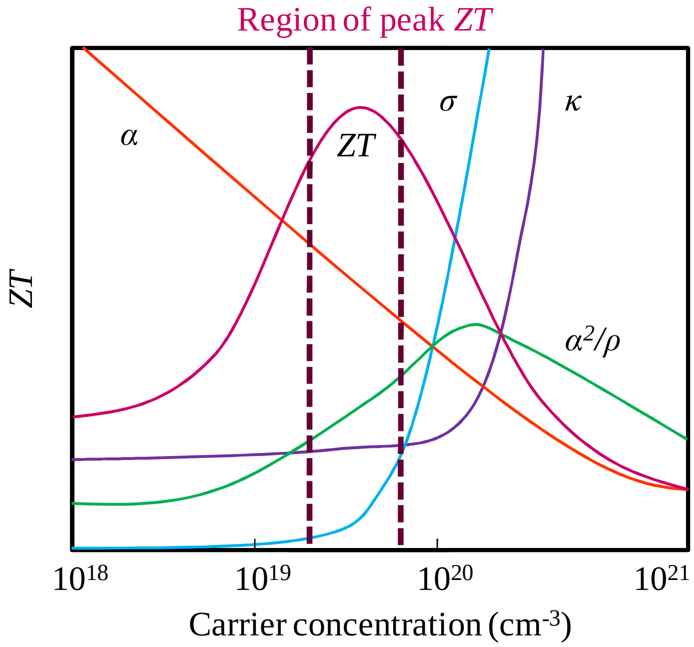

Fig. 1.7 Variation of α, σ, κ, power factor (α^2/ρ) and ZT on the carrier concentration (reproduced with permission from Snyder et al. Nat. Mater. 7 (2008) 105-114 © 2008 Nature Publishing group).

One of the critical requirements for the development of efficient thermoelectric devices is selecting proper materials with high figure-of-merit, ZT, which is defined as:

$$ZT = \frac{\alpha^2\sigma}{\kappa}T \tag{1.7}$$

where α is Seebeck coefficient, σ is electrical conductivity and κ is thermal conductivity[14,15,16]. The parameters α, σ and κ strongly depend on the carrier concentration (n) of the materials, and their dependences are schematically shown in Fig. 1.7.

It is evident from Fig. 1.7 that α decreases with increasing n (i.e. as one moves from insulating to metallic region), while σ and κ increases. As a result, the power factor ($\alpha^2\sigma$) and ZT show maxima for the n values in the range of 10^{19}-10^{20}cm^{-3}, indicating that highly degenerate semiconductors are good candidate for the thermoelectric applications. The high ZT of materials demand enhanced power factor ($\alpha^2\sigma$) but lower κ.

A degenerate semiconductor essentially is a semiconductor with high level of doping such that it behaves more like a metal than as a semiconductor. Therefore the σ of these materials can be expressed by:

$$\sigma = \frac{1}{\rho} = ne\mu \tag{1.8}$$

The dependence of α on σ has been derived using Boltzmann transport theory, which is expressed using the Mott equation [17,18,19,20]:

$$\alpha = \frac{\pi^2}{3}\frac{\kappa^2 T}{q}\frac{d\ln\sigma(E)}{dE}\bigg|_{E=E_F} \tag{1.9}$$

Where $\sigma(E)$ is the electronic conductivity determined as a function of the band filling or Fermi energy, E_F. If electronic scattering is independent of energy, then $\sigma(E)$ is just proportional to the density of states (DOS) at E_F. For degenerate semiconductors, if one ignores the effect of scattering, α can be also expressed in terms of DOS using [21]:

$$\alpha = \frac{\pi^2}{3}\frac{k_B}{q}k_B T\frac{DOS(E_F)}{\int_{E_F}^{E_V} DOS(E)dE} \tag{1.10}$$

where E_v is the valence band edge.

The Bethe-Sommerfeld equation of Seebeck coefficient for degenerate statistics and single-band case is given by [22,23]:

$$\alpha = \frac{\pi^2}{3}\frac{k_B}{q}\left(k_B T\right)\left[\frac{1}{n(E)}\frac{dn(E)}{dE} + \frac{1}{\mu(E)}\frac{d\mu(E)}{dE}\right]$$

$$= \frac{\pi^2}{3}\frac{k_B}{q}\left(k_B T\right)\left[\frac{g(E)}{n(E)} + \frac{1}{\mu(E)}\frac{d\mu(E)}{dE}\right] \qquad (1.11)$$

Where $\frac{g(E)}{n(E)}$ is DOS term and $\frac{1}{\mu(E)}\frac{d\mu(E)}{dE}$ is the scattering term.

It may be noted that DOS for free-electron case is related to m* by equation [21]:

$$DOS = \frac{\left(m^*\right)}{\pi^2\hbar^3}\sqrt{2E_F} \qquad (1.12)$$

Thus for metals and degenerate semiconductors (under the approximation of parabolic band and energy-independent scattering), the expression for α is inversely proportional to n and is given by [24,25,26]:

$$\alpha = \frac{8\pi^2 k_B{}^2}{3qh^2} m^* T\left(\frac{\pi}{3n}\right)^{2/3} \qquad (1.13)$$

where m^* is the effective mass, q is the electronic charge and h is the Planck's constant.

From above formulations, it is evident that the value of power factor ($\alpha^2\sigma$) depends on several conflicting parameters: (i) σ increases with n, but it leads to a decrease in α, (ii) α will increase if the m^* increases (eq. 1.13), but increasing m^* also implies that the μ would decrease, which in turn, will reduce σ. However, the relation between m^* and μ is complex and depends upon several factors such as electronic structure, scattering mechanism and anisotropy.

According to equation 1.7, the ZT can also be enhanced by reducing the thermal conductivity (κ), which comes from three sources i.e. electronic , lattice and bipolaronic [25,18]:

$\kappa = \kappa_e + \kappa_l + \kappa_{bi}$ (1.14)

Here κ_e is the heat transported by charge carriers (electron or hole) and is directly related to the σ through the Weidmann-Franz law $\kappa_e = L\sigma T = ne\mu LT$ [25, 18], where L is the Lorentz factor and its value for free electrons is 2.4×10^{-8} $J^2K^{-2}C^{-2}$, which however can vary with carrier concentration. κ_l is the lattice thermal conductivity due to the propagation of phonons, and κ_{bi} is the contribution due to bipolar diffusion and will be described later.

1.2.1 Thermoelectric refrigerators or Peltier coolers

The thermoelectric refrigerators make use of modules that contain a number of thermocouples connected electrically in series and thermally in parallel [1,27,28]. This enables the cooler or heat pump to be operated from a power source that delivers a manageable current with a reasonable voltage drop. The assumptions are that there will be no thermal resistance between the thermocouple and the heat source or sink and all the heat flow between the source and sink, takes place within the thermocouple. Thus, it will be supposed that thermal radiation and losses by conduction and convection through the surrounding medium are negligible [27]. The quantity of greatest importance for a refrigerator is the coefficient of performance (COP), which is defined as the ratio of the heat extracted from the source to the expenditure of electrical energy. If the thermocouple were free of losses associated with heat conduction and electrical resistance, the COP would reach the ideal value; that is, the value for a Carnot cycle [1,13]. The ideal COP can be much greater than unity as it is given by ${}^{T_c}\!/_{T_h - T_c}$ where T_h and T_c are the absolute temperatures of the source and sink, respectively. For thermoelectric cooling system the efficiency is given by its coefficient of performance, COP, which is given by

$$COP_{max} = \frac{T_c}{T_h - T_c} \frac{M - T_h / T_c}{M + 1} \tag{1.15}$$

where $M = (1 + \bar{ZT})^{1/2}$ with $\bar{T} = (T_h + T_c)/2$ and $\bar{ZT}$ is the average figure-of-merit of the material. Thermoelectric coolers usually utilize low band gap degenerate semiconductors e.g. Bi_2Te_3, having an energy gap of <0.3 eV.

1.2.2 Thermoelectric power generators

Thermoelectric power generators essentially consist of a large number of thermocouples (p and n legs) connected electrically in series and thermally in parallel to form a module. Heat from a variety of sources is supplied to one surface of the module (referred to as the hot side) and rejected at a lower temperature from the opposite surface (referred to as the cold side/ heat sink). The p- and n- legs are joined by a metal interconnect [27,29]. The voltage produced by the Seebeck effect will cause current to flow through the load, generating electrical power. The voltage at the load is reduced from the open circuit voltage by the Ohm's law (V = IR) voltage drop due to this internal resistance. Maximum efficiency (η_{max}) is reached when the load and internal resistances are nearly equal because this is close to the maximum power achieved from load matching and is given by [1,12,27]:

$$\eta_{\max} = \frac{T_h - T_c}{T_h} \frac{\sqrt{1 + \bar{ZT}} - 1}{\sqrt{1 + \bar{ZT}} + T_c / T_h} \tag{1.16}$$

The first term of the equation $\frac{T_h - T_c}{T_h}$ is the Carnot efficiency and the second term of the equation is the reduced efficiency which is a function of $\bar{ZT}$ i.e $\frac{\sqrt{1+\bar{ZT}}-1}{\sqrt{1+\bar{ZT}}+{}^{T_c}\!/_{T_h}}$. The schematic of the power generator is shown in Fig. 1.8. For power generators, depending upon the source temperature, materials having relatively narrow band gap degenerate semiconductors are utilized. For example, in the low temperature range Bi_2Te_3 is used, for the temperature range of 723-773 K, n-type PbTe (0.3 eV) [30,31] and p-type TAGS-85 (0.6 eV) [32] are utilized while for very high temperatures 1173-1273 K, SiGe (~1eV) [33,34] are employed.

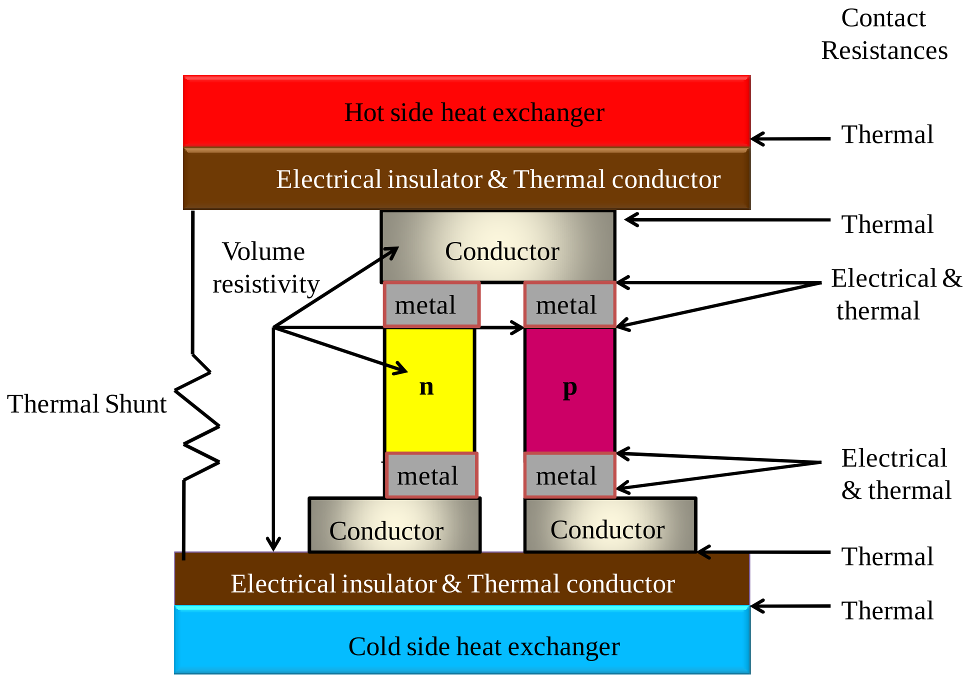

Fig 1.8 Schematic of a thermoelectric power generator showing different electrical and thermal interfaces. The electrical and thermal contact resistance should be minimum. Moreover, the device should have minimum thermal shunt path.

1.3 Fabrication issues with thermoelectric generators

As shown in Fig. 1.8, fabricating efficient thermoelectric generators from individual thermoelectric p- and n-legs is a big challenge and requires following three major key issues to be addressed [27,29]:

(i) Fabrication of n- and p-legs with high $\bar{ZT}$ in the temperature zone of application.

(ii) Electrical contacts having very low resistance at various interfaces, as schematically shown in Fig. 1.8.

(iii) Maximum heat transfer through device while minimizing the thermal shunt path.

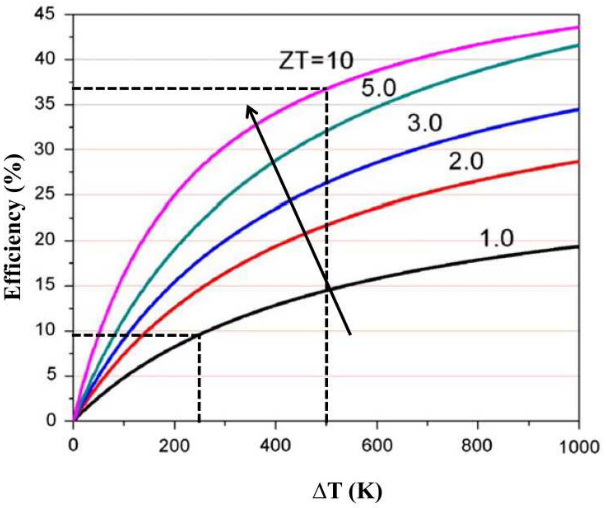

Fig 1.9 Theoretical maximum efficiency in electricity generation (cold source is at 300K) (reproduced with permission from Gang et al Progress in Natural Science: Materials International 6 (2012) 535–549. © 2012 Chinese Materials Research Society).

1.3.1 High ZT n- and p-legs

In order to have highly efficient TEG, the most important requirement is that materials of both n- and p-legs should have high *ZT* of nearly similar value at the operating temperature. The maximum theoretical efficiency expected for power generators as a function of temperature difference between the hot and cold ends (assuming the cold end is at 400 K) for materials having different *ZT* is shown in Fig 1.9. It is evident that theoretically for a material of *ZT* ~10, the theoretical conversion efficiency of ~35 % is possible for Δ*T* of ~500K [13,35].

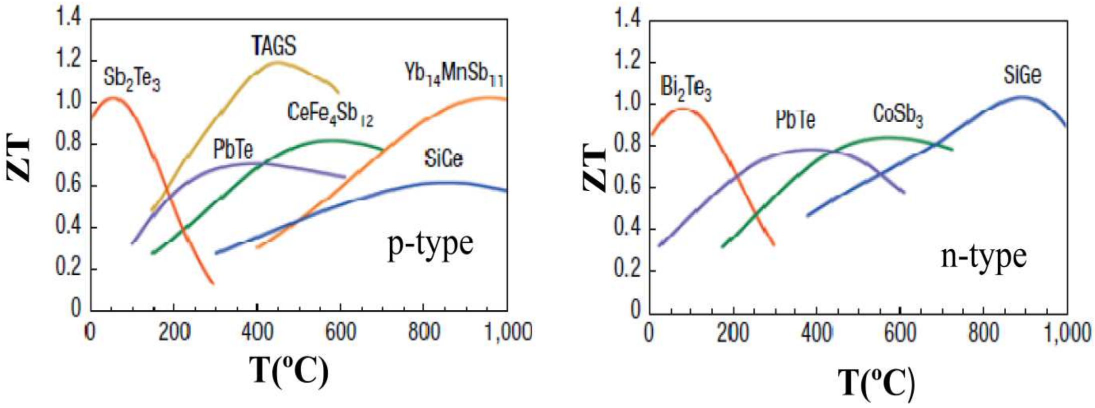

Fig 1.10 *ZT* vs *T* plots of conventional thermoelectric n- and p-type materials (reproduced with permission from Snyder et al. Nat. Mater. 7 (2008) 105-114.(c) 2008 Nature Publishing group).

On the experimental side however the situation for high *ZT* materials is quite different. The temperature dependence of *ZT* for various n- and p-type thermoelectric materials, commercially employed for device fabrication, are shown in Fig. 1.10. It is seen that the highest *ZT* of different materials lies in the range of 0.8-1.2 [25]. Depending upon the *ZT*, materials can be characterized based on their operating temperature range: (i) for low temperatures range 150-200°C: Bi_2Te_3 and Sb_2Te_3 [36,25]; (ii) mid temperature range 450-500°C: PbTe and TAGS-85 [25], and (iii) high temperature range (>800°C), SiGe alloys [25].

In order to achieve high efficiency in TEG, it is essential that devices are fabricated using high *ZT* materials with a large temperature gradient. Since *ZT* vary with temperature, it is not possible to use the same material throughout the entire, large temperature difference. One way to circumvent this problem is to use different materials that can be segmented together in such a way that a material with high *ZT* at high temperature is segmented with a different material with high *ZT* at low temperature. In this way, both materials operate in their most efficient temperature ranges [37,38,39,40]. However, when two materials are being segmented for large temperature gradient applications, one must consider the thermoelectric compatibility factor, expressed as: $S = \frac{\left[(1+ZT)^{\frac{1}{2}}-1\right]}{\alpha T}$ [41,42]. This is because to maintain maximum efficiency the same electrical current and similar heat must flow through each segment. If the compatibility factor differ by more than about a factor of 2, not all the segments will perform with the best efficiencies, and as a result, the overall efficiency of the devices will be substantially less than that predicted from the individual material's average *ZT* [42]. It is therefore evident that in order to obtain high efficiency, new materials exhibiting high *ZT* in different temperature range need to be investigated. In recent times a good efforts have been made in this direction, which are reviewed in the next Section.

1.3.2 Electrical contacts

As shown in Fig.1.8, the electrical resistance of the TEG depends not only on the electrical resistance of the thermoelectric legs but also the electrical resistance of the metal interconnects and the contact resistance between interconnects and thermoelectric legs. Moreover, in most of the materials, a metallized contact layer is required between the thermoelectric legs and interconnects. The contact layer and interconnects should have high thermal and electrical conductivity. All of these resistances are temperature dependent, and therefore, exact computation of the TEG resistance as a function of temperature is very complex. However, assuming temperature independence, the device resistance, R, can be approximated as [1]:

$$R = n\left[\frac{\rho_n l}{A_n} + \frac{\rho_p l}{A_p} + R_c\right] \tag{1.17}$$

Where, ρ is resistivity of legs, R_c is a sum of interconnect and contact resistance per couple, l is the length (height) and A is the cross-sectional area of the thermoelectric legs. If the contact resistance is very high then the devices efficiency reduces drastically as (i) the current generated by device will reduce, and (ii) the rise in temperature at contacts due to Joule heating will disturb the temperature gradient, leading to a decrease in thermopower. Making good electrical contacts in thermoelectric devices is challenging as the device operates under a large temperature difference, which leads to thermo-mechanical stress, diffusion and the chemical reaction between materials and interconnects. Ebling et al have reported both experimentally [43] and by simulation [44] that a major loss of average *ZT* and power output takes place due to poor contact . Ideal contact materials should have following properties:

(i) Electrical and thermal conductivities should be much higher as compared to thermoelectric material;

(ii) Coefficient of thermal expansion (CTE) should match with the thermoelectric material. This is because a good match of CTE between the contact and the thermoelectric material is necessary to have an efficient TEG. A system with significant CTE mismatch would experiences high interfacial stress, and thus, lead to high risk of in situ fracture of the device. This condition is not desirable as TEG's are mainly used for remote applications over the years. The acceptable limit of the CTE mismatch depends on the mechanical properties of both contact and thermoelectric material.

(iii) Chemically stable over the life time of the module and should not interact with the thermoelectric materials at the high working temperature [27]. A minor reaction between the TE materials and the contact barrier layers is sufficient to form a strong bond. This is because severe reactions between the contact and the TE materials lead to the formation of intermetallics, which contribute to high contact resistance. Moreover, the presence of voids or cracks at the interface causes failure of the contact. Thus, the selection of the contact material should be such that extensive reaction with the TE material and diffusion into the TE material are avoided. In addition, the thickness of the buffer layer should be minimized as it consumes ΔT and leads to parasitic loss.

(iv) Low contact resistance at the interface between the contact layer and the thermoelectric layer. In order to compare the quality of contacts fabricated with different cross-sectional area, the term specific-contact resistivity ρ_c (μΩ-cm^2) is used which can be estimated by multiplying the contact resistance by the cross-section area, $\rho_c = R_c \times A$, where R_c is the contact resistance and A is the cross- sectional area. Ideally, for good contacts ρ_c should be < 1 μΩ-cm^2 ·Reduction of specific contact resistivity is also a major criterion beside CTE matching and interfacial reaction. This problem arises due to the contact between the metal and semiconductor, which can be averted by band alignment between the contact layer and the TE material. The specific contact resistivity of a metal-semiconductor contact is related to the barrier height and doping concentration and according to Schottky-

Mott theory, is related to work function (φ) and electron affinity (χ) of these materials.

(v) Ability to be made very thin to reduce total electrical and thermal resistances;

(vi) Ability to form strong mechanical bonds with the thermoelectric layer.

These stringent requirements put the limitations on the choice of contact materials. Therefore, efforts are needed to make contacts that are not only with low resistances but should be mechanically/chemically strong for the operation of the device for prolonged periods, which are typically several years.

1.3.3 Minimization of thermal shunt path

In order utilize maximum heat available at the source, not only the good heat exchangers at hot and cold ends are needed but need to ensure an efficient flow of heat through the thermoelectric device. Similar to the electrical resistance, the total thermal conductance of the device can be approximated by [1]:

$$\kappa = n\left[\frac{\kappa_n A_n}{l} + \frac{\kappa_p A_p}{l} + \kappa_s\right] \tag{1.18}$$

where κ_S is the parallel thermal loss per couple, and needs to be minimized. In order to minimize the thermal shunt path, it is essential to use housing material in such a manner that its thermal conductivity is much lower than that of thermoelectric legs. In addition, the housing material should provide mechanical support for the device.

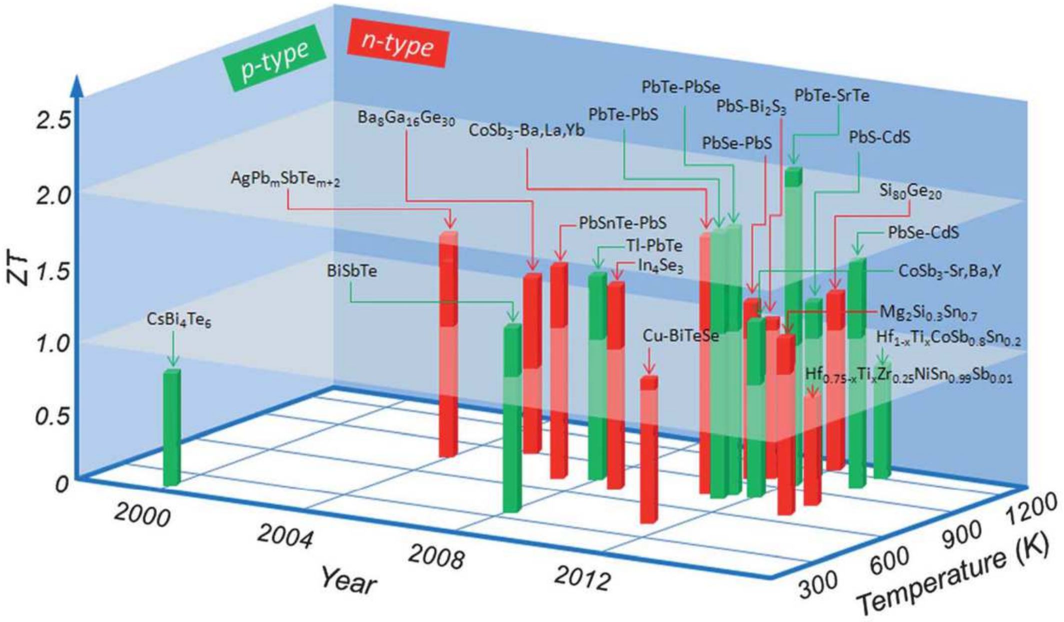

Fig.1.11 Current state of the art in bulk thermoelectric materials: *ZT* as function of temperature and year illustrating important mileston (reproduced with permission from Zhao et al, Energy Environ. Sci. 7 (2014) 251-268.(c) 2013 Royal society of chemistry).

1.4 Approaches to enhance the *ZT*

In recent years, there has been significant amount of research towards the synthesis of new thermoelectric materials with enhanced *ZT*. Fig 1.11 shows the major milestone achieved for *ZT* as a function of both year and temperature. Although this landscape is rapidly evolving because of continued advances in the field, only top performing materials are shown in this histogram [45].

In order to further discuss the approaches by which the *ZT* can be enhanced, equation 1.7 can be re-written as [46,47]:

$$ZT = \frac{\alpha^2 \sigma}{\kappa_e + \kappa_l} T = \left(\alpha^2 n\right)\left(\frac{\mu}{\kappa}\right) qT \tag{1.19}$$

It is evident that the *ZT* can be improved if both the terms i.e. $\alpha^2 n$ and μ/κ are increased. Unfortunately, the parameters of both the terms are counter-indicated i.e. if a mechanism that improves one can become deleterious to the other. In the case of $\alpha^2 n$, as shown in Fig. 1.7, the general rule in metals and doped semiconductors is that with increasing n, the value of α decreases (i.e. according to eqn. 1.19). Similarly, the term μ/κ is counter-indicated because introducing defects and impurities in the material scatters phonons which significantly reduces κ (beneficial effect), but they also reduce the μ (deleterious effect) owing to enhanced scattering of charge carriers. However, the requirement for improved *ZT* is that the material should have high μ along with low κ.

1.4.1 Enhancement of Seebeck coefficient

In order to enhance *ZT*, it is important to enhance the value of $\alpha^2 n$, which is purely an electronic property, and therefore, governed by the details of the electronic band structure and scattering mechanisms. The approaches to increase $\alpha^2 n$ are based on the engineering distortions of the DOS near the Fermi energy. In literature following approaches have been utilized to enhance $\alpha^2 n$. These include (a) modifying band structure by degeneration of multiple valleys, (b) Electronic resonance states, (c) Electron energy barrier filtering, (d) Highly mismatched isoelectronic doping, (e) Modulation doping and (f) Depressing bipolar effect .

a. Modifying band structure by degeneration of multiple valleys

As evident from equation 1.13, the thermopower at a given carrier concentration can be enhanced by increasing the overall DOS effective mass, m^*. The m^* is given by the expression: $m^* = N_V^{2/3} m_b^*$, where $m_b^* \sim 1/(d^2E/dk^2)$ is the band effective mass and N_v is the number of conduction bands [48, 49]. Thus, m^* can be enhanced either by a material having flat bands (i.e. high m_b^*) or by increasing the N_v (e.g. materials having multiple valleys). The implications of the enhancement of m_b^* and N_v are discussed below by citing appropriate examples.

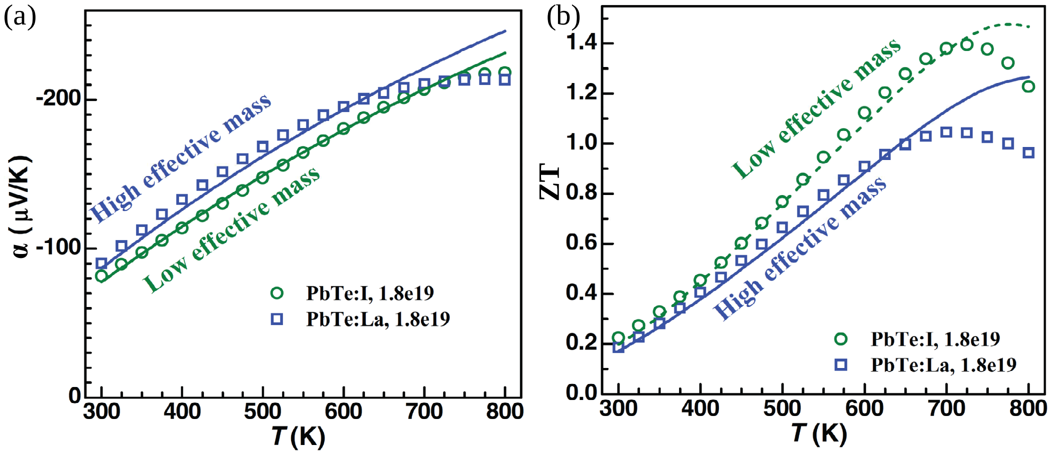

Fig. 1.12 Higher effective mass in La-doped PbTe leads to a higher Seebeck coefficient (a) but actually a lower *ZT* (b) in the entire temperature range (reproduced with permission from Pei et al, Adv. Mater. 24 (2012) 6125-6135. © 2012 WILEY-VCH Verlag Gm bH & Co. KGaA, Weinheim).

In case of materials having flat bands, the m^* would be very high, which will lead to a high α value. However, as discussed earlier, increased m^* also reduces the μ, and therefore, σ. As a result the overall power factor or *ZT* of the material may decrease. This in fact has experimentally shown by Pei.et al. They have doped n-type PbTe with either I on the Te site or La on the Pb site, in such a manner that the carrier concentration remains same (i.e. 1.8 $\times 10^{19}$ cm^{-3}). It has been shown that m^* in La doping is ~20% higher than that in I doping (near the optimal doping level) in the whole temperature range. The value of N_v was 4 in both the cases. The net effect of increased m^* is to increase α in La doped sample, as shown in Fig. 1.12(a). However, the overall ZT of La doped sample was found to be lower than the I doped samples, as shown in Fig. 1.12(b), mainly due to the reduction in the charge carrier mobility [49].

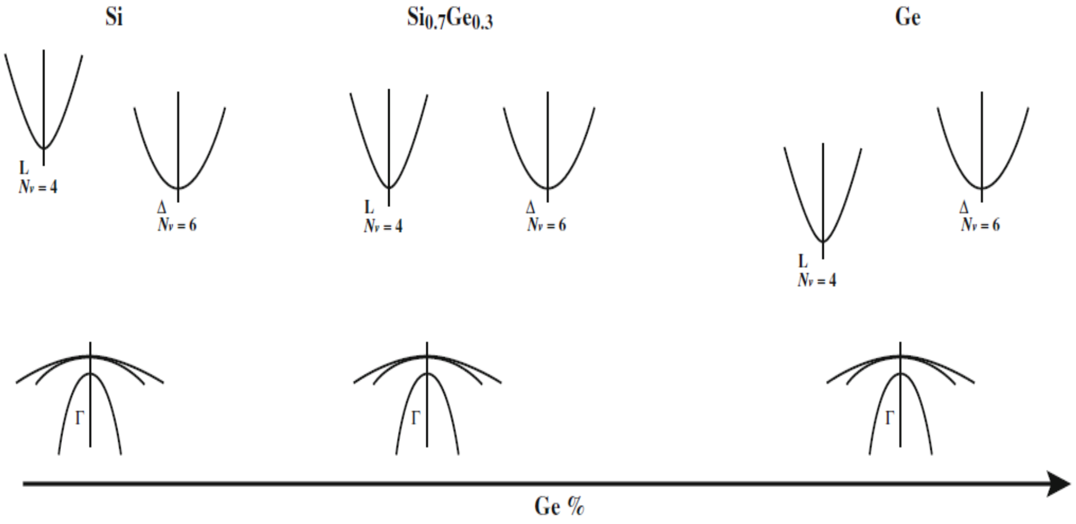

Fig. 1.13 The schematic band structure of SiGe alloy (reproduced from ref. 47).

.

The ZT of the materials can be improved through enhancement of m^* only if the charge carrier mobility is not affected and this can be achieved for materials having bands with multiple valleys. Thus in case of n-type materials to enhance the N_v, multiple band valleys should be in conduction band, while for p-type materials they should be in the valence band.

The n-type $Si_{1-x}Ge_x$ provides a classic example of band convergence in conduction band that increases N_v. Si and Ge, though similar in structure, are different in band configurations. The primary minimum of the conduction band in Si is found along the zone center and X point (Δ) with N_v =6 and the second minimum at the L point (L) with N_v =4. In Ge the band at the L point is the primary minimum with N_v =4 while the Δ band with N_v =6 is found at a higher energy. Alloying Si with Ge changes the energy position of L and Δ valleys relative to the top of valence band and it has been found that they cross each other around the composition of $Si_{0.7}Ge_{0.3}$, leading to an enhancement in the N_v value. As a result, the ZT of the n-type SiGe alloy is drastically improved [50].

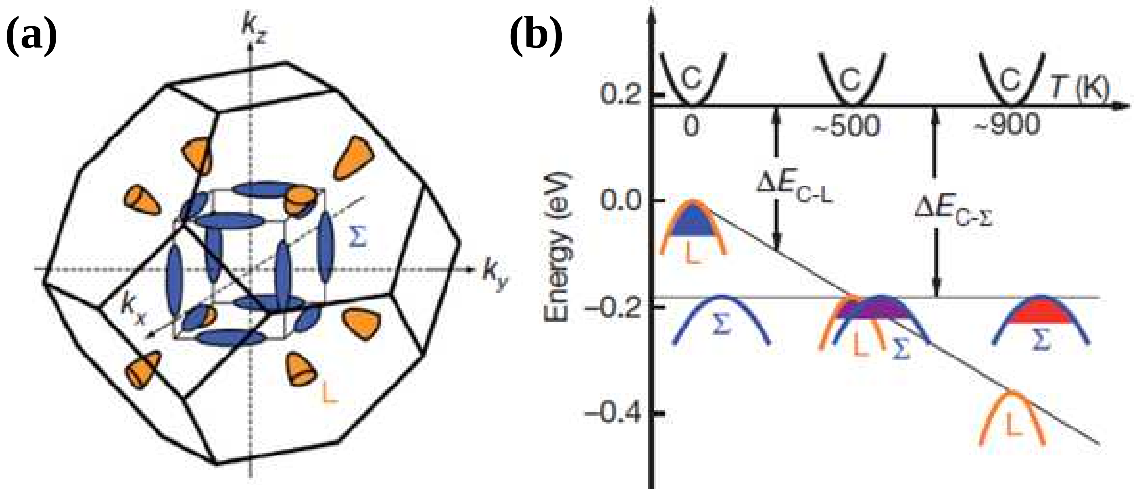

Fig. 1.14 (a) Brillouin zone showing the low degeneracy hole pockets (orange) centred at the L point, and the high degeneracy hole pockets (blue) along the Σ line. (b) Relative energy of the valence bands in $PbTe_{0.85}Se_{0.15}$. At, 500K the two valence bands converge, resulting in transport contributions from both the L and Σ bands. C, conduction band; L, low degeneracy hole band; Σ, high degeneracy hole band (reproduced with permission from Y. Pei et al Nature 473 (2011) 66-69. (c) 2011 Nature Publishing Group).

Another classic case of band convergence has been reported in lead chalcogenides, particularly PbTe and PbSe. Typical first Brillouin zone and valence band structure of PbTe is shown in Fig. 1.14. As shown in Fig. 1.14(a), there are 8 low degenerate half hole pockets (orange) centred at the L point (i.e. N_v=4), and the 12 high degenerate hole pockets (blue) along the Σ line (i.e. N_v=12). The corresponding relative energy of the Σ and L valence bands of PbTe is shown in Fig. 1.14 (b). It may be noted that there is only one conduction band. It has been shown that with increasing temperature, the energy position of the L band shifts downward and at 500K both Σ and L valence bands converge, resulting in enhancement in N_v [48].

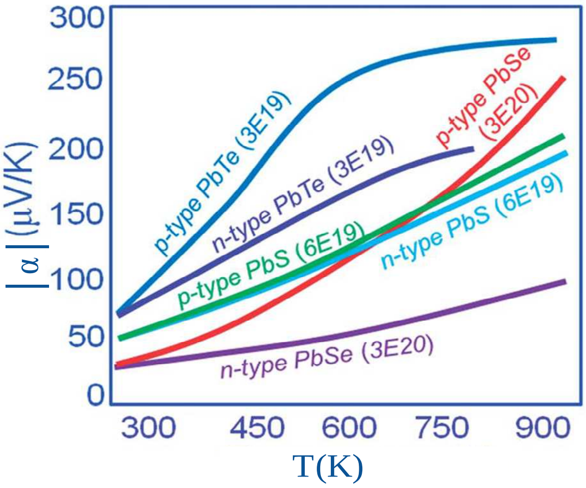

Fig. 1.15 Seebeck coefficient as a function of temperature for lead chalcogenides *viz.* PbTe, PbSe and PbS. The Seebeck coefficient is in general higher for p-type materials as compared with n-type analogues with a similar carrier concentration. . (reproduced with permission from Zhao et al, Energy Environ. Sci. 7 (2014) 251-268. (c) 2013 Royal Society of Chemistry).

The temperature dependent α for various lead chalcogenides is shown in Fig. 1.15. It is evident that for p-type lead chalcogenides the α is much higher than that of corresponding n-type with a similar n. For example, p-type PbTe the α is +270 μVK^{-1} (at 773 K) as compared to -180 $\mu V K^{-1}$ for n-type PbTe with same n of 3×10^{19} cm^{-3}. The excess α for p-type PbTe is attributed to additional contributions from Σ band [51,52,53]. The n-type PbTe do not exhibit such contribution because of the single band nature of the conduction band.

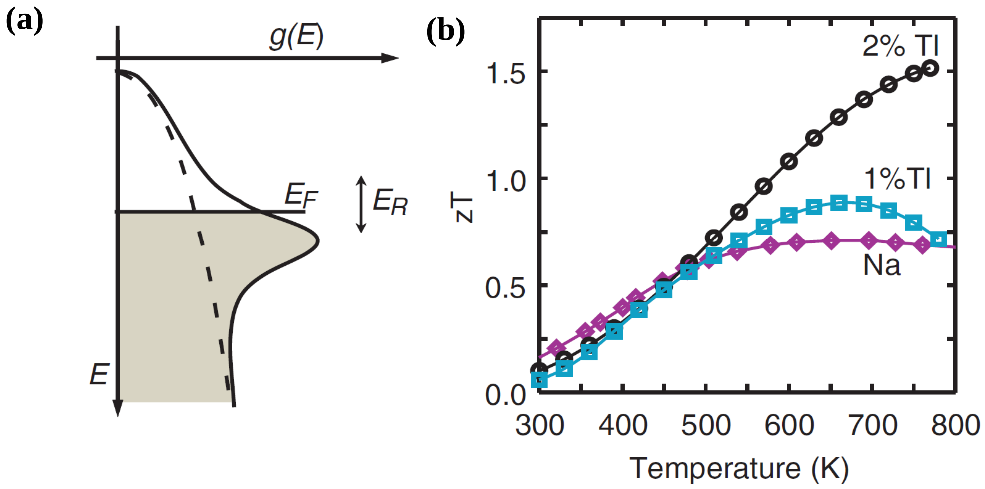

Fig. 1.16 Schematic representation of the DOS of the valence band of pure PbTe (dashed line) and Tl-PbTe (solid line) in which a Tl-related level increases the DOS. The temperature dependence of *ZT* for $Tl_{0.02}Pb_{0.98}Te$ (black squares) and $Tl_{0.01}Pb_{0.99}Te$ (blue circles) and reference sample Na-PbTe (purple diamonds) (reproduced from ref. 51).

b. Electronic resonance states

As represented by the equation 1.11, the α can be enhanced if the DOS at E_F can be enhanced significantly. In literature, in fact this has been achieved by doping the thermoelectric materials in such a way that the energy level of the dopant lies in the vicinity of the E_F of the thermoelectric material. The distortion due to resonance in the energy levels enhances DOS at the E_F [47] . In general, the sharper the local increase in DOS, the larger the enhancement in m^* and in α. For, $Tl_{0.02}Pb_{0.98}Te$, it has been shown that the α in the whole temperature range enhances by a factor between 1.7 and 3. However, the *ZT* value at 773 K was found to be 1.5, which is quite high as compare to undoped sample [54], see Fig. 1.16(b). It may be noted that the enhancement in α due to m^* compensates for the loss in mobility, as a result higher *ZT* is obtained. Similar behavior has been reported in Sn doped Bi_2Te_3 [55]. In this case, Sn provides excess DOS about 15 meV below the valence band edge at room temperature. Similarly, Cr is found to create impurity levels at 100 meV above the conduction band bottom of PbTe [56], Al doping forms resonant levels in PbSe [57] and Cd forms resonance level in PbTe [23].

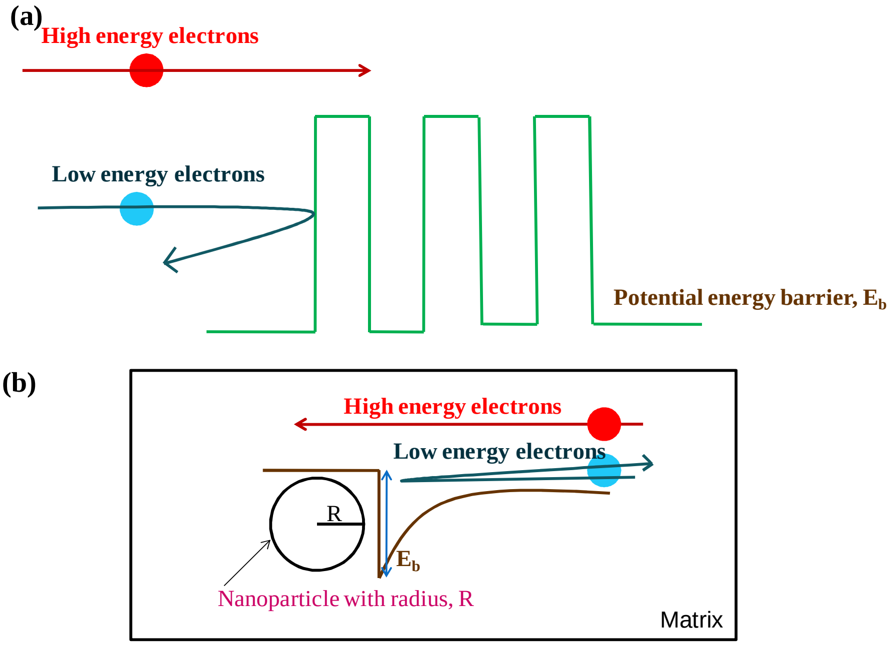

Fig 1.17 (a) Schematic showing the energy barrier filtering mechanism in (a) multilayers (b) nanoparticle dispersed in matrix. Due to the energy level mismatch at the interfaces, an energy barrier is created which filters the low energy electrons.

c. Electron energy barrier filtering

The magnitude of α is governed by the entropy per unit charge carried by electrical currents. Thus, α can be improved by an approach known as energy-filtering, whereby energy barriers are employed to block the low-energy electrons and therefore, increase the average heat transported per carrier by the high energy electrons [27]. Such effects has been observed in the thermoelectric multilayers, as shown in Fig. 1.17 (a) [58,59,60]. In case of bulk materials, nanostructured grains are often included in the matrix of thermoelectric materials, and the interfaces act as effective energy filters, as schematically shown in Fig. 1.17 (b). In both cases, grain boundaries act as barrier for filtering process i.e. low energy charge carriers ($E<E_b$) are blocked at the barrier, while high energy electron ($E>E_b$) pass through. It however may possible that these interfaces can also substantially reduce the carrier mobility, and therefore, energy filtering approach requires careful design of the nanostructures so that optimum power factor is obtained[27]. There are several reports claiming the observation of energy-filtering effects but these claims are limited to only small enhancements in the power factors. For example, in Pb-free β-Zn_4Sb_3 based composites incorporated with $(Bi_2Te_3)_{0.2}(Sb_2Te_3)_{0.8}$, ~30% increase in thermoelectric power factor has been obtained through an energy filtering effect caused by carrier scattering at interface barriers [61]. Dy doped TAGS-85 shows enhancement of the α due to an energy filtering mechanism. Here the potential barrier has occurred due to the mismatched atomic sizes and the large magnetic moment of the Dy atoms present in the lattice [62].

d. High mismatched isoelectronic doping

High mismatched alloys (HMA) are a kind of semiconductors containing isoelectronic elements with very large differences in terms of atom size, ionicity, and electronegativity, and therefore exhibit unusual and fundamentally different electronic/optical properties. As an example, proper alloying of (Si,Ge)Sn can result in a direct bandgap. The synthesis of HMA involves alloying of isovalent but highly electronegative mismatched constituents at dilute concentrations. However, due to large miscibility gaps, synthesis of HMA is usually difficult.

In HMAs, the hybridization between the extended states of the majority component and the localized states of the minority component results in a strong band restructuring, leading to peaks in the DOS and creation of new subbands near the original conduction or valence band edge. These narrow subbands formed in HMAs have a heavy effective carrier mass due to their localized origin and give rise to a sharp DOS distinct from those of the host material, which are responsible for high α [63].

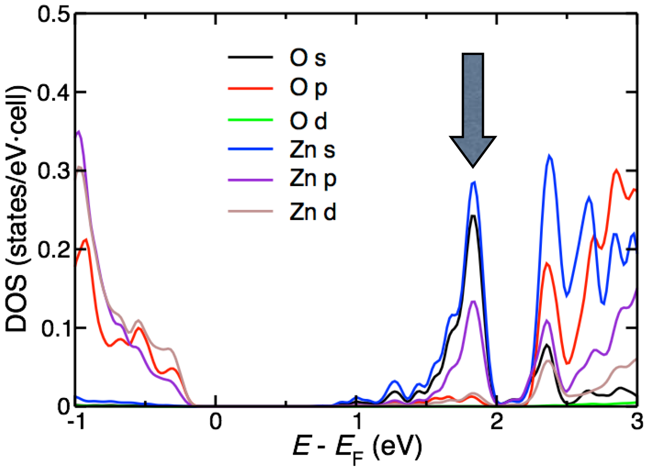

Fig. 1.18 DOS vs E-E_F plot of O impurity in ZnSe showing a peak in DOS near of E_F that enhances the α of the system. (reproduced from ref. 60).

In order to explain this strategy, Lee et al have investigated the effect of O impurities on the thermoelectric properties of ZnSe from a combination of first-principles and analytic calculations. It is demonstrated that dilute amounts of O impurities introduce peaks in the density of states (DOS) above the conduction band minimum and that the charge density near the DOS peaks is substantially attracted toward O atoms due to their high electronegativity, as schematically shown in Fig. 1.18. The impurity-induced peaks in the DOS result in a sharp increase of the room-temperature α and power factor from those of O-free ZnSe by a factor of 30 and 180, respectively.

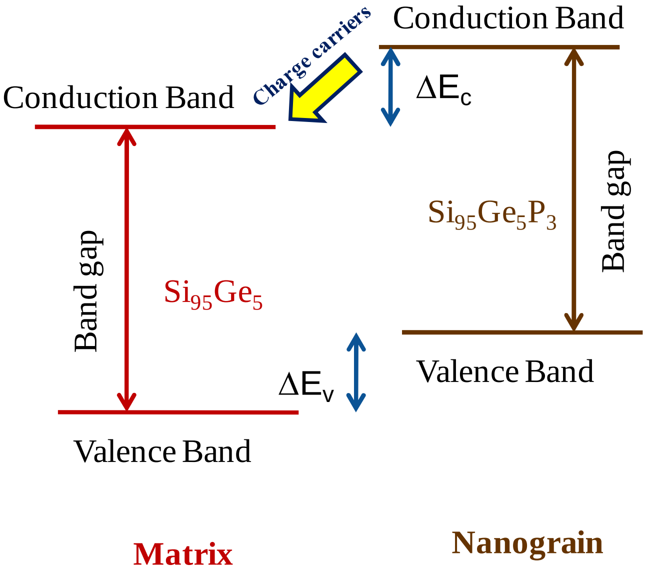

Fig 1.19 Schematic showing the modulation doping strategy for SiGe nanocomposite alloys.

e. Modulation doping

Modulation doping is implemented in such a way that the resulting free electrons are spatially separated from the positive donor ions and that the scattering of moving electrons by the dopant atoms is avoided. Due to the separation, electrons remain free and their mobility remains high. As a result the conductivity of the materials become high, leading to an enhanced power factor [64]. Modulation doped samples are usually two phase nanocomposites made out of two different types of nanograins. Rather than uniformly doping the sample, the dopants are incorporated into only one type of nanograins. Charge carriers spill over from the doped nanograins to the undoped or lightly doped matrix phase, leaving behind ionized nanograins. Thus the electrical conductivity of the two-phase composite can exceed that of the individual components, leading to a higher power factor [65]. Increase in the electrical conductivity also increases the electronic part of the thermal conductivity because the charge carriers are also heat carriers. So this strategy should also focus to reduce the lattice part of the thermal conductivity. Fig. 1.19 shows the schematic of modulation doping where $Si_{95}Ge_5$ has been considered as the matrix and $Si_{70}Ge_{30}P_3$ as nanograin (phosphorous is used as a dopant in the nanograin).

In this case, Si rich matrix ($Si_{95}Ge_5$) is chosen mainly due to the larger valley degeneracy of Si compared to Ge (as discussed earlier) [50], which leads to more available energy states for the carriers to fill in addition to the reduction in cost. The conduction band edge of the nanograin is higher as compared to that of matrix grains. This facilitates easy transfer of electrons from nanoparticles to matrix, which results in an increase in the mobility, as the ionized impurity is confined to the nanograin. The enhanced mobility increases the power factor by 20%. On the other hand, incorporation of $Si_{70}Ge_{30}P_3$ decreases the thermal conductivity. However, the increase in power factor compensates for the increase in thermal conductivity and as a result the *ZT* improves by 10% [64]. Power factor of the p-type $Si_{86}Ge_{14}B_{1.5}$ uniform sample was improved by 40% using the modulation-doping approach [65].

f. Depressing bipolar effect

As discussed earlier, the thermoelectric materials are narrow band gap semiconductors and thus have mixed carriers (electrons and holes) in each band, especially at high temperature, i.e. electrons in the valence band can partially hop to the conduction band and vice versa. This diffusion creates electron-hole pairs: the so-called bipolar effect [30, 30,46, 66]. Bipolar effect has the disadvantage because the minority charge carriers get thermally excited across the band gap and thus decreases the overall α [67,68,69].

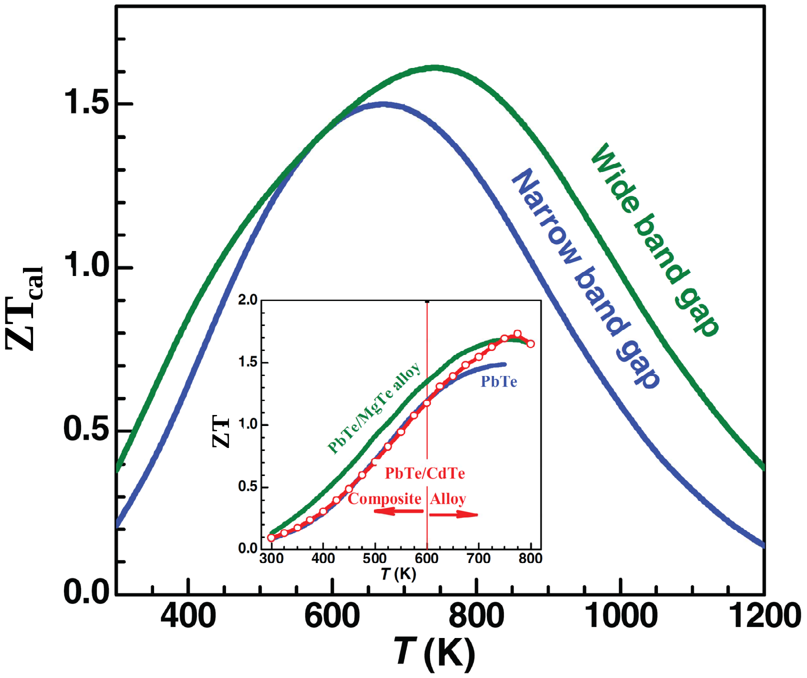

Fig. 1.20 Larger (or wider) band gap increases the *ZT* of a thermoelectric at high temperatures by inhibiting the formation of minority carriers of opposite sign, according to the model calculation. (Reproduced with permission from Pei et al, Adv. Mater. 24 (2012) 6125-6135. © 2012 WILEY-VCH Verlag Gm bH & Co. KGaA, Weinheim).

Bipolar effect can be depressed using following three ways: (i) increasing the majority charge carrier concentration which shifts the Fermi level and may decrease the onset of minority carrier effect by increasing the energy required to do so; (ii) increasing the band gap, which delays the onset of thermally activated minority carriers at high temperature [16,67,69, 70,71]; and (iii) synthesis of mesoscale microstructure with grain boundaries.

These grain boundaries act as an interface which produces interfacial potential and thus scatter electron and holes differentially, thereby deteriorating the bipolar effect [72]. The energy for bipolar diffusion can be roughly estimated as:

$$\kappa_{bi} = A\exp\left(\frac{-E_g^*}{2Tk_\beta}\right) \qquad (1.16)$$

Where κ_{bi} is the bipolar thermal conductivity, A is a constant, E_g* is the band gap for the bipolar diffusion , i.e. plot of $\ln(\kappa_{bi})$ vs $1/2\ (k_\beta T)$ gives E_g* (min. energy for bipolar diffusion to take place) and is comparable to the band gap of the material [31].

As shown in Fig. 1.20, it has been found that the *ZT* of wide band gap material is in general larger than that of low band gap materials, in particular at high temperature due to the depression of the bipolar effect. In order to prove this, PbTe has been alloyed with a wider band gap compound, such as MgTe [73,74] or CdTe [75,76] and the results are shown in the inset of Fig. 1.20. It is seen that MgTe has a good solubility in PbTe, which increases the band gap of the PbTe/MgTe alloy and therefore increases *ZT* value in the whole temperature range. On the other hand CdTe forms only composite with PbTe at low temperatures (<600 K), as a result there is no change in *ZT*. However, at high temperatures >600 K, PbTe/CdTe alloy formation takes place, which widens the band gap, and hence enhances the *ZT* [49].

1.4.2 Reduction in thermal conductivity

In addition to improving power factor, the *ZT* can be enhanced by reducing the thermal conductivity, in such a way that the charge carrier mobility is not reduced. The total thermal conductivity (κ) of a material is given by equation 1.14. Usually, the contributions from κ_e and κ_{bi} are much smaller than that of κ_l. However, κ_{bi} becomes dominant only at high temperatures. The κ_l is dominating as phonons of different wavelengths contribute to the heat conduction, and therefore, in literature various approaches have been adopted to reduce κ_l. In literature three general strategies have successfully adopted to reduce lattice thermal conductivity, which includes, (a) alloy point defect scattering [17], (b) complexity through disorder in unit cell [25] and (c) introduction of all length scale hierarchical architectures for scattering phonons of different wavelengths [72].

a. Alloy point defect scattering

The conventional method to reduce κ_l and to improve the *ZT* of the material is to decrease the phonon mean free path. This can be achieved by alloying, which creates point defects in the crystal lattice due to mass fluctuation. The judicious way to synthesis the alloy is to substitute the host atom by isoelectronic element which will minimize the carrier scattering . The classical example of this method is the $Si_{1-x}Ge_x$ alloy, where both Si and Ge have similar crystal structure and thus lattice order is preserved. Substitution of Si by Ge reduces the κ by an order of magnitude as compared to the undoped Si. However, in this process the μ gets reduced due to the fluctuation in the electric potential felt by charge carriers as they move through the crystal. This electrical potential is generated due to the difference in the electronegativity of Si and Ge. Despite μ being reduced, a net increase in *ZT* was obtained.

b. Complexity through disorder in the unit cell

Schematic of some of the complex crystal structures that yield low lattice thermal conductivity are shown in Fig. 1.21.

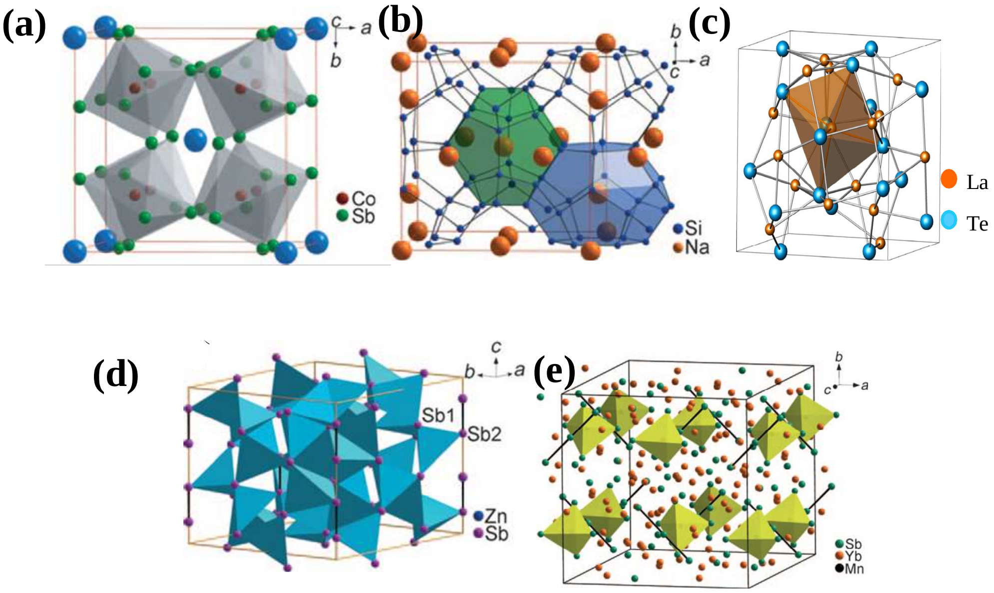

Fig. 1.21 Complex crystal structures of various thermoelectric materials (a) skutterudites (b) clathrates (c) $La_{3-x}Te_4$ (d) β-Zn_4Sb_3 (e) Zintl phase $Yb_{14}MnSb_{11}$ (reproduced with permission from Sootsman et al, Angew. Chem. Int. Ed. 48 (2009) 8616-8639.© 2009 WILEY-VCH Verlag Gm bH & Co. KGaA, Weinheim).

The skutterudite structure crystallizes in the $CoAs_3$- type structure which is composed of eight corner shared XY_6 (X=Co, Rh, Ir; Y=P, As, Sb) octahedra. In fact, the $CoAs_3$-structure type is a severely distorted version of the perovskite AB_3 type structure [18]. Fig 1.21 (a) shows that the linked octahedral produce a void at the centre of the $(XY_6)_8$ cluster which can accommodate large metal atom as a rattler. Fig 1.21(b) shows the type I structure of clathrate which can be represented by the general formula $X_2Y_6E_{46}$ (Na_8Si_{46} for example), where X and Y are “guest” atoms encapsulated in two different polyhedral cages E_{20} and E_{24}, while E represents tetrahedrally coordinate framework atoms. In these cages, the guest atoms are thought to effectively “rattle” and scatter lattice phonons, suppressing the lattice thermal conductivity [77]. La_3Te_4 exists in the Th_3P_4 structure [78] which is shown in Fig.1.21 (c). Te atoms sit on the P site and experience six-fold coordination with La via a distorted octahedron. The structure accommodates vacancies on the rare earth site, and up to one-ninth of the lanthanum atoms can be vacant. The presence of vacancies provides disorder and distortion in the lattice, which enhances phonon scattering and contributes to the low lattice thermal conductivity. The crystal structure of β-Zn_4Sb_3 is shown in Fig.1.21 (d), and has one Zn site and two independent Sb sites. One site is disordered in Zn and thus leads to some non-stoichiometry in the compound [79,80]. The complexity of the $Yb_{14}MnSb_{11}$ unit cell crystallizes in the complex structure of $Ca_{14}AlSb_{11}$ shown in Fig.1.21 (e) [42,81]. It consists of one $[AlSb_4]^{9-}$ tetrahedron, one $[Sb_3]^{7-}$polyatomic anion, four Sb^{3-} anions situated between $[AlSb_4]^{9-}$ and $[Sb_3]^{7-}$ units, and $14Ca^{2+}$ per formula. The Zintl formalism describes these units as covalently bound with electrons donated from the ionic Yb^{2+} sublattice to Sb atoms in the structure.

The temperature dependences of the lattice thermal conductivity for several materials having complex crystal structures are in Fig. 1.22. In Zn_4Sb_3, extremely low κ_l arises from scattering sources at multiple length scales which scatter a broad range of phonon frequencies. These sources include: (a) Partially occupied interstitial sites, leading to point defect scattering,(b) Soft, anharmonic bonding, as indicated by the high ionic conductivity and low energies of the various interstitial models [82], (c) 'Nanodomains' of the low temperature ordered structure revealed in the high temperature structure through pair distribution fuction (PDF) analysis [83] . In $Yb_{14}MnSb_{11}$, the low κ_l is primarily attributed to the ionically connected components providing a less rigid structure, in a manner similar to Zn_4Sb_3, except that for $Yb_{14}MnSb_{11}$, defects appear not to play role, in addition to the complexity (limiting the phonon mean-free path) and heavy atomic mass (reducing the fraction of atomic vibrational modes that carry heat efficiently) of the crystal. In case of skutterudites, the smaller and heavier ion in the voids, create disorder in the lattice, in addition to the rattling effect and thus reduces κ_l. The presence of vacancies in $La_{3-x}Te_4$, provides disorder and distortion in the lattice, which enhances phonon scattering and contributes to the low κ_l. In case of $Ba_8Ga_{16}Ge_{30}$ (clathrate), in addition to the open nature of the framework which reduces κ_l, the guest atoms inside, the cage are thought to effectively "rattle" and scatter lattice phonons, suppressing the κ_l. In case of Ag_9TlTe_5, one of the main reason for extremely low κ_l is relatively long Tl-Te bonds which produce very low frequency phonons [84]. In TAGS, the reduction in κ_l can be attributed to an increase in the anharmonicity of the lattice vibrations (phonons), which reduces heat propagation through the lattice.

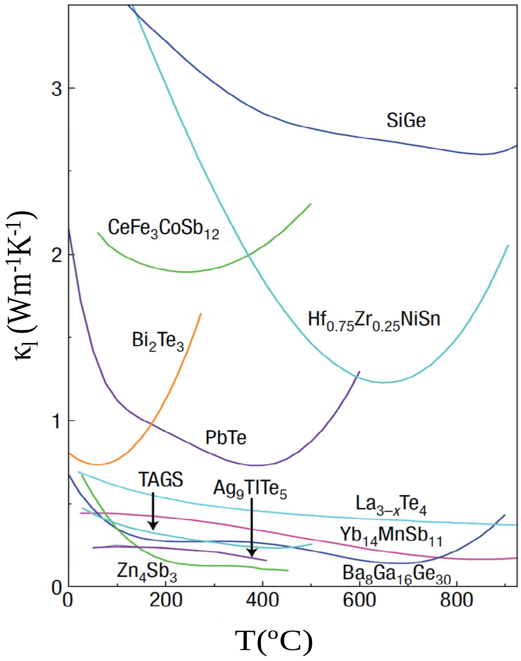

Fig. 1.22 Complex crystal structures that yield low lattice thermal conductivity (reproduced with permission from Snyder et al. Nat. Mater. 7 (2008) 105-114.(c) 2008 Nature Publishing group).

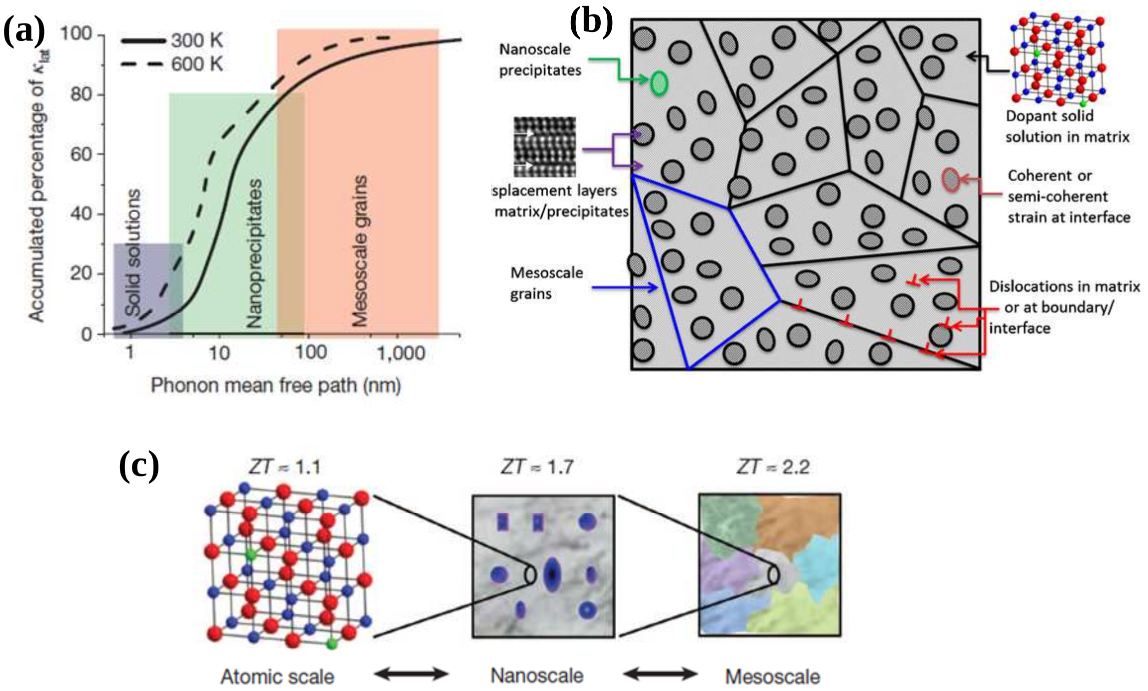

Fig 1.23 (a) Contributions of phonons with varied mean free paths to the accumulated κ_l value for PbTe at different temperature. (b) Schematic illustration of all length-scale structures for high performance thermoelectric systems where major contributing factors for reducing the lattice thermal conductivity are indicated. (c) maximum achievable *ZT* values for the respective length scales: the atomic scale (alloy scattering: red, Te; blue, Pb; green, dopant), the nanoscale (PbTe matrix, grey; SrTe nanocrystals, blue) to the mesoscale (grain-boundary scattering). (reproduced with permission from Biswas et al Nat. Chem. 3 (2011) 160-166 .(c) 2012 Nature Publishing group and J. He et al Mater. Today 16 (2013) 166-176.(c) 2013 Elsevier Ltd.).

c. All length scale hierarchical structuring

In thermoelectric materials the heat is carried away from hot end to cold end by phonons having a wide range of wavelengths i.e. from 1-1000 nm, and their contributions are schematically shown in Fig. 1.23 (a). In order to scatter these low, mid and long wavelength phonons, it is essential that the material contains scattering centres of the equivalent sizes, as schematically shown in Fig. 1.23(b). As discussed in the previous section, atomic defects, atoms of different masses in the lattice, dislocations, displacements of layers etc. acts as effective scattering centres for low wavelength phonons (0.2-5 nm). However, for mid and long wavelength phonons, one need to incorporate the nanoscale precipitates in the matrix. These nanoscale precipitates and their coherent and semi-coherent grain boundaries act as effective scattering centres for mid wavelength phonons (5-100 nm). Long wavelength phonons (>100 nm) are scattered by the mesoscale grain boundaries [72]. The enhancement of *ZT* due to the presence of the scattering cenetrs of different sizes is shown in Fig. 1.23 (c). It clearly indicates that the *ZT* is ~1.1, if the material has only atomic scale scattering centers. If the materials also have the nanoscale precipitates, the *ZT* enhances to ~1.7. By incorporating the mesocale grain boundaries, the *ZT* can further be enhanced to 2.2. For example in SiGe alloy, the *ZT* is ~1 due to the mass differences of Si and Ge, which reduces the κ. The varied contributions to phonon scattering by structures at all length scales i.e. atomic-, nano- and meso-scale, has been demonstrated in spark-plasma-sintered (SPS) samples of PbTe–SrTe (4 mol%) doped with 2mol% Na. A record *ZT* value of 2.2 (at 915 K) has been reported [85].

1.4.3 Slack's proposal: phonon glass and electron crystal (PGEC)

As discussed in the previous two sections that the enhancement of *ZT* requires (i) enhancement of power factor and (ii) reduction in the thermal conductivity. This implies that charge carriers should move in the thermoelectric materials with high mobility, which is analogous of having an electron crystal. On the other hand, all heat carrying phonons should be scattered, which is analogous of having a phonon glass. Slack has proposed that the material having "phonon glass electron crystal" (PGEC) like nature would exhibit very high *ZT* [1,86]. The PGEC approach has stimulated a significant amount of new research and has led to significant increases in *ZT* for several compounds.

1.5 Scope of the thesis

Currently, the efficiency of the thermoelectric generator is ~6-9%, which limits their use in commercial applications. It is evident from the earlier discussions that there are several issues in fabricating the high efficiency thermoelectric generator, which includes the *ZT* of materials and fabrication of low contact resistances. Therefore, the motivation of the present thesis is two folds:

(i) Synthesis of well established thermoelectric materials and fabrication of thermoelectric devices with low contact resistances. For this purpose, we have selected n-type PbTe and p-type TAGS-85 alloys, and the emphasis was on the preparation of metallic-interconnects with thermolegs having low contact resistances and fabrication of TEG with minimum thermal shunts. The prototype devices have been fabricated and tested for their long term stability. We have demonstrated thermoelectric devices with 6% efficiency.

(ii) Synthesis of high *ZT* materials through reducing the lattice thermal conductivity by introducing all-scale hierarchical defects i.e. from atomic, nano, meso to micro scale. The thermoelectric materials investigated include different selenides (i.e. Se doped PbTe, Cu-doped $TiSe_2$, $CuCrSe_2$, $AgCrSe_2$, $CuCrSe_2/AgCrSe_2$ nanocomposites) and nano-structutured SiGe alloys. These alloys have been synthesized using vacuum-melting, melt-and-quench, and/or high-energy ball milling. The synthesized alloys have been characterized for morphology, structure and temperature dependent thermoelectric properties. We have demonstrated *ZT* of 1.4 for $(AgCrSe_2)_{0.5}(CuCrSe_2)_{0.5}$ at 773 K and record value of 1.84 at 1073 K in SiGe alloys.

The experimental work and the obtained results obtained during the thesis work are organized as follows.

In Chapter 2, we describe the details of experimental methods used for the synthesis, and characterization of different types of thermoelectric materials and fabrication of devices. Details of the equipments used in the synthesis of thermoelectric materials viz. vacuum melting, melt-and-quench, and/or high-energy ball milling as well as the process of the synthesis (i.e. rocking furnace, induction melting furnace, ball-mill and vacuum hot press) are described. Overview of the various characterization techniques used in the thesis work are discussed, which includes X-ray diffraction (XRD), X-ray photoelectron spectroscopy (XPS), diffuse reflectance UV-Vis spectroscopy (DR-UV-Vis), Kelvin probe, scanning electron microscope (SEM), transmission electron microscope (TEM) and energy dispersive X-ray analysis (EDX). In addition, the details of the setups used for the temperature dependent measurements of Seebeck coefficient, electrical resistivity and thermal conductivity are described.

In Chapter 3, the results on the synthesis of single-phase n-type PbTe and p-type TAGS-85 thermoelectric materials as well as their morphological and structural characterization are discussed. SEM images and EDX analysis of electrode and thermoelectric material interfaces revealed chemically sharp interfaces even after a long period of operation of the devices. The average specific contact resistance (for all contacts in the devices) was found to be $\leq 10\ \mu\Omega cm^2$. For a hot end temperature of 773 K and a temperature difference of 683 K, two leg devices exhibited typical output power of ∼1.2W (at current of 17 A) with a working efficiency of 6%. The devices have been continuously operated for 8 months without any degradation.

In Chapter 4, we describe the thermoelectric properties of the selenides (i.e. Se doped PbTe, Cu-doped $TiSe_2$, $CuCrSe_2$, $AgCrSe_2$, $CuCrSe_2/AgCrSe_2$ nanocomposites) with an emphasis on enhancing their *ZT*. In the case of $PbTe_{1-x}Se_x$, a dramatic reduction in κ value has been achieved in n-type $PbTe_{0.5}Se_{0.5}$ due to atomic mass fluctuation in addition to the increase in thermopower. This has led to an increase in the dimensionless figure of merit *ZT* to 0.95 at 600 K. Usually, $TiSe_2$ is used as a low temperature thermoelectric material as the band gap is (<0.3 eV). In our study, Cu was intercalated in $TiSe_2$ and high temperature thermoelectric properties were measured. The samples exhibited very low κ value due to the layered growth structure and rattling effect of weakly bound Cu atoms in the van der Waals gaps of $TiSe_2$ layers. *ZT* value of 0.1 and 0.15 has been achieved for pure $TiSe_2$ and $Cu_{0.11}TiSe_2$ samples, respectively, at 650 K. Very low κ of $CuCrSe_2$ bulk has been achieved due to the phonon scattering by various sources such as (i) superionic Cu ions between $CrSe_2$ layers, (ii) nanoscale precipitates in the bulk and (iii) natural grain boundaries due to layered structure of the material. This led to a very high *ZT* ~1 at 773 K. High thermoelectric performance has been obtained in $(AgCrSe_2)_{0.5}(CuCrSe_2)_{0.5}$ nanocomposites due to the scattering of phonons by all-scale natural hierarchical architectures, which resulted in a high *ZT* of ~ 1.4 at 773 K.

In Chapter 5, we describe the results on the synthesis of $Si_{80}Ge_{20}$ alloys using ball milling as well as melt-quench methods. It has been shown that the ball-milled SiGe alloys exhibit much superior *ZT* values as compared to the material synthesized using melt-quench method. A highest value of *ZT* of ~1.84 at 1073 K has been obtained for ball-milled n-type SiGe nanostructured alloys, which is 34% higher than the reported value till date.

In Chapter 6, we summarize the main conclusions of the thesis. It has been conclusively demonstrated that by introducing various types of defects, such as, atomic scale disorder, nanoscale amorphous structure, grain boundaries at meso/microscales in the thermoelectric alloys, their ZT can be dramatically enhanced essentially by lowering κ.

Chapter 2

Experimental Techniques

2.1 Introduction

This chapter describes the details of experimental methods used for the synthesis and characterization of different types of thermoelectric materials (i.e. PbTe, TAGS-85, various selenides and SiGe alloys) and their characterization. For the synthesis of thermoelectric materials in this work, we have used melt-growth, melt-and-quench and mechanically alloying processes. For melt-growth and melt-and-quench processes, several facilities were fabricated in-house, including rocking furnace, induction melting casting furnace and vacuum hot press. On the other hand, the mechanically alloying of thermoelectric materials has been performed using high-energy ball milling. Specifically, tellurides and selenides were synthesized by melt-growth method, while the SiGe alloys were synthesized using either melt-and-quench method or by mechanical alloying method.

The synthesized thermoelectric alloys have been characterized for structure, composition and morphology. The structure of the materials have been investigated by X-ray diffraction (XRD); composition using energy dispersive X-ray analysis (EDX) and X-ray photoelectron spectroscopy (XPS); and morphology using scanning electron microscopy (SEM) and transmission electron microscopy (TEM). In some cases, the band gap of the alloys have been estimated using diffuse reflectance UV-Vis spectroscopy (DR-UV-Vis). Similarly the work function of the alloys has been estimated using scanning Kelvin probe method. A brief discussion on the working of these techniques is presented.

The thermoelectric properties, namely, Seebeck coefficient, electrical resistivity and thermal conductivity have been measured as a function of temperature. The details of the setups used for the measurements of thermoelectric parameters are discussed.

2.2 Synthesis of thermoelectric materials

Both tellurides and selenides have the congruent melting points of <1000°C, and therefore, they were synthesized using melt-growth method. On the other hand, SiGe not only have high melting temperature (>1350°C) but also have an issue of phase separation [1], which will be discussed in Chapter 5. These limitations demand SiGe to be synthesized using either melt-and-quench method or by mechanical alloying method. In this Section, we briefly present the methodology of these synthesis techniques.

2.2.1 Melt-growth method

In the melt-growth method, the constituents of the alloy being synthesized are mixed in the stoichiometric ratio and heated above the eutectic melting point of the alloy. This method is applicable only for eutectic mixtures i.e. the solidus and liquidus temperatures are identical, which indicates that the mixture melts completely at one temperature known as the eutectic point. A slow cooling of the melt results in the formation of ingots of the alloy. However, extreme care needs to be exercised particularly with respect to (i) any presence of oxygen, and (ii) segregation if the constituents have wide difference in their physical density.

Presence of oxygen easily oxidizes the material, which degrades the thermoelectric properties of the synthesized alloy. To avoid oxidation, we have filled the constituents of the alloy being synthesized in a clean and degassed graphite bottle, which is then sealed in a quartz ampoule under a vacuum of ~10^{-5} torr. A typical photograph of such an ampoule is shown in Fig. 2.1. The graphite bottle serves two purposes: (i) it avoids a direct chemical reaction of the melt with quartz ampoule; and (ii) in case of an increased vapour pressure of the melt, it shuns the explosion of the quartz ampoule.

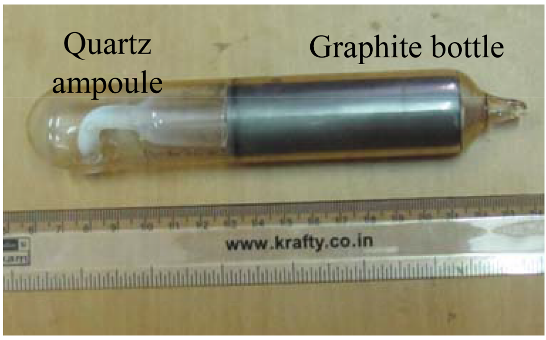

.

Fig. 2.1 A photograph showing the material filled graphite bottle enclosed in a vacuum sealed quartz ampoule.

Fig. 2.2 A photograph of the in-house built rocking furnace.

Another issue with melt growth can be the segregation of constituents if they have wide differences in their physical densities. For example, in PbTe, the densities of Pb and Te are respectively, 11.34 and 6.24 g/cm^3. In such a case, heavier element will settle down at the bottom of the melt, which eventually will result in the formation of an inhomogeneous alloy. In order to circumvent this problem, we have designed and fabricated a ‘Rocking Furnace”, as shown in Fig. 2.2, in which the cylindrical furnace (55 cm long and 30 cm diameter) oscillates by 45° (with respect to the horizontal plane) on either side. This movement of the furnace is accomplished by a stepping motor and a planetary gear head. A temperature of 1273 K can be attained in this furnace. The melt is cooled slowly to room temperature. A continuous rocking of the furnace allows homogeneous mixing of the constituents in the melt, and therefore, avoids any kind of segregation. The quartz ampoule is then break to obtain an ingot of the alloy. A typical photograph of a PbTe ingot is shown in Fig. 2.3. This ingot is subsequently grinded using mortar pestle to obtain a homogeneous powder of the alloy.

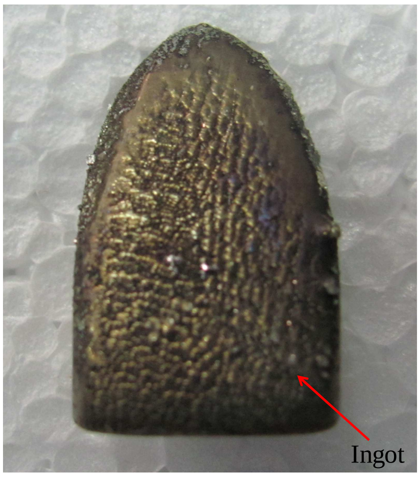

Fig. 2.3 Photograph of PbTe ingot obtained from the melt growth.

2.2.2 Melt-and-quench growth method

The melt-growth method, as discussed above, is not suitable if the solidus and liquidus lines of the mixtures are different e.g. in the case of SiGe which is described in Chapter 5. If a gap exists between the solidus and liquidus lines and the melt is cooled slowly then as per the Lever rule, inhomogeneous alloy composition may take place, which is undesirable for thermoelectric applications. Thus, in order to obtain an alloy of a single composition, melt is quenched to room temperature, and therefore, this technique is known as melt-and-quench method.

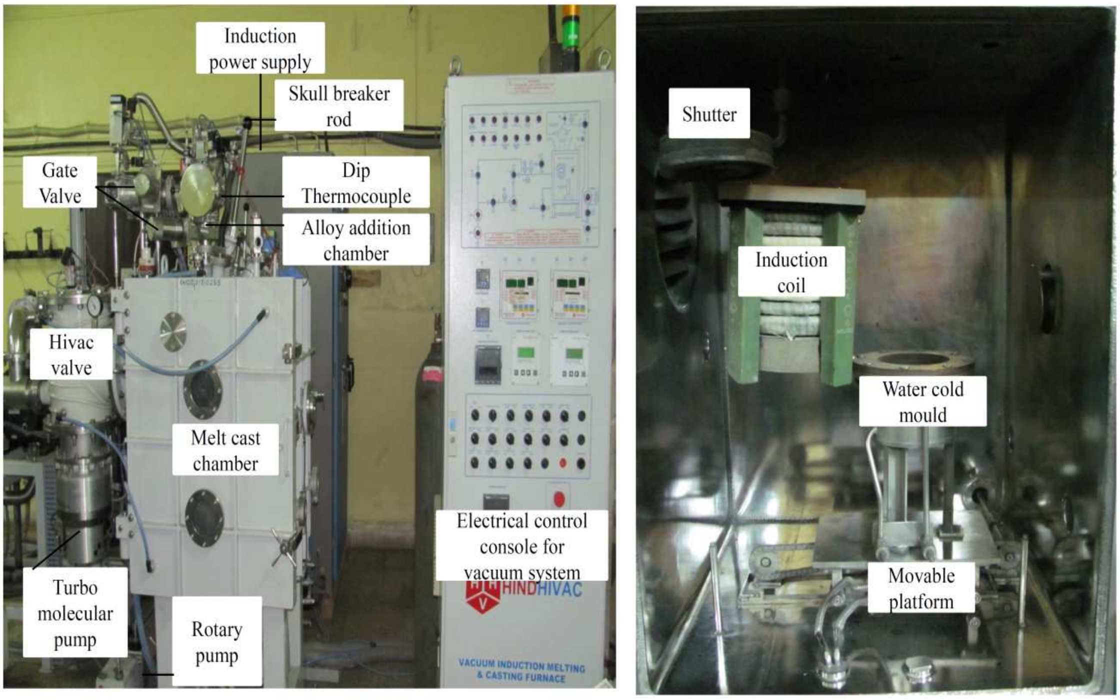

Fig. 2.4 (a) Photograph of the melting-casting furnace and (b) Photograph showing the inner view of the chamber with induction coil and water cooled Cu-mould.

For the melt-and-quench synthesis of alloys, we have designed an induction melting furnace, which was fabricated by Hind HiVac, Bangalore. The photograph of this system is shown in Fig. 2.4 (a). It essentially consists of an induction heater that can hold a crucible of 500 cc volume. The temperature of the crucible can be attained to a maximum of ~2000°C, either under a vacuum of 10^{-6} torr or under argon pressure. The vacuum is created using a turbo-molecular pumping system. The main features of this system are: (i) due to induction heating, the melt has a convection flow which shuns the segregation of the constituents, (ii) appropriate dopants can be added into the melt at high temperatures, and (iii) the graphite crucible can be tilted by >90° to facilitate the quenching of melt onto a water cooled Cu crucible.

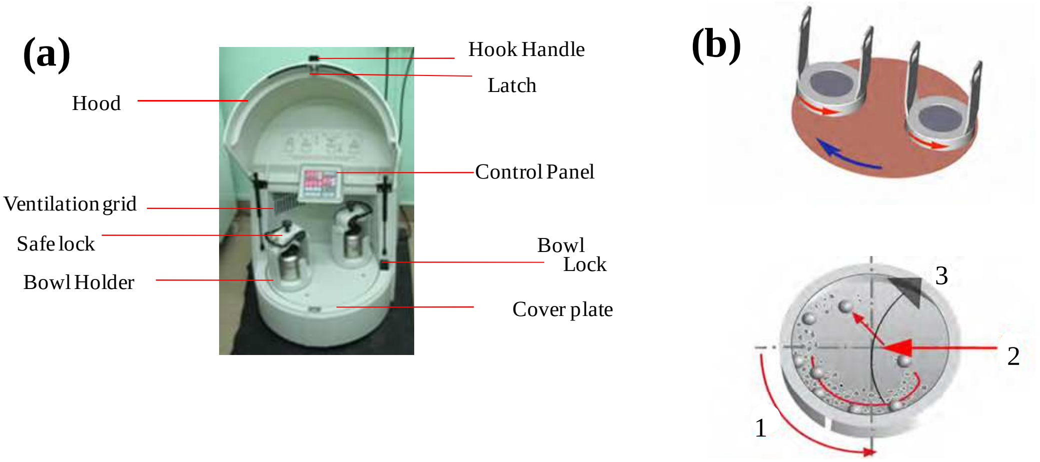

Fig 2.5 (a) Photograph of the ball mill used in the present work (Fritsch make Pulverisette 5). (b) Schematic showing: (1) rotation of the grinding bowls; (2) centrifugal force; and (3) movement of the support disc.

2.2.3 Mechanical alloying

Mechanical alloying is a solid-state powder processing technique in which constituent elements of the alloy are mixed using a high-energy ball mill. This technique is capable of synthesizing homogeneous equilibrium as well as non-equilibrium alloy phases. In addition, depending upon the time and energy of ball-milling, the grain size could be in nanoscale, which is beneficial for the reduction of thermal conductivity in thermoelectric alloys. In the present work, we have used the commercial ball milling (Fritsch make Pulverisette 5), and its photograph is shown in Fig. 2.5 (a). The grinding stock is crushed and ground by grinding balls in 2 grinding bowls which were allowed to rotate at 300 rpm. The centrifugal forces from the rotation of the grinding bowls around their own axis and from the rotating support disc act on the contents of the grinding bowl, which consists of material to be ground and the grinding balls. The grinding bowl and the support disc have opposite directions of rotation, as shown in Fig 2.5 (b), so that the centrifugal forces act alternately in the same direction and in the opposite direction. The result is that the grinding balls run down the inside of the bowl's wall as friction effect and the grinding balls hit the opposite wall of the grinding bowl as impact effect. The impact effect is amplified by the impact of the grinding balls against each other. The no loss of material is ensured by the hermetic seal between the grinding bowl and the lid.

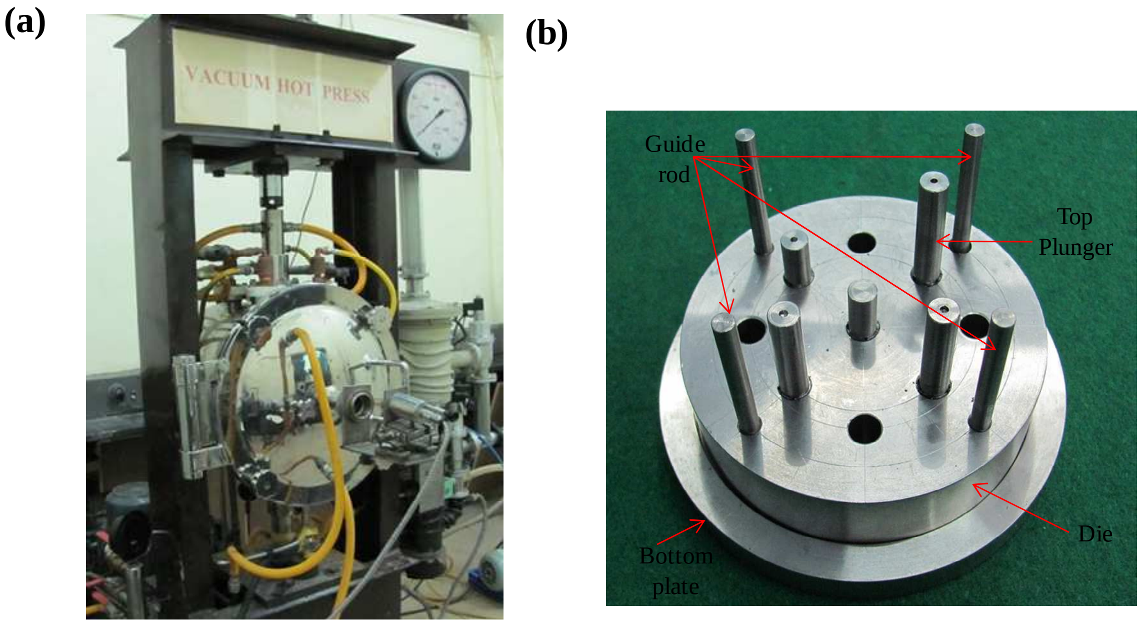

Fig. 2.6 (a) A photograph of the in-house built vacuum hot press. (b) Schematic of uniaxial compaction of material in a die.

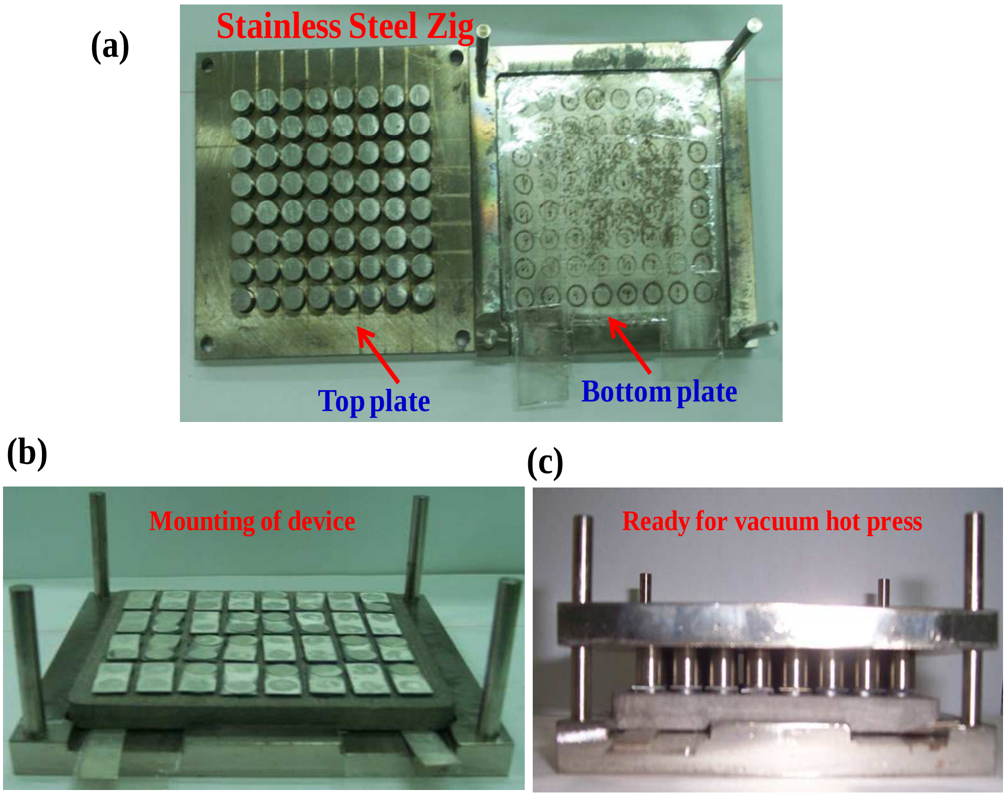

Fig. 2.7 (a) Photographs of a stainless steel zig for fabrication of devices. (a) top and bottom plates of the zig. (b) Mounting of p-n themolegs along with strips. (c) Mounted 16 p-n thermolegs device ready for vacuum hot pressing.

2.3 Fabrication of thermolegs and interconnects

Thermolegs are n-type or p-type pellets prepared from their respective powders (synthesized using melt-growth, melt-and-quench method or ball milling) in such a way that metallic strips (i.e. Ag, Ni, Mo, W used as interconnect) can be bonded to their ends with low contact resistance [87]. This is a very stringent condition due to following problems: (i) in most of the cases, the metal diffuses into thermoelectric material, which not only degrades the property the thermolegs but also increases the contact resistance; (ii) a large lattice and thermal expansion mismatch between metallic strip and thermolegs can lead to mechanical cracking at the interface, and therefore, are not suitable for long term use. To overcome these problems, thermolegs are often pressed from powders of graded layers so as metallic shoes are obtained at both the ends. The nature of graded layers depends upon the thermoelectric material, which will be discussed later. In order to fabricate thermolegs, we have designed and fabricated an uniaxial vacuum hot press, and its photograph is shown in Fig. 2.6 (a). This system consists of a vacuum chamber (base vacuum of ~10^{-6} torr) that houses a graphite heater furnace (upto ~1500˚C) and has a ramp for applying a pressure of upto 10 tons/cm^2 using a hydraulic press. The synthesized alloy powders are filled in a specifically designed stainless steel die in which 9 pellets can be uniaxially compacted simultaneously using vacuum hot furnace at high temperature and high pressure, as schematically shown in Fig. 2.6(b). The applied pressure and the temperature of compaction are decided by the material properties, such as melting point, vapor pressure etc.

The vacuum hot press is also used for making diffusion bonding between thermolegs and metallic strips as well as fabricating devices, whereby several p-and-n thermolegs are interconnected electrically in series by metallic strips. Diffusion bonding essentially is a solid-state welding technique that is capable of joining similar and dissimilar metals/alloys [88]. Diffusion bonding works on the principle of solid-state diffusion, wherein the atoms of two surfaces intermingle at elevated temperature and high pressure. For this purpose, a special stainless steel zig was fabricated so that 16 p-n thermolegs device can be fabricated. The photographs of top and bottom parts of this zig, mounting of thermolegs along with Ag strip on bottom part of zig and loading of the top part of zig are shown in Fig. 2.7. This zig is then transferred to vacuum hot press for diffusion bonding that is often carried at temperature range between 773-1173 K(depending upon the material and interconnect) under an applied pressured of 5-10 kg/cm^2.

2.4 Morphology and structural characterization techniques

2.4.1 Scanning electron microscopy equipped with EDX

We have used scanning electron microscope, SEM, (model: TESCAN VEGA) to investigate the surface morphology of the thermoelectric alloys. The SEM provides information relating to topographical features, morphology and phase distribution [89]. A photograph of SEM used for morphological characterization in the present study is shown in Fig. 2.8. SEM produces images of a sample when a focused beam of electrons is scanned across its surface. The electrons interact with atoms in the sample, producing various signals such as, secondary electrons and characteristics x-rays, which are then detected to obtain information about the sample's surface topography and composition, respectively. SEM can achieve resolution of ~10 nm.

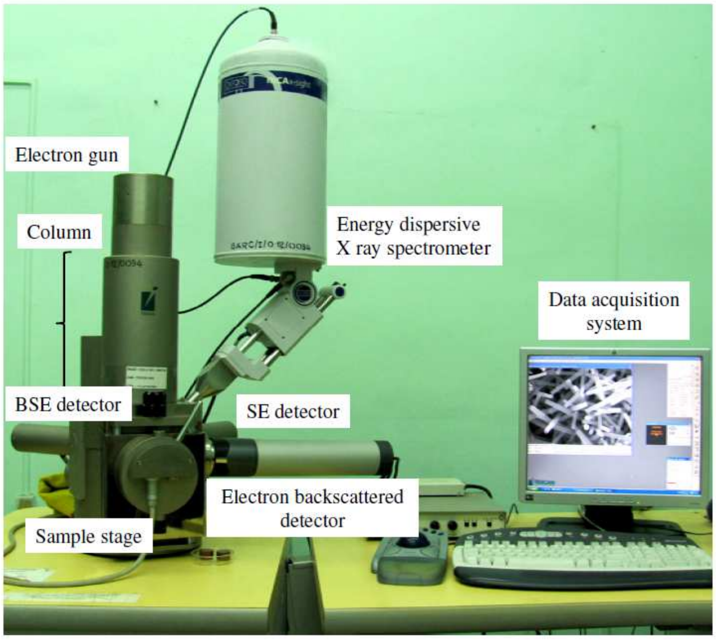

Fig.2.8 A photograph of the scanning electron microscope equipped with energy dispersive x-ray analysis system.

The compositional analysis has been carried out using energy dispersive x-ray analysis system (OXFORD INCA) equipped with SEM. The minimum detection limit (MDL) of the EDX is about ~1 wt%. X-rays are produced as a result of ionization of an atom by high-energy radiation wherein an inner shell electron is removed. To return the ionized atom to its ground state, an electron from a higher energy outer shell fills the vacant inner shell and, in the process, releases an amount of energy equal to the potential energy difference between the two shells. This excess energy, which is unique for every atomic transition, will be emitted by the atom either as an X-ray photon or will be self-absorbed and emitted as an Auger electron. For example, if the K shell is ionized and the ejected K-shell electron is replaced by an electron from the L shell, the emitted X-ray is labeled as characteristic Kα X-ray and is the signature of the elements present in the matrix. The hole that exists in L shell will be filled by an electron from a higher shell, say the M shell, if one exists. This M-L transition may result in the emission of another X-ray, labelled in turn according to one of the many M-L transitions possible. The cascade of transitions will continue until the last shell is reached. Thus, in an atom with many shells, many emissions can result from a single primary ionization. In EDX technique, quantitative estimation is done by the analysis of the X-rays. For this purpose, first X-ray spectrum is obtained for the specimen and standards under defined and reproducible conditions. Then the quantitative calibration is done by developing the X-ray intensity ratios using the specimen intensity and the standard intensity for each element present in the sample and carrying out matrix corrections (ZAF correction). In mixtures of elements, matrix effects arise because of differences in elastic and inelastic scattering processes and in the propagation of X- rays through the specimen to reach the detector. For conceptual as well as calculation reasons, it is convenient to divide the matrix effects into those due to atomic number, Z_i; X-ray absorption, A_i ; and X-ray fluorescence, F_i. Whenever the quantification is done, our instrument selects the ZAF correction by default and does the analysis.

2.4.2 Transmission electron microscopy (TEM)

Transmission electron microscopy was used to determine the presence of nanoparticles or secondary phase in the system. Here, high energy electrons (up to 300 kV accelerating voltage) are accelerated to nearly the speed of light. The electron beam behaves like a wavefront with wavelength about a million times shorter than light waves. When an electron beam passes through a thin-section specimen of a material, electrons are scattered. A sophisticated system of electromagnetic lenses focuses the scattered electrons into an image or a diffraction pattern, or a nano-analytical spectrum, depending on the mode of operation [90]. Each of these modes offers a different insight about the specimen. The imaging mode provides a highly magnified view of the micro- and nanostructure and ultimately, in the high resolution imaging mode a direct map of atomic arrangements can be obtained using high resolution TEM (HRTEM). The diffraction mode (electron diffraction) displays accurate information about the local crystal structure. The nanoanalytical modes (x-ray and electron spectrometry) tell which elements are present in the tiny volume of material. These modes of operation provide valuable information.

2.4.3 X-ray Diffraction

For determination of the structure of the thermoelectric alloys so obtained, x-ray diffraction measurements were carried out. We used powder X-ray diffractometer (Proto

XRD) in θ-2θ scan mode to characterize the orientation and structure of the samples. Fig. 2.9 shows the photograph of the Proto make XRD system.

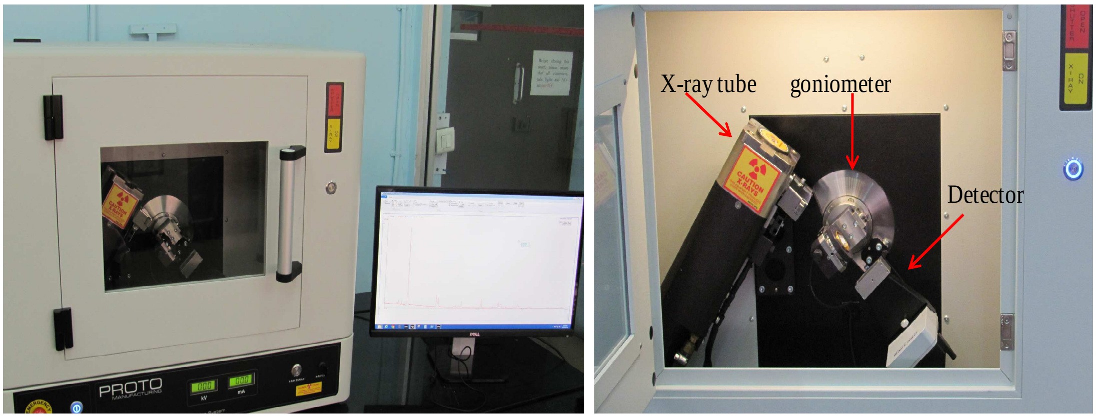

Fig.2.9 Photographs of the x-ray diffractometer (Proto XRD) used in the present work.

The X-ray source used was Cu K_α having wavelength of 1.54Å. For all samples, the diffracting surface of the sample must be flat and aligned with the plane of the sample plate. The desired area must be positioned on the rotation center of the goniometer. Since the wavelength (λ) of X-rays coincides with the atomic spacing (d) in the solids, it diffracts in those orientations of 2θ, where the Bragg condition of diffraction [91] i.e. $2d \sin\theta = n\lambda$ (θ being the angle which incident beam makes with the plane of the sample) is satisfied. High speed solid state linear detector (i.e. Si-strip detector having 64 mm × 8 mm sensor area) is employed. This detector allows simultaneous multiple channel collection that enables collection times up to 200 times faster than a conventional scintillation counter. The direct detection of x-rays using silicon strip technology also has the advantage of excellent signal-to-noise ratio. The recorded diffraction patterns were least square fitted using software, PD analysis, to determine the lattice parameters.

2.4.4 Diffuse reflectance spectroscopy

The energy gap (E_g) of the thermoelectric materials has been estimated using diffuse reflectance UV-visible-IR spectroscopy [92]. Since light cannot penetrate opaque samples e.g. thermoelectric alloys, it is reflected on the surface of the samples. If incident light reflects symmetrically with respect to the normal line, it is called "specular reflection," while incident light scattered in different directions is called "diffuse reflection." The diffuse reflectance measurements, as shown in Fig. 2.10, are carried out using integrating spheres by placing the sample in front of the incident light window, and concentrating the light reflected from the sample on to the detector using a sphere with a barium sulfate or KBr coated inside. The obtained value becomes the reflectance (relative reflectance) with respect to the reflectance of the reference standard white board, which is taken to be 100%. When light is directed at the sample at an angle of 0°, specular reflected light exits the integrating sphere and is not detected. As a result, only diffuse reflected light is measured.

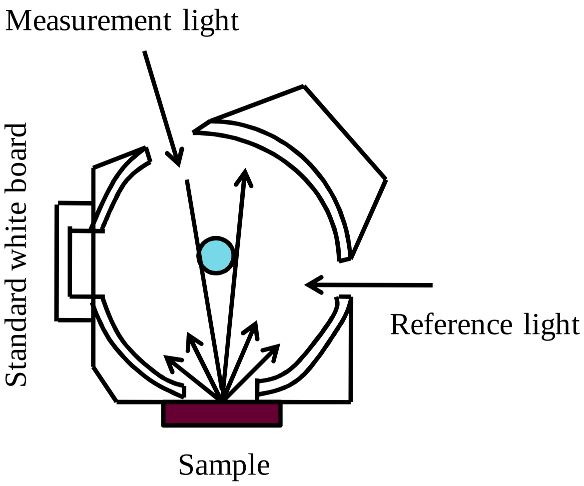

Fig.2.10 Schematic showing the principle of diffuse reflectance measurements .

The diffuse reflectance spectroscopy was carried using model Jasco V-670. The samples were prepared by piling a small amount of the thermoelectric alloy on a layer of barium sulfate powder, after which the sample powder was spread into a thin uniform layer using a glass rod. The E_g of the samples is measured using Kubelka-Munk equation $h\nu F(R_\infty) = \mathrm{A}(h\nu - E_g)^{1/n}$,where $F(R_\infty)$ is Kubelka-Munk function and is proportional to the absorption coefficient (α), h is Planck's constant, ν is frequency of vibration, A is proportional constant, and n = 1/2 is used that is applicable for samples having direct allowed transition. The $h\nu F(R_\infty)^2$ is plotted against the $h\nu$, and a tangent is drawn to the point of inflection on the curve. The point of intersection of the tangent line and the horizontal axis determines the E_g value.

2.4.5 X-ray photoelectron spectroscopy

XPS uses a soft X-ray source (Al-K_α or Mg-K_α) to ionize electrons (by knocking out the core-level electron) from the surface of a solid sample (top few atomic layers). The binding energies of these electrons are measured, which are characteristics of the elements and associated with chemical bonds (chemical state). The advantages of XPS technique are (i) quantitative analysis of elements and chemical states of all elements except hydrogen and helium, (ii) typical element detection limits are 0.1 atomic percentages from the top few nm, and (iii) samples can be conductors, semiconductors or insulators [93,94]. In this work, we have used XPS system (RIBER system model: FCX 700) consisting of Al-K_α (1486.6eV) and Mg-K_α (1253.6eV) X-ray sources and MAC-2 electron analyzer. The binding energy scale was calibrated to Au-4$f_{7/2}$ line of 83.95eV. For charge referencing adventitious C-1s peak set at 285eV was used. Each data set was first corrected for the non-linear emission background. The data was then fitted with Gaussian function to find the peak positions.

2.4.6 Kelvin Probe Microscopy

The work function of the sample was measured using ambient scanning Kelvin Probe Force Microscopy (SKP 5050) and its photograph is shown in Fig. 2.11. In brief, Kelvin Probe (KP) is a versatile technique that measures contact potential difference (CPD) between two surfaces brought in close proximity [95]. When electrically connected, electrons flow from the semiconductor with the smaller work function to the metal with the larger work function. The surfaces (not in physical contact) develop equal and opposite charges and act like a parallel plate capacitor. The voltage developed across capacitor is the CPD. The Kelvin apparatus consists of a probe surface and a sample surface acting together as a parallel plate capacitor. The work function of the probe is known by calibrating against a standard Au coated clean surface, so the work function of the sample can be determined. Backing voltage V_b is adjusted such that voltage across the circuit disappears, at which point V_b is equal to V_{CPD}. To ensure more than one measurements, entire charge from previous measurement should dissipate, therefore the probe is vibrated (ω = 27 kHz) to produce varying capacitance. The output voltage as a result of oscillation: $V_o = (V_{CPD} - V_b) R C_o \varepsilon \sin(\omega t + f)$, where, R is current-voltage converter feedback resistance, $\in$ is a ratio of average distance between probe and sample to the amplitude of oscillation called as modulation index, and C_o is the capacitance. Lock in amplifier which is a phase sensitive detector is appropriate to detect null output condition when signal to noise ratio is very low. It multiplies the input signal with a reference signal and integrates over a span of ms to s. The resulting signal is a DC signal, where the contribution from any signal that is not at the same frequency as reference is attenuated to zero. It also attenuates the out of phase signal of same frequency.

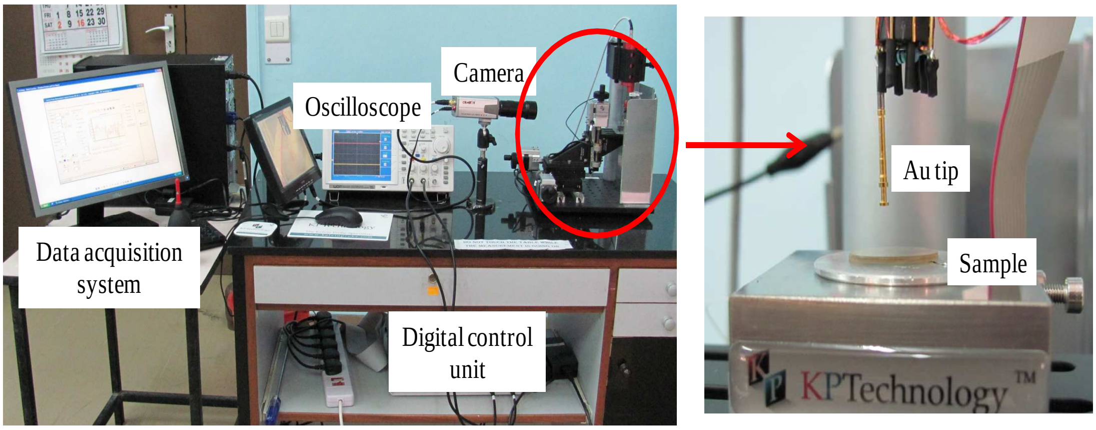

Fig. 2.11 A photograph of Kelvin Probe system.

2.5 Measurement of thermoelectric parameters

In order to measure the *ZT* of the synthesized materials, all the thermoelectric parameters, namely n, ρ, α and κ were measured as a function temperature. The details of the equipments used for these measurements are discussed below.

2.5.1 Hall effect measurement

Determination of carrier concentration 'n' in the thermoelectric alloys was performed by an in-house built Hall measurement set-up. The underlying principle in the Hall Effect is that the mobile charge carriers moving with velocity (v) in an electrical current (I_S) experience a force Lorentz from an applied magnetic field (B). This force, $F = q (v \times B)$, pushes the moving charges at right angles to the current [96]. As charge builds up on one side of the sample it produces a Hall voltage, where, q=-e for electrons and q=+e for holes and e the magnitude of the electron charge in coulombs. This voltage is perpendicular to both the current direction and the magnetic field direction, $V_H = \frac{(BI_S)}{(ned)}$, where n is the density of charge carriers in m^{-3}, B the field in tesla, I_s the current in amps, and d the sample thickness in meters.

2.5.2 Seebeck coefficient and electrical resistivity

Simultaneous temperature dependent measurements of the electrical resistivity and Seebeck coefficient of the samples in the range 303-1073 K were carried out using a commercial LSR-3 system manufactured by Linseis, GmbH, and its photograph is shown in Fig. 2.12.

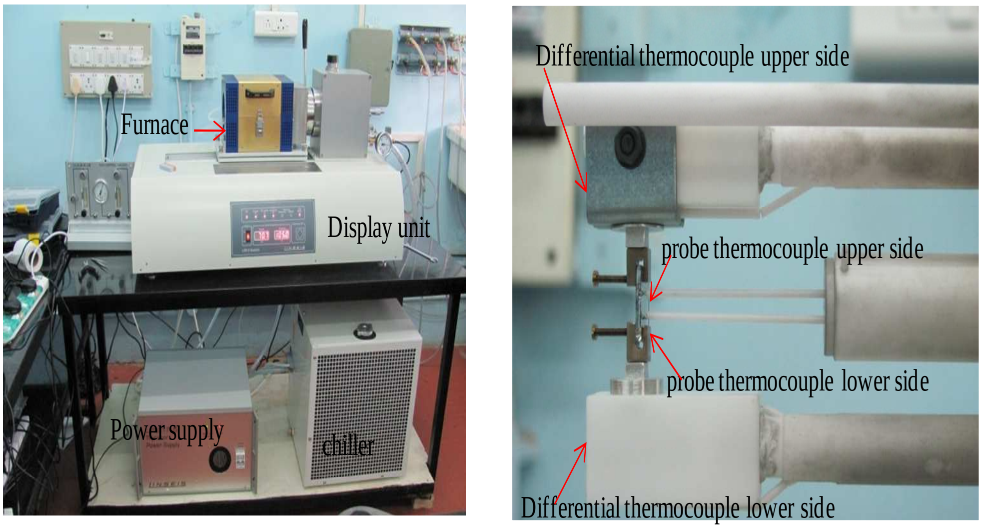

Fig.2.12. Photographs of the Seebeck and electrical resistivity measurement set up (model: LSR-3).

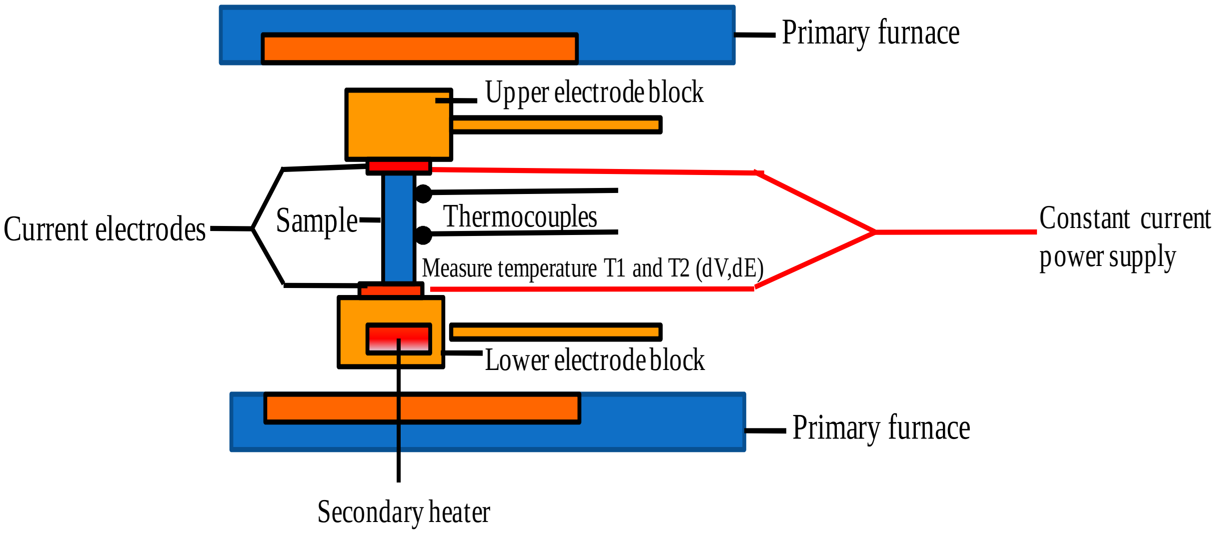

Fig.2.13. Schematic of the measurement set up of LSR-3.

The working principle of the system is schematically demonstrated in Fig. 2.13. A sample of cylindrical or prism shape is vertically positioned between two electrodes. The lower electrode block contains a heater, while the entire measuring arrangement is located in a furnace. The furnace surrounding the measuring arrangement heats the sample to a specified temperature. At this temperature the secondary heater in the lower electrode block creates a set temperature gradient. Two contacting thermocouples then measure the temperature gradient T_1 and T_2. A unique thermocouple contact mechanism permits highest temperature accuracy measurements of the electromotive force dV at one wire of each of the two thermocouples. The dc four-terminal method is used to measure the electric resistance of the sample. A constant current (I) is applied at both ends of the sample and change in voltage dV is measured. The thermocouple junction is pressed and held by mechanical springs to the samples surface creating a good thermal and electrical contact. The voltage leads are not a single wire, but are built to be both a voltage lead and thermocouple. The thermocouple leads (voltage leads) are housed in a twin bored ceramic tube. The junction, or head, of the thermocouple is exposed at the end of the ceramic tube, and the junction itself is carefully designed to be flat (parallel) to the samples surface. The errors associated with the measurement of Seebeck coefficient and resistivity is expected to be 3-5%.

2.5.3 Thermal conductivity

High temperature (303-973K) thermal conductivity of the sample is measured indirectly. There are several methods for indirectly measuring high temperature thermal conductivity, such as the comparative technique, transient line source method, and laser flash thermal diffusivity method [97]. In this thesis work, we have chosen laser flash method. For this method the total thermal conductivity is calculated using equation: $\kappa = DCpd$,where d is density, C_p is specific heat and D is thermal diffusivity. The determination of D, C_p and d are described below.

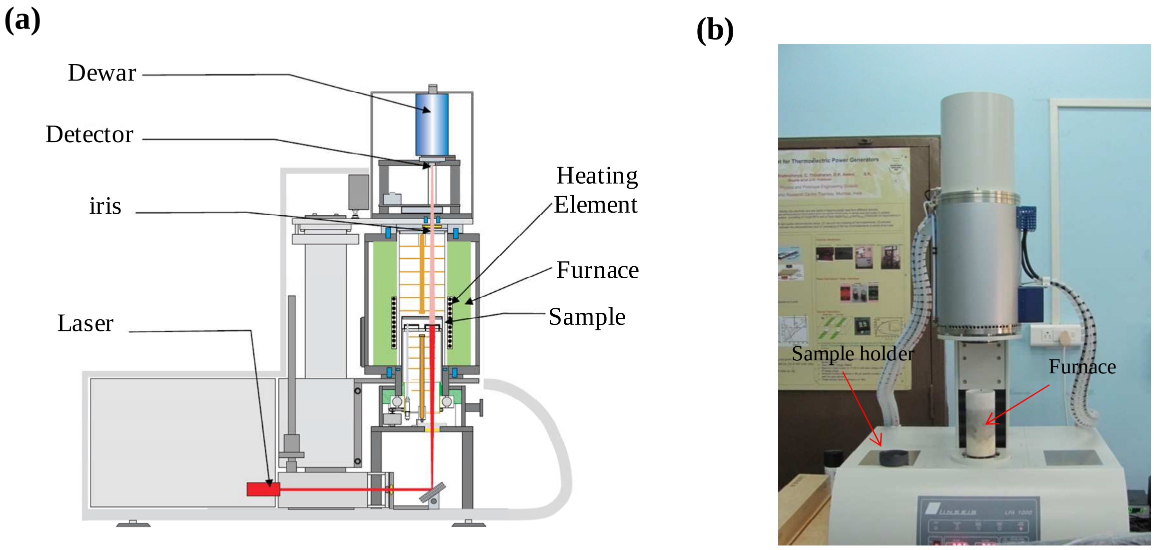

Fig.2.14 (a) Drawing of the system LFA-1000 and (b) photograph of the thermal diffusivity system, LFA-1000.

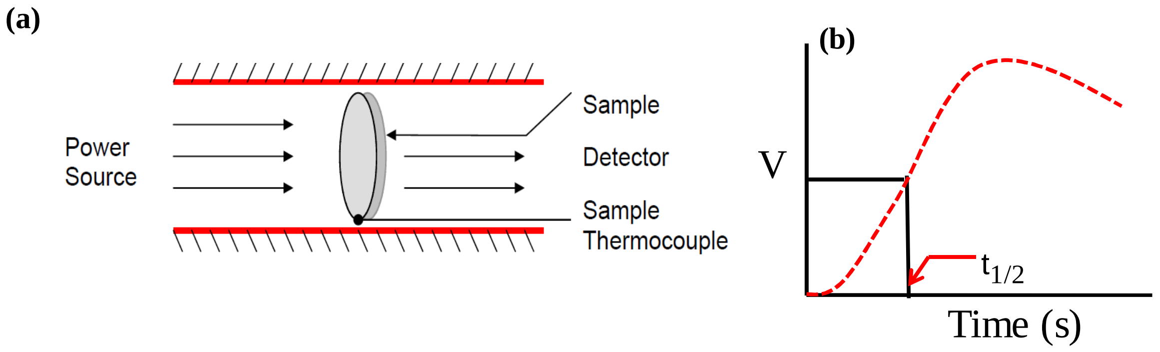

Fig.2.15 (a) Schematic of the determination of thermal diffusivity and (b) A typical experimental data of $t_{1/2}$ measurement by laser flash method.

Thermal diffusivity: The thermal diffusivity was measured using Linseis made LFA-1000, and its schematic drawing and photograph is shown in Fig. 2.14. This equipment works on the principle of Laser flash method, as schematically shown in Fig. 2.15. The size of samples needed for these measurements is: 1-2 mm thick and diameter of 10.2 mm or 12.7 mm and the laser source used is Nd-YAG laser. The infra red detector used is LN_2 cooled Hg-CdTe. Thin disc specimen is subjected to a high intensity short duration radiant energy pulse; see Fig. 2.15 (a). The energy of the pulse is absorbed on the front surface of the specimen and the resulting rear face temperature rise (thermogram) as a function of time is recorded; see Fig. 2.15 (b). The thermal diffusivity (D) is calculated from relation: $D = 0.138785\, {L^2}/{t_{1/2}}$, where L is the sample thickness, and $t_{1/2}$ is time required for the rear face temperature rise to reach 50 percentages of its maximum [98,99,100]. When the thermal diffusivity of the sample is determined over a temperature range, the measurements are repeated at each temperature. The scatter in D measurement can be as high as 5% at room temperature and almost 10 % at 500 K. The error can arise due to the variations in measured thickness of the sample. Another possible source of error can be the graphite coating which is employed in diffusivity measurement. Too thick coating or poor adhesion to the sample can cause significant errors, especially for thin samples [101].

***C_p* measurement:** The C_p measurement was done by comparative method. Here, the maximum of the temperature raise in the sample is compared to the maximum of the temperature raise of a reference sample. Both, the unknown and the reference sample were measured under the same conditions in a single run, using the sample robot. So the energy of the laser pulse and the sensitivity of the infrared detector were the same for both measurements. The temperature raise in the sample can be calculated according the following equation: $\Delta T = \frac{E}{m * C_p}$, where ΔT is raise in temperature (K), m is weight of the sample (g), and E is Energy (J). Since the energy is the same for sample and reference, the C_p of the sample can be calculated according the following equation: $Cp_S = \frac{Cp_r \Delta T_r m_r}{\Delta T_s m_s}$, where the subscript '*S*' and '*r*' stands for the sample and reference respectively. In order to achieve a good accuracy, the absorbability and emissivity of sample and reference must be the same (same coating), and the absolute heat capacity ($C_p \times Weight$) of sample and reference must be similar. A scatter in heat capacity of 15% has been observed. The primary sources of error are operator error, baseline shift and inappropriate reference sample. Ideally the reference should be chosen to give a signal close to the measured sample to reduce errors. Otherwise, above the Debye temperature and in the absence of phase transitions, C_p normally increases slightly with temperature. The best data quality check is comparison to the Dulong-Petit law which states that the constant volume heat capacity above the Debye temperature is approx.

$3k_B$ per atom, or $C_V^{DP} = \frac{3N_A k_B}{M}$. C_V is related to C_P by $C_P = C_V^{DP} + {9\alpha^2 T}/{\beta_T D}$, α is the linear coefficient of thermal expansion, β_T is the isothermal compressibility and D is the density. The measured C_p above the Debye temperature should be close or slightly above than the Dulong-Petit value and increases slowly with temperature. When the correction is applied, the measured and calculated heat capacities (by Dulong-Petit law) usually agree within 2%. When the values disagree more than about 5%, extra verification is recommended before using the measured values. If the measured values are unexplainable, it is recommended to use the corrected Dulong-Petit value.

Density measurement: The geometric density of the sample is measured by calculating the volume from the geometry and dimensions of the sample (for regularly shaped sample). The density of the sample was also measured by Archimedes's method by immersing the sample in a liquid. But this method can overestimate the density measurement if the liquid is absorbed in the pores. This can be checked by measuring the weight in air both before and after the measurement in the liquid. But the density measurement is fairly accurate at room temperature and it is assumed to be independent of temperature.

2.5.4 *ZT* calculation

As discussed in Chapter 1, the figure-of-merit (*ZT*) is calculated from the equation: $ZT = \frac{\alpha^2}{\rho\kappa}T$. As mentioned by Hsin et al, the differences in *ZT* calculation can be 20% and that uncertainty increases with *T*. The heat capacity is the largest contribution to the error in κ which can be significantly reduced by comparison to the Dulong-Petit value. In addition systematic differences due to different techniques in measuring Seebeck coefficient can add on the order of 5% uncertainty, which also increases strongly with T.

2.6 Setup for evaluation of thermoelectric generators

2.6.1 Efficiency measurements

In order to estimate the efficiency of thermoelectric generators, a setup was fabricated and its photograph is shown in Fig. 2.16. It essentially consists of a 2 inch diameter uniform heater, which can be heated upto 873 K using a temperature controller. The temperature of the heater can be controlled within ±1 K. The heater is mounted upside down on a spring-loaded movable mount. The basement of the mount consists of a water cooled cylinder. The thermoelectric device is mounted between the heater and water cooled cylinder. For testing, the voltage across the device arising due to the temperature gradient between hot and cold is measured using a multimeter. The temperatures of hot and cold ends were measured using thin wire (25μm) thermocouples placed between the hot/cold ends and the devices. The efficiency is estimated from the ratio of output power of the thermoelectric generator and the power supplied at the input of the generator.

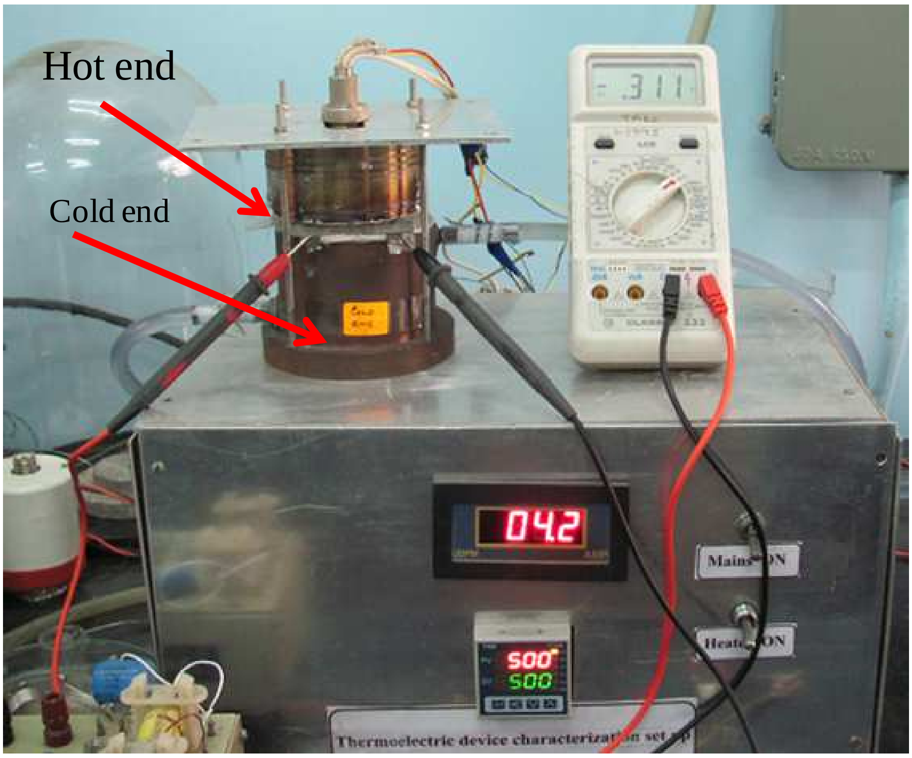

Fig. 2.16. Photograph of the device characterization set up.

2.6.2 Setup for thermal stability measurements

A set up has been fabricated to test the long term stability of thermoelectric materials. The photograph of the set up is shown in Fig. 2.17(a) which comprises a steel chamber with four pressure contacts for the measurement of resistivity of the sample at high temperature for prolonged period.

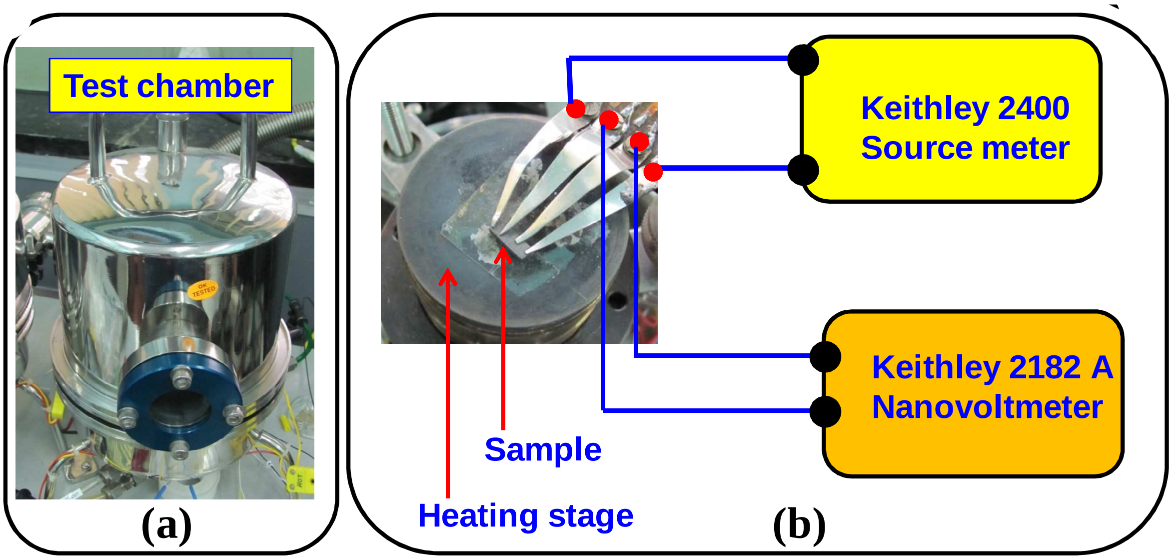

Fig. 2.17. (a) Photograph of the long term stability measurement set up. (b) The four-probe resistivity measurement of sample at high temperatures.

In order to measure the long term stability of thermoelectric samples, they are mounted on a heater placed inside a steel chamber and electrical contacts are taken by four fingers of silver (pressure contact), as shown in Fig. 2.17 (b). Before starting the resistivity measurement, first the chamber was evacuated to 2×10^{-2} mbar and after that argon gas was purged in the chamber and a pressure slightly higher than atmospheric pressure was maintained by argon gas. The resistivity of the sample is measured as a function of time at elevated temperature to ensure the thermal stability of thermoelectric materials.

Chapter 3

Thermoelectric Generators based on PbTe and TAGS-85 Alloys

3.1 Introduction

In this Chapter we present various results on the technology development of thermoelectric power generators using conventional semiconductor alloys. As discussed in Chapter 1 (Section 1.3.1), depending upon the ZT_{max}, thermoelectric materials can be characterized based on their operating temperature ranges: (i) low temperatures range (150-200º C) : Bi_2Te_3 and Sb_2Te_3; (ii) mid temperature range (450-500ºC): PbTe and TAGS85, and (iii) high temperature range (>800ºC): SiGe alloys. Thermoelectric devices, operating in the low temperature range are manufactured by some of the international companies such as Toshima Manufacturing Co. Ltd. , Japan, as Peltier coolers, whereas PbTe/TAGS-85 based TEG and SiGe based TEG's were used by NASA in their space missions. These devices are however commercially unavailable. Therefore, it is essential to develop an indigenous technology for the fabrication of these TEG. As discussed in Chapter 1, the TEG fabrications have several challenging issues, including synthesis of high *ZT* single phase n- and p-type materials, fabrication of thermolegs having low contact resistances with interconnects, and suitable packing of the device with minimum heat shunt path.

In this Chapter, we present our results on the technology development of TEG based n-type PbTe and p-type TAGS-85 alloys, which can be operated at a hot temperature of 450-500ºC for prolonged durations. First we briefly present the crystal structures of PbTe and TAGS-85. We then describe the synthesis of single phase n-type PbTe and p-type TAGS-85 alloys using melt growth method. The synthesized materials have been characterized for structure, morphology and thermoelectric properties. We discuss how graded layers of different materials are essential for the fabrication of n-type PbTe and p-type TAGS-85 thermolegs with metal shoes having very low contact resistances. Finally we demonstrate fabrication of TEG having different numbers of thermolegs, and their evaluation. We demonstrate that fabricated devices exhibit an efficiency of ~6% and are stable under continuous operating conditions for more than 2 years.

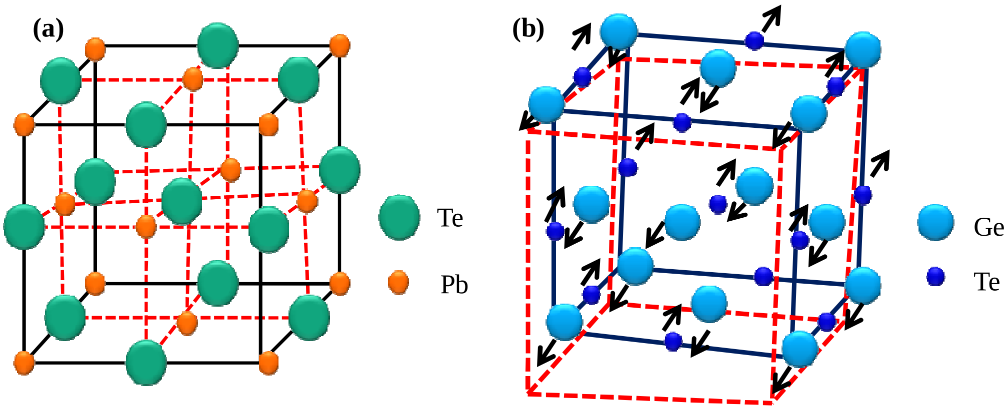

Fig. 3.1 Crystal structures of: (a) PbTe, and (b) TAGS-85, which undergoes a transition from low temperature cubic (dashed line) to high temperature rhombohedral phase (solid line).

3.2 Crystal structure of PbTe and TAGS-85

The crystal structures of PbTe and TAGS-85 are shown in Fig. 3.1. PbTe crystallizes in the face centered cubic phase (rocksalt-type) having space group $Fm\bar{3}m$ with lattice parameter a =6.463 Å [102,103]. The cubic phase of PbTe is retained when subjected to thermal cycling. The TAGS-85 alloy has the composition of $(GeTe)_{0.85}(AgSbTe_2)_{0.15}$, which retains the crystal structure of GeTe with Ag and Sb on the Ge sublattice. GeTe exists in two major crystalline forms: room-temperature α (rhombohedral $R3m$) and high-temperature β (cubic $Fm\bar{3}m$, rocksalt-type) phases [104,105,106]. The temperature of the transition from the rhombohedral to the cubic phase depends on the composition: in the presence of excess Ge, the transition takes place at 733 K, while in the presence of excess Te, it occurs at 663 K

[105]. This phase-transition temperature has implication in weakening of the mechanical properties of the material.

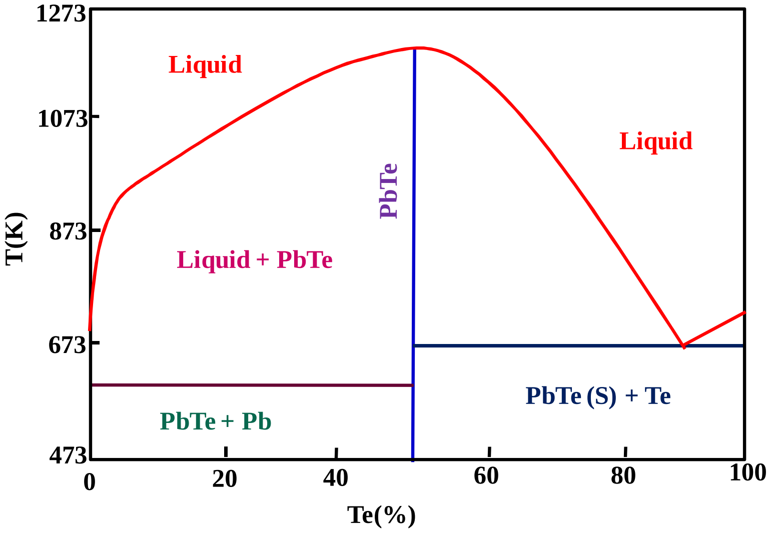

Fig. 3.2 Phase diagram of PbTe.

3.3 Synthesis of single phase PbTe and TAGS-85

In this Section we describe the synthesis of n-type PbTe and p-type TAGS-85 single phase alloys using melt-growth method, as described in Chapter 2.

3.3.1 Phase diagram and synthesis of PbTe

The phase diagram of PbTe is shown in Fig. 3.2, which indicates that stochiometric PbTe has a congruent melting point at ~ 1197 K. The Pb-Te system forms an eutectic at 83.5 at% Te with a melting point of 678 K [107,108,109,110]. PbTe alloy solidified from a stoichiometric melt exhibits a carrier concentration of the order of ~10^{18} cm^{-3} at room temperature. For lower Te concentration, cooling of the PbTe melt other than the congruent melting point, results in Pb as secondary phase in PbTe. Thus the alloy becomes n-type in nature. On the other hand, for higher Te concentration, cooling of the PbTe melt other than the congruent melting point, results in Te as secondary phase in PbTe that makes it p-type [111,112]. Thus, the nature of carrier type and its concentration can be tailored by an appropriate thermal annealing.

In order to synthesize n-type PbTe, Pb and Te constituents were weighed in stoichiometric ratio and filled in a graphite bottle, which was then enclosed in a vacuum sealed quartz ampoule. The quartz ampoule was then heated at 1223 K in a rocking furnace to obtain a homogeneous melt. The melt was slowly cooled (333 K/h) to room temperature. It was observed that some of the Te vapors (at high temperature) leaked out of the graphite bottle, which is expected as the Te has significantly high vapor pressure. As a result the obtained ingot is expected to be slightly deficient in Te.

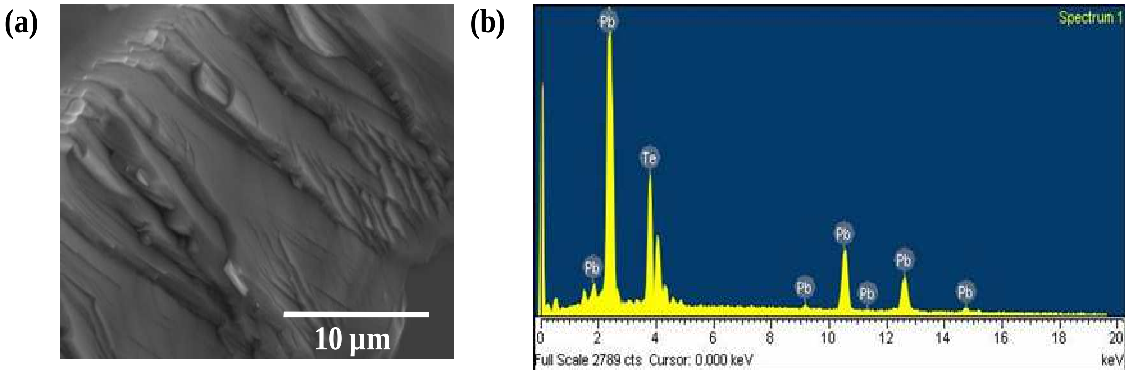

Fig. 3.3 (a) SEM image and (b) EDX spectrum of PbTe alloy.

Typical SEM image of a fractured surface of the ingot as well as a recorded EDX pattern is shown in Fig. 3.3. The SEM image exhibits a microstructure that is dense and textured, a typical of molten alloys. Analysis of EDX spectrum revealed that there are no traces of impurities. The composition of the sample was found to be rich in Pb i.e. $Pb_{1+x}Te$ (composition normalized with respect to Te). The value of x in different experiments was found to vary between varied 0.02 and 0.06. This result is expected as some loss of Te was found during the melting of the sample, as discussed above. This indicates that the synthesized alloy is n-type, which was independently confirmed by the Hall and four probe measurements. The carrier concentration of the n-type PbTe alloys were estimated as $\sim 5\times10^{20}$ cm^{-3} at room temperature.

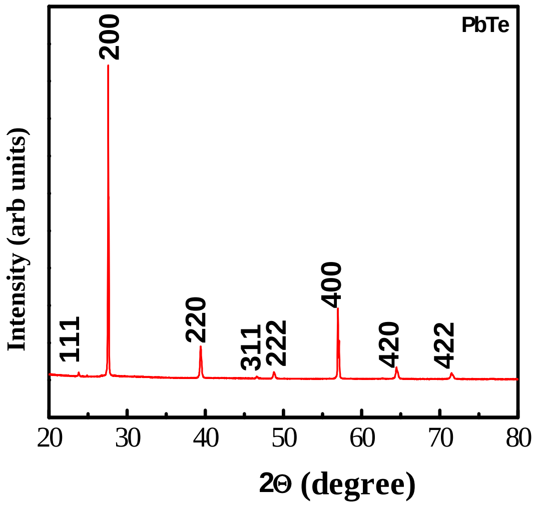

Fig. 3.4 Powder XRD pattern of the synthesized PbTe alloy.

The XRD pattern recorded for the powdered n- type PbTe alloy is shown in Fig 3.4. No peaks corresponding to the unreacted elements or impurities were observed, which is in agreement with EDX results. The patterned could be fitted to the cubic (rocksalt-structure) with lattice parameter of 6.463 Å, which is in agreement with reported literature.

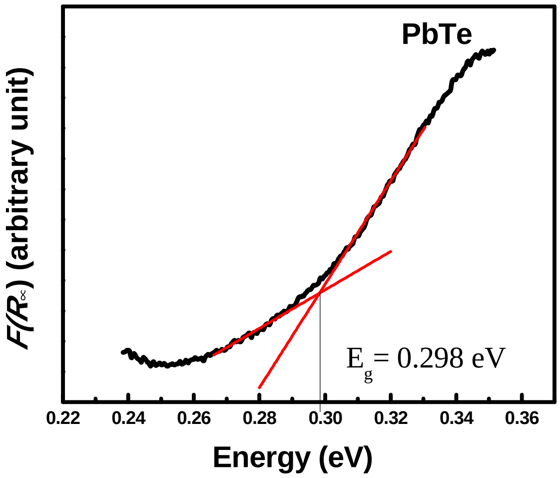

Fig. 3.5 Tauc plot for the synthesized PbTe alloy.

The band gap of the PbTe alloy was measured using diffuse reflectance spectroscopy, and a resultant Tauc plot is shown in Fig. 3.5. A band gap value of ~ 0.29 eV has been estimated, which is close that reported (0.31eV) in literature [30].

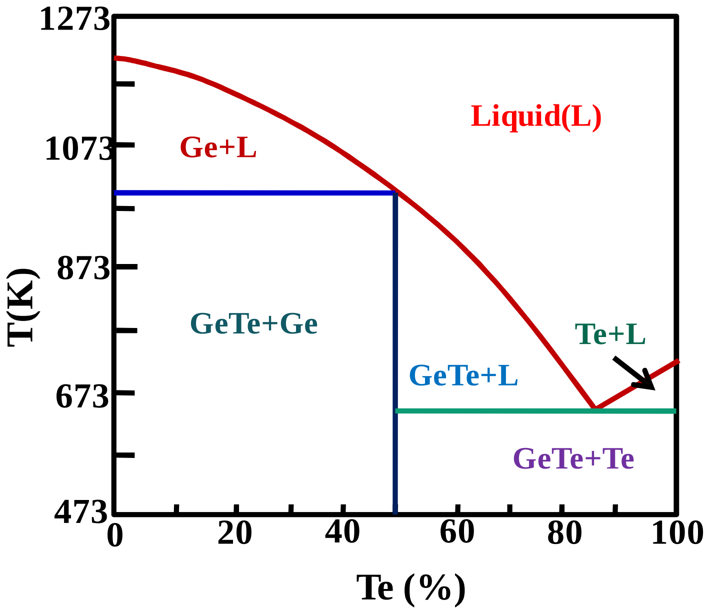

Fig. 3.6. Phase diagram of GeTe.

3.3.2 Phase diagram and synthesis TAGS-85

TAGS-85 [$(AgSbTe_2)_{15}(GeTe)_{85}$] contains 85 mol% GeTe and 15% ($AgSbTe_2$), and behaves like GeTe as Ag and Sb occupy the Ge sublattice. The phase diagram of GeTe is shown in Fig. 3.5. Stoichiometric GeTe melts congruently at 998 K. The Ge-Te system forms a eutectic at 85 at% Te with a melting point of ~ 673 K. The investigation of pseudo-binary phase diagram between $AgSbTe_2$ and GeTe (assuming both of them as single entities) was found to be very complex, as there were indication of several peritectic compound formation at TAGS-85 compositions alongwith various minor phases of Ag/Te, Sb/Te, Sb and Ge [113]. Thus, the synthesis of TAGS-85 is usually carried out from the mixture of stoichiometric constituents melted at ~1223 K.

In our experiments, Ag, Sb, Te, and Ge constituents were weighed in stoichiometric ratio and filled in the quartz ampoule, which was then vacuum sealed. The quartz ampoule was heated at 1273 K, slowly cooled (333 K/h) to 798 K and annealed for 5 h before cooling to room temperature.

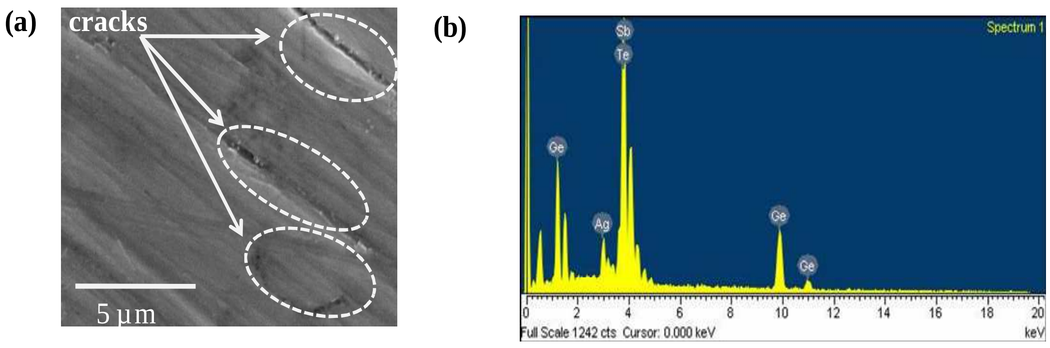

Fig. 3.7 (a) SEM image and (b) EDX spectrum of TAGS-85 material.

A typical SEM image of the surface of fractured TAGS-85 alloy is shown in Fig. 3.7(a), which indicates a textured morphology with some cracks. The cracks are expected to occur during the cooling when the sample undergoes a phase transition from high temperature cubic phase to low temperature rhombohedral phase. Absence of other phases indicates the formation of homogenous material. The EDX spectrum, as shown in Fig. 3.7(b), indicates the presence of only Te, Ag, Ge and Sb and the quantitative analysis exhibited the composition of $(AgSbTe_2)_{14.6}(GeTe)_{85.4}$, which is close to the stoichiometric TAGS-85. It may be noted that unlike PbTe that becomes Te deficient, TAGS-85 remains stoichiometric after synthesis. This difference is due to the fact that PbTe is synthesized in graphite bottle which is vacuum sealed in quartz ampoule. At high temperature, the Te vapor leaks out of the graphite bottle making PbTe slightly deficient in Te. On the other hand, as the constituent elements of TAGS-85 do not react with the quartz ampoules, and therefore, constituents are taken directly into the ampoules and sealed. In absence of any leakage, TAGS-85 remains stoichiometric. The Hall measurements revealed that the synthesized matter is p-type with carrier concentration of $\sim 8\times10^{20}$ cm^{-3} at room temperature.

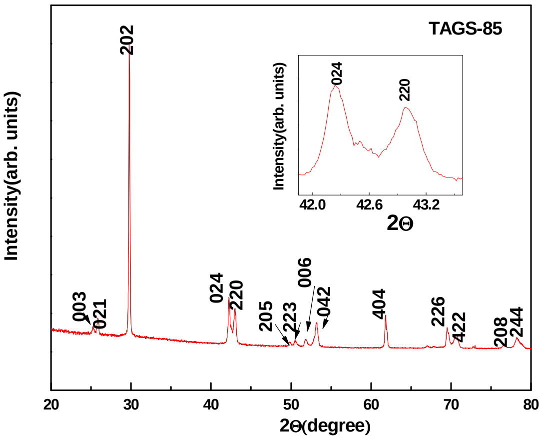

Fig. 3.8 Powder XRD pattern of TAGS-85 material.

The Powder XRD pattern of synthesized TAGS-85 material is shown in Fig. 3.8, which is identical to that of GeTe, confirming that Ag and Sb occupy the Ge sublattice. The peak positions at (024) and (220) in the XRD pattern is indication of Ag/Sb ratio in the sample. It has been reported that the peaks at (024) and (220) shifts toward lower 2Θ value with the increasing Ag content [104]. The peak positions of (024) and (220) of our sample, as shown in the inset of Fig.3.8, corresponds to Ag/Sb ratio of 1.

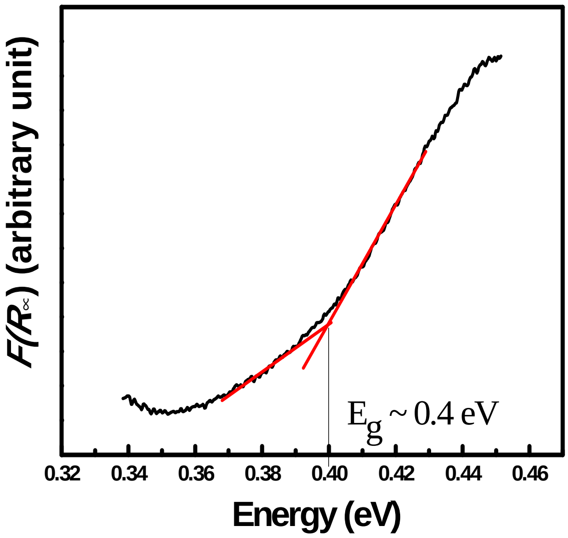

Fig. 3.9 Tauc plot for the synthesized TAGS-85 alloy.

The band gap of the synthesized TAGS-85 alloy was measured using diffuse reflectance spectroscopy, and a resultant Tauc plot is shown in Fig. 3.9. A band gap value of ~ 0.4 eV has been estimated, which is close that reported (0.6 eV) in literature [32]. It may be noted that the energy band gaps of $AgSbTe_2$ and GeTe are 0.007eV [114] and 0.6 eV, respectively. Therefore, observation of a band gap of 0.4 eV supports the inference that

TAGS-85 is not a composite of $AgSbTe_2$ and GeTe, rather it is an alloy in which Ag and Sb occupy the Ge sublattice.

3.4 Thermoelectric properties of PbTe and TAGS-85

In order to calculate the temperature dependence of *ZT* for synthesized n-type PbTe and p-type TAGs-85, all the three parameters α, ρ and κ were experimentally measured, which are discussed below.

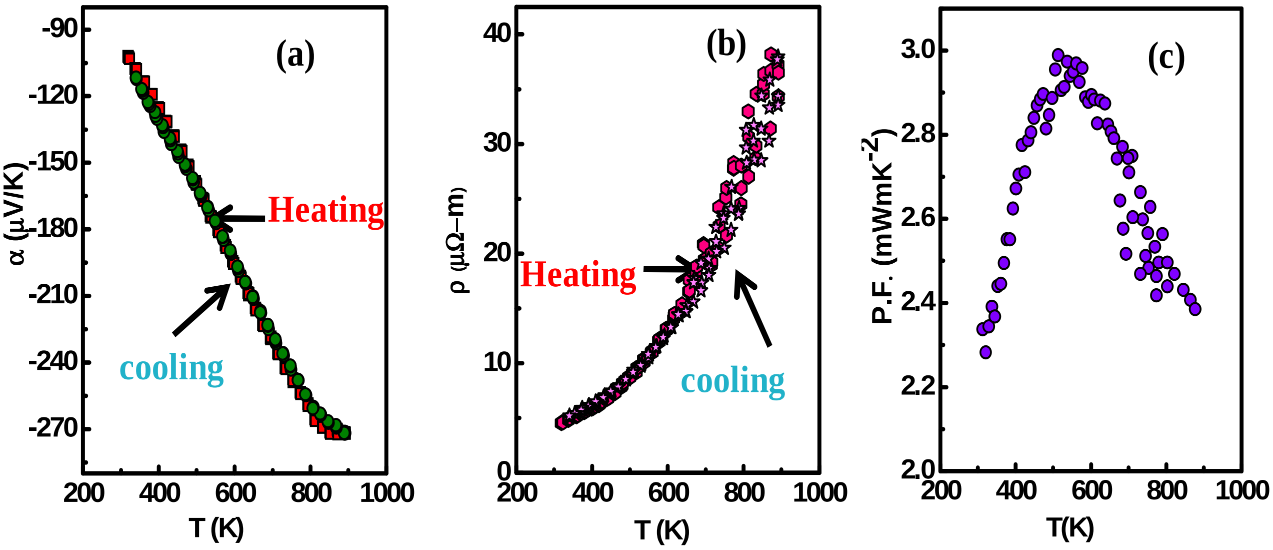

Fig.3.10 Temperature dependence thermoelectric parameters of n-type PbTe (a) α (heating and cooling data) (b) ρ (heating and cooling data) (c) Power factor calculated during the heating cycle.

3.4.1. Temperature dependent thermoelectric properties of PbTe

(a) Temperature dependence of α and ρ

The temperature dependences of α and ρ were measured for n-PbTe samples in the temperature range of 300-900 K during both heating and cooling cycles. The obtained results along with calculated temperature dependence of power factor (PF= α^2/ρ) are shown in Fig. 3.10. The major inference drawn from these figures are:

(i) The ρ value at 300 K is ~4.8 μΩ-m which monotonically increased to ~38μΩ-m at 900 K. This behavior is typical of highly degenerate semiconductor. The μ of the alloy at room temperature was calculated to be 26 $cm^2V^{-1}s^{-1}$. It may be noted that for cleaved PbTe single crystal samples the ρ value at 300 K is in the range of 0.12-0.67 μΩ-m, which is lower by nearly an order of magnitude. Similarly, the μ of the cleaved PbTe single crystal samples was found to be in the range of 500-1000 $cm^2V^{-1}s^{-1}$[115]. These results clearly indicate that the scattering of grain boundaries in our polycrystalline samples increases the ρ mostly due to the lowering of charge carrier mobility.

(ii) The room temperature values of α is -100μV/K, which linearly increased to ~ -280μV/K at 850 K. These values are similar to those reported for polycrystalline PbTe samples. The negative sign of the α indicates that synthesized alloy is n-type. However for temperature >850 K, the α shows an upturn which is attributed to the onset of bipolar diffusion as intrinsic carriers are excited across the energy gap. This onset is also reflected in the κ (discussed later). The bipolar diffusion adversely affects α due to a rising contribution of minority carriers and increased activation energy at elevated temperatures (as discussed in Section 1.4.1f). The negative effect of the onset of bipolar diffusion on α can be obtained by calculating the band gap (E_g) using the equation [116]:

$$E_g = 2e\alpha_{\max}T_{\max} \tag{3.1}$$

where e is the electronic charge. The $T_{\max}$ in equation 3.1 is the temperature at which the transport property changes due to the change in the transition from majority charge carriers to bipolarons. The value calculated using this relation comes out to be 0.46 eV which is slightly higher than that obtained by diffuse reflectance method.

(iii) No appreciable hysteresis has been measured on repeated thermal cycling, indicating that the alloy does not degrade upon heating to high temperatures. This has an implication that the synthesized n-type alloy is suitable for TEG applications whereby TEG's are subjected to a repeated thermal cycling.

(iv) The power factor (P.F.) shows a maximum value of 3000 μWmK^{-2}at ~550K. The P.F. decreases at high temperature due to the increase in the ρ which outweighs the increase in α.

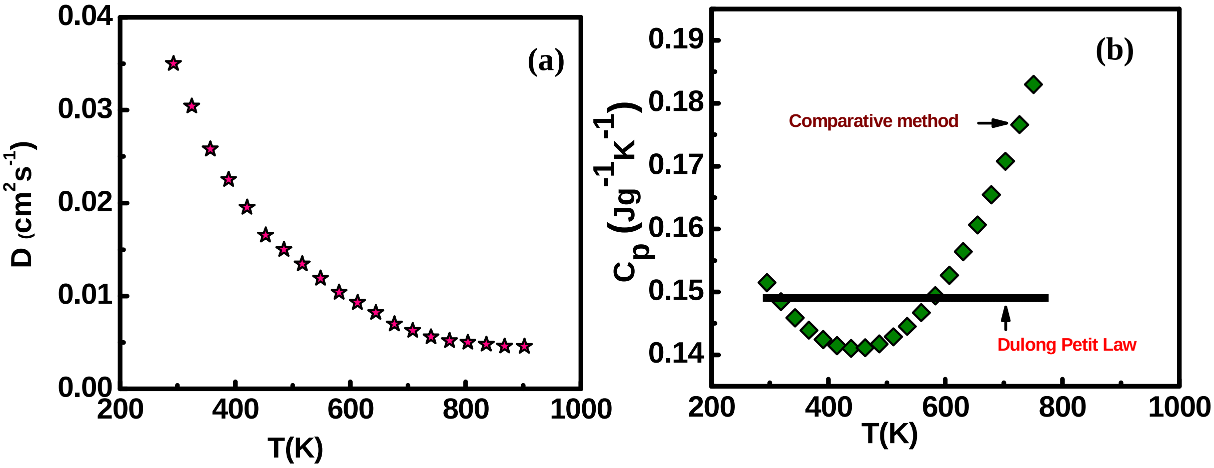

Fig.3.11 Temperature dependence of (a) D and (b) C_p of n-type PbTe.

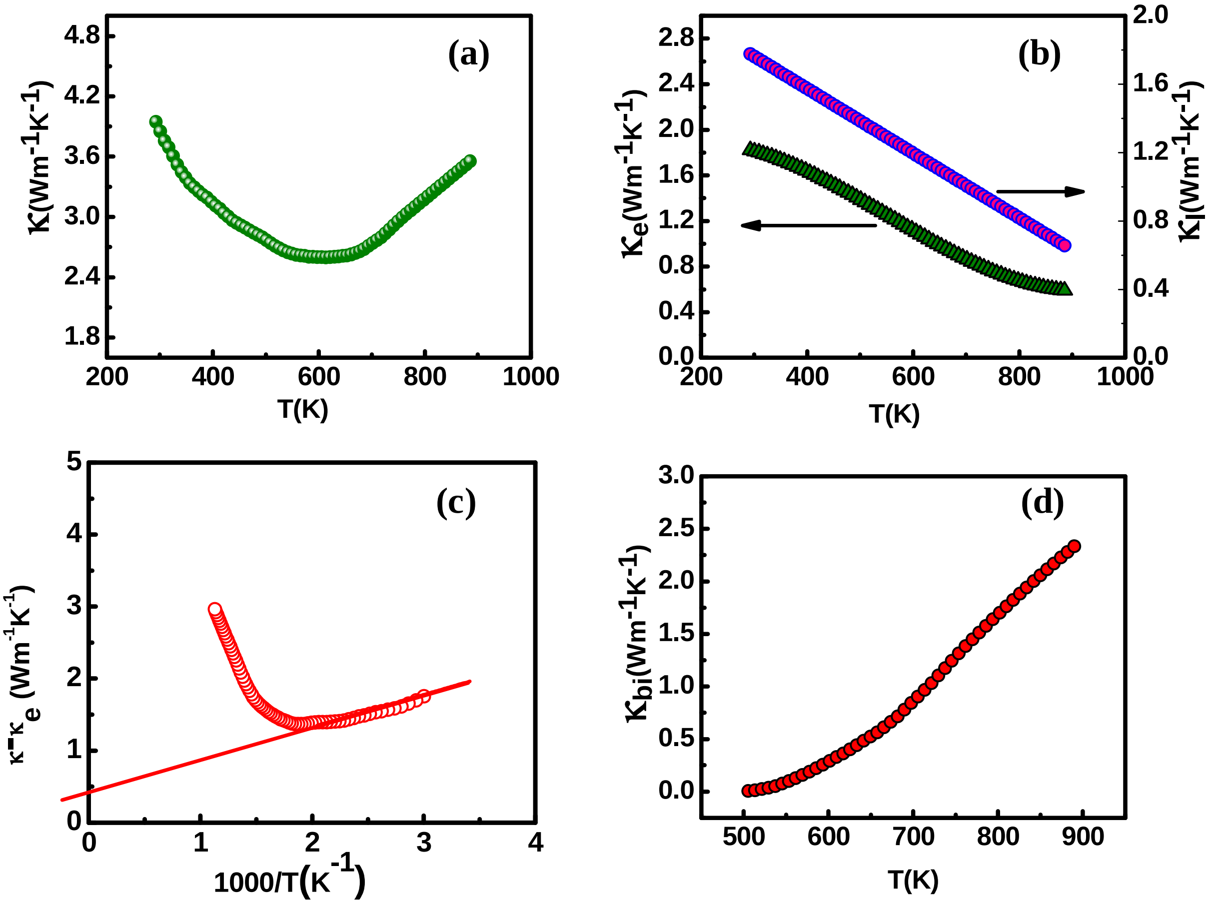

Fig.3.12. Temperature dependence (a) total thermal conductivity, κ (b) electrical (κ_e) and lattice (κ_l) components of thermal conductivity (c) difference of total and electronic thermal conductivity (κ_{total}-κ_e) and (d) bipolar thermal conductivity, κ_{bi} plot of n-type PbTe.

(b) Temperature dependence of κ

As discussed in Section 2.5.3, temperature dependence of κ was calculated from the temperature dependence of thermal diffusivity (D) and specific heat plots (C_p). Typical plots recorded for the synthesized PbTe samples are shown in Fig. 3.11 with an assumption that the mass density of the sample remains unaltered with temperature. The C_p calculated by the comparative method at room temperature is 0.15 Jg^{-1}K^{-1} which matches well with the value obtained by Dulong Petit law i.e. 0.149 Jg^{-1}K^{-1}. This value is also close to that reported in literature (i.e. 0.2 $Jg^{-1}K^{-1}$) which was obtained using DSC [117]. As mentioned in Section 2.5.3, the C_p value is the primary source of error in ZT calculation [101]. The density of the sample was calculated to be 7.5 g cm^{-3}, which is 93% of theoretical density.

As shown in equation 1.14, the total thermal conductivity is the summation of the three components, κ_e , κ_l and κ_{bi}.. At high temperature, the minority carriers generated in intrinsic excitations not only decreases the Seebeck coefficient, but also increases the thermal conductivity due to the bipolar diffusion. In order to clarify the contribution of bipolar thermal conductivity, κ_{bi} at high temperature, the κ_{bi} is separated from the κ_{tot} according to the proposed method $\kappa_{tot} - \kappa_{ele} = \kappa_{lat} + \kappa_{bi}$, where, κ_{ele}, was calculated by Wiedemann's Franz law. Since the acoustic phonon scattering is predominant at low temperature before bipolar diffusion is significant, $\kappa_{tot} - \kappa_{ele}$ equals to κ_{lat}, which is proportional to T^{-1}in accordance to the equation

$$\kappa_{lat} = 3.5\left(\frac{\kappa_\beta}{h}\right)^3 \frac{MV^{1/3}\theta_D^3}{\gamma^2 T} \tag{3.2}$$

where κ_β is the Boltzmann's constant, h is the Planck's constant, M the average mass per atom, γ the Grϋneisen parameter, V the average atomic volume and θ_D the Debye temperature. As the temperature is increased to higher temperature, $\kappa_{tot} - \kappa_{ele}$ starts to gradually deviate from a linear relationship between κ_{lat} and T^{-1} because the bipolar diffusion starts to contribute to the thermal conductivity. The κ_{bi} at high temperatures was estimated by extrapolating the linear relationship between κ_{lat} and T^{-1}.

Fig. 3.12 shows the temperature dependence of κ, κ_e , κ_l , κ- κ_e and κ_{bi}. The major inference drawn from these figures are:

(i) The κ shows an initial decrease with temperature upto 630 K, which at higher temperatures take an upturn. The initial decrease in κ is expected because in case of degenerate semiconductors the phonon scattering increases with temperature. The increase in κ for temperatures >630 K is attributed to the ambipolar diffusion of electrons and holes i.e. bipolar contribution (as discussed in Section 1.4.2). In order to gain an insight into the contribution of κ_{bi} at high temperatures, its value was estimated [31].

(ii) κ_e was calculated from the Widemann Franz law i.e. $\kappa_e = L\sigma T$, where L is the Lorenz number (2.44x10^{-8} WΩK^{-2}), which is plotted in Fig. 3.12 (b).

(iii) $\kappa - \kappa_e$ is plotted against T^{-1}, as shown in Fig. 3.12(c). At low temperatures, scattering of acoustic phonon is predominant and follows linear dependence on T^{-1}, which is evident in Fig. 3.12(c) as the experimental data fit linearly (shown by solid line). Thus in this temperature range, $\kappa - \kappa_e$ equals to κ_l .

(iv) However, for temperatures >630 K, $\kappa - \kappa_e$ deviates from the linearity and show an upturn due to the bipolar conduction. Thus, the contribution of κ_{bi} is estimated by subtracting the extrapolated value of κ_l (i.e. the fitted line) from $\kappa - \kappa_e$, which is plotted in Fig 3.12(d) shows the κ_{bi} vs T plot at high T. It is evident that at high temperatures, the contributions from κ_{bi} are predominant, which should be effectively suppressed as it degrades κ in addition to α.

(c) Temperature dependence of *ZT* for n-type PbTe

Based on the experimentally measured α, ρ and κ the temperature dependence of *ZT* is calculated and is shown in Fig. 3.13. It is seen that *ZT* attains a highest value of ~ 0.7 in the temperature range of 675 -725 K. This curve is almost identical to that reported in literature and shown in Fig. 1.10. This data show that the synthesized n-type PbTe material can be effectively used for devices operating upto 730 K.

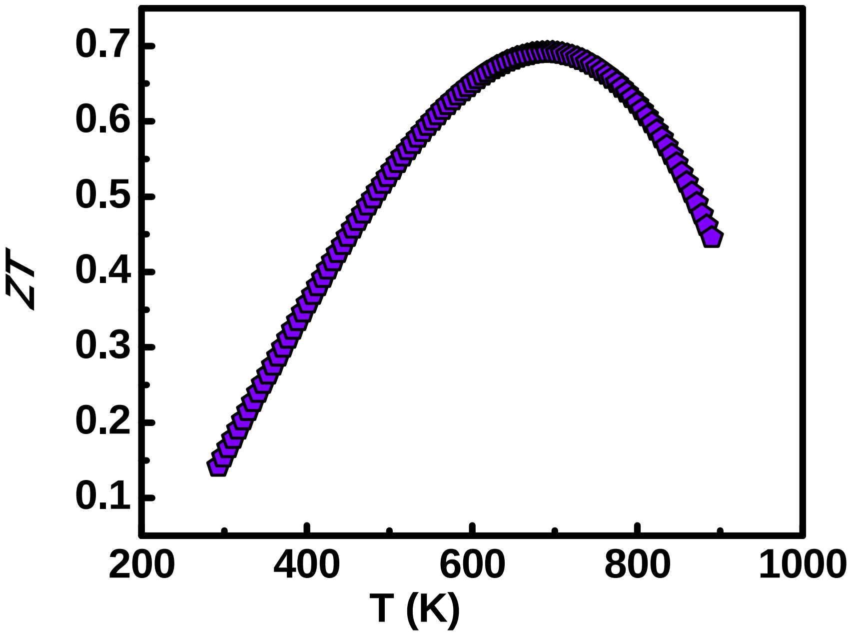

Fig. 3.13 Temperature dependence *ZT* of n-type PbTe.

3.4.2. Temperature dependent thermoelectric parameters of TAGS-85

The temperature dependences of α, ρ, and α^2/ρ for the synthesized TAGS-85 alloys are shown in Fig. 3.14. It is seen that all three curves exhibit a change in slope near 773 K, which is related to the phase transition from a low-temperature rhombohedral structure to high temperature cubic phase, as discussed earlier. The positive sign of the α indicates TAGS-85 has p-type conduction with holes as the majority charge carriers. Hall measurements show the hole concentration of ~1×10^{20} cm^{-3} at room temperature. The value of α at 300 K is +102.3 µV/K, which increases to +199.7µV/K at 748 K. A decrease in α for temperatures >750 K, as discussed, is due to the bipolar diffusion. The temperature dependence of the ρ is typical of degenerate semiconductors where the increase of the ρ with temperature is mostly associated with an increase in carrier scattering by phonons. The plateau of the ρ vs T plot is associated with the phase transition as discussed earlier. Beyond 700 K, the ρ value decreases with temperature and this is attributed to the onset of intrinsic conduction. The power factor thus calculated from α and ρ values is shown in Fig. 3.14(c), which shows a nearly constant power factor value for temperatures >500 K.

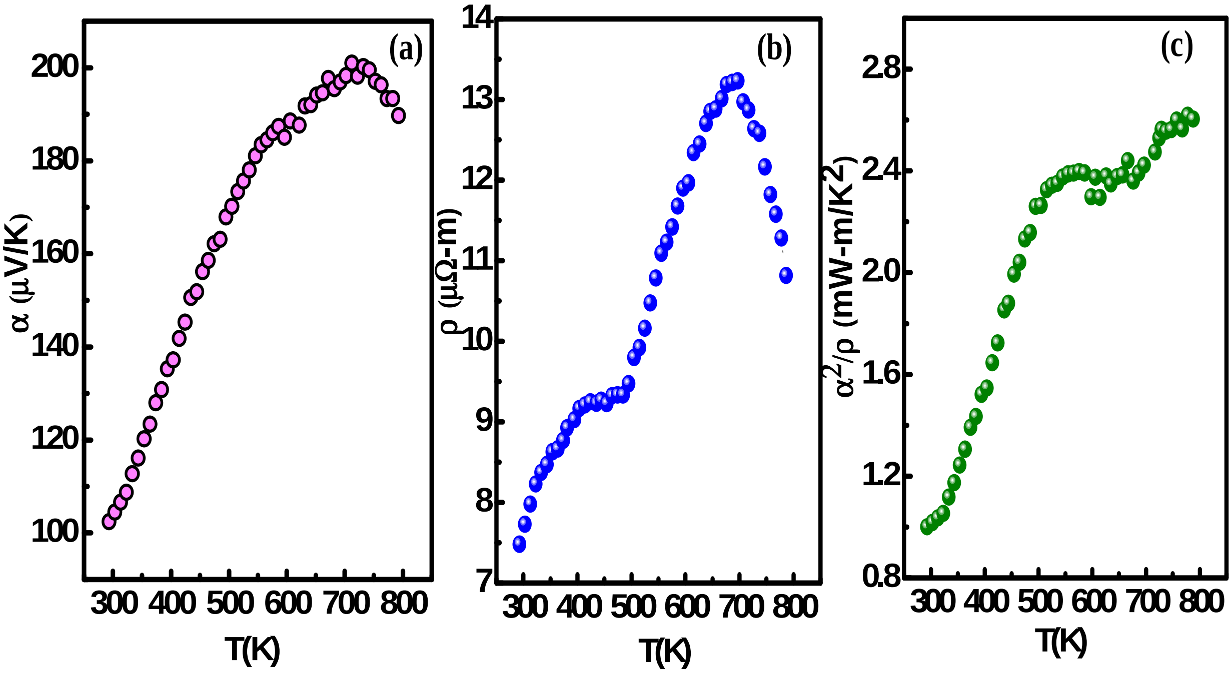

Fig. 3.14 Temperature dependence of thermoelectric parameters: (a) α (b) ρ and (c) power factor of p-type TAGS-85.

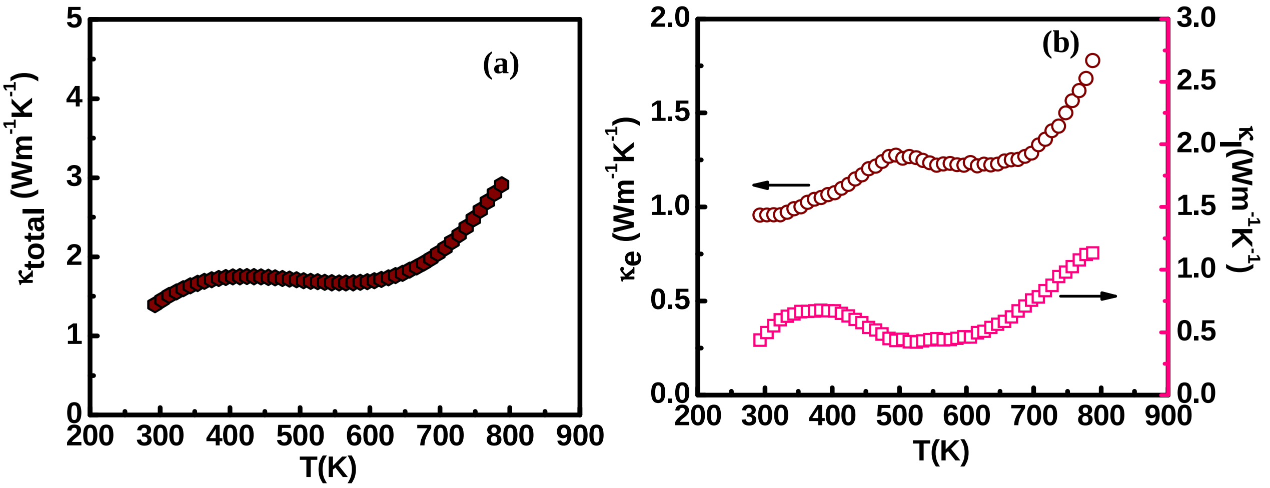

Fig. 3.15 Temperature dependence of : (a) κ (b) κ_e and κ_l of p-type TAGS-85.

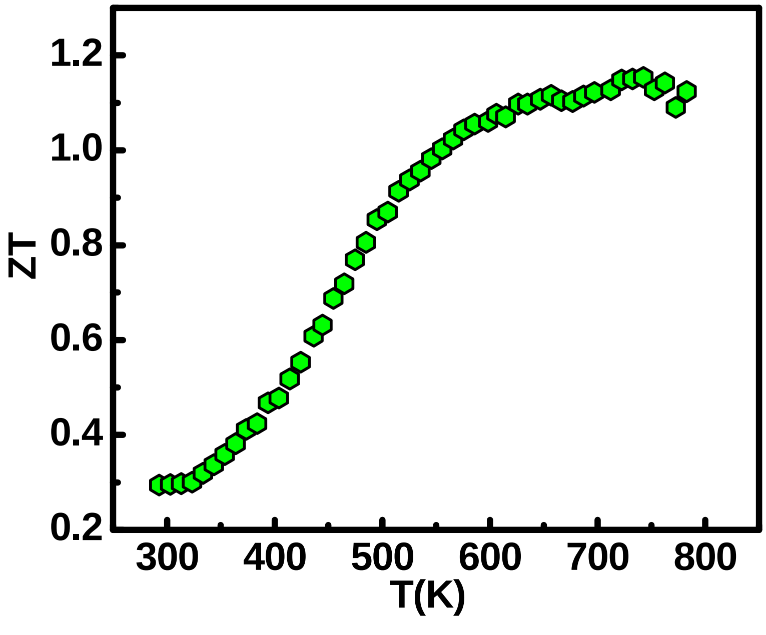

Fig. 3.16. Temperature dependence of *ZT* for p-type TAGS-85.

The temperature dependence of κ measured for the the TAGS-85 alloy is shown in Fig. 3.15, which is quite complex owing to rhombohedral to cubic phase transition as well as contributions from bipolarons. A change in the slope in the κ at ~400 K is attributed to the phase transition from low temperature rhombohedral to the high temperature cubic phase. This phase change is also evident in κ_e and $\kappa_{l,}$ as shown in Fig. 3.15(b). At temperatures >620 K, an increase in the κ is attributed to the onset of bipolar diffusion. Since the ρ of the sample is low, κ_e is dominates over $\kappa_{l.}$ The calculated temperature dependence of *ZT* is shown in Fig. 3.16, which exhibits a highest value of ~1.2 at 730 K. This temperature dependent of *ZT* is almost identical to that reported in literature.

3.5 Preparation of thermolegs with low contact resistances

As discussed in Chapter 1, one of the biggest challenges in fabrication of thermoelectric devices is optimization of n-type and p-type thermolegs having suitable metallic shoes with Ohmic interface contact resistances. The metallic shoe is essential for connecting n-type and p-type thermolegs using metallic interconnects. In this Section, we present fabrication of n-type PbTe and p-type TAGS-85 thermolegs with metallic shoes based on the concepts of graded layers, which not only takes care of CTE mismatch between different layers, but also prevents the inter-diffusion of interconnect material into n and p-type thermolegs. In this regard, thermolegs with diameter ranging from 5 mm to 15 mm and height with aspect ratio 1:1 were fabricated. In ideal case, the dimension of the thermolegs of the device should exhibit similar resistance so that equal current passes through both the legs. This can be possible by either altering the diameter of the pellets or by matching the resistance of the two pellets. In our case, the diameter and height of the two pellets were kept same. So the resistance of the two thermolegs were matched by altering the thickness of the different buffer layers which were intentionally introduced to take care of the coefficient of thermal expansion mismatch between different layers and prevention of inter-diffusion of interconnect material into n- and p-type thermolegs.

In our device fabrication, we have used thermolegs of diameter 7.5 mm and height of 8 mm based on the mechanical strength of the thermolegs and optimum size of the final device. Thermolegs of smaller diameter were also pressed but it seems to be fragile whereas larger diameter thermolegs yielded bigger size of the device.

3.5.1 n-type PbTe thermolegs

In order to prepare n-type PbTe thermolegs, we have used the graded layers as schematically depicted in Fig. 3.17. The die was filled with different powders in the sequence Ag disc/ Fe/PbTe+Fe/PbTe/PbTe+Fe/Fe/Ag disc. Ag is chosen as shoe at both ends because Ag strips can be utilized for connecting various thermolegs and Ag-Ag bonding can be easily made by diffusion bonding process. However, Ag cannot be directly connected to PbTe, as Ag diffuses into PbTe, which hampers the long term stability of the thermoleges. This has demanded the introduction of interfacial Fe layer between Ag and PbTe. The good part of Fe is that it is immiscible with Ag at equilibrium i.e. they do not interdiffuse [118,119, 120,121]. However, the negative aspect is that the thermal expansion coefficients of PbTe (28.9 μm K^{-1} at 298K) and Fe (11.8 μm K^{-1} at 298K) are very different. Therefore, hot-pressing of Ag/Fe/PbTe/Fe/Ag thermolegs lead to cracking at the Fe/PbTe interface and the thermolegs are easily broken. In order to solve this problem, a graded layer of a homogeneous material consisting of 50% Fe +50% PbTe was inserted between Fe and PbTe, as the mixture has the intermediate value of thermal expansion coefficient.

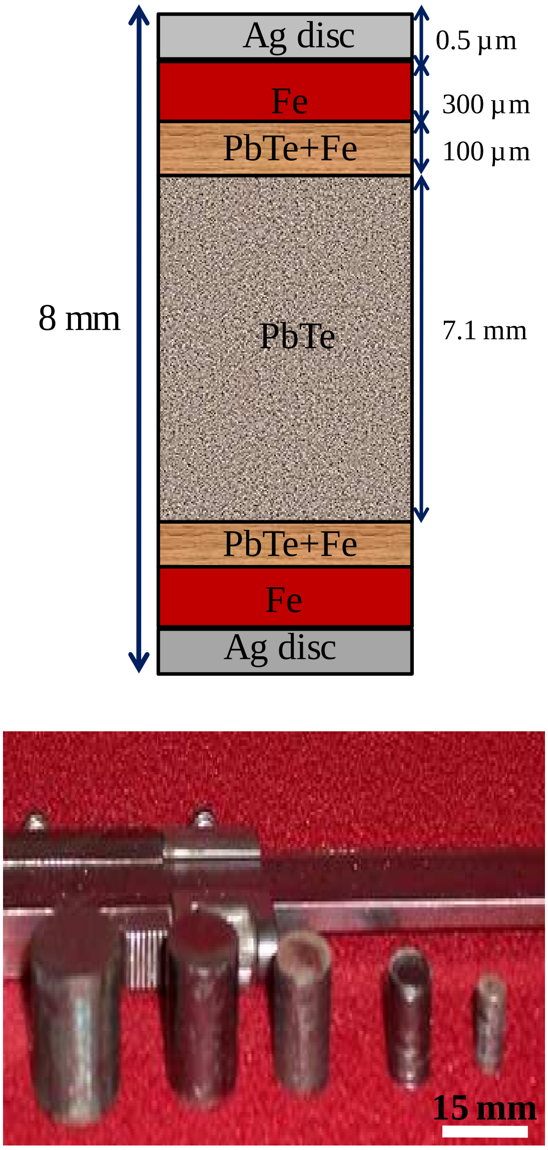

Fig. 3.17. (a) Sequence of filling the materials in die for the preparation of n-type PbTe thermolegs using vacuum hot press. (b) Photographs of typical n-type thermolegs of different sizes.

The S.S. die filled with the materials in the sequence shown in Fig. 3.17 was vacuum hot pressed at ~873 K under a base vacuum of 2 x10^{-5} torr by applying a load of 700 kg/cm^2 for 2 h. The load was released at the beginning of the cooling schedule. It may be noted that 873 K is the optimum pressing temperature of n-type PbTe. At temperature <873K, the thermolegs have poor mechanical strength; while for temperatures >873 K the PbTe tends to sublime. Similarly, the applied load of 700 kg/cm^2 was found to be optimum, as at low pressures the density of the pellets was low while at higher pressures the pellets were found to deform. Photographs of different n-type PbTe thermolegs having different sizes are shown in 3.17. However, for device fabrication, thermolegs of 7.5 diamater and 8 mm height were optimized based on the mechanical strength of the thermolegs and optimum size of the final device. Smaller diameter thermolegs were fragile while larger diameter thermolegs yielded bigger size of the devices of similar output voltage.

One of the requirements of the good thermolegs is that the interface should be stable for a long period under operating conditions. To investigate this, we have kept n-type PbTe thermolegs at 773 K for 4 weeks. The thermolegs were cut along the vertical axis and polished. The cross-section of the sample was imaged using SEM and elemental x-ray mapping and typical images are shown in Fig. 3.18. The back-scattered image of PbTe element (shown at the centre of Fig. 3.18) clearly reveals chemically sharp interfaces between Ag, Fe, (PbTe + Fe) and PbTe. This is further supported by the x-ray elemental mapping of Ag, Fe, Pb and Te elements (shown as side images in Fig. 3.18). No interaction between PbTe and Fe is observed. These results are in agreement with the reported phase diagrams of PbTe–Fe and Fe/Ag and indicate the high quality of the bonding achieved between PbTe and Fe[122]. The contact resistance was calculated for the interface of different graded layer(both at the top and bottom) and PbTe material by the simple equation, $R_{PbTethermoleg} = 2XR_{gradedlayers} + R_{PbTe}$ and it came out to be 0.1mΩ.($R_{PbTethermoleg}$ =1.3mΩ and R_{PbTe} = 1.1mΩ).

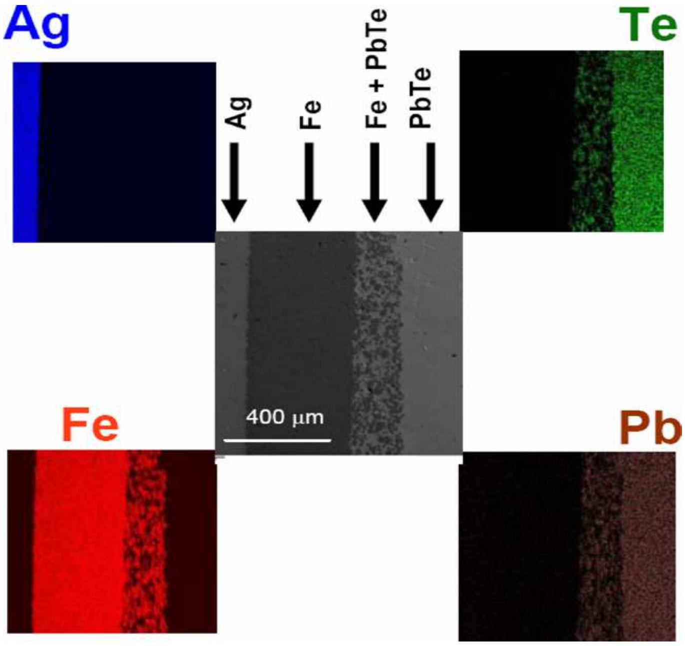

Fig. 3.18 SEM image showing various interfaces in a PbTe thermoleg. Side images show the elemental x-ray mapping of Ag, Fe, Pb and Te.

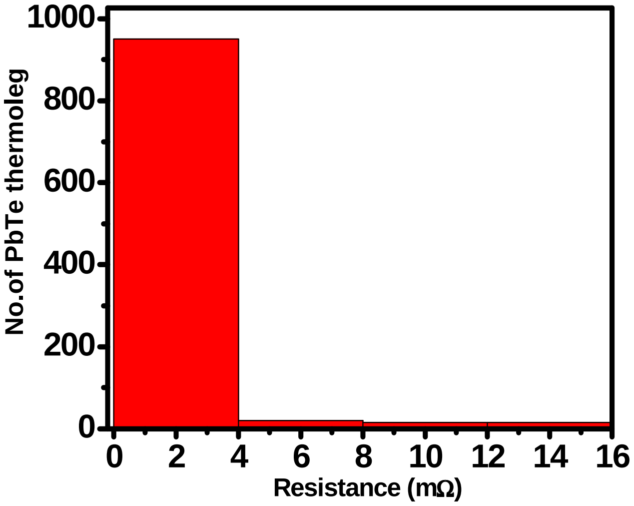

Fig.3.19 Bar chart showing the variation in resistance of n-type PbTe thermoleg.

More than 1000 n-type PbTe thermolegs (size: 7.5 mm dia and 8 mm height) were prepared. The resistance of the thermolegs were measured using four-probe method, and the statistics showing the resistance variations is shown in Fig. 3.19. It is seen that majority of the thermoleg have resistance < 4 mΩ, which were used for the device fabrication. It may be noted that some sample exhibited high resistance, which were due to the presence of cracks at the interfaces and were not used for the device fabrication.

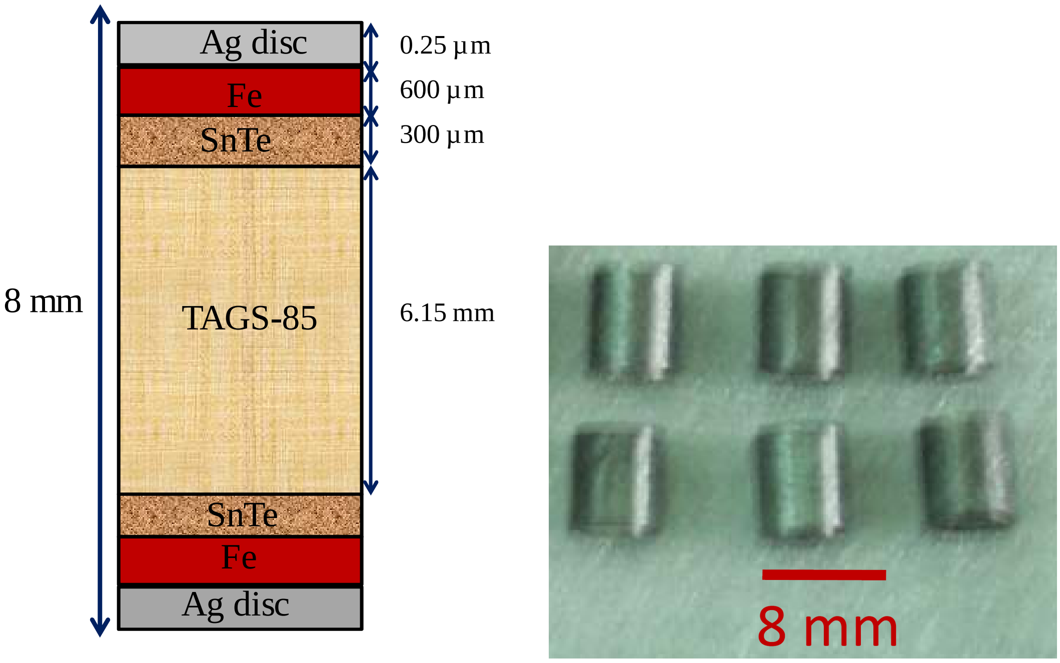

Fig. 3.20. (a) Sequence of filling the materials in die for the preparation of p-type TAGS thermolegs using vacuum hot press. (b) Photohraphs of TAGS thermolegs.

3.5.2 p-type TAGS-85 thermolegs

The preparation of p-type TAGS-85 thermoleg, as schematically, as shown in Fig. 3.20, is similar to that of n-PbTe thermolegs except the fact that buffer layer used in this case is SnTe. The use of SnTe buffer layer has two advantages: (i) it is p-type thermoelectric materials [123,124] (ii) its thermal expansion coefficient 13×10^{-6} µm K^{-1} (at 298 K) is in between the values for Fe (12×10^{-6} µm K^{-1}) and TAGS-85 alloy (14×10^{-6} µm K^{-1}) (iii) it acts as a diffusion barrier to Ag in TAGS-85 and (iv) provides low bond resistance and good aging characteristics [1] . As a result SnTe minimizes thermal stress induced cracking at the interface. However, SnTe being a layered material having weak mechanical strength, a very thin layer of SnTe is added during pellet fabrication. The die filled with the materials in the sequence shown in Fig. 3.18 was vacuum hot pressed at ~823 K under a base vacuum of 2 $x10^{-5}$ torr by applying a load of 650 kg/cm^2 for 2 h. The load was released at the beginning of the cooling schedule. The vacuum hot pressing parameters were optimized in such a way that both PbTe and TAGS-85 thermolegs are of similar heights.

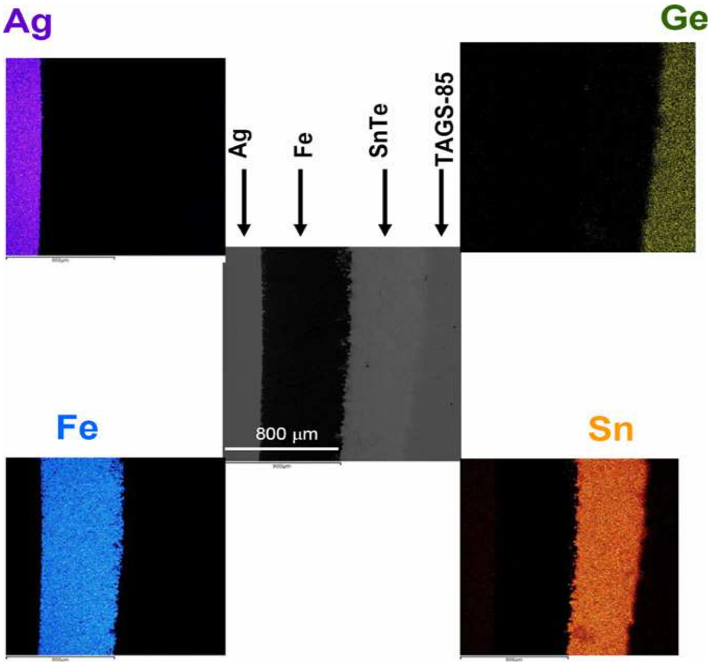

Fig. 3.21. SEM image showing various interfaces in a TAGS thermoleg. Side images show the elemental x-ray mapping of Ag, Ge, Fe and Sn.

The cross-sectional SEM image and elemental x-ray mapping for TAGS-85 thermolegs are shown in Fig. 3.21. The back-scattered image (shown at the centre of Fig. 3.21) clearly reveals chemically sharp interfaces between Ag, Fe, SnTe and PbTe. This is further supported by the x-ray elemental mapping of Ag, Fe, Sn and Ge elements (shown as side images in Fig. 3.21). No reactions between PbTe and SnTe as well as SnTe and Fe are observed. These results clearly indicate that SnTe is an excellent buffere layer for preparation of p-type TAGS-85thermolegs with Ag metallic shoes.

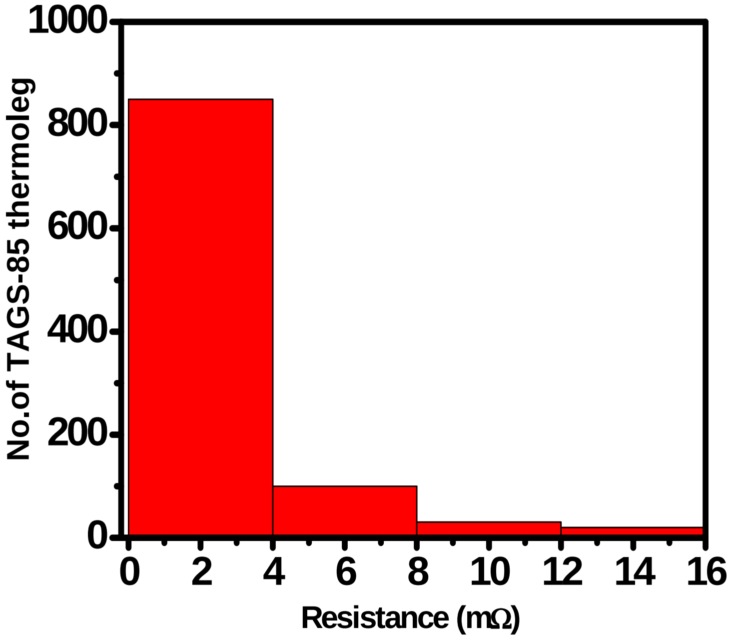

Fig.3.22. Bar chart showing the variation in resistance of p-type thermolegs.

More than 1000 p-type TAGS-85 thermolegs (size: 7.5 mm dia and 8 mm height) were prepared. The bar chart depicting the statistics of resistance variations is shown in Fig. 3.22. It is seen that majority of the thermoleg have resistance <4 mΩ, which were used for the device fabrication. However samples exhibiting high resistance (i.e. >4 mΩ) are much higher in numbers as compared to that of n-type PbTe. This is attributed to a phase transition in TAGS-85 that occurs from high temperature cubic phase to low temperature rhombohedral.

This structural phase transition might generate stresses at the interface leading to cracks and hence high resistance. For the same reason, TAGS-85 thermolegs were more fragile as compared to n-type PbTe, and therefore, handling of TAGS-85 thermolegs requires a bit extra care. The contact resistance was calculated for the interface of different graded layer(both at the top and bottom) and TAGS-85 material by the simple equation, $R_{TAGS-85thermoleg} = 2XR_{gradedlayers} + R_{TAGS-85}$ and it came out to be 0.05mΩ.($R_{PbTethermoleg}$ =1.1mΩ and R_{PbTe} = 1.0mΩ).

3.6 Fabrication of thermoelectric generators

3.6.1 Fabrication process

As discussed in Chapter 1, apart from the preparation of n-type and p-type thermoelectric thermolegs having ohmic contact resistance metallic shoes, appropriate housing that only cannot hold the thermolegs but also minimizes the shunt heat from hot end to cold end. This implies that the housing material should have: (i) much lower thermal conductivity as compared to that of n- and p-thermolegs, and (ii) it should be machinable. In this regard, asbestos (κ = 0.14 Wm^{-1}K^{-1}) and zircar (κ = 0.1 Wm^{-1}K^{-1}) are found to be suitable. Asbestos though inexpensive but is known to cause serious health hazards in humans, and therefore handling requires special care. We have used both asbestos and zircar for the housing of the thermoelectric devices. Typical photographs of the zircar housing suitable for mounting n-type and p-type thermolegs in square and linear arrays are shown in Fig.3.23. The size of the drilled holes are meant to tight fit the thermolegs and protrude 0.5 mm each side for making interconnects with silver strips.

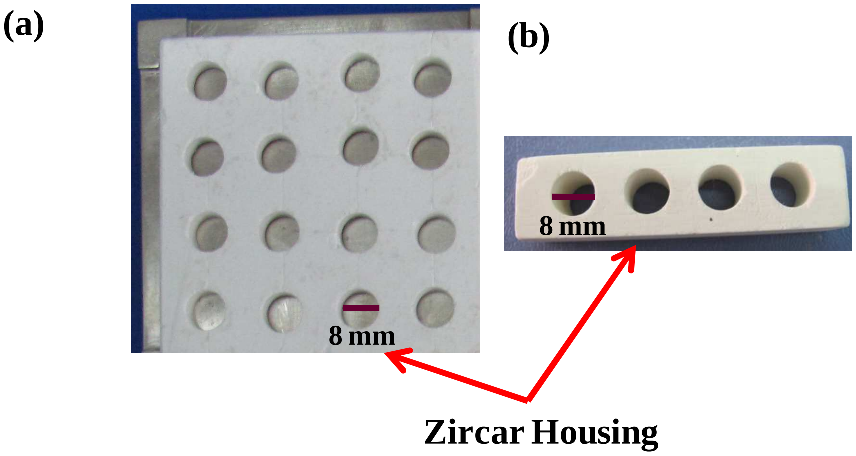

Fig. 3.23. Photograph of the zircar housing for holding thermolegs in (a) square array and (b) linear arrays.

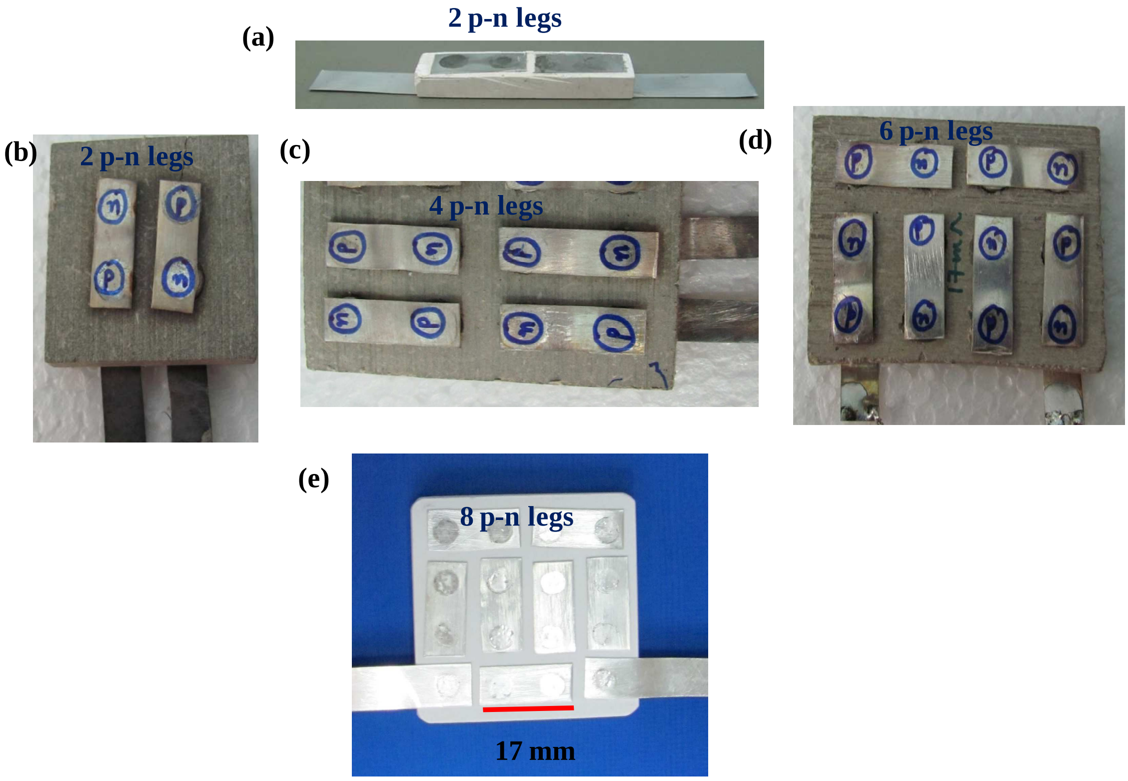

Fig.3.24. Photographs of the various thermoelectric generators. (a) 2 p-n thermolegs linear thermoelectric generators. Square array thermoelectric generators (b) 2p-n legs (c) 4p-n legs (d) 6 p-n legs and (e) 8 p-n legs.

After fitting the n-type PbTe and p-type TAGS-85 thermolegs in the housing, they were mounted in the zig, as described in Chapter 2. The silver strips were placed on the top and bottom sides of the thermolegs in such a way that n-type and p-type thermolegs are connected electrically in series, and then covered by the upper part of the zig. The mounted zig was loaded to vacuum hot press (base vacuum of 2×10^{-5} torr) and the diffusion bonding of silver strips with thermolegs was achieved at a temperature of 673 K under a pressure of 5 kg/cm^2. The bonded silver strips were found to be mechanically strong. The photographs of various linear and square-array thermoelectric devices are shown in Fig. 3.24.

3.6.2 Evaluation of the thermoelectric generators

(a) Characteristics of thermoelectric generators

All the fabricated thermoelectric generators were evaluated for their heat-to-electricity conversion using a home-made setup described in Chapter 2. To begin with, we describe characteristics of a two-thermolegs thermoelectric generator having total resistance of 4 mΩ, which was placed between hot (773 K) and cold surfaces (363 K). This has resulted in a constant temperature difference of 683 K between hot and cold ends of the device. The device exhibited an open circuit voltage of 130mV. Typical characteristics of the thermoelectric generator as a function of load resistance (R_L) are shown in Fig. 3.25 (a). It is seen that the voltage (V_L) across the load increases as the R_L increases. The load current (I_L) is calculated from the V_L/R_L ratio, and is plotted in Fig. 3.25(b). The I_L decreases and the R_L increases. The output power of the thermoelectric generator is shown in Fig. 3.25(c), and it is evident that the maximum output power of ∼1.2 W is obtained for R_L of 4 mΩ, which is equal to that of device resistance (in accordance to the maximum power transfer theorem). At peak power, the values of V_L and I_L are respectively, 68mV and 17 A. It is therefore evident that the thermoelectric generators are low voltage high current devices. Similarly all other devices were characterized under identical conditions and the obtained parameters are summarized in Table 3.1. It is seen that the output power is proportional to the number of thermolegs in the thermoelectric generator.

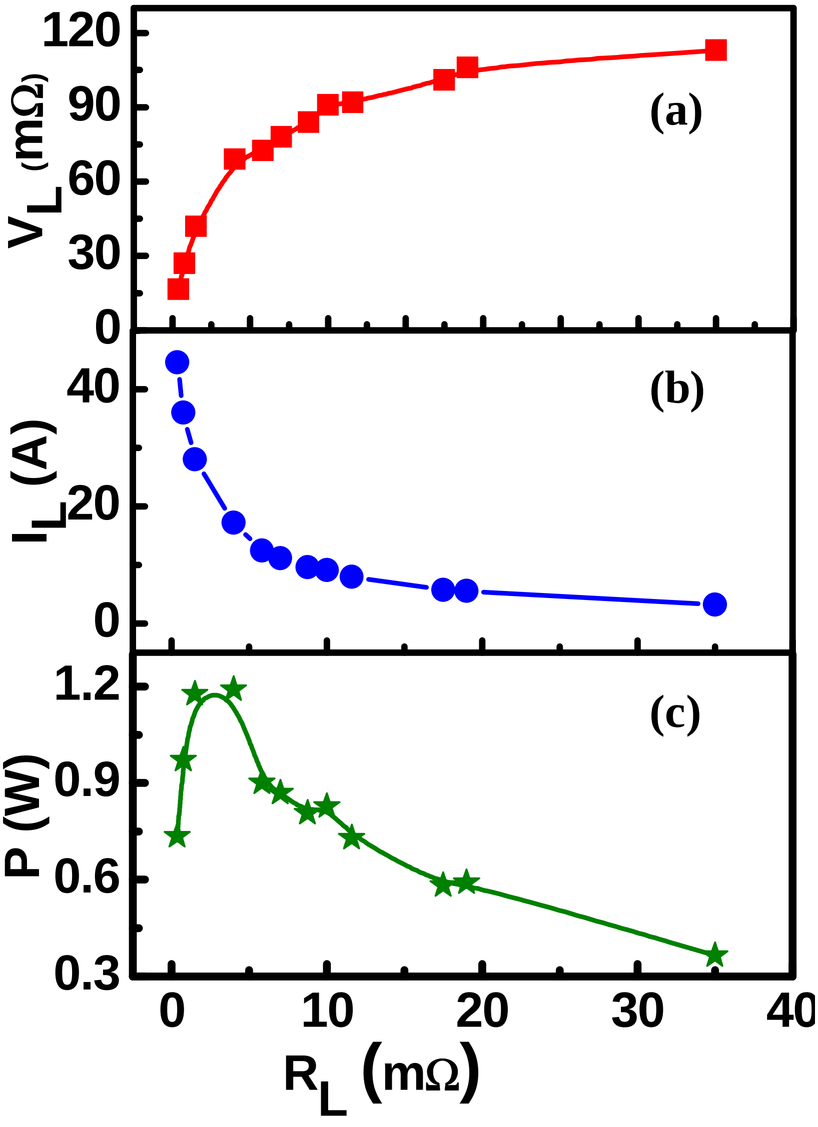

Fig. 3.25. Output of a 2 p-n thermoleg generator as a function of load resistance (R_L): (a) load voltage (V_L) (b) current (I_L) and (c) power (P).

Table 3.1: Summary of various parameters of different thermoelectric generators.

Generator	**V_{oc} (mV)**	**R_L (mΩ)**	**V_L (mV)**	**I_L (Amp)**	**P_{out} (Watt)**
2 p-n legs (square array)	102	4	69	17	1.2
2 p-n legs (linear array)	100	3.8	68	18	1.2
6 p-n legs	450	19	285	13.0	3.7
8 p-n legs	568	25	318	12.7	4

(b) Contact resistance of the thermoelectric generators

I–V characteristics of all the generators were found to be linear showing ohmic contacts. The internal resistance (R_{int}) of a generator has two contributions. The first contribution is due to material resistance (R_m) contributed by (a) PbTe (R_{PbTe}) and TAGS (R_{TAGS}) cylindrical shaped pellets, (b) SnTe (R_{SnTe}) or PbTe + Fe ($R_{PbTe+Fe}$) and Fe layers (R_{Fe}) in TAGS/PbTe elements and (c) silver discs and strips (R_{Ag}). The second contribution is combined contact resistance (R_c) of all the interfaces in each element. Materials resistance contributions, R_m, were determined by measurement of four probe resistivity of each material (using rectangular bar-shaped samples as described earlier) and for a two legs generator were found to be R_{PbTe} = 1.1mΩ, R_{TAGS} = 0.75 mΩ, R_{SnTe} = 45.4 μΩ, $R_{PbTe+Fe}$ = 5μΩ, R_{Fe} = 0.87μΩ and R_{Ag} = 9.82μΩ yielding a total materials resistance of R_m = 3.84mΩ . The resistance of a complete two legs device (having four thermolegs) was measured by the four probe technique to be 3.98mΩ (the resistance of the complete thermoelectric generator was also calculated by measured voltages across a load and open circuit voltage of the generator. Both measurements yielded similar results). This yields average contact resistance of two contacts for each element to be 35μΩ (specific contact resistance = 7.6μΩcm^2). The contribution of contact resistance to total device resistance is found to be 3.5%. Similar results were obtained for four and six legs devices. It may be noted that the fractional loss of power due to contact resistance is approximately equal to the ratio of contact and thermoelectric material resistances. For contacts of given specific resistance, fractional loss of power is independent of element area but is inversely proportional to element length. As the four probe resistance of the device can be measured accurately (<0.1% error), error in the measurement of contact resistance arises from errors in the measurement of resistivity of each material (10%).

(c) Efficiency of the thermoelectric generators

The efficiency of the thermoelectric generators was directly measured as a ratio of electrical power output to heat flow through the device. For determination of heat flow through device elements, radiation loss from heater and heat flow through housing were first determined using thermally insulating material and plain asbestos sheets. For the two legs generator, heat flow was found to be 22W, using the equation, $Q = \kappa A \frac{dT}{dx}$ where, Q is the total heat flow, κ is the thermal conductivity, A is the cross sectional area, dT is the temperature difference and dx is the length of the pellet.

For typical 2 p-n leg generator, having two PbTe thermolegs and two TAGS-85 thermolegs, the heat flow was calculated to be $2(Q_{PbTe} + Q_{TAGS-85})$, which comes out to be ~ 22W. For calculating Q_{PbTe}, κ_{PbTe} was taken from Fig. 3.12(a) and for calculating $Q_{TAGS-85}$,

$\kappa_{TAGS-85}$ was taken from Fig. 3.15(a) at 773 K, yielding a typical device efficiency of ~6%, which is same as that reported for the commercially available best devices.

(d) Figure of merit of the device

As discussed in equation 1.16, the figure-of merit of the device was calculated using the efficiency obtained for the n-type PbTe and p-type TAGS-85 devices, by measuring the total power output based on the input power given. The $\overline{ZT}$ was found to be ~0.41.

Moreover, $\overline{ZT}$ was calculated for n-type PbTe and p-type TAGS-85 from the ZT vs T plot and it was found to be ~ 0.5 and 0.8 respectively. Since both n- and p- type thermolegs are connected electrically in series, therefore the lower ZT material will dictate the efficiency of the device. The $\overline{ZT}$ of the device calculated by the above two methods deviate from each other by 10%. The deviation can be due to the fact that the $\overline{ZT}$ calculated by equation 1.16 takes into consideration the various contact resistances present in the device, for e.g. the contact resistance between the heat source and the device, the contact resistance between the heat sink and the device and the Ag interconnect and the Ag-disc placed at the top of the thermoleg in addition to the contact resistances developed between various buffer layers added in the thermolegs. On the other hand, the $\overline{ZT}$ calculated from the ZT vs T plot considers only the contact resistances developed between the buffer layers added in the thermolegs.

3.6.3 Long term stability of thermoelectric generators

Another important characteristics of good thermoelectric devices is that they should work unattained for prolonged period without any fail. In order test the long term stability of our devices, we have kept a 2 p-n thermolegs device for its continuous operation under T_h of 773 K with a temperature difference (ΔT) of 683 K in air for almost one year. The V_L of the device was measured after a certain period of time, and the obtained result is shown in Fig. 3.26. It is seen that the V_L and out power of the device remained constant for a period of 300 days. These results clearly indicate the stability of the devices for their long term operation. Several such devices were operated continuously for more than 12 months without any measurable degradation.

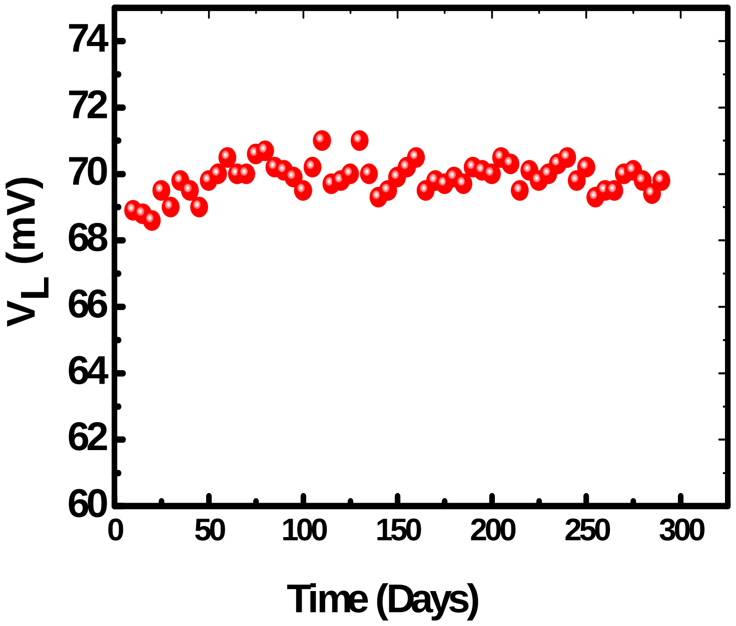

Fig. 3.26. Long term stability of 2 p-n leg generators for 300 days.

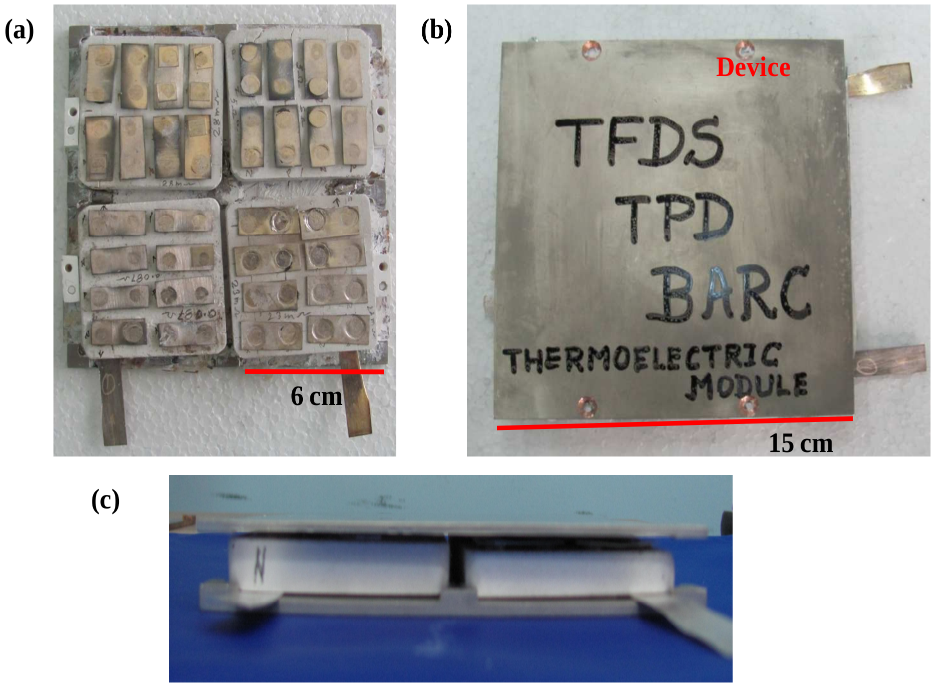

Fig. 3.27 (a) Integrated thermoelectric module consisting of four 8 p-n leg generators connected electrically in series. (b) Top view and (c) Side view of the module.

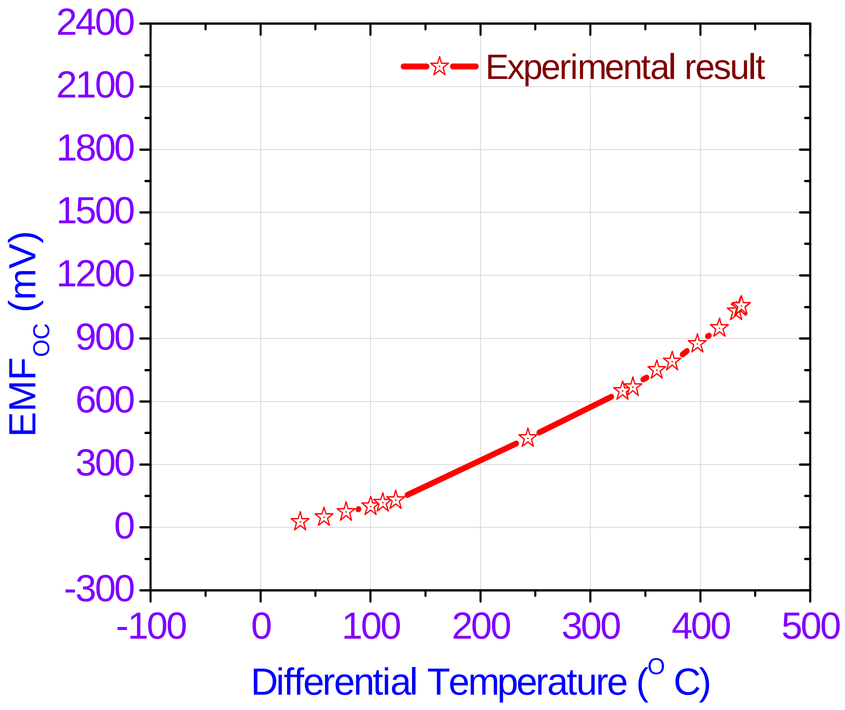

Fig. 3.28. The open circuit voltage of thermoelectric module as a function of temperature difference between hot and cold ends.

3.6.4 Integrated thermoelectric modules

As the developed devices are low voltage and high current with relatively low efficiencies, large modules need to be fabricated to generate reasonable amount of power to drive the electronic equipments. For this purpose we, have fabricated large module that consists of four 8 p-n thermolegs devices connected electrically in series, as schematically shown in Fig. 3.27. For this purpose nickel-plated copper plates were used to pack these devices from top and bottom ends. These open circuit voltage of the module was measured as a function of temperature difference between hot and cold ends, and the resultant data is plotted in Fig. 3.28. It is seen that the open circuit voltage of the device attains a value of 1000mV.

3.7 Conclusions

In this Chapter we have successfully demonstrated fabrication of thermoelectric generators based on conventional n-type PbTe and p-type TAGS-85 thermolegs. Single-phase n-type PbTe and p-type TAGS-85 thermoelectric materials were synthesized using melt-and-rock method. The temperature dependence of α, ρ and κ were measured for both PbTe and TAGS-85 samples. For both the samples, ρ was found to increase with temperature, which is typical of degenerate semiconductors, as scattering of charge carriers with phonons increases with temperature. However, TAGS-85 samples exhibited down-turn at ~625 K, which is attributed to intrinsic excitation due to narrow band gap. The κ, in the temperature 300-600 K, decreases with increasing temperature and follows κ ~1/T behaviour, indicating predominant scattering of acoustic phonons. However at temperatures >600 K, κ starts increasing, which is attributed to the additional contribution from diffusion of bipolarons. The peak *ZT* values obtained for PbTe and TAGS-85 samples were respectively 0.8 and 1.15.

A new strategy was adopted to fabricate the n- and p-type legs that have metallic shoes with ohmic contacts. In order to minimize the thermal and lattice expansion mismatch between metallic shoe and legs, layer-structured legs i.e. Ag/Fe/PbTe+Fe/ PbTe/ PbTe+Fe/Fe/Ag and Ag/Fe/SnTe/TAGS-85/SnTe/Fe/Ag, were fabricated. The cross-sectional back-scattered electron images of the legs clearly revealed that all the interfaces are chemically sharp i.e. minimal inter-diffusion. The specific contact-resistances estimated were ~7-10 $\mu\Omega cm^2$. Thermoelectric power generators were fabricated by packing the n- and p-type legs using zircar housing and interconnecting them by silver strips through diffusion bonding. For a hot end temperature of 773 K and a temperature difference of 683 K, two legs generators exhibited typical output power of ~1.2W (at current of 17 A) with a working efficiency of 6%. The generators have been continuously operated for more than 12 months without any degradation. In addition, we have fabricated integrated thermoelectric module consisting of four 8 p-n leg device connected electrically in series.

Chapter 4

ZT Enhancement in Selenides

4.1 Introduction

In the previous chapter we have demonstrated the fabrication of thermoelectric generators having an efficiency of ~6% using conventional n-type PbTe and p-type TAGS-85 alloys. These devices though can be used for specific applications, such as, in space and in remote locations, however their use in common place is restricted due to the fact that Te is one of the rarest stable solid elements in the earth's crust and its abundance is about 1 µg/kg, as a result the Te is very expensive. It is therefore important to find suitable replacements of n-type PbTe and p-type TAGS, which on one hand either reduces or minimizes the use of toxic or expensive elements, while on the other hand, the *ZT* of the material is not compromised. In this Chapter, we present our investigations on the measurements of thermoelectric properties of various selenides. Selenides are selected as abundance of Se is 50 times more than Te and costs lower by factor of 5. Moreover, the Se is relatively nontoxic material until consumed in large quantities. Various selenides investigated in this chapter are $PbTe_{1-x}Se_x$ Cu intercalated $TiSe_2$, $CuCrSe_{2,}$ $AgCrSe_2$ and $CuCrSe_2$/$AgCrSe_2$ nanocomposites.

4.2 $PbTe_{1-x}Se_x$

Commercialized thermoelectric material such as PbTe is facing severe challenge due to its low reserve. PbSe compound having similar crystal structure and similar transport properties to its Te analogue was less investigated due to its higher band gap and low carrier mobility originating from the larger ionic component of the Pb-Se bond. In order to minimize the use of Te, selenides were considered for thermoelectric study. Here, Te was substituted by the isoelectronic Se, since a successful strategy to increase the *ZT* value has been to modify an already promising compound by introducing point defects through the synthesis of isostructural solid solutions. The solid solutions provide an environment of atomic mass fluctuation throughout the crystal lattice (i.e. disorder) which induces strong phonon scattering and generally can lead to significantly lower thermal conductivity and a larger *ZT* value. The canonical example of this is the Bi_2Te_3 system for which the $Bi_{2-x}Sb_xTe_3$, $Bi_2Te_{3-x}Se_x$ solid solutions are superior to the parent Bi_2Te_3 compound.

4.2.1 Synthesis of $PbTe_{1-x}Se_x$ alloy

The nominal compositions of the sample $PbTe_{1-x}Se_x$ (x= 0.0,0.1,0.25,0.5,0.8,1.0), were prepared by melt growth technique as discussed in section 2.2.1. In accordance to the phase diagram as described in Section 3.2.1, the heating and cooling program was set in such a way that the alloy becomes Pb-rich with n-type conductivity without doping deliberately.

4.2.2 Structure and morphology of $PbTe_{1-x}Se_x$ alloy

As discussed in section 3.2.3, PbTe crystallizes crystallizes in the NaCl- type cubic structure (space group $Fm\bar{3}m$), without any noticeable second phase or impurities as shown in Fig. 4.1(a). It is interesting to note that all XRD peaks shift systematically towards the higher 2θ values with increasing x. A more elaborate view of most intense (*200*) peak for different x values is shown in Fig.4.1 (b). The shift of XRD peak to the higher 2Θ value can be explained as follows: The metallic radius of Pb, Te and Se are respectively, 180, 142 and 100 pm, indicating that Se in principle can substitute for Te. Thus, by substituting Se at Te position should lead to a decrease in the lattice parameter and hence the cell volume [125,126]. This in fact has been observed and the results are shown in inset of Fig. 4.1(b), which reveals that there is a linear decrease in lattice parameter with increasing x. According to the Vegard's Law - crystallographic parameters of a continuous substitutional solid solution vary linearly with concentration at constant temperature when the nature of the bonding is similar in the constituent phases. The XRD results confirms that in all the samples Se is substituting Te and the crystal structure and cubic symmetry are maintained in all the samples [125,126,127,128].

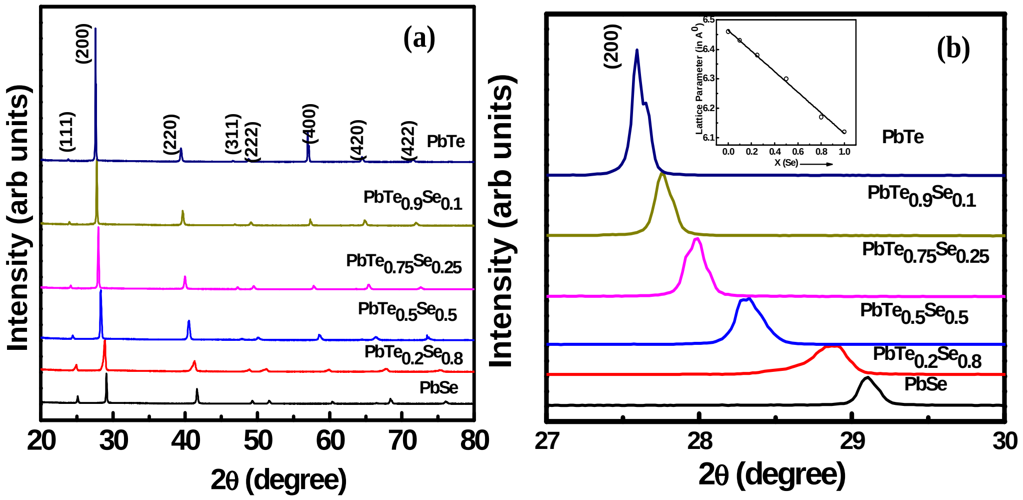

Fig. 4.1. (a) Room temperature powder x- ray diffraction patterns of $PbTe_{1-x}Se_x$ (b) Magnified (220) peak of $PbTe_{1-x}Se_x$. Inset shows the lattice parameter of $PbTe_{1-x}Se_x$ as a function of x.

Typical SEM images of the fractured surface of synthesized $PbTe_{1-x}Se_x$ (x= 0, 0.5, 1.0) were shown in Fig.4.2, it reveals the lamellar structures for all the samples, which is more prominent for the sample having x = 0.5. The result confirms that doping by Se does not change the morphology of the samples. Table 4.1 summarizes the chemical composition of the samples measured using EDX analysis, which is normalized with respect to the Pb (at%). The measured composition was found to be close to the nominal composition used for the sample preparation, suggesting there is no loss of material during the synthesis. In addition, the EDX analyses of various regions (micron size) across the samples reveal no significant variation in the composition, indicating that all the samples are highly homogeneous.

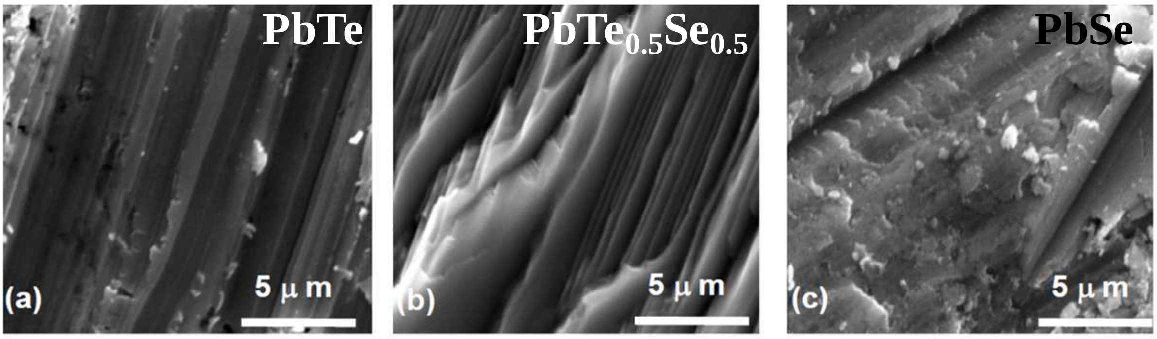

Fig. 4.2. SEM images of (a) PbTe (b) $PbTe_{0.5}Se_{0.5}$ and (c) PbSe.

Table 4.1: Chemical composition of the synthesized $PbTe_{1-x}Se_x$ samples.

Nominal Composition	EDX measurement
PbTe	$PbTe_{0.99}$
$Pb\ Te_{0.9}\ Se_{0.1}$	$PbTe_{0.95}\ Se_{0.15}$
$PbTe_{0.75}\ Se_{0.25}$	$Pb\ Te_{0.63}\ Se_{0.27}$
$PbTe_{0.5}\ Se_{0.5}$	$PbTe_{0.43}\ Se_{0.57}$
$PbTe_{0.2}\ Se_{0.8}$	$Pb\ Te_{0.31}\ Se_{0.69}$
PbSe	$PbSe_{1.02}$

4.2.3 Temperature dependence of thermoelectric properties of $PbTe_{1-x}Se_x$

Fig. 4.3 (a) shows the temperature dependence of α for all the samples. (-) ve sign indicates n-type conductivity. It can be seen that in the entire temperature range, $PbTe_{0.5}Se_{0.5}$ shows the highest value of α, and the maximum value of α ~ -292 μV/K is observed at 700 K. Fig. 4.3 (b) shows the temperature dependence of ρ for all the samples. It reveals that at a particular temperature ρ increases with x, however for x = 0.5 there is a dramatic enhancement of ρ. At room temperature, the pure PbSe (x =1) shows the lowest ρ ~1.49 μΩ-m, while for $PbTe_{0.5}Se_{0.5}$ the ρ ~ 31.43 μΩ-m.

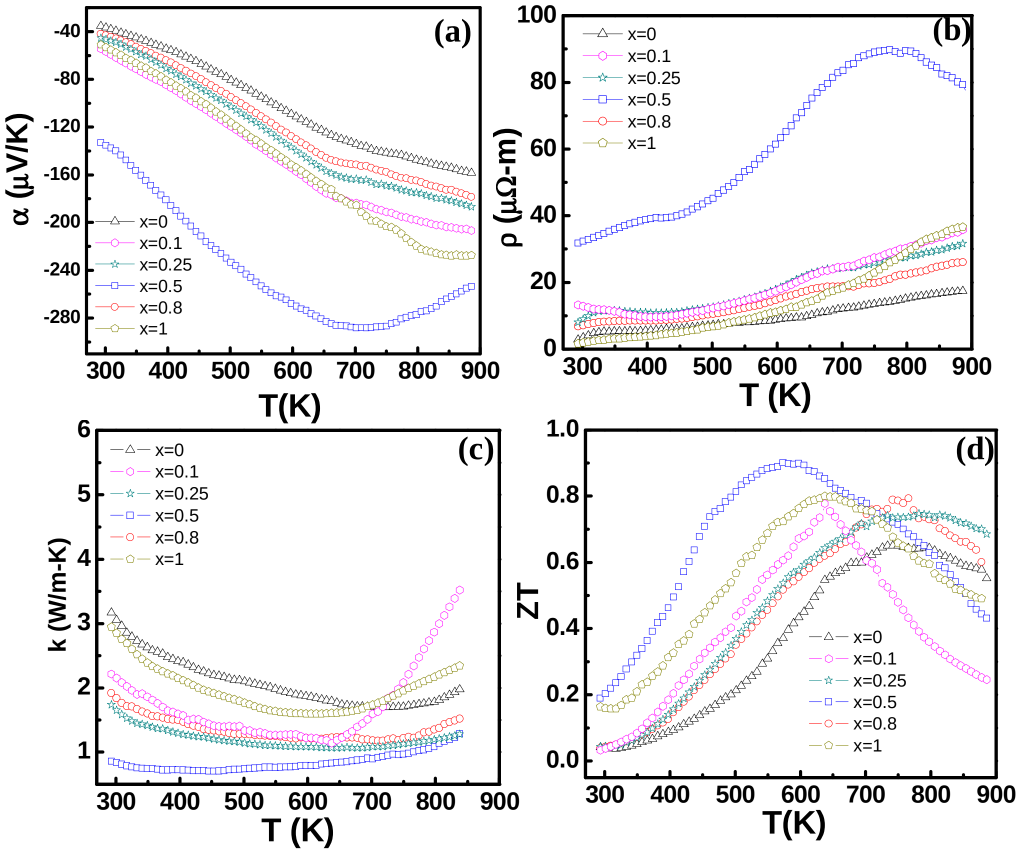

Fig. 4.3. Temperature dependence of (a) Seebeck coefficient (α) (b) electrical resistivity (ρ) (c) thermal conductivity (k) and (d) dimensionless figure of merit ZT for $PbTe_{1-x}Se_x$.

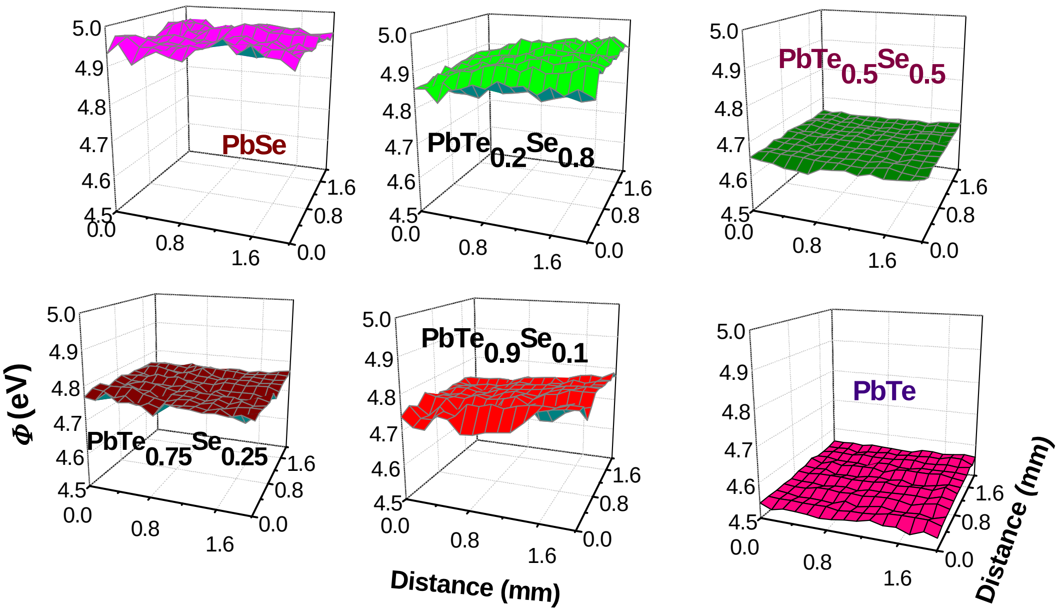

Fig. 4.4. Work function of $PbTe_{1-x}Se_x$ as a function of x.

According to Boltzmann transport theory, which describes both the electronic and thermal transport properties of solids, the α is given by the Mott equation [20] as discussed in section 1.10 . If the electronic scattering is independent of energy then σ (E) is just proportional to the DOS at E [129]. At x = 0.5, there occurs a maximum atomic mass fluctuation; i.e., the disorder in the lattice is maximum, and so the high density of defect states scatter the electrons independent of energy. Consequently, the $\frac{d\ln\sigma(E)}{dE}$ term, which indicates the variation of the DOS at E, is high for x = 0.5, resulting in a large α. The enhancement in α for $PbTe_{0.5}Se_{0.5}$ is 36% compared with PbTe and 54% compared with PbSe. The large α value for $PbTe_{0.5}Se_{0.5}$ is also supported by the work function measurement by Kelvin probe method. The details of work function (energy difference between the Fermi level and vacuum level) mapping on an area of size 2 mm x 2 mm is shown in Fig.4.4 . These images also reveal that samples are highly homogenous. Both the binary compounds PbSe and PbTe show the respective work function values of 4.93 eV and 4.53 eV whereas for $PbTe_{0.5}Se_{0.5}$, the work function is 4.65 eV. In other words, it can be said that Fermi level of $PbTe_{0.5}Se_{0.5}$ lies in between the Fermi level of PbTe and PbSe. Since both PbTe and PbSe are isostructural, the difference in the work function can be attributed to the difference in n and thus is evident in the α vs T plot in accordance to eqn. 1.9.But for $PbTe_{0.5}Se_{0.5}$, the lowering of the workfunction can be attributed to the introduction of defect states near to the bottom of the conduction band edge which increases the DOS and thereby increases m^* in addition to the change in n value. Thus the α of $PbTe_{0.5}Se_{0.5}$ is high in comparison to other samples.

In addition, the dramatic increase in ρ is seen for $PbTe_{0.5}Se_{0.5}$ compared to PbTe and PbSe which can be due to the fact that the large atomic mass fluctuation in the crystal structure of PbTe in Fig. 3.1, increases the degree of defect formation, which increases the scattering of electrons and hence the ρ value. Since κ_e varies inversely with the ρ, i.e., $\kappa_e \infty \rho^{-1}$, the increase in ρ for x = 0.5 causes a reduction in κ_e and so an almost 50% reduction in the κ is seen compared with PbSe and PbTe at 700 K, as shown in Fig.4.3©. At room temperature, the κ of $PbTe_{0.5}Se_{0.5}$ was 0.85 W/m-K, whereas PbSe shows 3.16 W/m-K. Moreover, the phenomenon of κ reduction resulting from alloying due to phonon scattering by point defects is well known, being proposed by Ioffe before 1957 [16]. In the case of $PbTe_{0.5}Se_{0.5}$, the resulting defect states, i.e., disorder in the crystal lattice [18], scatter the majority charge carriers along with phonons so that the electrical and thermal conductivities decrease. The enhancement in the α and the reduction in the thermal conductivity outweigh the increase in the ρ, especially at higher temperature, which causes the ZT to increase to 0.95 at 600 K and is shown in Fig.4.3(d).

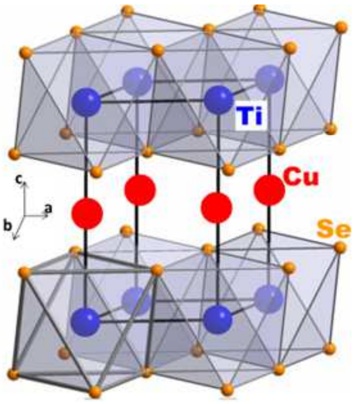

Fig. 4.5. Crystal structure of Cu intercalated $TiSe_2$.

4.3 Cu intercalated $TiSe_2$

In this Section we discuss the thermoelectric material, $TiSe_2$ which belongs to the family of transition metal dichalcogenide (TMDCs). This material is of great interest as it belongs to a class of low dimensional material which forms a stack of strongly bonded layers interconnected with a weak van der Waals attraction. This allows an easy intercalation of various guest species (e.g. alkali metal atom, 3d transition metal atom, or molecules) between these layers [130,131, 132,133]. For example, Fig. 4.5 shows the schematic of the layered crystal structure of Cu_xTiSe_2, in which Cu atoms occupy positions between the $TiSe_2$ layers (which otherwise are bonded with van der Waals forces); and in $TiSe_2$ layers, Ti atoms are in octahedral coordination with Se. This intercalated foreign atom allows to finely tune the electron occupation of the relatively narrow 'd' bands existing in these solids which helps in tailoring the electronic property of the material in a controllable way and can be understood in terms of charge transfer and increased interlayer separation. Here, we report the high temperature thermoelectric performance of Cu intercalated $TiSe_2$ material (belongs to

TMDC) above room temperature prepared in broad composition range. $TiSe_2$ parent compound exhibits p-type conducting nature, which transforms to n-type conducting nature upon Cu intercalation. Extremely low κ was observed in this material which significantly enhances the *ZT* of the material above room temperature. A 4-thermoleg generator was fabricated using this combination of material.

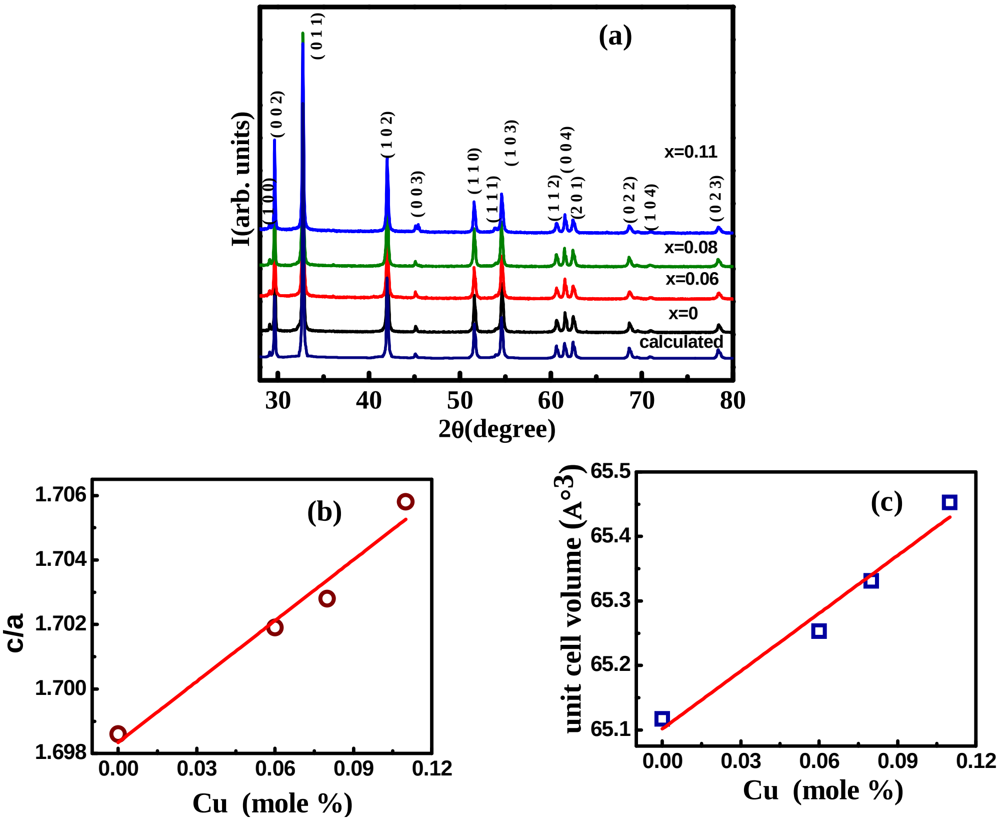

Fig. 4.6. (a) Representative experimental x-ray diffraction data and simulated data for Cu_xTiSe_2 (x= 0, 0.06, 0.08, 0.11). (b) c/a ratio and (c) unit cell volume as a function of x.

4.3.1 Synthesis of the Cu_xTiSe_2 alloy

Polycrystalline samples of Cu_xTiSe_2 (x =0-0.11 at.%) were prepared using melt growth method. The stoichiometric amounts of Cu (99.99%), Ti (99.99%) and Se (99.99%)

were sealed in a quartz ampoule under a vacuum of 2×10^{-5} Torr and heated at 923 K for 20 h. After the completion of heating procedure shiny purple material was obtained and no signature of any reaction between material and ampoule wall were observed indicating complete reaction among the elements. The obtained powder samples from the ampoule was finely ground, pelletized and resealed in evacuated silica ampoule. The samples were again sintered at 923 K for 50 h to obtain highly compact pellets.

Table 4.2: Consolidated result of change of lattice parameter and unit cell volume as a function of Cu mol%.

Cu mol% (x)	Lattice parameter	Unit cell volume
0.0	1.698	65.12
0.06	1.702	65.25
0.08	1.703	65.33
0.11	1.706	65.45

4.3.2 Structural and morphological characterization of Cu_xTiSe_2 alloy

The XRD patterns for pure $TiSe_2$ and Cu_xTiSe_2 (x= 0, 0.06, 0.08, 0.11) are shown in Fig. 4.6 (a) which confirms the formation of pure $TiSe_2$ phase [JCPDF 830980]. The XRD data of all samples were refined using FullProf suite and the analyses show that the data is refined to space group $P\bar{3}m1$ by considering the preferred orientation. It is seen that Bragg peak position of the experimental data perfectly matches with the simulated pattern. The ratio of lattice parameter (c/a) and lattice volume plotted as function of Cu content in the sample were also calculated from the fitting and is shown in Fig. 4.6 (b) and (c). It is seen that both c/a ratio and unit cell volumes increase with Cu content in the samples, which indicates elongation of lattice parameter along the c-axis. This confirms that Cu is intercalated at octahedral sites in the van der Waals gap between the $TiSe_2$ layers, which is in agreement with the crystal structure [134]. Table 4.2 shows the consolidated result of change of lattice parameter and unit cell volume as a function of Cu mol%.

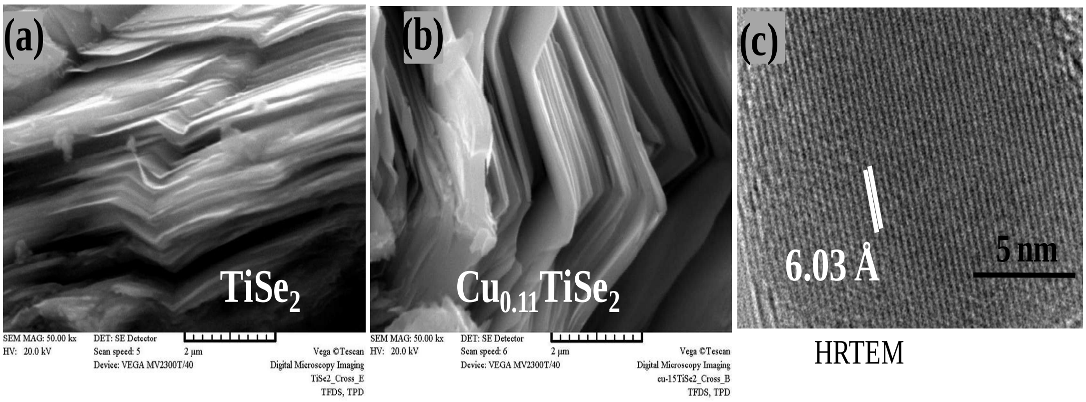

Fig. 4.7. SEM image of fractured surface of (a) $TiSe_2$ and (b) $Cu_{0.11}TiSe_2$, and (c) HRTEM image of $Cu_{0.11}TiSe_2$.

The SEM images of the fractured pure $TiSe_2$ and Cu intercalated $TiSe_2$ samples are shown in Fig. 4.7. The samples exhibit layered morphology, which is typical of 2-D transition metals dichalcogenides alloys. The observed grains in these sintered materials are densely packed and show prefferd layered growth. A high resolution transmission electron microscopy (HRTEM) image of the $Cu_{0.11}TiSe_2$ sample, reveal sharp lattice fringes with a interlayer spacing of around 6.03 Å.

The homogeneity of the prepared samples has been confirmed by performing the X-ray elemental mapping. Fig. 4.8 shows a large area (45µm×45 µm) back-scattered electron image of $Cu_{01.1}TiSe_2$ as well as elemental mapping of Cu, Ti and Se. The images clearly reveal uniform distribution of the elements all over the sample. The results of SEM, TEM and XRD results suggests that the synthesized samples are uniform with texturing over few microns in size, which is expected due to layered structure of $TiSe_2$. The Cu atoms intercalates between $TiSe_2$ layers at random positions, which are capable of creating local and short range disorder in the system and alters the thermal transport property of the system. These Cu atoms not only can scatter the phonons but also alter the electrical transport properties owing to the elongation of c-axis of the system.

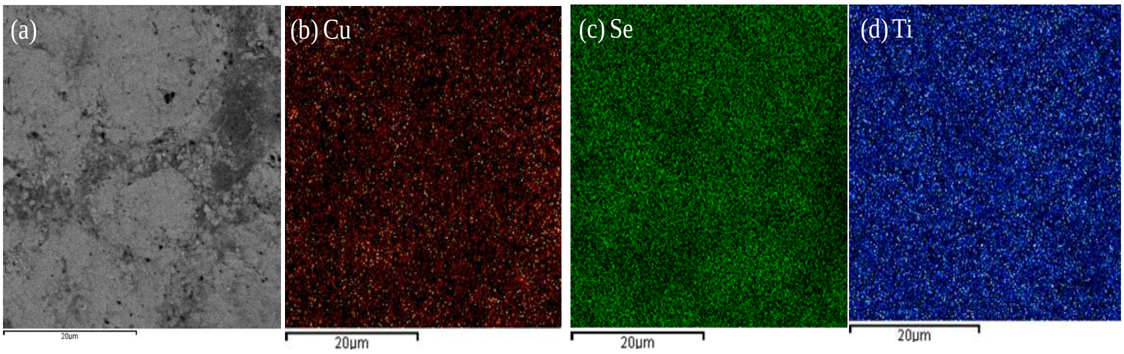

Fig. 4.8. (a) Back scattered electron image of $Cu_{0.11}TiSe_2$ and elemental x-ray mapping of (b) Cu-K_α, (c) Se-L_α and (d) Ti-K_α.

4.3.3 Temperature dependent thermoelectric properties of Cu_xTiSe_2

(a) Temperature dependence of ρ and α

Fig. 4.9 shows the temperature dependent ρ and α data as a parametric function of x in Cu_xTiSe_2. All the samples show small ρ values at room temperature (of the order of μΩ-m) and follow common metallic trend. For lower Cu content ($x \leq 0.04$), the ρ values are higher as compared to pure $TiSe_2$. This is attributed to: (a) lattice deformation due to Cu intercalation and expansion of c-parameter and (b) quenching of majority charge carriers holes due to electrons donated by intercalated Cu (indicated by lower positive α value for x= 0.005). However, the systematic decrease in the magnitude of ρ is observed as x increases in Cu_xTiSe_2, attributed to the increasing carrier concentration. The '*n*' of the Cu intercalated $TiSe_2$ samples at room temperature was calculated using Hall coefficient measurement, $n = 1/e|R_H|$. The carrier concentration for pure $TiSe_2$ was found to be 3.3 x 10^{18} cm^{-3} which reaches to maximum value 2.2 x 10^{20} cm^{-3} at x= 0.11. The inset in Fig. 4.9(a) shows the σ of the material at temperature of 670 K as a function of carrier concentration. With increasing *n*, σ is increasing which is directly proportional to the μ of the free charge carrier.

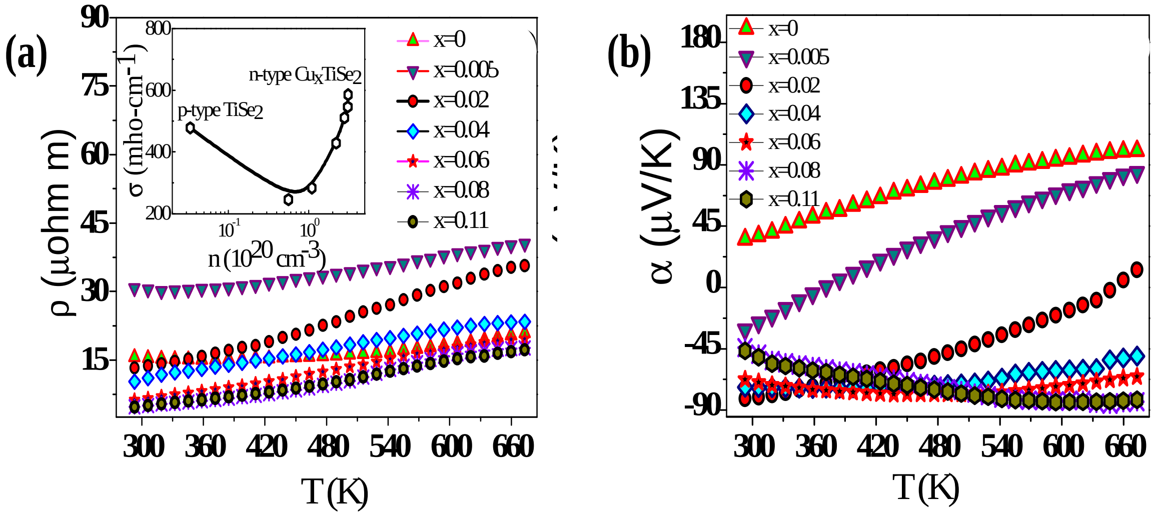

Fig. 4.9. Temperature dependent (a) resistivity and (b) Seebeck coefficient for Cu_xTiSe_2 (x= 0, 0.005, 0.02, 0.04, 0.06, 0.08, 0.11). Inset shows electrical conductivity with increasing carrier concentration.

The α of pure $TiSe_2$ shows p-type conducting nature and exhibits large value of ~100 μV/K. Cu atom has one free electron in 4s outer shell thus intercalation of Cu introduces free electron in $TiSe_2$. Small Cu intercalation (x=0.005) do not effectively change the majority charge carrier in pure $TiSe_2$ and shows comparatively reduced α value which may be attributed to the quenching of holes due to transferred electron. Increasing Cu content shows systematic increase in the α values with negative magnitude revealing transformation from p-type to n-type conducting nature. α values with increasing Cu gets saturated to nearly -80 µV/K at temperature of 650 K. The thermal energy band gap of this material can be estimated from the maximum value of the α using the equation, 3.1[135]. Here the α is considered to be a function of Fermi level thus shifting of Fermi level even by few k_BT towards any of the band will significantly affect the ratio of the hole or electron charge carriers. This change in the ratio of the n is directly reflected on the sign of α. The calculated band gap value for $TiSe_2$ and $Cu_{0.11}TiSe_2$ comes out to be 0.13 eV and 0.11 eV respectively. The temperature dependence of ρ and α data upto 650 K shows characteristic of conduction by extrinsic charge carriers, and indicate that Cu_xTiSe_2 in this composition range exhibits degenerate semiconductors type nature. The p-type to n-type transition upon Cu intercalation in pure $TiSe_2$ shows the possibility of using this combination of materials in developing thermoelectric device.

(b) Temperature dependence of κ

The κ in anomalous layer structure compounds as M_xTiZ_2 (M- transition metal or organic molecule and Z – S, Se, Te) are expected to be lower comparatively due to the formation of bulk superlattice structures which lowers the mean free path of phonons transferring heat. The temperature dependent κ data of the Cu_xTiSe_2 samples is shown in Fig.4.10 (a).

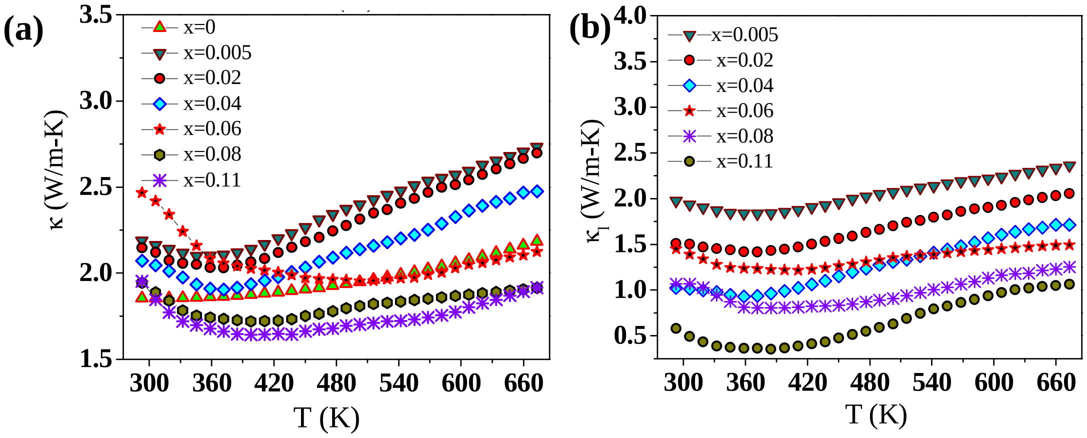

Fig. 4.10. Temperature dependent (a) total thermal conductivity and (b) lattice thermal conductivity *($\kappa_l = \kappa - \kappa_e$)* for Cu_xTiSe_2 (x= 0, 0.005, 0.02, 0.04, 0.06, 0.08, 0.11)

The κ of pure $TiSe_2$ material was found to be nearly 1.85 W/m-K at 300 K which is quiet low and comparable to the κ reported in bulk superlattice structure[135]. Such a low κ is attributed to the layered growth microstructure of the material which introduces large number of interfaces acting as an active phonon scatterer. The κ of semiconductor mainly consists two preferred contribution, according to equation 1.14. The electronic thermal conductivity (k_e) values of Cu_xTiSe_2 has been determined using Weidemann–Franz law ($\kappa_e = L_0\sigma T$; where L_0 is Lorentz number, σ is the electrical conductivity and T is temperature) which is valid for metal and heavily doped semiconductor. Since $TiSe_2$ is a semimetal and has carrier concentration of the order of 10^{18} cm^{-3} we have not calculated the electronic contribution for pure $TiSe_2$ using this law . The variation of k_l i.e. (k-k_e) with Cu-intercalation, as shown in Fig. 4.10(b) clearly indicates a monotonic decrease. Although k_e increases with x due to increasing carrier doping (n), the reduction of k_l is observed whichoccurs due to loosely bound Cu atoms. These freely bound atoms rattle and act as an additional phonon scatterer leading towards lowering the κ_l contribution. Cu intercalated

$TiSe_2$ (x=0.11) shows minimum κ showing the dominance of the rattling phenomenon over the contribution of the k_e.

(c) Temperature dependence of *ZT*

Fig. 4.11 shows the temperature dependence of the calculated *ZT* value. The *ZT* of the material depend upon the power factor ($\alpha^2\sigma$) and κ which are primarily affected by the microstructure, structural ordering and availability of the majority charge carriers in the sample. The change in *ZT* at 670 K with increasing Cu content is shown in inset of Fig. 4.10.

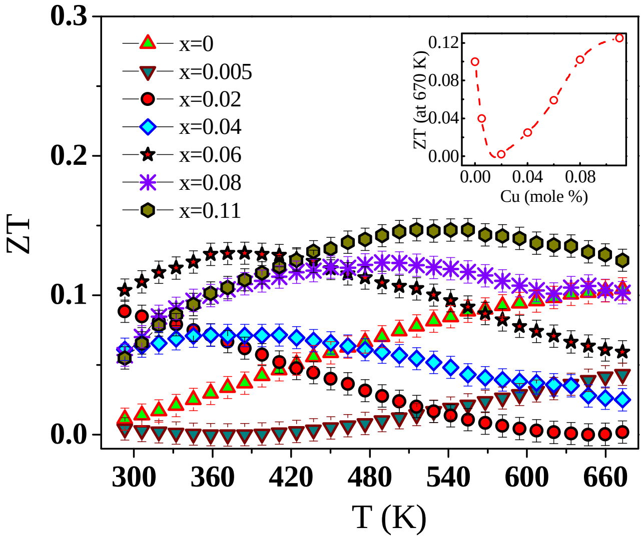

Fig. 4.11. Temperature dependent *ZT* plot for Cu_xTiSe_2 samples. Inset shows the *ZT* at 670 K as a function Cu content.

At lower Cu content *ZT* initially decreases which is attributed to the reduction in power factor value due to decreased σ and small α in addition to enhanced κ. Further increasing the Cu content x>0.02, systematic increase in *ZT* value is observed due to dominating contribution from power factor and reduced κ due to enhanced rattling phenomenon. Maximum *ZT* value of 0.1 at 670 K has been achieved for parent $TiSe_2$ compound exhibiting p-type conducting behaviour. However, for n-type Cu_xTiSe_2 (x>0.005) , *ZT* increases with increasing Cu content in the sample.The maximum *ZT* value of ~0.15 has been achieved for $Cu_{0.11}TiSe_2$ sample.

4.3.4 Thermoelectric generator fabrication

Since pure $TiSe_2$ and Cu intercalated $TiSe_2$ give similar *ZT* value of ~0.15 at 650 K, both can be used as a possible combination of p-type and n-type material for generator fabrication.

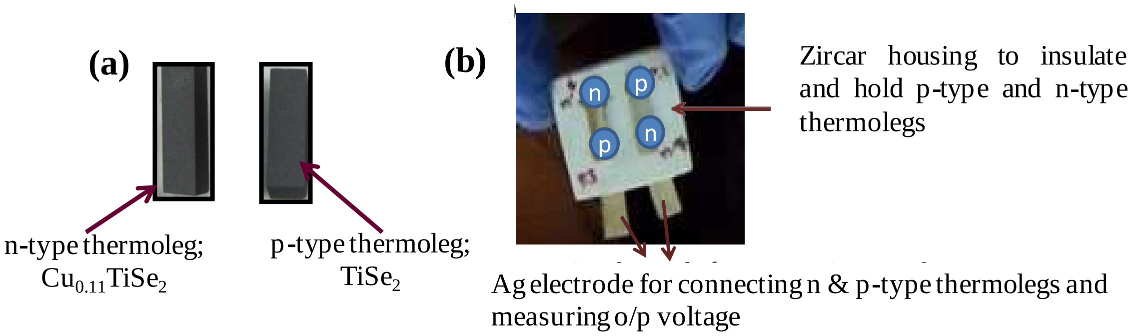

Fig. 4.12. Photograph of (a) n- and p-type thermolegs of $Cu_{0.11}TiSe_2$ and $TiSe_2$ respectively, and (b) 4 thermoleg generator.

To accomplish this, rectangular legs of $TiSe_2$ and $Cu_{0.11}TiSe_2$were cut into a dimension of 2mm x 3mm x 8mm as hown in Fig. 4.12 (a). The *n*-type and *p*-type legs were packed inside a Zircar housing which is a thermally insulating microporous ceramic material.

This housing minimizes the heat loss in the surrounding of the modules and supports the heat flow in vertical direction from hot to cold end. The thermoelectric elements were then subsequently connected in series using silver as an electrode. In order to compensate the CTE between thermoelectric elements and the silver electrode, a thin layer of silver paste mixed with small quantity of Cu_xTiSe_2 (x=0 and x=0.11) powder was applied at the interfaces of both the ends of thermoelectric legs prior to making contacts. The total device resistance measured using a standard four-probe technique was found to be 65 mΩ. As described in section 3.5.2, the contact resistance came out to be 42 mΩ that is nearly 5 mΩ for each contact. The elemental efficiency ($\eta_{elemental}$) was theoretically estimated using the equation 1.16.

Considering the *ZT* value for concentration x=0 and x=0.11 at 650 K and temperature gradient of 323 K, ideally the efficiency should be ~0.45 %. The device was tested in the set up as described in section 2.6. According to the maximum power transfer theorem, which has been explained in chapter-3, the maximum output power achieved from 2 p-n thermoleg module at 550 K was found to be 0.64 mWatt. The heat flow in this device was found to be 0.45 W which gives a device efficiency of 0.1%. Low output power value in present device is mainly attributed to the high contact resistance of the material. Fig. 4.12 (b) shows the digital photograph of the device.

4.4 $CuCrSe_2$

In this research work, the search for the telluride free thermoelectric material has led to the study of $CuCrSe_2$ which is an example of superionic conductor with liquid like substructures (i.e. diffusion of ions within the crystal sublattice) [136] where the concept of

PGEC has been extended and a new concept of phonon-liquid electron-crystal (PLEC) has been given. In PLEC concept the strategy is to reduce the κ_l below that of glass not only by reducing phonons mean free path but also eliminating some of the phonon vibration modes by using a superionic conductor with liquid like substructures (i.e. diffusion of ions within the crystalline sublattice).

4.4.1 Synthesis of $CuCrSe_2$ alloy

As discussed in section 2.2.1, polycrystalline samples of $CuCrSe_2$ was prepared by melt growth method by grinding stoichiometric quantities of copper, chromium and selenium powder and then sealing it in a quartz ampoule under a vacuum of ~ 3.5×10^{-5} mbar. The sealed quartz ampoules were heated at a temperature of 1173 K for 72 hrs and finally slowly cooled to the room temperature. The ingot obtained was re-grinded into fine powder and Vacuum Hot Pressed (VHP) at 973 K to form dense pellets.

4.4.2 Crystal Structure of $CuCrSe_2$

The layered structure of $CuCrSe_2$ is shown in Fig.4.13. It consists of CdI_2 type layers of $CrSe_2^-$ in which the Se^{2-} anions form distorted octahedral coordination sphere around Cr^{3+} cations.[137,138] The interlayer space between $CrSe_2^-$ layers is filled by the Cu ions occupying two different tetrahedral spaces [139]. At low temperatures only one of the tetrahedral sites is occupied by the Cu and with increasing temperature Cu ions migrates to other tetrahedral site and a strong kinetic disorder is induced above 365 K[140,141,142]. This strong disorder of Cu ions in $CuCrSe_2$ structure is expected to yield very low κ and high σ.

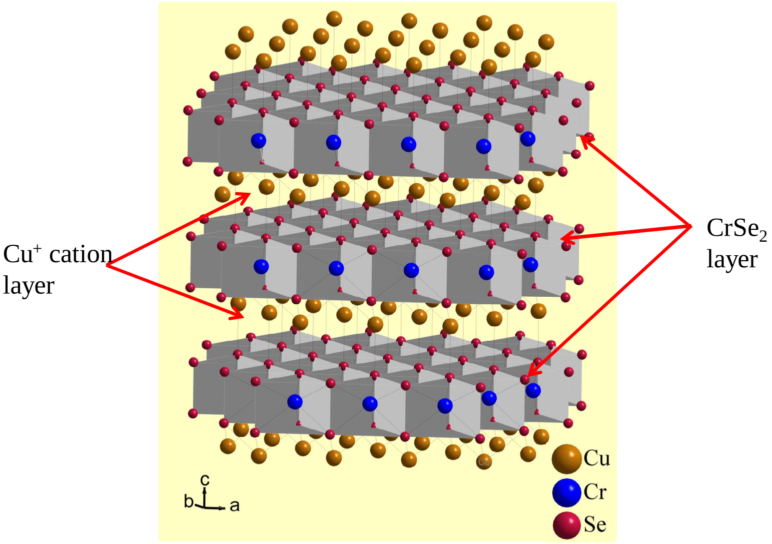

Fig.4.13. Structure of CuCrSe$_2$ with CdI$_2$ type layers of CrSe$_2$ (represented as edge shared octahedra) and disordered Cu+ cations layers.

4.4.3 Structure of CuCrSe$_2$ alloy

The room temperature powder XRD pattern of powder samples of CuCrSe$_2$ obtained after grinding of high density pellets is shown in Fig.4.14 (a) . Presences of multiple oriented peaks in the XRD spectra suggest the polycrystalline nature of the samples. It can be seen that diffraction pattern can be indexed using the space group R3m (160), using the PCPDF file No. 74-0194. The lattice constants calculated using the least-square refinement of the peak positions and are found to be: a = b = 3.678 Å and c = 19.372 Å; which are in good agreement with the reported values [137,138]. Energy dispersive X-ray analysis (EDX) gives the elemental ratio Cu : Cr : Se around 1.03:1.05: 2.01, also confirming the CuCrSe$_2$ stochiometry of the synthesized material. The backscattered electron image and X-ray elemental mapping of Cu, Cr and Se elements for CuCrSe$_2$ powder sample are shown in

Fig.4.14 (b). The uniform distributions of Cu, Cr and Se for $CuCrSe_2$ samples suggest that synthesized material is quite homogenous.

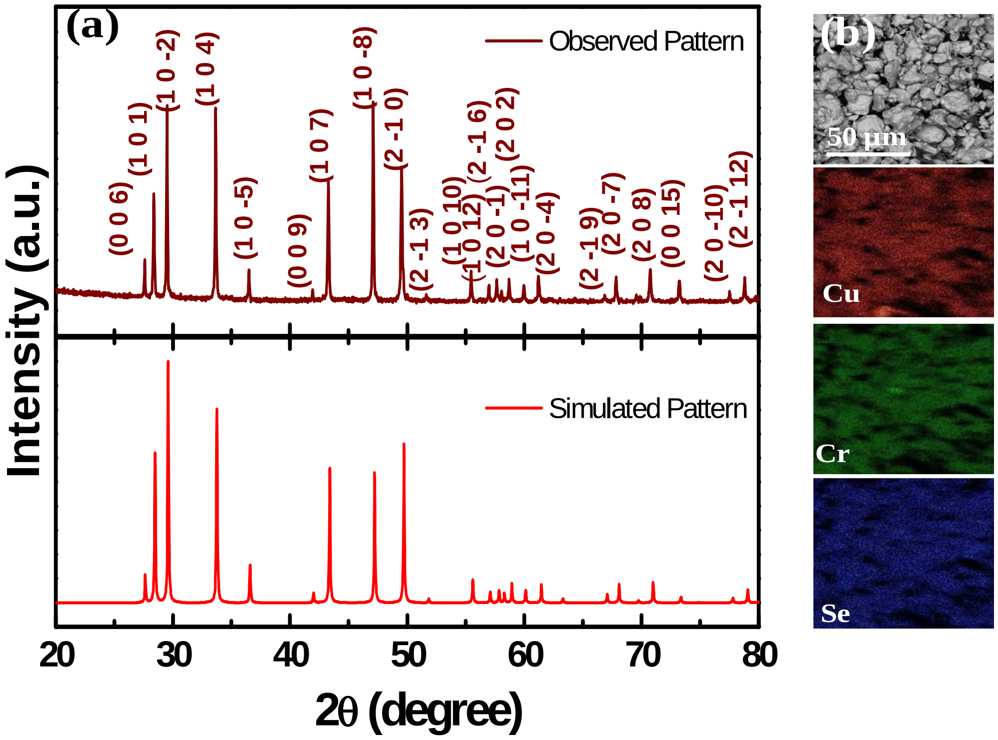

Fig.4.14. (a) Experimentally observed and simulated powder X-ray diffraction pattern for $CuCrSe_2$. (b) Back scattered electron (BSE) image and X-ray elemental mapping of Cu, Cr and Se in the powder $CuCrSe_2$ samples.

4.4.4 Morphology of $CuCrSe_2$ alloy

The cross sectional scanning electron microscope (SEM) images recorded for the fractured hot pressed pellet at different magnifications are shown in Fig.4.15. It is evident that the material is composed of randomly oriented grains having the layered structure, suggesting that the measured thermoelectric properties will not exhibit any anisotropic property.

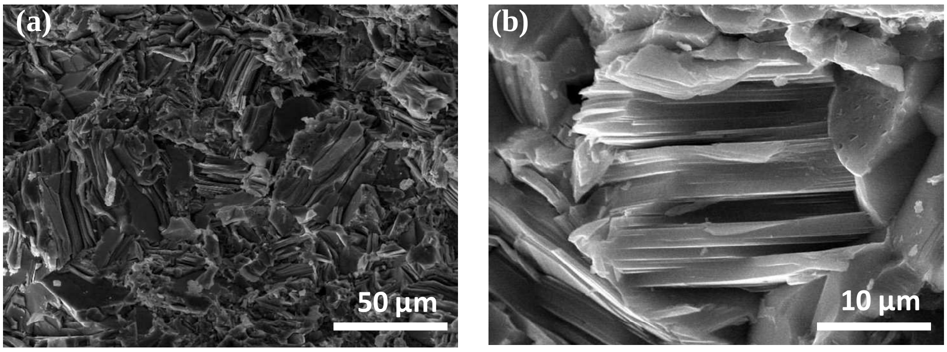

Fig.4.15. Scanning electron microscope (SEM) image of the fractured surface obtained from the hot pressed pellet of $CuCrSe_2$ (a) and (b) respectively shows low and high magnification images.

The high resolution TEM images of $CuCrSe_2$ are shown in Fig.4.16. White line shown in Fig.4.16 (a) represents a grain boundary present between the crystallites. The image shown in Fig.4.16(b) and (c) reveals that within the micron size crystalline grains there are nanoscale amorphous regions (marked with enclosed white lines). Fig.4.16 (d) shows the magnified view of the region marked by white boundary square in Fig.4.16(c), which clearly shows the nanoscale amorphous regions. Research in the field of bulk nanostructuring has shown that nanostructuring of materials scatters the phonons with short and medium mean free path (~ 3-100 nm), however in order to scatter phonons with long mean free path micron size grains, grain boundaries and layered structures are required [17,70,143,144,145]. Although in the present study of $CuCrSe_2$, these various nano-scale and micro-scale features in the $CuCrSe_2$ matrix are not created intentionally but these substructures can have a significant role in the scattering of phonons, hence in lowering of κ_l.

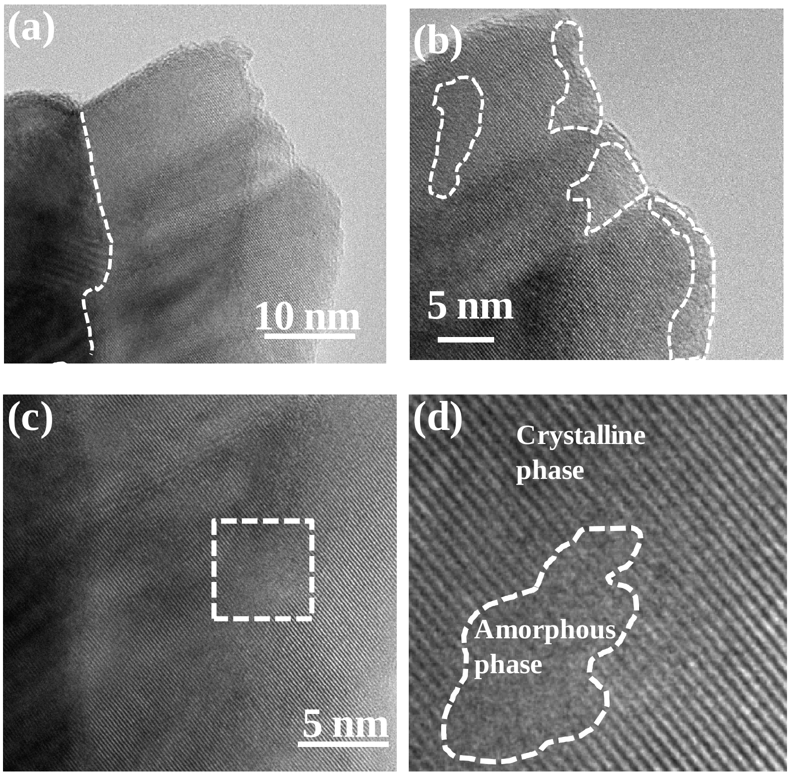

Fig 4.16. High resolution transmission electron microscope (TEM) image of hot pressed $CuCrSe_2$. In the image (b) white dotted line shows the grain boundary and image (c) the region inside white dotted lines shows the presence of nanoscale precipitates with amorphous structure inside a crystalline matrix. For clarity the white dotted region of image (c) is magnified as image (d).

4.4.5 Temperature dependent thermoelectric properties of $CuCrSe_2$ alloy

(a) Temperature dependence of ρ and α

Fig. 4.17(a) exhibits the temperature dependence of ρ in the temperature range of 300 K -773 K. The room temperature value of ρ for $CuCrSe_2$ is 2 mΩ-cm. The effect of disordered Cu ions above 365 K is also witnessed in the temperature dependence of ρ. One of the interesting features of Fig. 4.17(a) is that the ρ increases very rapidly up to 365 K and after that it shows a very weak temperature dependence (with a slight negative slope showing the trace of a semiconducting behavior in the range 365 K $< T <$ 773 K).

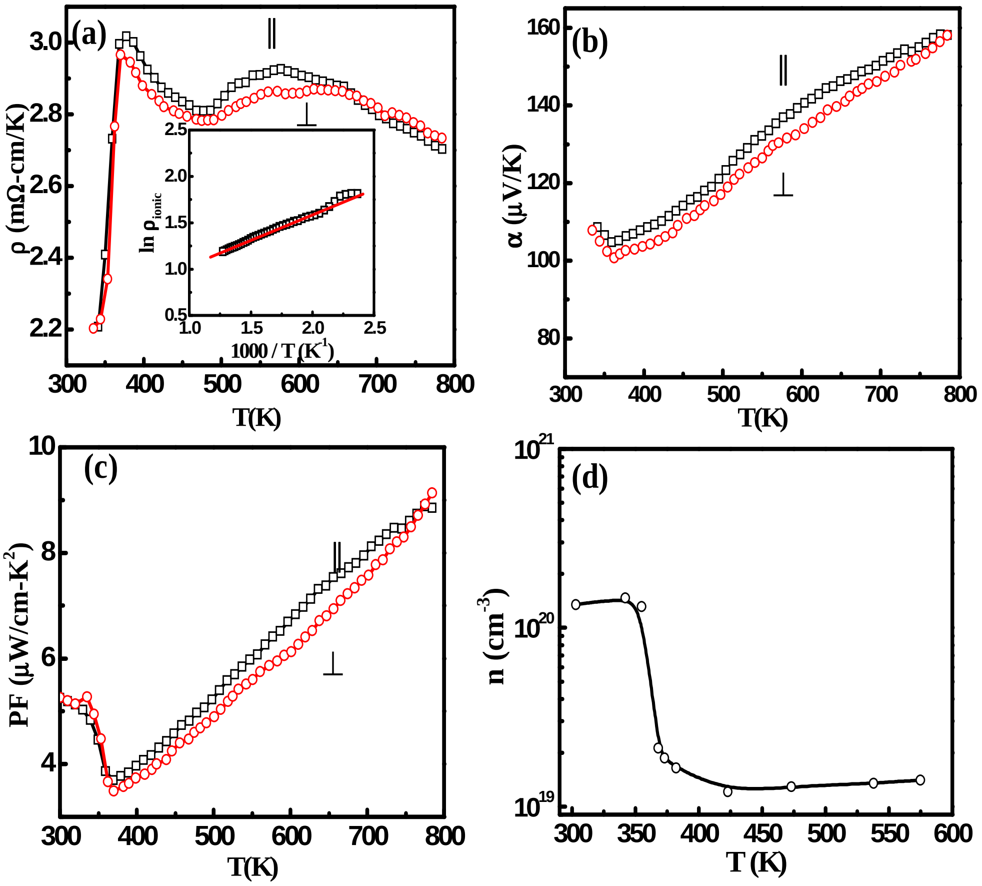

Fig. 4.17. Temperature dependence of the thermoelectric properties of hot pressed $CuCrSe_2$ (a) electrical resistivity (ρ). Inset shows the plot of ln ρ_{ionic} versus $1/T$ for T > 365 K. (b) Seebeck coefficient (α). (c) Temperature dependence of the power factor. Parallel (∥) and perpendicular (⊥) symbol represents the measurement of samples sliced from the hot pellet in parallel and perpendicular to the hot press direction (d) Temperature dependence of carrier concentration (n) derived from Hall effect measurement.

Weak temperature dependence of resistivity for T > 365 K is possibly due to the competition between increasing electronic contribution of resistivity (i.e. due to enhanced electron-phonon scattering) and decreasing ionic resistivity contribution (thermally activated behavior due to enhanced hopping of the Cu ions between defect sites). Since in the low temperature range 300 K <T < 365 K electronic contribution ($\rho_{\text{electronic}}$) governs the total resistivity therefore by extrapolation of resistivity from this range we have obtained the $\rho_{\text{electronic}}$ for T > 365K. By subtracting the extrapolated $\rho_{\text{electronic}}$ from the total resistivity we have obtained the ionic contribution (ρ_{ionic}) of the resistivity in the temperature range 365 K <T < 773 K. The plot of ln ρ_{ionic} with 1/T (for T > 365 K) is shown in the inset of Fig. 4.17(a), a linear fit of the data suggest the semiconductor behavior of resistivity that is associated with hopping of Cu ions between the defect states. Weak semiconducting behavior of temperature dependent resistivity of $CuCrSe_2$ for T > 365 K is consistent with other ionic semiconductors such as $AgCrSe_2$ [146]. Fig. 4.17(b) shows the temperature dependence of α in the temperature range of 300 K to 773 K. It can be seen that α of $CuCrSe_2$ increases from 100 µV/K at room temperature to 160 µV/K at 773 K. The positive sign of α indicates the hole as majority charge carriers (i.e. p-type nature) in the material. Fig. 4.17(c) shows the temperature dependence of the P.F. for the $CuCrSe_2$, which clearly shows a dip at 365 K. For temperatures > 365 K, P.F. increases with the rise in temperature, and reaches a value of 9 µW/cm-K^2 at 773 K i.e. nearly three time lower than the state of art thermoelectric materials such as PbTe [147] and TAGS-85[148]. It is important to note that measurement of ρ and α from the samples sliced from a big pellet in parallel and perpendicular to the hot pressing direction exhibit nearly same results. Temperature dependence of n (estimated from Hall Effect measurement) is shown in Fig.4.17(d). At room temperature n was found to be 1.3×10^{20} cm^{-3}, and above 365 K the concentration drops down to 1.4×10^{19} cm^{-3}.

(b) Temperature dependence of κ

Temperature dependence of thermal diffusivity for $CuCrSe_2$ is shown in Fig.4.18(a) , which clearly shows a jump at 365 K. It is seen that after the phase transition, the diffusivity remains nearly constant throughout the high temperature range indicating the characteristics behavior of glassy materials. In Fig.4.18 (b) we have also plotted the temperature dependence of specific heat (C_p), which also shows the evidence of a structural phase transition at 365 K. It may be noted that the high temperature C_p value was found to be 0.39 J/g-K, which compares very well with estimated Dulong-Petit value ~ 0.37 J/g-K. κ was calculated as discussed in section 2.5.3, with the assumption that sample remains constant over the entire temperature range and the estimated value of mass density for $CuCrSe_2$ is 6.31 g/cm^3.

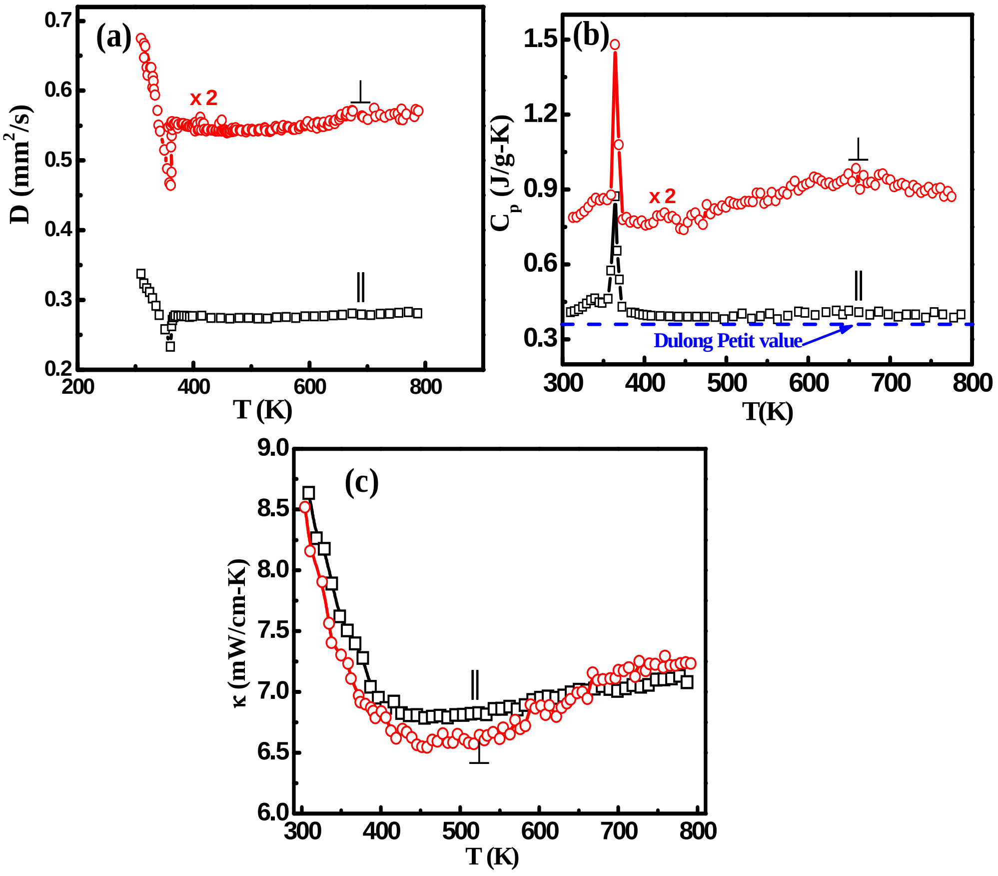

Fig.4.18. Temperature dependence of (a) thermal diffusivity (b) specific heat (c) thermal conductivity for $CuCrSe_2$. In the diffusivity and specific heat plots, the data for sample sliced perpendicular (shown by ⊥) to the hot pressing direction is multiplied by 2 to show them clear.

From Fig. 4.18 (c) it can be seen that the at room temperature k ~ 8.6 mW/cm-K and it decreases with increasing the temperature up to 365 K and followed by a temperature independent value of 7 mW/cm-K up to 773 K. It is important to note that for $CuCrSe_2$ the observed high temperature κ is comparable to the recently investigated various ionic semiconductor such as $AgCrSe_2$ [146], Zn_4Sb_3 [149,150] and $Cu_{2-x}Se$ [136]. Overall extremely low κ value for $CuCrSe_2$ in the present case can be related to the scattering of heat carrying phonons by:

(i) Amorphous and crystalline nanoscale precipitates inclusion in the crystalline matrix of the $CuCrSe_2$, which essentially scatters the phonons with mean free path < 100 nm.

(ii) The micron size layered grain structure which scatters phonons with higher mean free path ~ few µm and

(iii) The high kinetic disorder (almost like a fluid like arrangement) produced by the movement of light Cu ions, probably which not only scatters the phonons of mean free path of atomic dimensions but also cut off some phone modes[136].

(c)Temperature dependent Raman spectroscopy

Since in crystalline solids Raman spectroscopy deals with phonons, therefore temperature dependent Raman spectra were recorded for $CuCrSe_2$ below and above the phase transition temperature (~ 365 K) in the temperature range from 300 K to 443 K. The temperature dependent Raman spectra, shown in Fig.4.19, reveals two main peaks at 220 cm^{-1} and 259 cm^{-1}, which can be associated with the A_{1g} and E_g phonon modes of bulk $CuCrSe_2$, respectively [151].

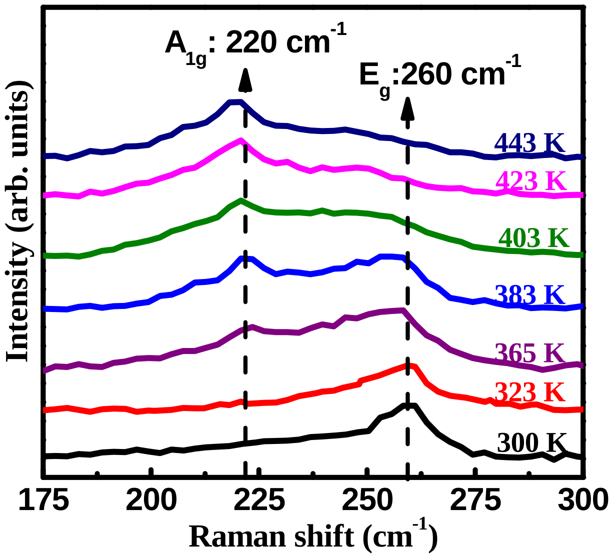

Fig.4.19. Temperature dependence of the Raman spectra for $CuCrSe_2$ in the temperature range 300 K – 443 K.

The A_{1g} phonon mode is formed by the displacement of Cu and Cr atoms along the z direction (i.e. along c axis) and E_g mode is formed by the displacement of Cr and Se atoms along the x or y-directions (i.e. in the ab plane). It can be seen that near the transition temperature of 365 K, A_{1g} mode becomes a well resolved peak as the temperature increases above 365 K, and at the same time E_g mode become quite broad with decreased intensity. This data clearly indicates that at temperatures above 365 K, some of the phonon vibration modes gets disrupt due to the kinetic disorder of Cu atoms along the c - axis.

(d)Temperature dependence of *ZT*

Lastly we have evaluated the *ZT* by using measured values of α, ρ and k. Fig.4.20 shows the temperature dependence of *ZT* for $CuCrSe_2$, and it can be seen that highest *ZT* ~ 1 is obtained at 773 K. As discussed above, the P.F. of $CuCrSe_2$ is one order of magnitude lower than the state of art thermoelectric material but the thermoelectric performance which is evaluated by *ZT* is comparable to them. In $CuCrSe_2$, a clear separation between the electron conducting channel (i.e. covalently bonded $CrSe_2^-$ slabs) and the zone of phonon scattering (disordered Cu ions above 365 K) yields low ρ along with the low κ, hence exhibit an enhanced *ZT*. This unique feature of $CuCrSe_2$ resembles with many high *ZT* thermoelectric materials such as $Cu_{2-x}Se$ and Zn_4Sb_3. In these materials Se or Sb atoms forms a suitable crystalline structure for electronic conduction and Cu or Zn atoms forms a disordered channel that scatters the phonons.

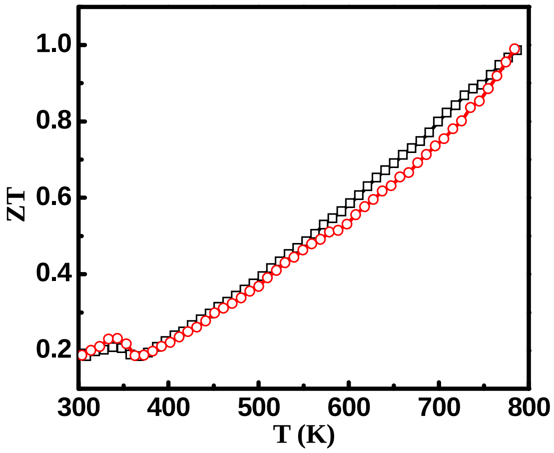

Fig.4.20. Temperature dependence of dimensionless Figure of Merit (*ZT*) for $CuCrSe_2$.

Table 4.3: Summary of the thermoelectric parameters obtained for $CuCrSe_2$. For comparison purpose results reported for $CuCrSe_2$ in other work is also given.

Temperature	**n(cm^{-3})**	**ρ (mΩ-cm)**	**α (μV/k)**	**k (mW/cm-K)**	***ZT***	**Reference**
300 K	$1.7x\ 10^{20}$	1.74	100	-	-	
300 K	$1.3\ x10^{20}$	2	100	8.6	0.18	This work
773 K	$1.4\ x10^{19}$	2.7	160	7	1	This work

A summary of the estimated thermoelectric parameters for $CuCrSe_2$ is shown in Table 4.3. From table 4.3 it can be seen that room temperature values of n, ρ and α for our synthesized $CuCrSe_2$ matches very closely with the reported value.

4.5 $AgCrSe_2$/$CuCrSe_2$ nanocomposite

As discussed in section 1.4.2(c), the hierarchical architecture plays an important role in phonon scattering. In any material, phonons have a wide spectrum of wavelengths and these contribute to the total κ. Analogous to $CuCrSe_2$, $AgCrSe_2$ also exhibit particles of varied dimensions to scatter the phonons. In the case of $AgCrSe_2$ and the composite, the nanoparticles and the mesoparticle were not added deliberately to the system. Instead these particles were formed during synthesis process and were very effective to scatter the wide spectrum phonons. For scattering of phonons the dimensions of the defects / inclusions should be comparable to their wavelength. In alloys (i.e. an atomic scale disorder), mostly there is a strong scattering of short wavelength (~ 1- 10 nm) phonons due to mass-mismatch of individual constituent atoms or due to the local bond strain induced by defects. The scattering of the mid wavelength (~ 10- 100 nm) phonons is achieved through the nanostructuring. The interface between nanoscale feature and matrix plays an important role in such scattering. The scattering of the long wavelength (> 100 nm) phonons is achieved by the meso-scale grain boundaries present in the material. $AgCrSe_2$ also belongs to the similar class of superionic conductor. Here, we report the promising thermoelectric properties of a composite consisting of $AgCrSe_2$ and $CuCrSe_2$ for mid temperature application. These composites are free from Te and other heavy elements and exhibits better performance than tellurides.

4.5.1 Synthesis of $AgCrSe_2$/$CuCrSe_2$ nanocomposite

The polycrystalline samples of $AgCrSe_2$ and $CuCrSe_2$ were prepared separately by melt growth method using the similar heating and cooling program as described earlier for $CuCrSe_2$. Composites $(AgCrSe2)_{1-x}$ $(CuCrSe2)_x$ with x= 0-1 samples were prepared by uniform mixing of pure $AgCrSe_2$ and $CuCrSe_2$ in different molar ratio followed by vacuum hot pressing.

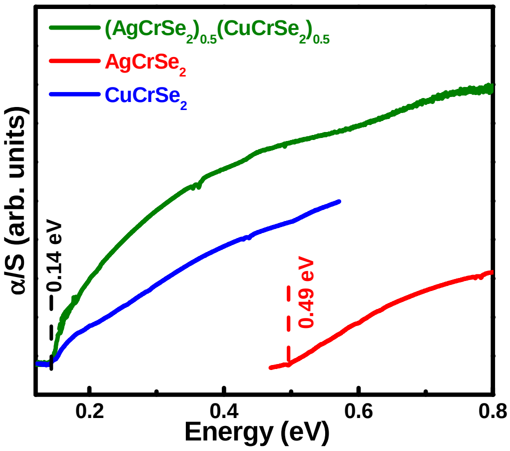

Fig.4.21. Electronic absorption spectra for the samples.

4.5.2 Energy bandgap of $CuCrSe_2$, $AgCrSe_2$ and $AgCrSe_2$/$CuCrSe_2$ nanocomposites

Room temperature optical diffused reflectance measurements were performed on hot pressed samples to estimate the optical energy gap of the materials. The spectra were taken in the mid IR range (400- 7000 cm^{-1}) using a FTIR spectrometer (Bruker 80 V). The reflectance versus wave number data were used to estimate the band gap shown in Fig. 4.21, by converting reflectance to the absorption data according to Kubelka-Munk equations as discussed in section 2.4.4.

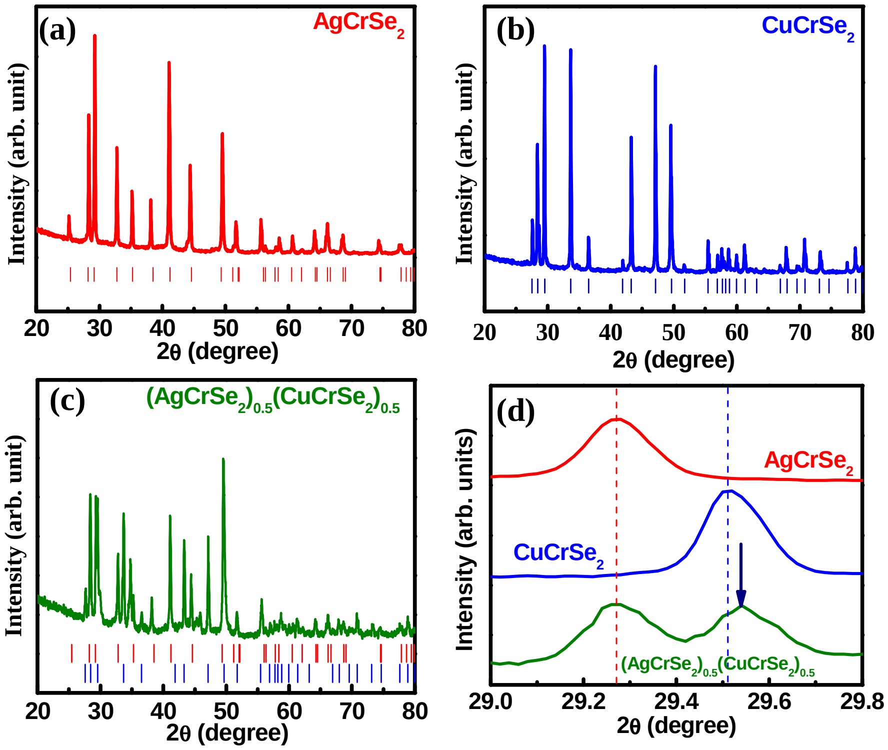

Fig.4.22. Powder X-ray diffraction pattern for (a) AgCrSe$_2$, (b) CuCrSe$_2$ (c) (AgCrSe$_2$)$_{0.5}$(CuCrSe$_2$)$_{0.5}$ composites. (d) Magnified view of the highest intensity (*012*) XRD peak for all samples.

4.5.3 Structural analyses of the nanocomposites

The room temperature powder XRD patterns of powder samples of AgCrSe$_2$, CuCrSe$_2$ and (AgCrSe$_2$)$_{0.5}$(CuCrSe$_2$)$_{0.5}$ obtained after grinding of hot pressed pellets are shown in Fig. 4.22(a-c). Presences of multiple oriented peaks in the XRD data of all samples suggest the polycrystalline nature of the samples. The bottom streaks in Fig.4.22(a-c) shows the peak position obtained using powder cell software and reported crystal information file (.cif) files for $AgCrSe_2$ and $CuCrSe_2$.

From Fig. 4.22 (d), it is important to note that for (012) diffraction peak corresponding to $CuCrSe_2$ in composite samples exhibit shift (shown by arrow) with respect to the pure $CuCrSe_2$ samples, suggesting the possibility of reaction between the constituents. The lattice parameters obtained from the analysis of the XRD spectra of these samples is summarized in Table-4.4, from there it can be seen that lattice parameters obtained for the pure and composite samples exhibit major change in the c-lattice parameter.

Table-4.4**:** Lattice parameters of $AgCrSe_2$, $CuCrSe_2$ and $(AgCrSe_2)_{0.5}(CuCrSe_2)_{0.5}$ obtained from the analysis of XRD data.

Sample	**Lattice parameters**
$AgCrSe_2$	$a = b = 3.68$ Å and $c = 21.22$ Å
$CuCrSe_2$	$a = b = 3.68$ Å and $c = 19.39$ Å
$(AgCrSe_2)_{0.5}(CuCrSe_2)_{0.5}$	a= b=3.66 Å c = 21.13Å ($AgCrSe_2$) a= b=3.68 Å c =19.36 Å ($CuCrSe_2$)

The c-lattice parameters of $AgCrSe_2$ component in the composite sample reduced from 21.22 Å to 21.13Å. Since ionic radius of Cu (~ 128 pm) is smaller than the ionic radius of Ag (~ 144 pm), it suggest the possibility of partial substitution of Cu at the Ag site resulting in the contraction of c-lattice parameter of the composite samples. In order to observe whether there is any texturing with respect to hot pressing direction, we have recorded the XRD pattern of hot pressed pellet, the data shows the absence of any preferred orientation. Fig.4.23 shows the XRD pattern of hot pressed pellet.

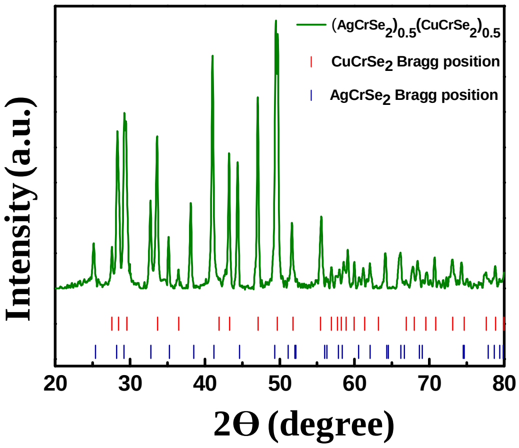

Fig 4.23. XRD pattern for the hot pressed $(AgCrSe_2)_{0.5}(CuCrSe_2)_{0.5}$ pellets.

4.5.4 Morphology of the nanocomposite

The cross sectional scanning electron microscope (SEM) images recorded for the fractured hot pressed pellets of all samples are shown in Fig.4.24 (a-c). The SEM image of the composite sample (Fig. 4.24(c)) also indicates that it has more numbers of grain boundaries (due to smaller grain size) as compared to the pure sample. From these SEM images it is also evident that all samples have layered structure. Since the typical size of these grains with layered structure varies from 10 to 30µm, therefore measured thermoelectric properties which normally measured over a length scale of few mm. will not exhibit any anisotropic behavior. In our previous study on pure $CuCrSe_2$ compound we demonstrated that thermoelectric properties of the hot pressed sample does not exhibit any anisotropy with respect to hot pressing direction.

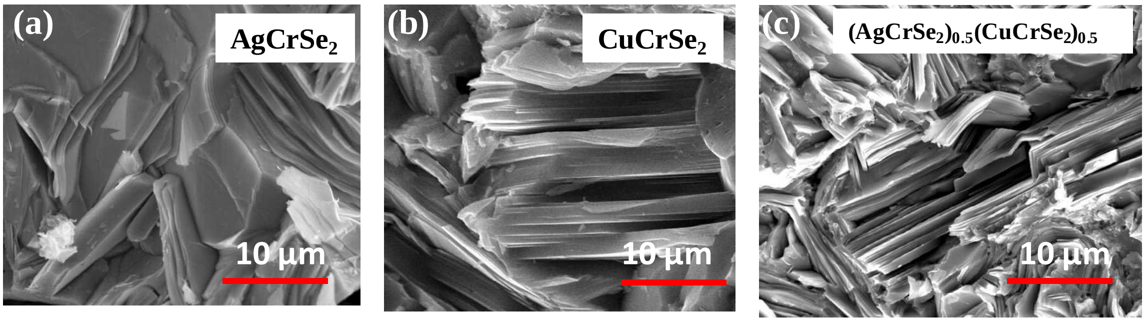

Fig. 4.24. SEM images of (a) AgCrSe$_2$ (b) CuCrSe$_2$ (c) (AgCrSe$_2$)$_{0.5}$(CuCrSe$_2$)$_{0.5}$ composites.

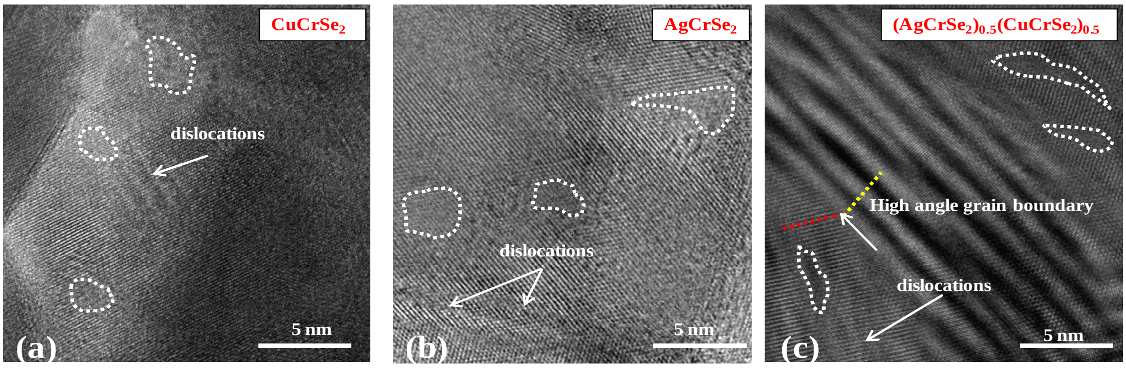

Fig.4.25. Transmission electron microscope (TEM) image of (a) CuCrSe$_2$ (b) AgCrSe$_2$, and (c) (AgCrSe$_2$)$_{0.5}$(CuCrSe$_2$)$_{0.5}$. In the images, region inside white dotted lines shows the presence of nanoscale features with amorphous structure.

The high resolution transmission electron microscope (TEM) images of the samples are shown in Fig.4.25(a-c) . For all samples it can be seen that within the crystalline grains there are nanoscale amorphous regions (marked with enclosed white lines). In addition to this, large numbers of dislocation can be seen in the microstructure of the all samples. It is also interesting to note that in the composite sample there is a presence of wrinkled grain, which is separated from another grain by the large angle grain boundary (grain boundary angle >10˚).

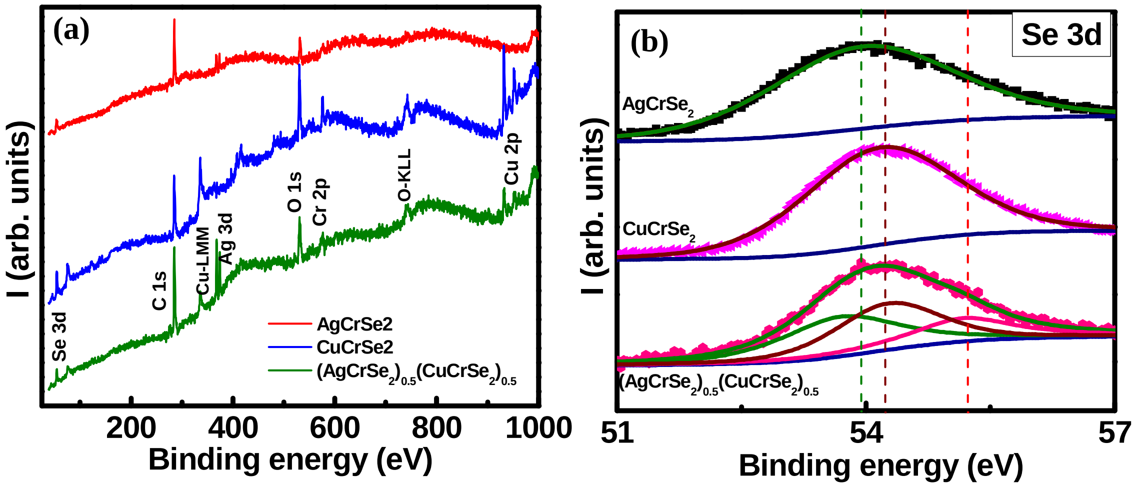

Fig.4.26. (a) Survey (b) Se 3d XPS spectra of pure $AgCrSe_2$, $CuCrSe_2$ and $(AgCrSe_2)_{0.5}(CuCrSe_2)_{0.5}$ samples.

4.5.5 Chemical analysis of $(AgCrSe_2)_{0.5}(CuCrSe_2)_{0.5}$ nanocomposites

The evidence of reaction between $AgCrSe_2$ and $CuCrSe_2$ is witnessed by the X-ray photoelectron spectroscopy (XPS) results shown in Fig.4.26. The survey XPS spectra for pure and composite samples are given in Fig. 4.26(a). In the survey XPS spectra of composite samples signal from each element such as Ag, Cu, Se and Cr are seen. In addition all samples exhibit the presence of physisorbed oxygen (shown as O1s peak). A careful examination of the high resolution XPS data corresponding to each elements suggest that major changes has been observed for Se 3d peak. High resolution Se 3d XPS spectra for all samples are plotted in Fig. 4.26(b), from this data it can be seen Se 3d peak appears at 54 eV and 54.2 eV for $AgCrSe_2$ and $CuCrSe_2$ sample. It is interesting to note that for composite sample the Se 3d peak consist of three components. The Se 3d peak at binding energy value ~ 53.8 eV is assigned to the Se from $AgCrSe_2$, peak at binding energy of 54.2 eV is assigned to $CuCrSe_2$, while the peak at ~ 55 eV is assigned to the Se from intermixed Cu-Ag region. Since Cu or Ag layers are sandwiched between Se layers therefore Se 3d peaks are expected to be most affected on replacement of Ag by the Cu atoms. In summary, XPS data also confirm some intermixing of Cu and Ag atoms in the composite.

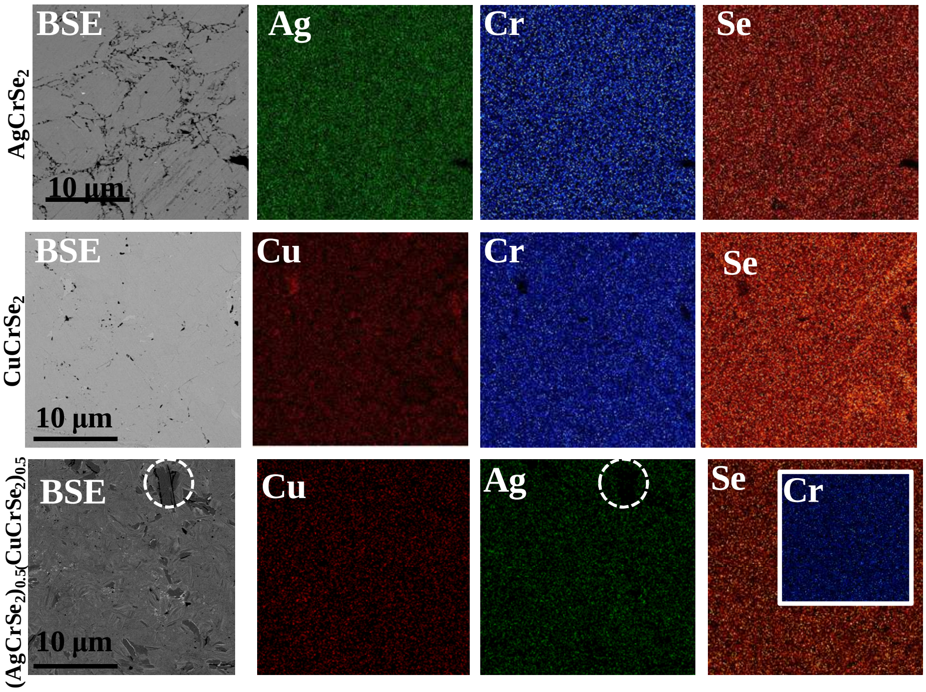

Fig 4.27. Back scattered electron (BSE) image and X-ray elemental mapping of Cu, Cr and Se in the $AgCrSe_2$, $CuCrSe_2$ and $(AgCrSe_2)_{0.5}(CuCrSe_2)_{0.5}$ samples.

EDX of pure $CuCrSe_2$ and $AgCrSe_2$ samples gives the elemental ratio Cu/Ag : Cr : Se around 1.03:1.05: 2.01, confirming the stoichiometry of the synthesized samples. The backscattered electron image (BSE) and X-ray elemental mapping of Ag, Cu, Cr and Se elements for pure and composite samples are shown in Fig. 4.27. The uniform distributions of Ag, Cu, Cr and Se for pure samples suggest that they are quite homogenous. The BSE image of $(AgCrSe_2)_{0.5}(CuCrSe_2)_{0.5}$ composite samples show the presence of nano- and meso-scales features (seen as dark spot) in the microstructure. The elemental mapping of composite sample suggests that some of these mesoscale features has absence of Ag (shown within the white dotted circle as voids in the Ag elemental mapping image).

The inhomogeneous compositional structure of $(AgCrSe_2)_{0.5}(CuCrSe_2)_{0.5}$ composite samples is also witnessed in the energy dispersive X-ray analysis (EDX) spectrum of two different region of the sample as shown in Fig. 4.28. EDX spectrum 1 obtained at a particular region shows that here sample does not have Ag while spectrum 2 shows the presence of both Cu and Ag. These results suggest, in the composite sample, we have a very uniform matrix (mixed at nanoscale level) of $AgCrSe_2$ and $CuCrSe_2$ along with some mesoscale precipitate of $CuCrSe_2$.

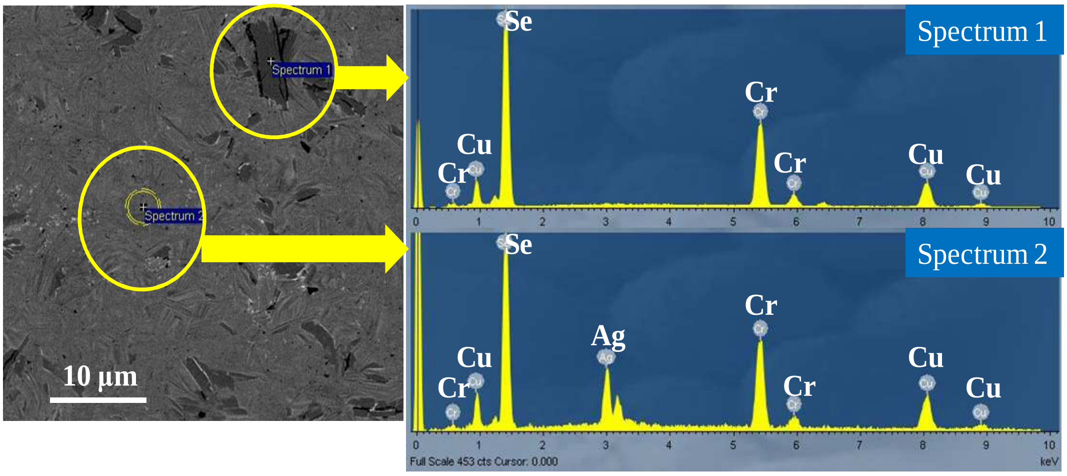

Fig.4.28. Back scattered image of hot pressed $(AgCrSe_2)_{0.5}(CuCrSe_2)_{0.5}$ sample. The EDX spectrum of two different regions of the sample is shown at right.

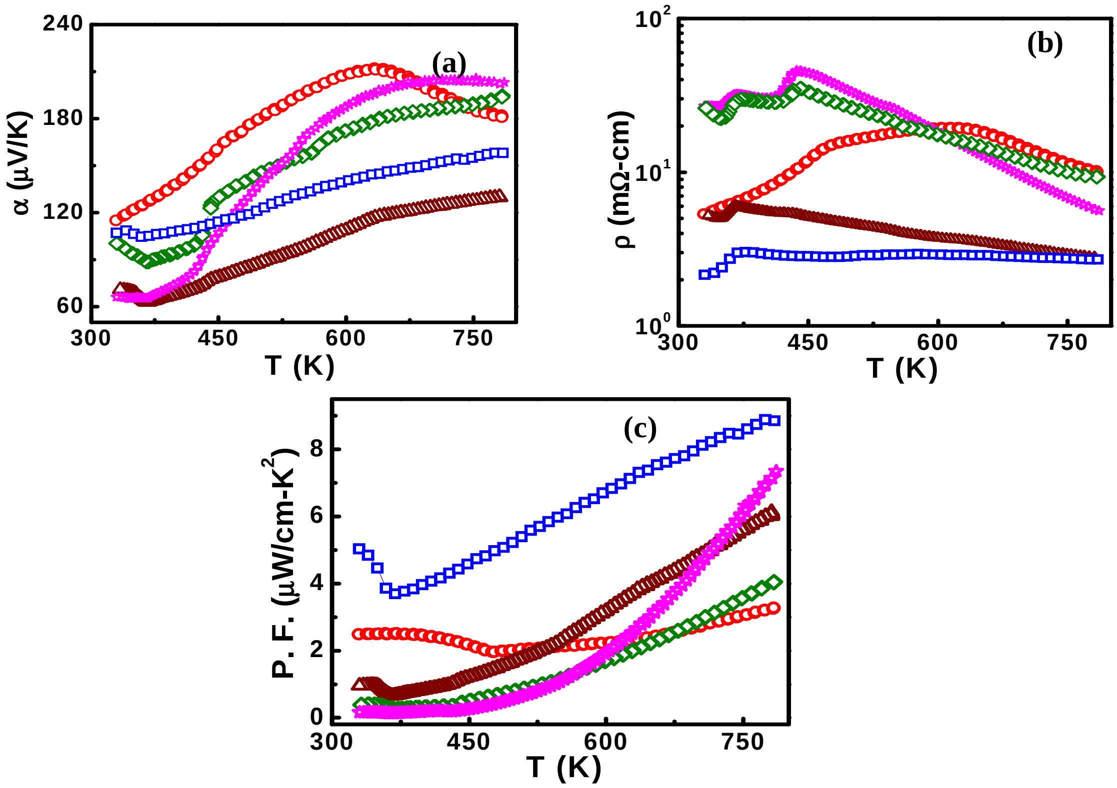

Fig.4.29. Thermoelectric properties of all hot pressed samples (a) Seebeck coefficient (α) (b) electrical resistivity (ρ). (c) Power factor (α^2/ρ).

4.5.6 Temperature dependence thermoelectric properties of $(AgCrSe_2)_{0.5}(CuCrSe_2)_{0.5}$

(a) Temperature dependence of α and ρ

Fig.4.29 (a) shows the temperature dependence of α in the temperature range of 300 K to 773 K. The positive sign of α for all the samples indicates the hole as majority charge carriers (i.e. p-type nature) in the material. Fig.4.29 (b) exhibits the temperature dependence of ρ for all samples in the temperature range of 300 K -773 K. For pure $AgCrSe_2$ and

$CuCrSe_2$ samples the resistivity increases rapidly upto 470 K and 365 K respectively, after that ρ shows weak temperature dependence. These ρ humps at 475 K and 365 K for both pure samples can be correlated with the disordering of the Ag and Cu ions in the pure sample [137,140,141,142,146,152]. For composite samples it is interesting to note that disordering transitions temperature corresponding to the $AgCrSe_2$ shift to lower value (~ 434 K) while the transition corresponding to the $CuCrSe_2$ remains same and 365 K. This result again supports the partial substitution of Cu at the Ag sites in the composite sample. Fig. 4.29(c) shows the temperature dependence of the P.F. for all the samples. The P.F. for pure $CuCrSe_2$ and $AgCrSe_2$ samples respectively shows a dip at 365 K at 450 K, after that it increases with the rise in temperature. The P.F. (at 773K) calculated for the pure $CuCrSe_2$, $AgCrSe_2$ and $(AgCrSe_2)_{0.5}(CuCrSe_2)_{0.5}$ samples are 8.8 µW/cm-K^2, 4.2 µW/cm-K^2 and 4.1 µW/cm-K^2 respectively.

(b) Temperature dependence *D*, C_p and κ

The temperature dependence of *D* and C_p data for all samples is shown in Fig. 4.30. For pure samples the presence of transitions can be clearly seen at 365 K (for $CuCrSe_2$) and 450 K (for $AgCrSe_2$). However, a shoulder in the C_p curve of $CuCrSe_2$ is seen and the origin of this is not yet understood. In the composite sample data, transition features for both $CuCrSe_2$ and $AgCrSe_2$ components can be clearly seen. It may be noted that the experimentally obtained high temperature C_p values were found to be 0.4 J/g K, 0.3 J/g K and 0.33 J/g K for $CuCrSe_2$, $AgCrSe_2$ and composite samples respectively and compares very well with theoretically estimated Dulong-Petit value. The Dulong-Petit C_p values were respectively found to be 0.37 J/g K, 0.31 J/g K and 0.32 J/g K for $CuCrSe_2$, $AgCrSe_2$ and composite samples. In the calculation of κ, the mass density (estimated using Archimedes method) used for pure $CuCrSe_2$, $AgCrSe_2$ and composite samples were respectively 6.31, 6.69 and 6.49 g/cc.

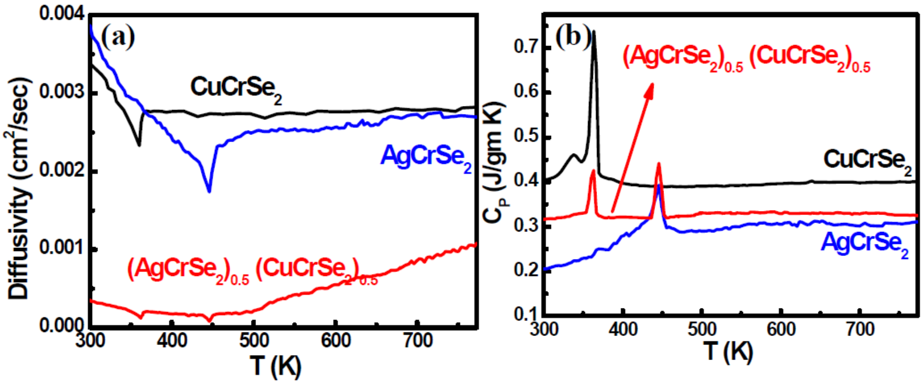

Fig.4.30. (a) Thermal diffusivity (D) and (b) specific heat (Cp) results for $AgCrSe_2$, $CuCrSe_2$ and $(AgCrSe_2)_{0.5}(CuCrSe_2)_{0.5}$ samples.

The most significant lowering (nearly one third of the pure compounds) of the κ is observed for the composite $(AgCrSe_2)_{0.5}(CuCrSe_2)_{0.5}$ sample. Temperature dependence κ for all the samples is shown in Fig.4.31, which shows that in the entire temperature range all composite samples exhibit low κ than the pure compounds.

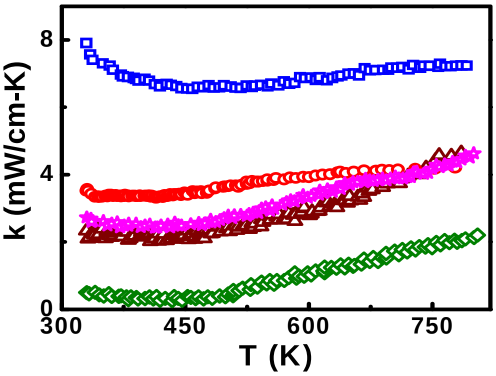

Fig.4.31. Temperature dependence of thermal conductivity (κ).

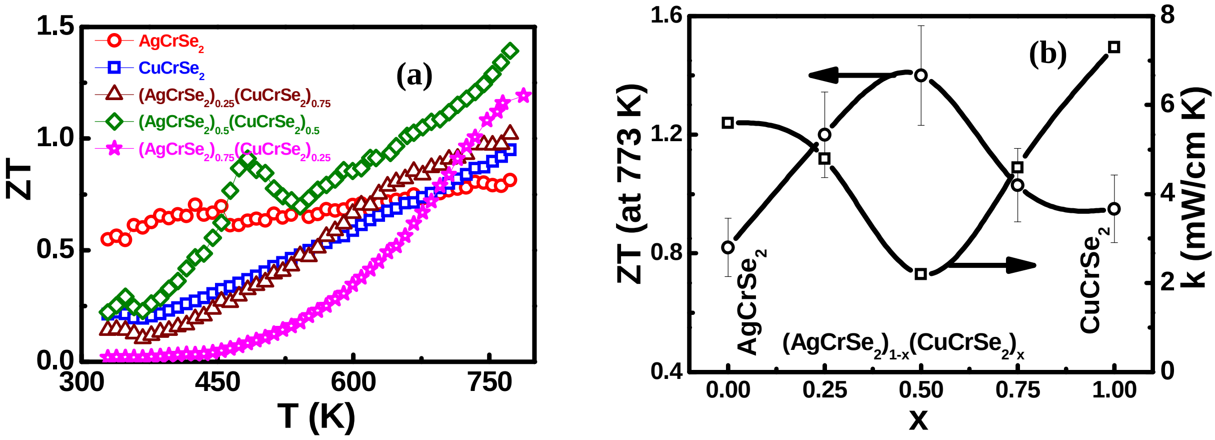

Fig.4.32. (a)Temperature dependence of the *ZT* for all hot pressed samples. (b) x dependence of *ZT* and *k* (at 773 K) for (AgCrSe$_2$)$_{1-x}$(CuCrSe$_2$)$_x$.

Table 4.5: Summary of the thermoelectric parameters obtained for AgCrSe$_2$, CuCrSe$_2$ and (AgCrSe$_2$)$_{0.5}$(CuCrSe$_2$)$_{0.5}$.

Sample	***μ*** **(cm^2 V^{-1}s^{-1})** **at 300 K**	***ρ*** **(mΩ-cm)** **at 773K**	***α*** **(μV/k)** **at 773K**	***k*** **(mW/cm-K)** **at 773K**	***ZT*** **at 773 K**
AgCrSe$_2$	72.8	7.8±0.2	181±9	4±0.2	0.81±0.11
CuCrSe$_2$	165.3	2.7±0.1	160±8	7±0.4	0.95±0.11
(AgCrSe$_2$)$_{0.5}$(CuCrSe$_2$)$_{0.5}$	75.5	9.2±0.3	194±9	2.2±0.1	1.44±0.17

(c)Temperature dependence of *ZT*

Finally we have evaluated the *ZT* and Fig. 4.32 (a) shows the temperature dependence of *ZT* for all the samples. In Fig. 4.32 we have plotted the *ZT* (at 773 K) for all the sample, and it can be seen that pure samples exhibit *ZT* ≤ 1, while the composite (AgCrSe$_2$)$_{0.5}$(CuCrSe$_2$)$_{0.5}$ sample exhibit the highest *ZT*~ 1.4. It is important to note that, the P.F. of composite (AgCrSe$_2$)$_{0.5}$(CuCrSe$_2$)$_{0.5}$ sample is nearly seven times lower than the state of art thermoelectric material such as PbTe or TAGS-85 but the thermoelectric performance which is evaluated by *ZT* is comparable or better to them. A summary of the measured thermoelectric properties for all samples are shown in Table 4.5.

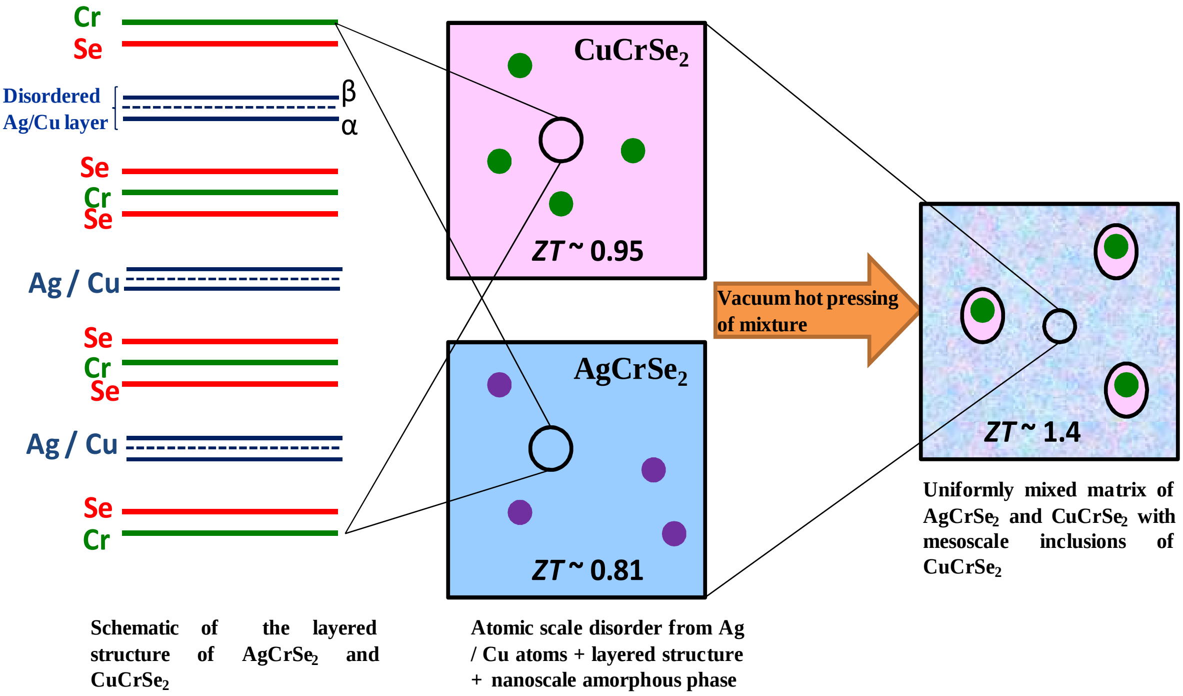

Fig.4.33. Schematic showing naturally obtained hierarchical architecture of the $(AgCrSe_2)_{0.5}(CuCrSe_2)_{0.5}$ sample. In the composites, the atomic scale (due to the disordered Ag and Cu atoms at high temperature), nanoscale (due to the presence of amorphous phase, dislocations, grain boundaries) and mesoscale ($CuCrSe_2$ precipitates in the uniformly mixed matrix of composite) disorders results in scattering of phonons of all wavelength. The green and purple circles in the middle schematic shows the presence of nanoscale disorder in the pure $CuCrSe_2$ and $AgCrSe_2$ matrix.

4.5.7 Reason for exhibiting low κ by the composite $(AgCrSe_2)_{0.5}(CuCrSe_2)_{0.5}$

In the light of micro-structural investigation of hot pressed $(AgCrSe_2)_{0.5}(CuCrSe_2)_{0.5}$ samples using TEM (and also by SEM) and electrical transport data, the overall extremely low *k* value for composite samples in the present case can be related to the scattering of heat carrying phonons by:

(i) Atomic scale disorder: the high kinetic disorder produced by the movement of Ag/Cu ions, which scatter very low mean free path (~ 1-10 nm) phonons.

(ii) Nanoscale features: amorphous nanoscale precipitates inclusion in the crystalline matrix of the composites, large number of interfaces including high angle grain boundaries between the nanosized grains of $AgCrSe_2$ and $CuCrSe_2$ in the materials, which scatters mid wavelength (~ 10- 100 nm) phonons

(iii) The mesoscale $CuCrSe_2$ precipitates, which scatters phonons with higher mean free path (> 100 nm).

In summary the detailed microstructure investigation of the composite suggest that it is an ideal example of a natural all scale hierarchical architecture (schematically shown in Fig. 4.33) which is essential for scattering of all wavelength phonons.

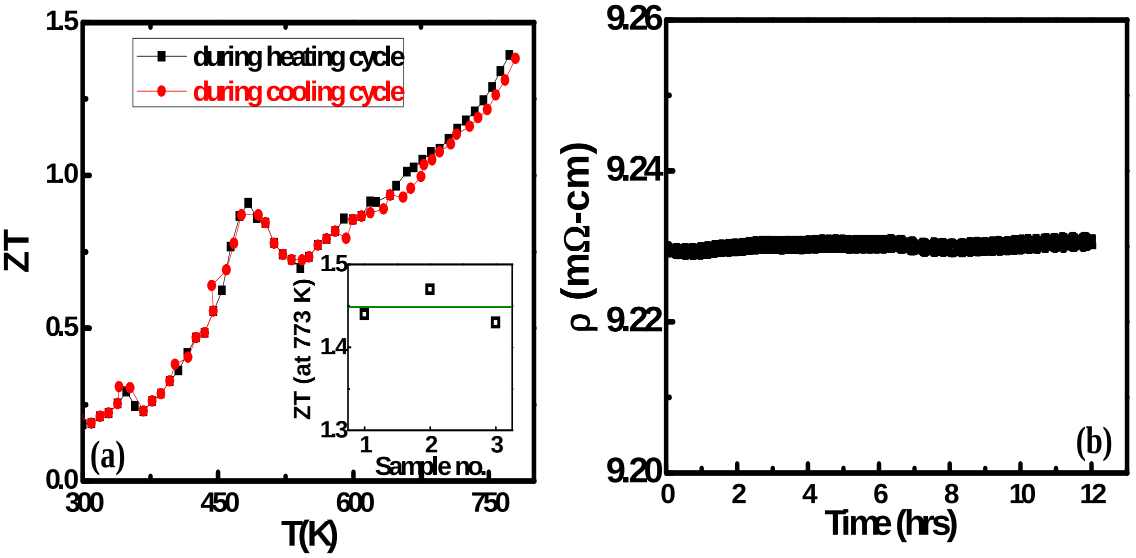

Fig.4.34. (a) Estimated *ZT* for $(AgCrSe_2)_{0.5}(CuCrSe_2)_{0.5}$ sample during the heating and cooling cycle. Inset shows *ZT* (at 773 K) for three numbers of $(AgCrSe_2)_{0.5}(CuCrSe_2)_{0.5}$ samples prepared under same synthesis run. (b) Time dependence of the electrical resistivity (ρ) for $(AgCrSe_2)_{0.5}(CuCrSe_2)_{0.5}$ sample at constant temperature of 773 K.

4.5.8 Reproducibility and thermal stability test of $(AgCrSe_2)_{0.5}(CuCrSe_2)_{0.5}$

From the application point of view the reproducibility and thermal stability of $(AgCrSe_2)_{0.5}(CuCrSe_2)_{0.5}$ is of great concern. In the present work, all three thermoelectric parameters (α, ρ and k) were measured from 330 K-773 K during heating and cooling cycle and both cycle gives repeatable results without any hysteresis confirming high temperature stability of the materials. The estimated *ZT* during heating and cooling cycle is plotted in Fig.4.34 and from this it can be seen that prepared compounds are quite repeatable results.

For testing the reproducibity, three set of $(AgCrSe_2)_{0.5}(CuCrSe_2)_{0.5}$ samples were prepared under similar condition and typical *ZT* values of all samples shows a deviation of ± 3% around 1.44 (shown in inset of Fig. 4.34(a)). Since the stability of ionic semiconductors such as copper sulphides (Cu_2S) and copper selenides (Cu_2Se) compounds is under doubt due to the electro migration of Cu at high applied current density [153,154]. In the work reported by the group of K. Nielsch, they have observed a visible change at the surface of Cu_2S pellet due to segregation of Cu during the preparation of sample by spark plasma sintering. The electro migration of Cu in Cu_2S also takes place under high current density (~ 12 A/cm^2) and segregation of Cu can be seen visibly at the one side of rectangular sample. In their study it is interesting to note that for CuS and $Cu_{1.8}S$ samples even on application of very current density ~ 48 A/cm^2, there was no noticeable degradation. The degradation of Cu_2Se material was observed by the group of Snyder. They also reported about the migration of Cu in Cu_2Se at high current density ~ 9 A /cm^2. These studies highlight the importance of the stability of ionic semiconductor based thermoelectric material under high current density. The stability issue needs to be discussed from application point of view because thermoelectric devices generate high current during operation. In order to test the stability of our composite samples, we have carried out the time dependent measurement (up to 12 hrs) of ρ (at high unidirectional current density ~ 50 A/cm^2) at constant temperature of 773 K. The measurement of ρ was carried out in especially home-made test set up and the obtained result is plotted in Fig. 4.34(b), from there it can be seen that ρ almost remains constant for a period of 12 hrs. It is important to note that during measurement of ρ, current was kept continuously ON for 12 hrs and data was recorded at intervals of 20 seconds. We have also visually inspected the sample surface before and after of stability test, we did not see any changes such as segregation of Cu at the sample surface. The digital photograph of the samples before and after performing stability experiment is shown in Fig.4.35. With respect to the reported work on copper sulhphides and copper selenides, our composite selenides samples exhibit a good stability at high current density.

Fig.4.35. (a) Sample photograph before stability test (b) Sample photograph after stability test.

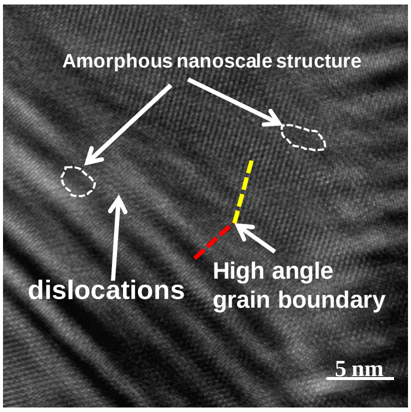

Fig.4.36. Transmission electron microscope (TEM) image of $(AgCrSe_2)_{0.5}(CuCrSe_2)_{0.5}$ samples after 12 hrs of annealing at 773 K. In the image, region inside white dotted lines shows the presence of nanoscale features with amorphous structure.

A TEM image of the sample was also taken after the stability experiment and the nanoscale defect structure of the sample looks to be nearly same as that of fresh sample (shown in Fig. 4.36).

4.6 Conclusions

In this Chapter, we have investigated the thermoelectric properties of the selenides namely, $PbTe_{1-x}Se_{x}$, Cu intercalated $TiSe_2$, $CuCrSe_2$, $AgCrSe_2$ and $CuCrSe_2$/ $AgCrSe_2$ nanocomposites with an emphasis on enhancing their *ZT*. The results obtained on various selenides are summarized below.

(i) **$PbTe_{1-x}Se_x$:** The effect of Se substitution has been systematically investigated $PbTe_{1-x}Se_x$. For a particular composition of x =0.5, α is highest ~ 292 μV/K, while κ is lowest ~ 0.75 W/m-K, resulting in the highest *ZT* of ~0.95 at 600K. The increase in α for x=0.5 is attributed to the high distortion in the crystal lattice which leads to the formation of defect states. These defect states scatters the majority charge carriers leading to high α as well as high ρ. The dramatic reduction of κ for x=0.5 is also attributed to the scattering of the phonons by the defect states.

(ii) **Cu intercalated $TiSe_2$:** High temperature (300–650K) thermoelectric performance of Cu intercalated Cu_xTiSe_2 (x=0-0.11) material show that Cu intercalation transforms the p-type $TiSe_2$ to n-type Cu_xTiSe_2 with α value saturating to ~ -90 μV/K (for x≥0.06) at 650 K. Spanning the entire range of Cu_xTiSe_2 samples, very low κ has been observed which is attributed to the layered growth structure and rattling effect of weakly bound Cu atoms in the van der Waals gaps of $TiSe_2$ layers.

At 650 K, the *ZT* values of 0.1 and 0.15 are achieved for pure $TiSe_2$ and $Cu_{0.11}TiSe_2$, respectively. A prototype generator has been fabricated using n-type $TiSe_2$ and p-type Cu intercalated $TiSe_2$, as their *ZT* values were nearly same (i.e. ~0.15 at 650 K). However, the efficiency found was only 0.1%, which is due to low *ZT* as well as very high contact resistances.

(iii) **$CuCrSe_2$ and $AgCrSe_2$:** Both $CuCrSe_2$ and $AgCrSe_2$ are p-type emerging thermoelectric materials due to their complex layered structure and acts like a phonon liquid electron crystal (PLEC) system. The κ (at 773K) values obtained for $CuCrSe_2$ and $AgCrSe_2$ were found to be ~ 7 and ~4 $mWcm^{-1}K^{-1}$ respectively. The low κ values are attributed to various phonon-scattering sources i.e. superionic Cu/Ag ions between $CrSe_2^-$ layers, nanoscale precipitates and natural grain boundaries. The low κ values yield *ZT* of 1 and 0.8 respectively for $CuCrSe_2$ and $AgCrSe_2$.

(iv) **$(AgCrSe_2)_{0.5}(CuCrSe_2)_{0.5}$ nanocomposites:** A further improvement of *ZT* has been obtained in the $(AgCrSe_2)_/(CuCrSe_2)$ nanocomposites through hierarchically organized microstructures that significantly lowers the lattice thermal conductivity without any appreciable change in the power factor. $(AgCrSe_2)_{0.5}(CuCrSe_2)_{0.5}$ nanocomposites synthesized via the vacuum hot pressing of a mixture of the constituents consisted of phonon scattering centers in a multiscale hierarchical fashion, i.e. atomic scale disorder, nanoscale amorphous structure, natural grain boundaries due to layered structure and mesoscale grain boundaries/interfaces. XRD results show that in composite samples there is a slight migration of Cu into the Ag site. Nanocomposite samples exhibit extremely low κ of ~2 $mWcm^{-1}K^{-1}$ at 773 K, which is much lower than that of $AgCrSe_2$ and $CuCrSe_2$. The composite samples exhibit a high *ZT* of 1.4 at 773 K.

In summary, the high thermoelectric performance and thermal stability of selenide composites make them promising materials to be used in thermoelectric generators for waste heat recovery. However, making ohmic electrical contacts on these p-type selenides as well as finding equivalent n-type materials are the major challenge in thermoelectric generator fabrication, and therefore, require detailed investigations.

Chapter 5

ZT Enhancement in SiGe and Thermoelectric Generators

5.1 Introduction

This chapter mainly describes the synthesis of SiGe thermoelectric alloy and fabrication of thermoelectric generators based on it. SiGe is known for its wide application in space missions. The potential of SiGe solid solutions as a thermoelectric was shown in 1958 by Steele and Rosi [155]. In 1964, Dismukes et al. provided the foundation for future optimizations with their work on silicon-rich SiGe alloys [156]. Although carried out for the U.S. Navy, this work was later employed by NASA on Radioisotope Thermoelectric Generators (RTGs) operating from 600−1000ºC [1,157]. Specifically, SiGe alloys synthesized by the time consuming zone leveling process were first used on the 1965 NASA SNAP-10 mission. An example of a multihundred watt (MHW) RTG using SiGe modules was employed on the Voyager space mission.

In the late 1960’s grain boundary scattering and the use of fine-grained alloys in order to lower lattice thermal conductivity were studied for SiGe [158,159], and Rowe et al have investigated the grain size effect on the thermal conductivity of SiGe alloys [160,161]. In the mid-1970’s Sandia Laboratories published reviews on the synthesis of SiGe materials by the chill casting method [162,163,164]. Other investigations during the 1970’s included various milling, sintering, and pressing techniques [165,166]. By 1976, SiGe had become the sole material used in RTGs for all deep space power generation applications [1]. The 1980’s saw a diminished interest in all thermoelectric research as NASA was looking for an alternative of SiGe alloys. But later on it was found that in spite the promise of other advanced materials when it came to providing power SiGe alloys remained the material of choice due to their robust nature [167]. In 1989, work done by Cook et al at Ames laboratory introduced mechanical alloying, as opposed to zone leveling, as a simpler way to synthesize SiGe alloy [168]. The advantages of SiGe alloys for fabrication of TEG include: (i) stability at higher temperatures; (ii) ease of synthesis in bulk quantity, (iii) strong mechanical properties [169], and SiGe alloy can be easily made to p- and n-type material by appropriate doping. In 1964, Dismukes et al presented a detailed investigation of thermal and electrical properties of these alloys as a function of composition, doping concentration and temperature [156,170]. The requirements of a large energy gap to minimize intrinsic conduction at high temperature and that of a high melting point favors silicon rich alloys. Substitution of Si by Ge reduces the κ by an order of magnitude as compared to the undoped Si. For e.g. κ of undoped Si is 12×10^{-3} W/cm-K. By using a simple linear interpolation from Si to Ge it was estimated that at high temperatures, i.e.; above 300 K, the minimum lattice thermal conductivity of 70Si-30Ge is: $9 \pm 1\times10^{-3}$ W/cm-K. Consequently, the most extensively investigated alloys were of $Si_{0.7}Ge_{0.30}$, $Si_{0.80}Ge_{0.20}$, and $Si_{0.85}Ge_{0.15}$, compositions [171]. In this research work, the stoichiometry was based on eighty percent Si and twenty percent Ge molar ratios. The dopant of P for n-type samples or B for p-type samples was calculated on top of these values. The reason that P or B produces n-type or p-type conductors can be understood by observing the valence band structure for Si or Ge. As, Si and Ge both have 4 valence electrons in a shell that has eight available spaces for electrons. Therefore, Si or Ge can share electrons to covalently bond with four other atoms of each other. Hence, a lattice of bonded Si and Ge atoms can be formed. A small number of impurity atoms can be introduced to a Si/Ge lattice. Depending on the number of valence electrons of the impurity atom, an electron will be donated or accepted from the semiconductor’s conduction band. Boron acts as an acceptor impurity creating a hole, while phosphorus acts as a donor impurity giving an electron to the conduction band.

The driving force for synthesis of SiGe alloys and fabrication of TEG in this thesis work is dictated by the requirement of indigenous technology for such generators for space mission of Indian Space Research Organization (ISRO), as they are commercially unavailable. In this research work both n- and p- type $Si_{0.8}Ge_{0.2}$ alloys were synthesized using melt-quench as well as ball milling methods. We also discuss the challenges in fabricating efficient thermoelectric generators.

5.2 Crystal structure of SiGe

Si and Ge both have diamond structures and thus SiGe has a diamond lattice (space group *Fd3m*) consisting of two inter penetrating face-centered cubic primitive lattices as shown in Fig 5.1 . The lattice constant is constituent dependent and follows the Vegard's law [172]

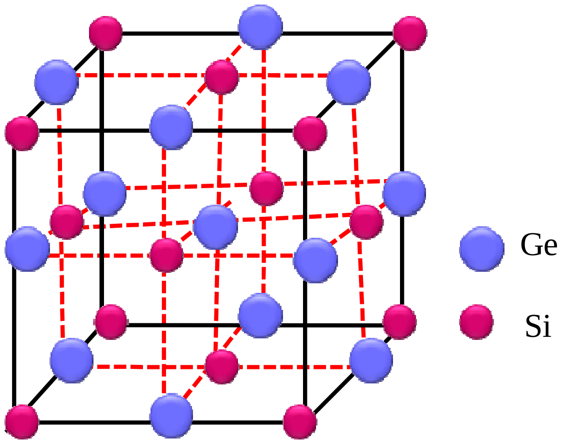

Fig.5.1. Crystal structure of SiGe alloy.

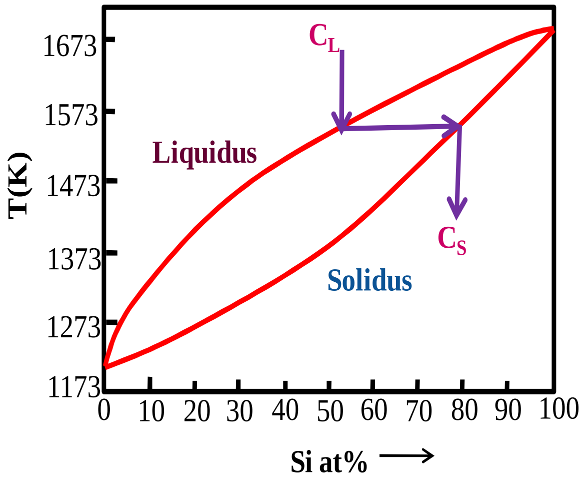

Fig. 5.2. Si-Ge phase diagram indicating the solidification of $Si_{0.8}Ge_{0.2}$.

5.3 Synthesis of SiGe alloy

5.3.1 Phase diagram of SiGe alloy

Although Si and Ge are completely miscible in both the liquid and solid states, a large separation exists between the solidus and the liquidus, which makes the synthesis of homogeneous SiGe alloy difficult. Fig. 5.2 illustrates solidification of $Si_{0.8}Ge_{0.2}$ (C_S) from a liquid with composition $Si_{0.545}Ge_{0.455}$ (C_L). Upon cooling, the first solid deposited is enriched in Si, compared to the melt, and as a result cast ingots typically exhibit severe alloy segregation. Preparation of homogeneous solids requires either a method to maintain the composition of the melt during solidification or some process to homogenize the solid phase [1]. Based on the above fact two techniques were adapted to synthesize the $Si_{0.8}Ge_{0.2}$ alloy.

5.3.2 Melt-quench method

SiGe alloys were synthesized using melt-quench technique as described in Chapter 2 [162,163,164]. In this method, brief chunks of Si and Ge materials (in stoichiometric ratio of

Si 80 mole% and Ge 20 mole%) were kept in a graphite crucible under vacuum (~ 10^{-6} mbar) and subsequently heated at 1350ºC for 10 minutes using induction heating. In the molten state of materials the stirring action is provided by the eddy currents. For preparing the p-type material boron (0.2 at%) was intentionally added as the dopant (mixed with the initial grinded Si and Ge materials). The quenching of molten material was done by pouring it into a water cooled copper crucible, which helps in avoiding the segregation of Si or Ge during the alloy formation.

Fig. 5.3. SiGe alloy synthesized by melt quench method (a) highly oxidized surface with greenish yellow tint and (b) surface appears grey and dull compared to (a) indicating slight oxidation.

For preparing n-type SiGe alloy, red phosphorus (1.25 mole%) was added as dopants. Since the red phosphorus vaporizes at 883 K, the problem with the technique is that the dopant gets lost during the process of synthesis (as the alloy formation take place at ~1723 K). In order to avert the problem, the dopants were kept in the water cooled Cu-crucible. But it was found that in this process, the dopants were confined only to the lower portion of the melt. Moreover, the problems with the ingots obtained by this technique are: (i) The material tends to be very abrasive, thus making it difficult to maintain low impurity levels. (ii) The ingots are not homogeneous and Si-rich portions are more difficult to reduce than Ge-rich portions. Therefore, the fines tend to be Ge-rich and the coarser powder Si-rich. Fig. 5.3 shows the photograph of the SiGe alloy synthesized by melt-quench technique. Some portion of the sample exhibits greenish yellow tint, indicating the oxidation of the sample. The inner part of the sample has metallic luster, which is un-oxidized. Additional attention has always been given to synthesize n-type SiGe [10], as phosphorus is held in a water cooled hopper as well as added to the SiGe melt just before quenching [162,163,164] .

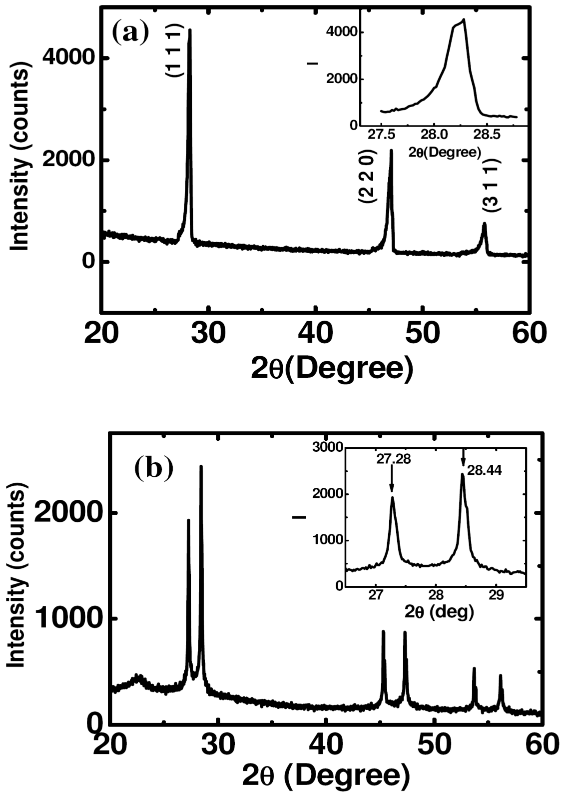

Fig. 5.4. XRD pattern of SiGe alloys: (a) rapid quenched and (b) slow cooled (Inset shows separate (111) peaks of Si and Ge).

The XRD patterns of the melt-quench SiGe alloy and the sample prepared by slow cooling of SiGe melt are shown in Fig. 5.4. In case of slowly cooled SiGe melt, the peaks corresponding to Si and Ge are well separated, indicating that SiGe alloy does not form and Si and Ge phase are segregated. On the other hand for rapidly melt-quenched samples, three broad peaks corresponding to (111), (220) and (311) are observed, which indicates formation of single phase SiGe alloy. Therefore, in order to synthesize SiGe alloy rapid quenching of melt is essential, which is in accordance with the phase diagram shown in Fig. 5.2.

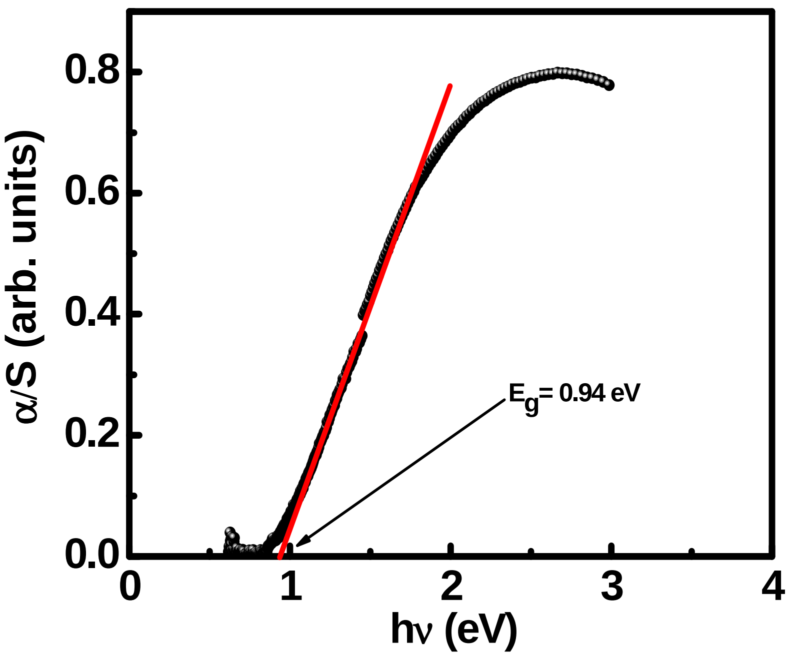

Fig 5.5. Band Gap of $Si_{0.8}Ge_{0.2}$ by diffuse reflectance UV spectroscopy.

The energy band gap (E_g) of the melt-quenched $Si_{0.8}Ge_{0.2}$ alloy is estimated from the by diffuse reflectance near IR spectroscopy and the obtained data reordered at room temperature is presented in Fig. 5.5. The value of E_g was found to be 0.94 eV. It has been empirically established that for $Si_{1-x}Ge_x$, where x<0.85, the band gap can be estimated using the following equation:

$$E_g = 1.12 - 0.41 * x + 0.008(x)^2 \qquad (5.1)$$

The obtained value of E_g using this expression is found to be ~1 eV, which is close to that obtained experimentally.

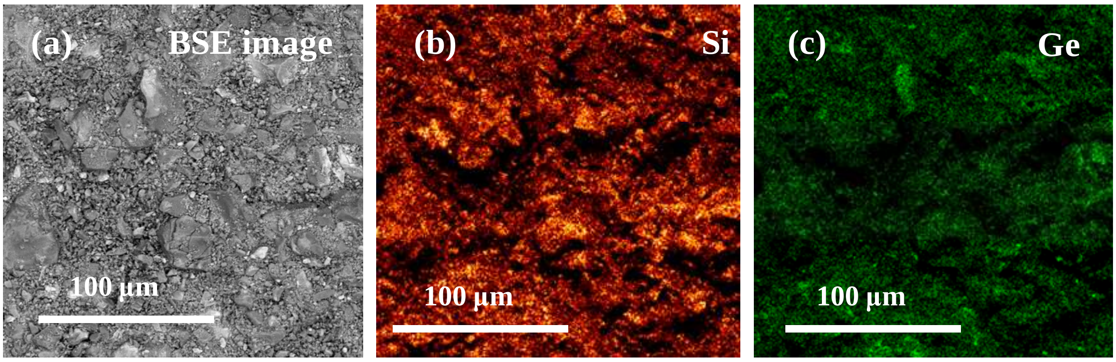

Fig.5.6. Back scattered electron images and the corresponding x-ray elemental mapping images of melt quenched SiGe alloy.

The BSE image and X-ray elemental mapping of Si and Ge obtained for the melt-quenched samples are shown in Fig. 5.6. It is seen that both Si and Ge are uniformly distributed, which supports the XRD results that single phase SiGe alloy has been formed.

In order to estimate the density of p-type and n-type SiGe alloy, they were pressed into pellets using vacuum hot press at ~1000 °C under a pressure of 500 Kg/cm^2. The density of the SiGe alloys measured using Archimedes' principle exhibited values in the range of 2.7-2.8 g/cm^3. However, the theoretical density of the alloy is composition dependent and is given by [172]

$$Si_{1-x}Ge_x\left(g/cm^3\right) = \left(2.329 + 3.493x - 0.499x^2\right) \qquad (5.2)$$

Thus, for $Si_{0.8}Ge_{0.2}$ the theoretical density is 3.00 g/ cm^3. Thus, our samples exhibit ~ 93% of the theoretical density.

It may be noted that the p-type SiGe (B as dopant) synthesized by melt-quench technique is comparatively easier unlike n-type SiGe alloy. This is because, B is highly stable and does not melt until 2349 K, and therefore, direct doping of B is possible. It is well established that 0.4 at% is the maximum solubility of B in Si. Based on the information available, 0.2 at% B was added in the melt of $Si_{0.8}Ge_{0.2}$ alloy. Oversaturation should be avoided as it leads to deterioration of the properties. The structural and morphological properties of p-type SiGe alloys were almost similar to the properties of n-type SiGe, as described above.

5.3.3 Mechanical alloying method

In this method, constituent elements such as Si, Ge and the dopants such as red P for n-type and boron for the p-type were loaded into robust vials with several balls made of tungsten carbide, as described in Chapter 2. Chunks of silicon and germanium were chosen over their respective powders to reduce the oxide contamination in SiGe alloy [173,174]. Powders were milled in a planetary mill (Fritsch make) at 400 rpm under argon atmosphere for a time period of 24 hrs, 48 hrs, 72 hrs and 96 hrs. Here, the milling time is the total run time excluding the pauses during the milling. 15 minutes pause time was introduced after each run of 30 min to prevent overheating of the bowl. Powders were extracted at different time intervals such as 24 hrs, 48 hrs, 72 hrs and 96 hrs. The vials were then locked as shown in Fig. 2.6. The striking of the balls against the sides of the vial allows for the repeated fracturing and cold welding of the materials resulting in a fine alloyed powder. Since oxidation will always be a concern for SiGe materials, the alloying was performed in the positive Argon pressure. Due to powder lost in the milling process excess P and B were added to the vials.

In our work, we have used 10 at% P as dopant for n-type and 0.2 at% B as dopant for p-type, SiGe thermoelectric samples. As discussed in the literature, over saturating of the dopants, specifically B, is common in SiGe. This over saturating causes the samples thermoelectric properties to vary as B or P precipitates out of the sample into the grains [175]. This precipitation will not be seen in any of the P samples because of the required heating and time required to degrade the samples properties, but it is very important to be aware for the B samples. In this thesis, detailed study of the n-type SiGe alloy was performed as loss of dopant for n-type alloy remained as a problem in melt quench method. The mechanically alloyed nanopowders were filled in graphite die set (diameter: 20 mm, thickness: 20 mm) and rapidly heated (rate 20°C/min) through graphite heaters) to 1050°C then compacted for 60 minutes. After hot pressing, samples were rapidly cooled to room temperature for avoiding the segregation of the dopant atoms. Hot pressed samples prepared from 24 hrs, 48 hrs, 72 hrs and 96 hrs ball milled powders will be designated as SiGe-24, SiGe-48, SiGe-72, SiGe-96 respectively.

The XRD pattern of mechanically alloyed SiGe-6, SiGe-24, SiGe-48, SiGe-72 and SiGe-96 samples are shown in Fig. 5.7. For SiGe-6 sample, separate diffraction peaks of Si and Ge are observed, indicating that alloy formation does not take place, and therefore, further milling is required for the alloy formation. XRD results suggest that powders prepared by ball milling for duration ≥ 24 hrs (at 400 rpm) are mechanically alloyed, which are polycrystalline in nature without any presence of secondary phases.

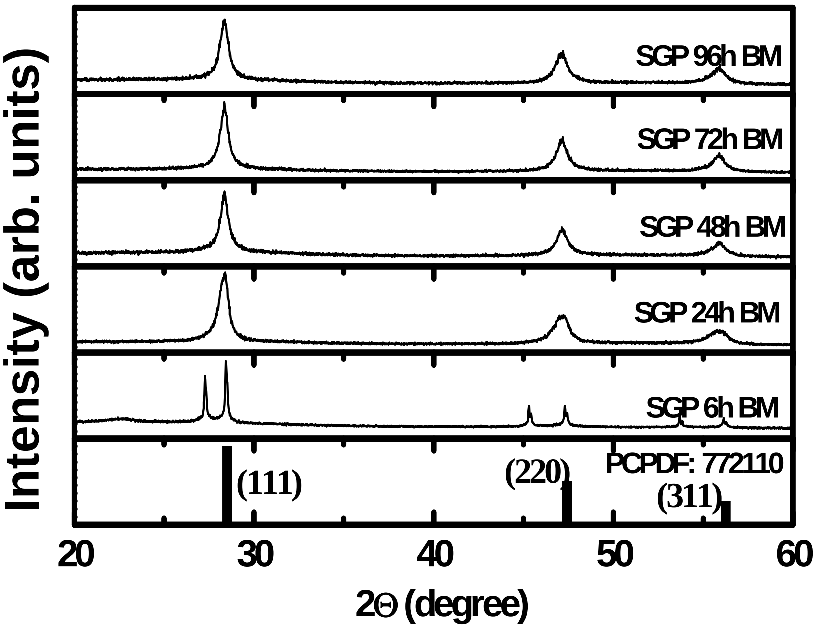

Fig. 5.7. XRD pattern of SiGe alloy milled for 6, 24, 48, 72 and 96 hrs.

It may be noted that in our experiment minimum time required (~ 24 hrs) for mechanical alloying of Si and Ge are four times less than earlier report [178], which may be possible due to the high rotation frequency, use of tungsten carbide balls and bowls during our ball milling experiments.

The impact and shear forces during ball milling process depends on various parameters such as hardness of the milling media, rotation frequency etc. From Fig. 5.7, it can also be seen that XRD peaks of the ball milled samples were significantly broadened (full width at half maximum ~ 0.6˚) indicating the presence of nanocrystallites. From XRD data mean size of the crystallite was obtained using Williamson-Hall method [176]. In contrast to the anticipated trend, the crystallite size remains nearly constant between 9 -12 nm for all samples. The observed trend may be due to the competing effects of downsizing of crystallites and fusion of crystallites by the friction induced heat during the ball milling. Apparently, no peak that could have been attributed to any secondary phase was identified, indicating that all the samples were nominally monophasic. Moreover, there is a small line intensity variation and systematic blue shift in the Bragg position as compared to that of the bulk Si samples. These can be attributed to the expansion of the cell and decrease in the crystallite size.

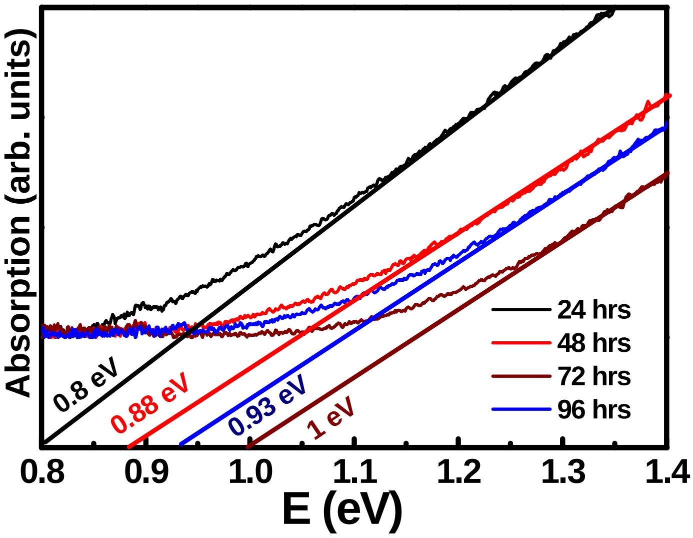

Fig.5.8. Electronic absorption spectra for SiGe alloy powder ball milled for 6, 24, 48, 72 and 96 hrs.

For all ball milled SiGe alloy samples, the E_g was experimentally determined by the diffuse reflectance near IR spectroscopy, and the obtained spectra are shown in Fig.5.8. The band gap value for SiGe-24 sample is found to be 0.8 eV, which systematically increases up to 0.99 eV with increase of ball milling time up to 72 hrs. The evolution of the band gap of SiGe alloy as a function of ball milling time can be attributed to the building up of stress in the material due to creation of defects. However, for SiGe-96 sample E_g value decreases to 0.93 eV, which is possibly due to the release of stress (less defects in the material). The band gap values obtained in the present work are consistent with earlier reports [177]. The theoretical density of hot pressed SiGe-6, SiGe-24, SiGe-48, SiGe-72 and SiGe-96 samples measured was ~2.9 g/cm^3, which is 96% of theoretical density.

In order to obtain the information regarding the chemical homogeneity of the mechanically alloyed n-type SiGe BSE and x-ray elemental mapping image of Si, Ge and P of hot pressed alloy was acquired as shown in Fig. 5.9 (a-p).

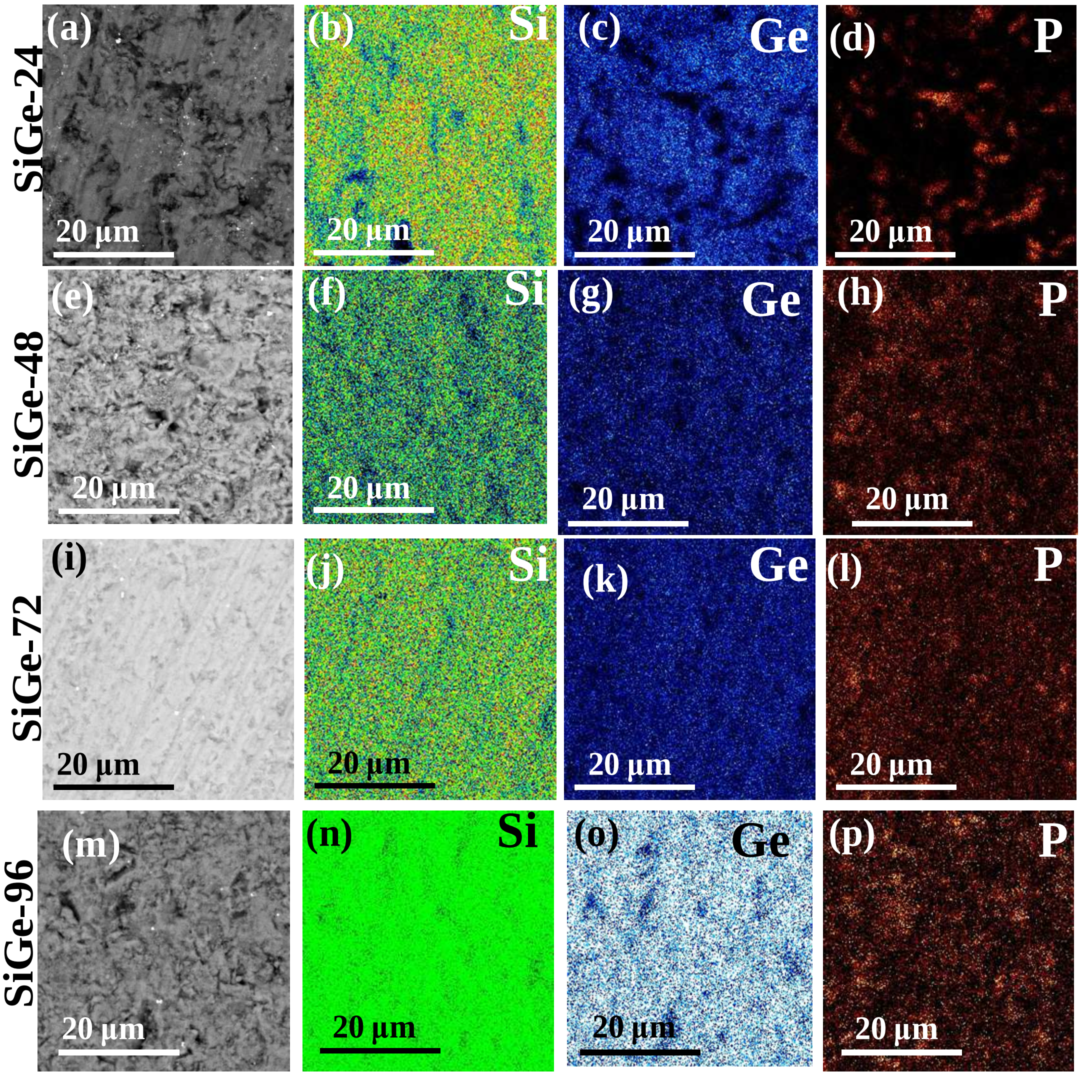

Fig.5.9. BSE and x-ray elemental mapping image of Si, Ge and P of hot pressed n-type SiGe alloy.

The detailed microstructural analyses of mechanically alloyed SiGe samples were performed using TEM. It is interesting to note that TEM images of all ball milled powder samples, as shown in Fig. 5.10 (a-d)) exhibits amorphous / crystalline nano-scale features (encircled with white dotted line). However for 72 hrs ball milled powder sample, in addition to the amorphous/crystalline nano-scale features in the bulk, large numbers of dislocations are also seen in the image (marked by arrows in Fig. 5.10 (c)). The origin of dislocations can be attributed to the repeated deformation of the material during the ball milling process.

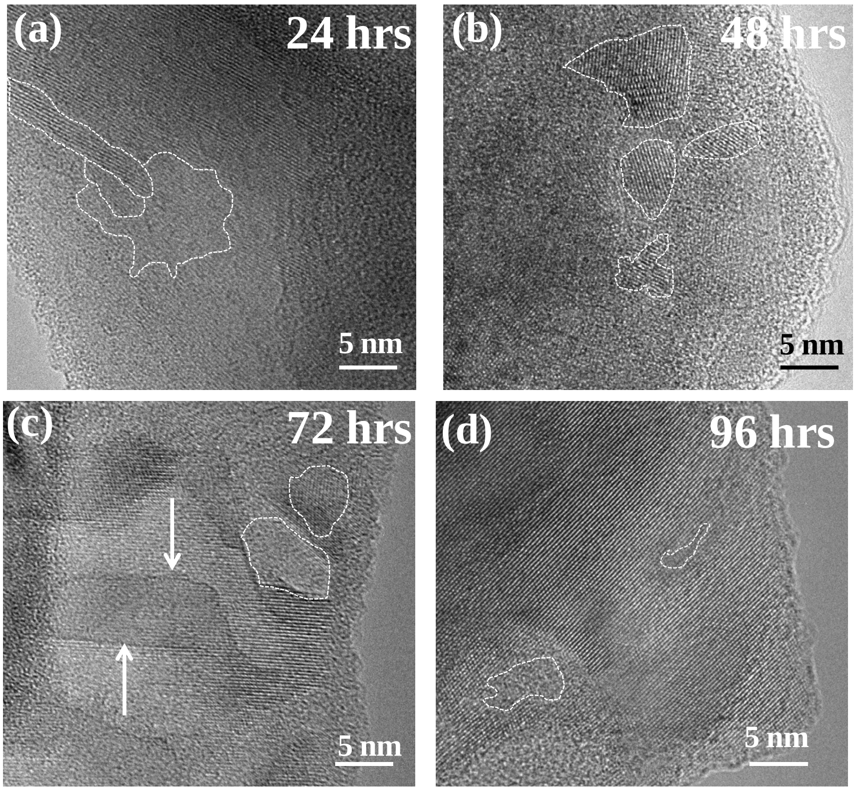

Fig. 5.10. TEM images (a) 24 hrs (b) 48 hrs (c) 72 hrs (d) 96 hrs ball milled n type – SiGe alloy. The region within dotted white line shows the nanoscale features within the bulk. The arrow marked in image (c) shows the presence of dislocation.

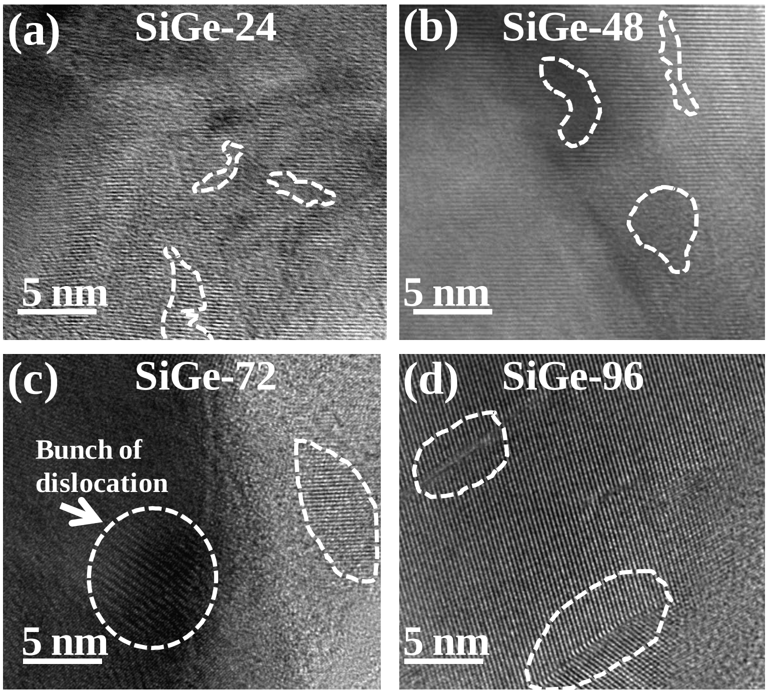

Fig. 5.11. TEM images of hot pressed SiGe alloys samples prepared (for different ball milling time) from the SiGe alloys powder. The region enclosed within the white dotted line shows the nanoscale defect structure in the SiGe matrix.

Fig 5.11 shows the TEM images of the vacuum hot pressed SiGe alloys samples. From these images it can be seen that each sample exhibit the incorporation of the different type of nanoscale defects structure (encircled with white dotted line) in the bulk. For SiGe-24 (Fig. 5.11(a)) and SiGe-48 (Fig. 5.11(b)) samples, nanoscale amorphous/crystalline structures can be seen in the matrix. A comparison of the TEM images of the 72 hrs ball milled powder (Fig. 5.11(c)) and SiGe-72 sample (Fig. 5.11(c)) suggest that the dislocation formed during the ball milling process forms a bunch after hot pressing. The formation of dislocation bunch in the SiGe-72 sample could be due to the movement of dislocation due to application of high temperature and deformation of material (due to application of load) and their subsequent pinning at some defect sites. From Fig. 5.11(d) it can be seen that for SiGe-96 sample only few defects (sub boundaries) can be seen.

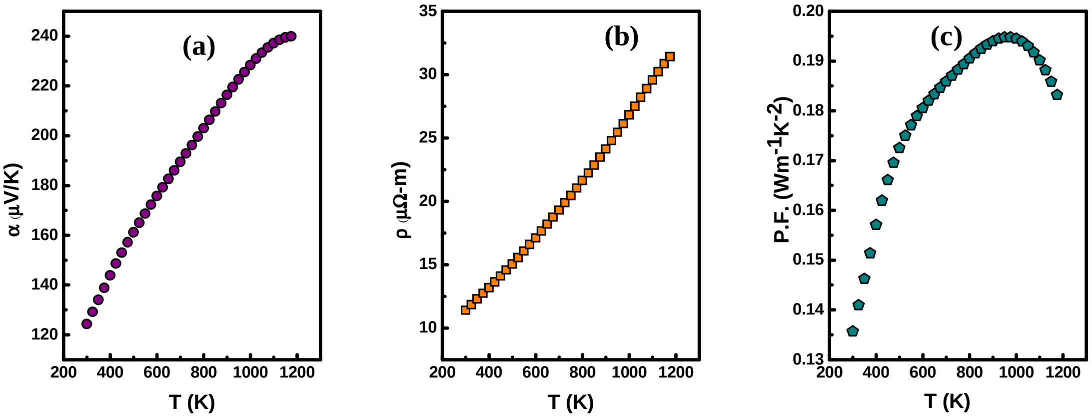

Fig. 5.12. Temperature dependence of (a) α, (b) ρ and (c) power factor of melt-quenched p-type SiGe alloy.

5.4 Thermoelectric properties of melt-quench SiGe alloys

5.4.1 Temperature dependence of *ZT* for p-type SiGe alloy

The α and ρ were measured for p-type SiGe samples in the temperature range of 300-1200 K. The obtained results along with calculated temperature dependence of power factor (PF= α^2/ρ) are shown in Fig.5.12. The observations drawn from these figures are:

(i) The room temperature values of α is 124.3 μV/K, which linearly increased to ~ 240 μV/K at 1175 K. These values are higher to those of the mechanically alloyed and hot pressed samples. The positive sign of the α indicates that synthesized alloy is p-type. However, above 1200 K, the α shows an upturn which is attributed to the thermal excitation of the minority carriers across the gap. Thus a negative contribution arises from the conduction band carriers and the net α is reduced. This is also regarded as the onset of bipolar diffusion as mentioned in chapter 1.

(ii) The ρ value at 300 K is ~11.4 μΩ-m which increases to ~31.4 μΩ-m at 1200K. The increase in the ρ value is expected as the B-doping in the SiGe alloy makes it a degenerate semiconductor.

(iii) The power factor shows a maximum value of 0.195 WmK^{-2}at ~975 K.

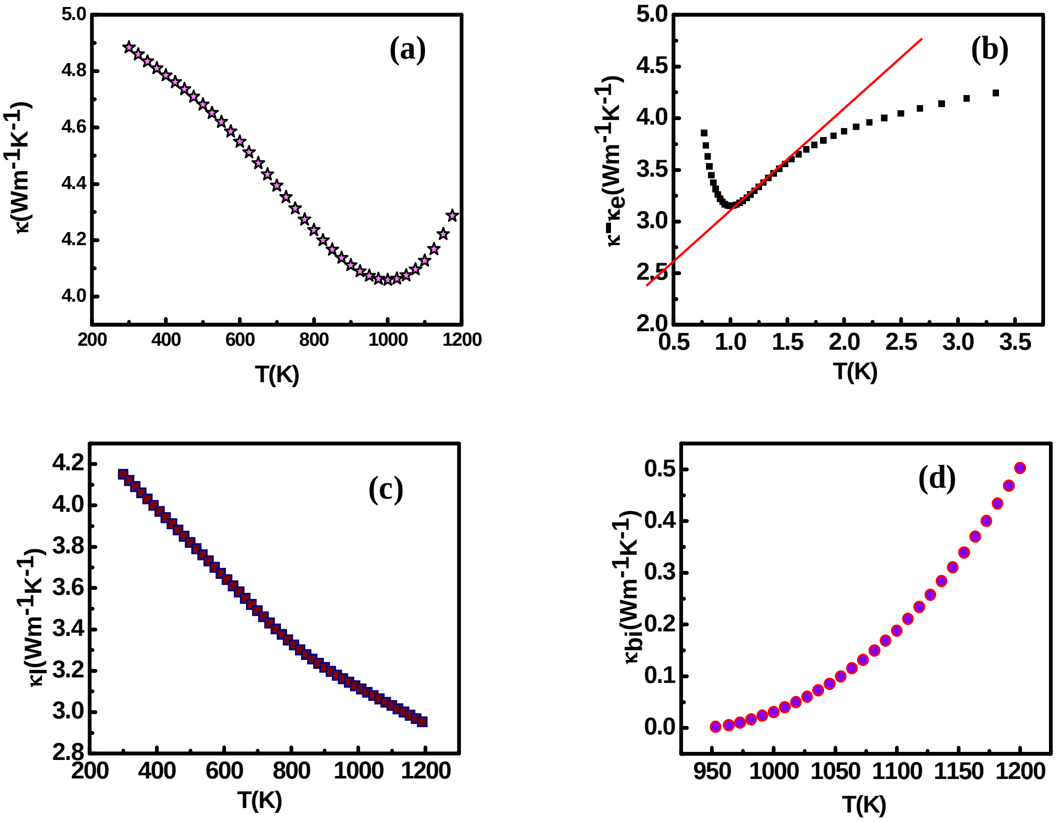

Fig. 5.13. Temperature dependence of (a) κ (b) κ-κ_e (c) κ_l and (d) κ_{bi} of melt-quench p-type SiGe alloy.

Fig. 5.13 shows the temperature dependence of κ, κ - κ_e, κ_l and κ_{bi}. The κ shows an initial decrease with temperature upto 1000 K, which at higher temperatures take an upturn. The initial decrease in κ_{total} is expected as it is case of degenerate semiconductors where the phonon scattering increases with temperature. The increase in κ for temperatures >1000 K is attributed to the ambipolar diffusion of electrons and holes i.e. bipolar contribution (as discussed in Section 1.4.2. In order to determine the contribution of κ_{bi} in κ, κ_{bi} was estimated at high temperatures similar to that discussed in sec. 3.3.1. Thus in this temperature range, κ- κ_e equals to $\kappa_{l,}$ shown in Fig. 5.13 (c). However, for temperatures >1000 K, κ- κ_e deviates from the linearity and show an upturn due to the bipolar conduction. Thus, the contribution of κ_{bi} is estimated by subtracting the extrapolated value of κ_l (i.e. the fitted line) from κ- κ_e, which is plotted in Fig 5.13(d), shows the κ_{bi} vs T plot at high T. It is evident that at high temperatures, the contributions from κ_{bi} are predominant, which needs to be suppressed effectively as it degrades κ in addition to α.

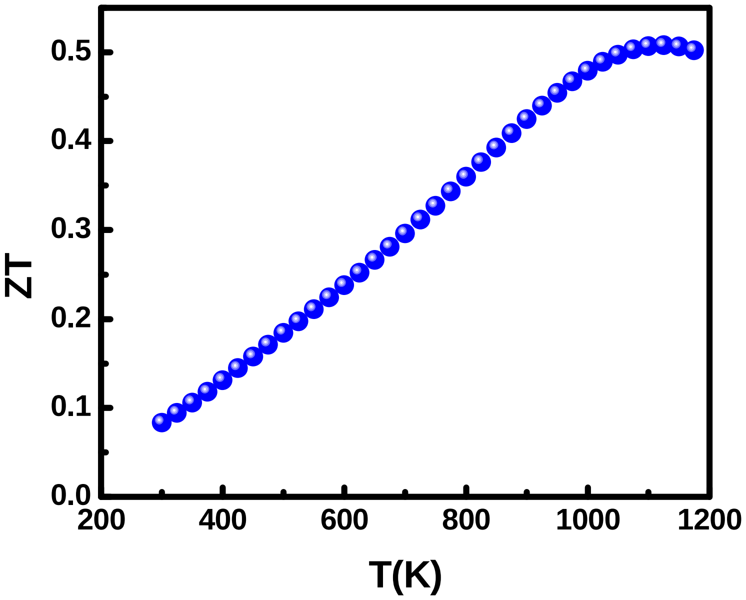

Fig.5.14 Temperature dependence of ZT of melt quench p-type SiGe alloy.

Based on the experimentally measured α, ρ and κ the temperature dependence of *ZT* is calculated and is shown in Fig. 5.14. It is seen that *ZT* attains a highest value of ~ 0.5 in the temperature range of 1100 K, which is the operating temperature range of the SiGe based TEG . The data matches close to the RTG data given in the literature [178].

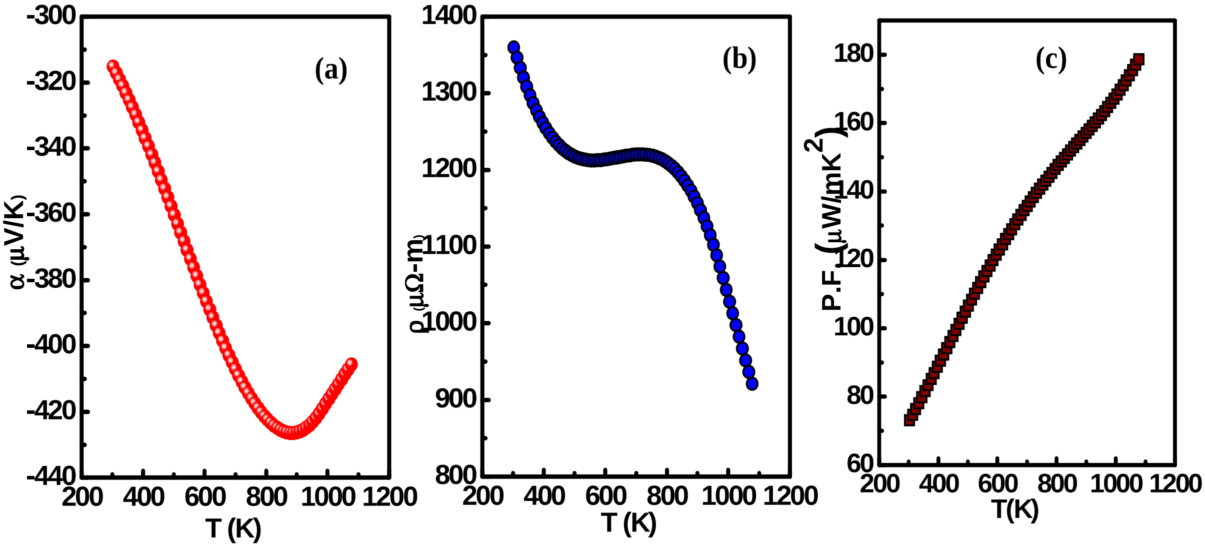

Fig. 5.15. Temperature dependence of (a) Seebeck coefficient (b) resistivity and (c) power factor of melt quench n-type SiGe alloy.

5.4.2 Temperature dependence of *ZT* for n-type SiGe alloy

The temperature dependences of α and ρ were measured for n-type SiGe samples in the temperature range of 300-1200 K, shown in Fig. 5.15 (a) and (b). The obtained results along with calculated temperature dependence of power factor (PF= α^2/ρ) are shown in Fig.5.15 (c). The major inference drawn from these figures are:

(i) The room temperature values of α is -315 μV/K, which linearly increased to ~ -430 μV/K at 850 K. These values are higher to those of the mechanically alloyed and hot pressed samples. The negative sign of the α indicates that synthesized alloy is n-type.

However, above 800 K, the α shows an upturn which is attributed to the thermal excitation of the carrier across the gap. Thus a negative contribution arises from the conduction band carriers and the net α is reduced. This is also regarded as the onset of bipolar conduction as mentioned in chapter 1.

(ii) The ρ value at 300 K is ~1400 μΩ-m which decrease to ~1200 μΩ-m at 600K, remains constant till 800 K and again decreases to 900 μΩ-m at 1100 K. The ρ value was quite high and shows insulating type behavior. Actually the melt quench method struggles with achieving the optimal carrier concentration in n-type phosphorus doped materials. Since synthesis of alloys materials is carried at 1723 K, the phosphorus is literally lost through vaporization. This process can easily be seen occurring by watching the dynamic vacuum of the melt quench system, which begins to spike around the vaporization temperature of red phosphorus 883 K. Thus, it is no surprise that the final phosphorus dopant levels are very different from the initial nominal compositions in the melt quench process i.e. the material is deficient of the dopant and thus there occurs decrease in the carrier concentration. Moreover, the wide gap between the solidus and liquidus lines in Si-Ge phase diagram leads to the formation of inhomogeneous alloy as shown in Fig. 5.3. The stagnant part in the ρ vs T plot can arise due to inhomogeneity in the bulk SiGe alloy and/or inhomogeneous distribution of the dopant phosphorus.

(iii) No appreciable hysteresis has been measured on repeated thermal cycling, indicating that the alloy does not degrade upon heating to high temperatures. This has an implication that the synthesized n-type alloy is suitable for device applications whereby devices are subjected to a repeated thermal cycling.

(iv) The power factor shows a maximum value of 180 μWmK^{-2}at ~1100 K. The low P.F. is due to the high ρ value.

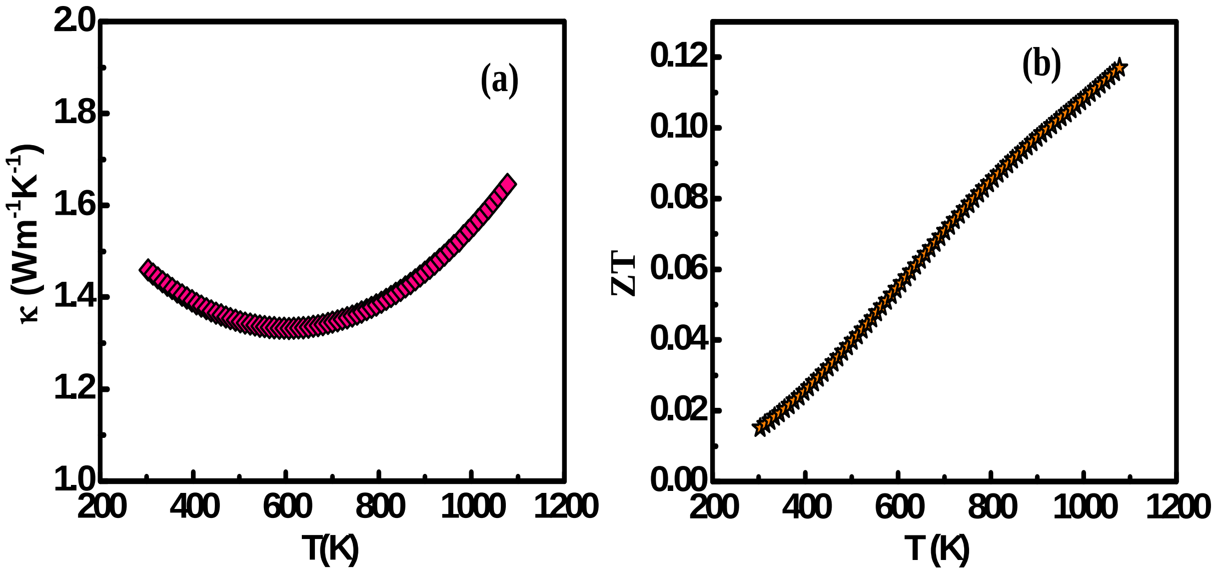

Fig.5.16. Temperature dependence of (a) thermal conductivity and (b) *ZT* of melt quench n-type SiGe alloy.

Fig. 5.16 shows the temperature dependence of κ. The κ shows an initial decrease with temperature upto 700 K, which at higher temperatures take an upturn. The initial decrease in κ_{total} is expected because in case of degenerate semiconductors the phonon scattering increases with temperature. The increase in κ for temperatures >700 K is attributed to the thermal excitation across the band gap (as discussed in Section 1.4.2). In order to gain an insight into the contribution of κ_{bi} at high temperatures, it values was estimated. At room temperature, the κ_e was estimated to be 0.00468 W/m-K. The low κ_e can be due to the high resistivity of the material. So it can be said that, the major component of κ was κ_l i.e. heat conduction was through phonons. Although, the effect of bipolar conduction is seen, its value is negligible compared to κ_l and thus not plotted. Fig. 5.16(b) shows the *ZT* as a function of T. At 1100 K, the *ZT* shows a value of 0.12, which is too low.

5.5 Thermoelectric properties of mechanically alloyed n-type SiGe alloys

5.5.1 Temperature dependence of *ZT*

Fig. 5.17 (a-f) shows the temperature dependence of thermoelectric properties of the hot pressed n-type SiGe, which were prepared from the nanopowder ball milled for different duration. In general spark plasma sintering (SPS) technique is used for making bulk nanostructures samples [143]. In SPS process to arrest the grain growth, pulse current with very short time scale is passed through the green pellet of nanopowders and it momentarily generates a plasma (with high localized temperature) at the high resistance regions of grain boundaries. However in our work, simple vacuum hot pressing of ball milled powders was carried out with rapid heating and cooling rates for preserving nanostructure. For comparison purpose, thermoelectric properties of SiGe alloys reported by other groups (143,178,179) are also shown in Fig. 5.17 (a-f).

Fig.5.17 (a) shows the temperature dependence of ρ of ball-milled and hotpressed samples and ball-milled and spark plasma sintered (SPS) SiGe alloy. The ρ exhibited by the hot-pressed samples were higher than the SPS samples. Actually this trend should have been opposite as the grain growth takes place during the hot pressing. A high ρ in the hot pressed samples can be due to the loss of dopant as well as the bunching of the defects created during the ball milling. The presence of defects reduces the charge mobility, which in turn lead to an increase in ρ.

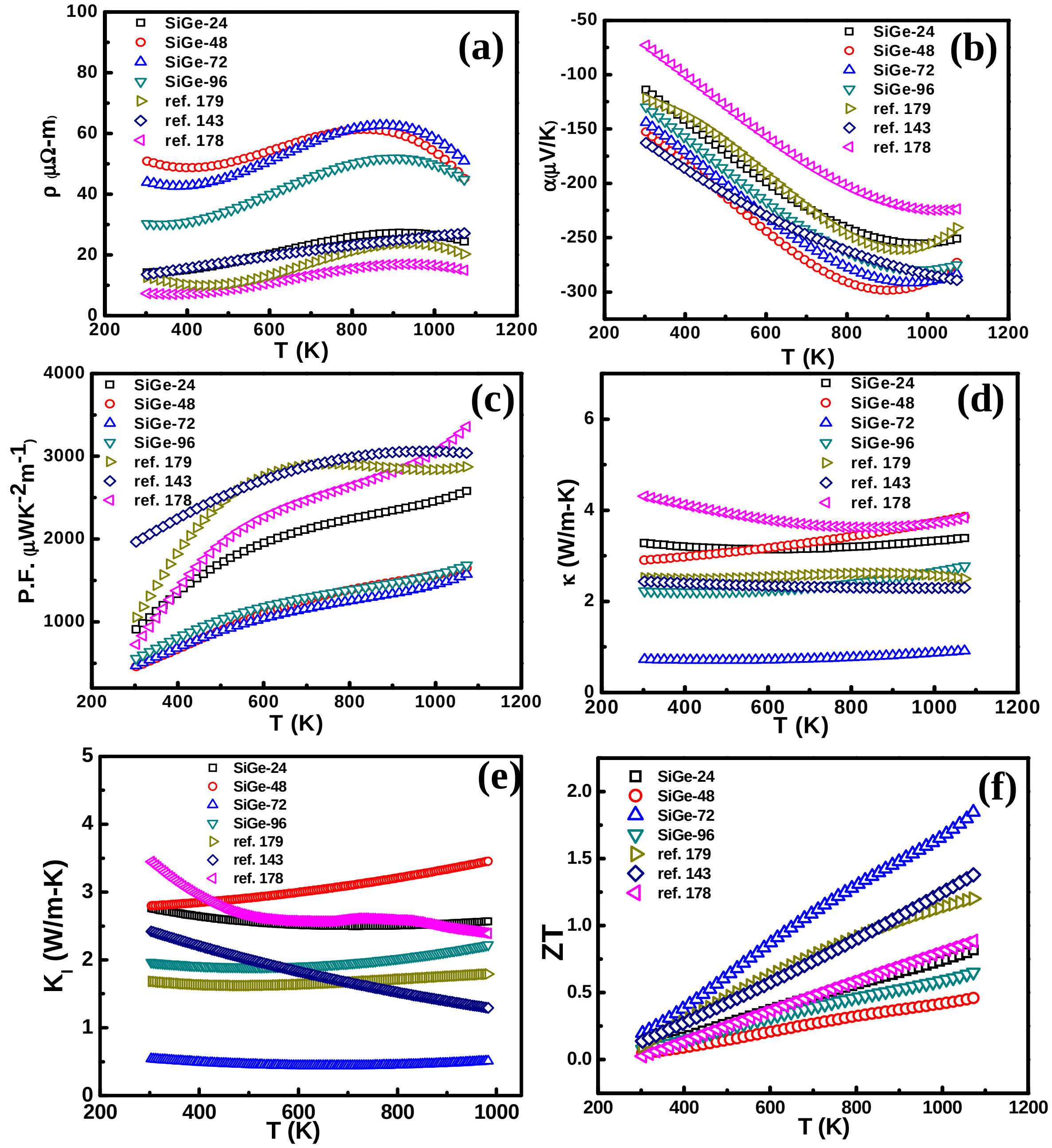

Fig.5.17. Temperature dependence of the thermoelectric properties of hot pressed Si-Ge alloy (a) electrical resistivity (b) Seebeck coefficient (c) power factor and (d) total thermal conductivity. (e) Lattice thermal conductivity (f) figure of merit. For comparison purpose the results of other groups are also plotted in the same figure.

For all samples ρ increases with temperature up to 800 K, which is a characteristic feature of the highly degenerate semiconductors [180]. Above 800 K, for all samples a decrease in ρ is attributed to the onset of intrinsic conduction due to thermal excitation of charge carriers across the band gap. In order to see, the dependence of the ρ on the ball milling time, we have estimated the free carrier concentration (n) of synthesized sample at room temperature using Hall measurement. At room temperature all samples exhibits nearly same value $n \sim 1.03\times10^{20}$ cm^{-3}, which suggest that synthesized material is heavily doped and difference in ρ of the samples is purely due to difference in their charge carrier mobility (μ).

In general μ is a reflection of crystalline structure of the semiconductors. From the room temperature value of n and ρ, we have derived the μ using relation $\rho = {}^{1}\!/\!_{ne\mu}$. Typical room temperature value of μ for SiGe-24, SiGe-48, SiGe-72 and SiGe-96 samples were respectively found to be 43, 12, 14 and 20 cm^2/V-s. The initially lowering of μ from 43 cm^2/V-s to 12-14 cm^2/V-s can be correlated with creation of more and more number of defects within the material due to increasing ball milling time up to 72 hrs. With further ball milling of the SiGe alloys the defects created earlier can get annihilated, hence μ starts increasing again for SiGe-96 sample. These results are in agreement with the microstructure of the prepared samples as discussed in the later section.

The temperature dependence of the α is shown in Fig.5.17 (b), the negative sign of α suggests electrons as majority charge carriers (i.e. n-type nature) in the material. In the temperature dependence of α, the effect of onset of intrinsic electrical conduction is also seen above 800 K as a decrease in α. SiGe alloys have a finite band gap and above 800 K, the thermal excitation of carriers across the gap is possible. As a consequence, a negative contribution to α arises from the valence band carriers and the net α is reduced [181,182].

From the temperature dependence of α or ρ, one can also estimate the band gap (E_g) of material using eqn. 3.1,[135]. Using this equation the E_g values was found as 0.78, 0.88, 0.99 and 0.93 eV respectively for the SiGe-24, SiGe-48, SiGe-72 and SiGe-96 samples. The E_g values obtained from the temperature dependence of α or ρ are in good agreement with the E_g estimated from the diffused reflectance data.

The temperature dependent power factor (α^2/ρ) of the samples is plotted in Fig. 5.17(c), which shows that among all the samples, highest (~ 2586 $\mu WK^{-2}m^{-1}$) and lowest power factor (~ 1570 $\mu WK^{-2}m^{-1}$) are respectively observed for the SiGe-24 and SiGe-72 samples in the entire temperature range. This result suggests that ball milling time has a significant effect on the electronic transport properties of the hot pressed SiGe samples. From Fig.5.17 (c), it may be seen that power factor of the samples synthesized in the present work is lower compared to the earlier reported work, possibly due to the difference in doping and internal structure of the samples.

Temperature dependence of k is plotted in Fig.5.17(d), it reveals that SiGe-72 sample exhibit lowest k ~ 0.93 W/m-K. More important, k of SiGe-72 sample is much lower than that reported by other groups. From the k, electronic contribution (k_e) of the k can be estimated by Wiedemann-Franz law using the Lorentz number as 2.14×10^{-8} $W\Omega K^{-2}$. By subtracting k_e from k, we obtain the lattice contribution (k_l) to the total k. Fig. 5.17 (e) shows the temperature dependence of estimated k_l , which reveals that SiGe-72 sample exhibit the lowest k_l ~ 0.5 W/m-K at 1073 K along with a very weak dependence on temperature (signature of glassy behaviour).

A brief summary of the thermoelectric parameters of the hot pressed SiGe alloys at 1073 K is given in Table-5.1.

Table 5.1 : Summary of thermoelectric properties of SiGe alloys at 1073 K.

Sample	α (μV/K)	ρ (μΩ-m)	κ (W/m-K)	*P.F.* (μW/ m K^2)	*ZT*	Ref.
SiGe- 24	250	24.1	3.4	2587	0.81	This work
SiGe-48	274	50.9	3.8	1670	0.45	This work
SiGe-72	284	45.3	0.93	1575	1.84	This work
SiGe-96	274	45.2	2.8	1693	0.65	This work
SiGe	241	20.4	2.5	2884	1.2	180
SiGe	288	27.2	2.3	3032	1.38	143
RTG	223	14.7	3.8	3373	0.89	179

The obtained results suggest that thermoelectric properties of synthesized sample depend on ball milling time. It is interesting to note that although the power factor is lowest (~ 1575 μW/K^{2}m) for the SiGe-72 sample among all samples, but very low value of thermal conductivity ~ 0.93 W/m-K results in highest *ZT* ~ 1.84 ever reported for SiGe alloys as shown in Fig. 5.17 (f). The obtained *ZT* value is about 34% improvement over the best reported value so far reported for n-type SiGe alloys [179].

5.5.2 Sources of error associated in *ZT* estimation

Since the most common source of error in the estimation of *ZT* could be the errors in the estimation of k (particularly due to errors in C_p measurement). However to confirm our results, significant attention has been paid for the estimation of k of SiGe-72 sample and hence C_p was estimated in three different ways: comparative method using laser flash apparatus, differential scanning calorimeter (DSC), and from Dulong-Petit law. The results of

C_p measurement are shown in Fig. 5.18 (a), it can be seen that the C_p values obtained from DSC are 18% higher as compared to that obtained from comparative method.

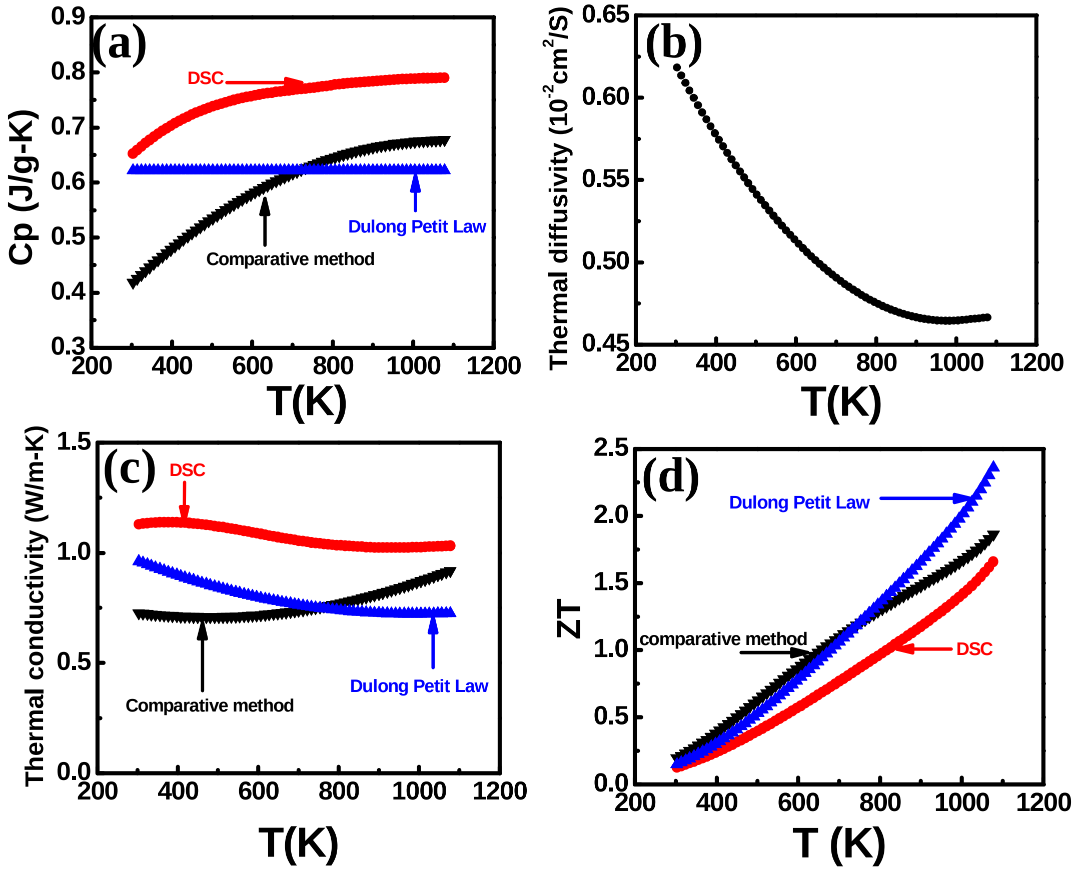

Fig.5.18. Temperature dependence of the thermoelectric properties of hot pressed SiGe-72 alloys sample (a) C_p estimated by different methods (b) Thermal diffusivity (c) Thermal conductivity and (d) Figure of merit (*ZT*).

Fig. 5.18 (c) and Fig. 5.18(d) respectively shows the temperature dependence of thermal conductivity and *ZT* estimated from C_p data obtained in different ways. It can be seen that near room temperature the *ZT* obtained from DSC and comparative method are nearly close, while at 1073 K the comparative method gives 8 % higher value.

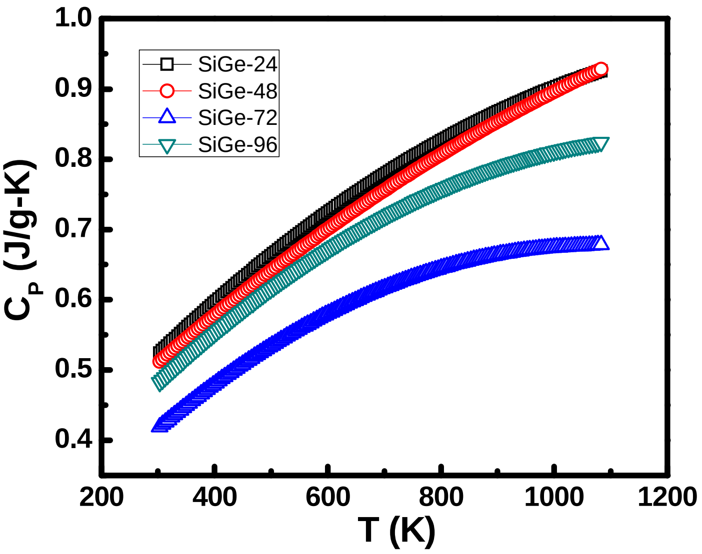

Fig.5.19. Temperature dependent specific heat (Cp) of hot pressed SiGe alloy samples.

From Fig. 5.19, it is interesting to note that although all samples have identical chemical composition but there Cp differs significantly over the entire temperature range. In order to explain why Cp systemically lowers down for the hot pressed samples prepared from the powder obtained at higher ball milling time, we propose the following: The specific heat of a material is basically the ability to absorb the thermal energy. On a microscopic scale each materials absorbs thermal energy according to the few degrees of freedom (such as translation, rotation vibration etc) available to it and it contributes to the specific heat. The specific heat has two contribution i.e. lattice and electronic. In the non-metallic solids, at high temperature the lattice contribution for specific heat dominates. Due to the presence of defects in the lattice (microstructure) of the material, some of these degrees of freedom are not available for storing the thermal energy; in such cases the specific heat will be lower as compared to ordered material with identical composition.

5.5.3 Reason for High *ZT* of SiGe-72 from microstructural point of view

Now, we shall discuss the role of these defect structures in the scattering of phonons. The mechanism of phonon scattering depends on their wavelength. In any material, phonons have a spectrum of wavelengths and mean free path and these contribute to the total thermal conductivity. When the dimensions of the defects / inclusions are comparable to the mean free path, this phonon gets scattered. In alloys, mostly there is a strong scattering of short wavelength (~ 1- 10 nm) phonons due to mass-mismatch of individual constituent atoms or due to the local bond strain induced by defects. Therefore alloying was a conventional approach in the beginning to achieve the low thermal conductivity. The scattering of the mid wavelength (~ 10- 100 nm) phonons is achieved through the nanostructuring [27,28,70]. The interface between nanoscale feature and matrix plays an important role in such scattering. The scattering of the long wavelength (>100 nm) phonons is achieved by the meso-scale grain boundaries present in the material. In view a combination of inter-atomic scale features (alloying) and larger features (nano-scale, meso-scale grain boundaries and dislocations) can effectively scatter phonons over a large range from small to long wavelengths. Hence microstructure investigation of SiGe alloys suggest that significant reduction of k in the hot pressed SiGe-72 sample is mainly due to the scattering of the spectrum of phonons by atomic level defects (due to mass difference of Si, Ge and P), amorphous / crystalline nano-scale features, grain boundaries between the different bulk and nanocrystallites and from large amount of dislocation containing regions. It may be noted that apart from dislocation other defects/ nanoscale features are present in all other samples prepared from ball milled powder therefore it can be concluded that dislocation plays a very important role in scattering of phonons. Fig.5.20 shows the bar chart representation of the summary of *ZT* research in SiGe alloy till date and schematic showing mechanism of wide spectrum of phonon scattering.

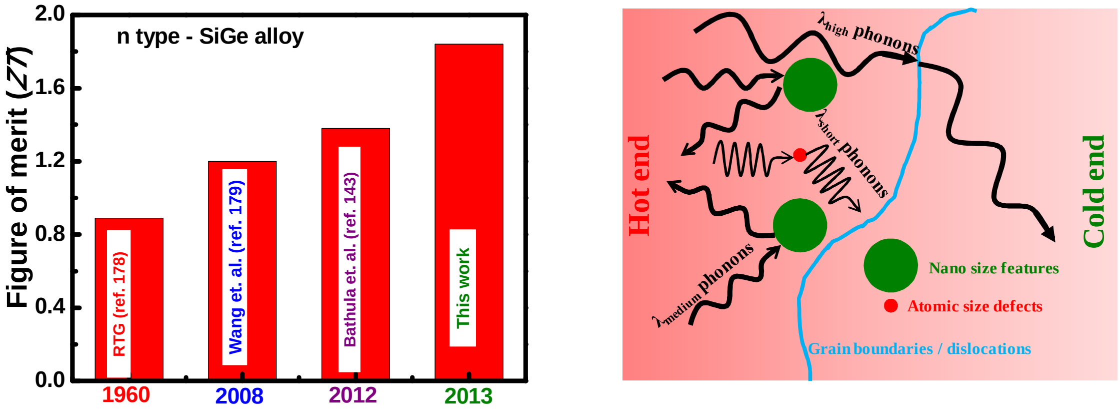

Fig. 5.20 (a) Bar chart showing the *ZT* research in SiGe alloy till date and (b) schematic representing mechanism of wide spectrum of phonon scattering.

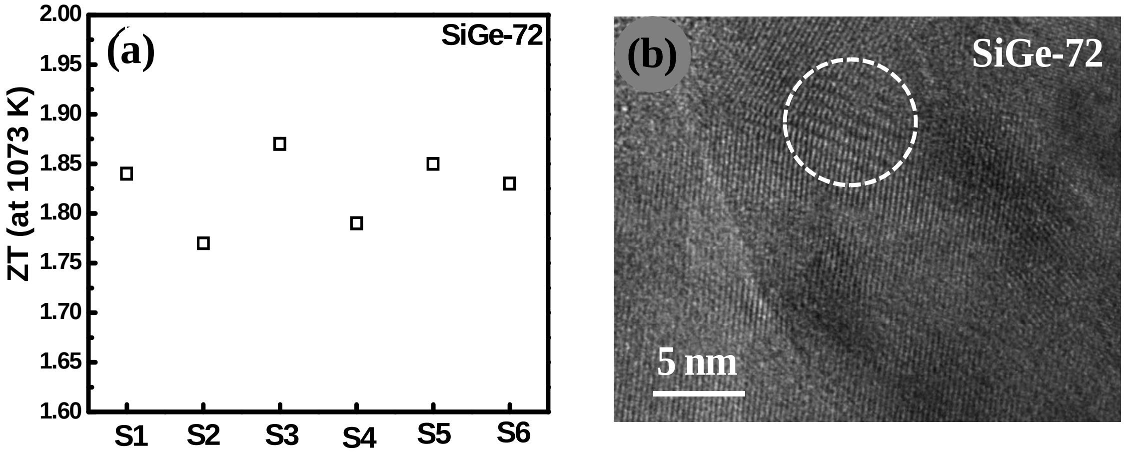

Fig.5.21. (a) TEM image of the SiGe-72 sample after annealing at 1000°C for 4 days. The region encircled with white dotted line shows the presence of dislocations in the sample. (b) *ZT* values (at maximum temperature ~ 1073 K) for the six numbers (S1-S6) of SiGe-72 samples prepared under same experimental condition.

5.5.4 Reproducibility and thermal stability

From the application point of view the reproducibility and thermal stability of such nanostructured SiGe alloys is of great concern. For testing the reporoducibity six SiGe-72 samples were prepared under similar condition and typical *ZT* values of all samples shows a deviation of ± 5% around 1.8 (Fig. 5.21(a). We have also carried a thermal stability test by annealing SiGe-72 samples in a furnace for 4 days at 1000°C in air and we did not notice any significant degradation of the thermoelectric properties. In the TEM images of the annealed sample dislocations bunch can also be seen (Fig. 5.21(b).

5.6 Fabrication of unicouple SiGe based thermoelectric generators

In the previous sections, we have demonstrated that SiGe alloys can be synthesized using both melt-quench as well as mechanical alloying. The *ZT* of n-type SiGe synthesized using mechanical alloying was as high as 1.8. However, p-type SiGe with matching ZT could not be synthesized using mechanical alloying, for which efforts are underway. Therefore, the thermoelectric generators could not be fabricated using materials synthesized using mechanically alloyed materials. On the other hand, the *ZT* values melt-quenched n- and p-type SiGe alloys were in the range of 0.1-0.5 (at 1073K), which is largely due to the phase segregations and grain growth. The advantage of this method is that both n- and p- type $Si_{80}Ge_{20}$ can be prepared in large quantities for device fabrication. Thus we have fabricated prototype generators using Mo as interconnect. Fig. 5.22 (a) shows the schematic diagram for the fabrication of single p-n-couple Si-Ge based devices. Here n- and p-type thermolegs having carbon layer at the ends were placed in asbestos housing and joined using molybdenum (Mo) strip and Ag-disc as brazing material. The carbon layer serves two purpose: (i) it is effective in absorbing thermal stress caused by a mismatch of thermal expansion between Mo, Ag-disc and Si-Ge alloy (ii) it avoids the direct reaction between Ag and Si-Ge thermoelements, which otherwise leads to very high contact resistance [10]. The entire assembly was vacuum hot pressed (vacuum ~ 2×10^{-5} Torr) at optimized bonding temperature of 1323 K. The photograph of fabricated generator is shown in Fig. 5.22(b).

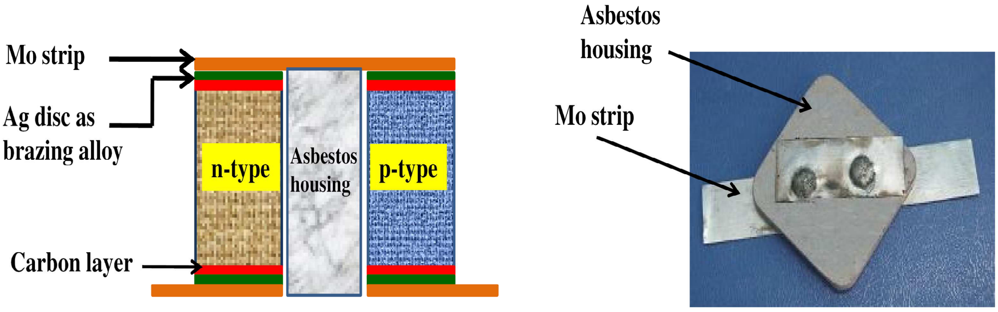

Fig.5.22. (a) schematic and (b) photograph of the unicouple SiGe based TEG.

The four probe resistance of the geneartor was found to be 58 mΩ. In order to characterize the generators, they were placed in a home-made testing set up having a spring-loaded hot surface and water-cooled copper base. The temperature of hot surface and water-cooled surface was determined by thermocouple attached to them by thermally conducting cement. The thermoelectric generator was sandwiched between hot and cold surface. The testing setup along with the device was kept in a vacuum chamber evacuated to 4×10^{-3} mbar of vacuum. After achieving the vacuum, argon gas was introduced in the chamber through the needle valve maintaining a dynamic argon pressure of 500 mbar and heating of the device was started. Characteristics for a typical one leg generator as function of hot side temperature are shown in Fig. 5.23.

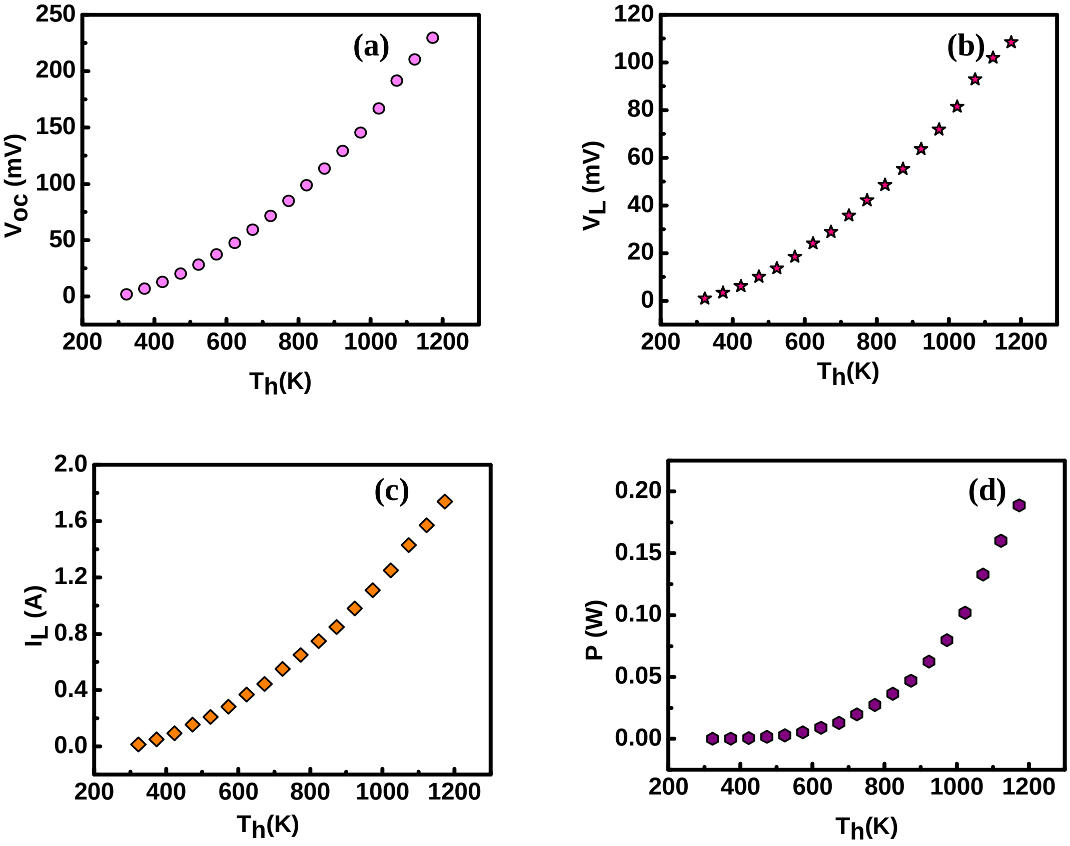

Fig. 5.23. Characteristics of typical single p-n couple SiGe based TEG as a function of T (a)open circuit voltage (V_{OC}) (b) load voltage (V_L) (c) load current (I_L)and (d) power output (P).

For hot end temperature of 1173 K and temperature difference of 873 K, the generator shows an open circuit voltage(V_{OC}) of 230 mV and maximum output power of ~ 0.2 W (with load voltage of 120 mV and current of 1.74 A). Heat flow for this generator is found to be 16 W, hence the working efficiency of the thermoelectric generator is ~ 1.2%. Contributions to R_m were determined by measurement of four probe resistivity of each material and for a one leg generator was found to be, $R_{n\text{-}SiGe}$ = 7 mΩ, $R_{p\text{-}SiGe}$ = 11 mΩ, R_{Mo} = 12 mΩ, R_{carbon} = 0.1 mΩ, and R_{Ag} = 0.0006 mΩ yielding a total materials resistance of R_m = 30 mΩ. The difference between device resistance (58 mΩ) and the material resistance R_m

yields specific contact resistance for each element to be 6.5 mΩ·cm^2 (3.25 mΩ·cm^2 for each contact). For Si-Ge based single leg generator, the contribution of contact resistance to total device resistance was found to be 50%, hence these thermoelectric generators shows low efficiency (~ 1.2%). Further efforts are being made to reduce the contact resistance.

5.7 Conclusions

In conclusion, we have demonstrated synthesis of both n- and p-type SiGe alloy by melt-quench method. Synthesis of n-type SiGe is a bit tricky as P is vaporizing and less stable, and therefore, a trick, of keeping the P on the copper mould before SiGe melt is quenched onto it, was employed. However, synthesis of p–type SiGe is comparatively easier. The temperature dependences of α, ρ, κ and ZT were measured for both the n-and p-type SiGe alloy. The ZT of n-type and p-type SiGe alloys were found to be 0.12 and 0.5, respectively. Lower ZT for n-type SiGe alloys is due to loss of P. The advantage of this method is that both n- and p- type $Si_{80}Ge_{20}$ can be prepared in large quantities for device fabrication. A prototype unicouple SiGe thermoelectric generator was fabricated using the n- and p-type SiGe alloy with Mo as interconnect. The generator, for hot end temperature of 1173 K and temperature difference of 873 K, yielded a maximum output power of 0.2 W with working efficiency of 1.2%. This efficiency is quite low, and in order to improve the efficiency it is essential to have the materials of high ZT and the methodology of obtaining the low contact resistances.

The n-type SiGe alloy was also synthesized using ball-milling method. A highest reported ZT ~ 1.84 at 1073 K in hot pressed nanostructured bulk SiGe alloys was demonstrated. Although the power factor (α^2/ρ) of our SiGe alloy is lower compared to the earlier reported values but large improvement in *ZT* is the result of a significantly low thermal conductivity *k* ~ 0.93 W/m-K at 1073 K in these samples. Very low value of thermal conductivity in these samples is attributed to the scattering of the spectrum of phonons by dislocations, nanoscale amorphous / crystalline features and grain boundaries introduced in the bulk during the process of synthesis. Synthesis of p-type SiGe alloy with matching *ZT* using mechanical alloying as well as fabrication of the thermoelectric generators with low contact resistances is underway.

Chapter 6

Summary and Conclusions

The motivation of this dissertation was to develop indigenous technology for thermoelectric power generators using conventional heavily doped semiconductor alloys, such as, PbTe, TAGS and SiGe alloys. These generators are needed by Indian Space Research Organization for their space missions. In addition, thermoelectric properties of new materials were investigated from the view points of increasing their figure-of-merit. The materials investigated in this thesis are: n-type PbTe and p-type TAGS-85; n-type SiGe and and p- type SiGe, p-type $TiSe_2$ and n-type Cu_xTiSe_2, $PbTe_{1-x}Se_x$, $CuCrSe_2$ and $CuCrSe_2/AgCrSe_2$. Thermoelectric power generators require n-type and p-type themolegs with matching *ZT*, which are connected electrically in series and thermally in parallel. Apart from high *ZT*, fabrication of efficient thermoelectric generators requires electrical contacts having very low resistance at various interfaces, as well as maximum heat transfer though device while minimizing the thermal shunt path.

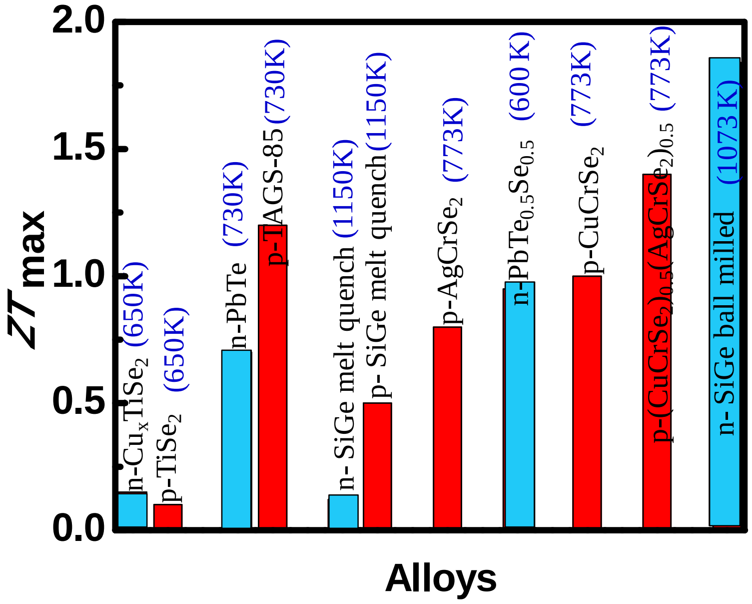

Fig. 6.1. ZT_{max} of various materials studied in this thesis.

In this thesis work, thermoelectric materials were synthesized using melt-and-rock (e.g. PbTe and TAGS alloys), melt growth (all selenides), melt-and-quench (n- and p-type SiGe) and mechanical alloying (n-type SiGe) methods. The synthesized materials have been characterized for structure and morphology. The carrier concentrations in all the materials were in the range of 10^{19}-10^{21} /cm^3. The temperature dependence of thermopower, electric resistivity and thermal conductivity were measured to estimate the value of ZT. The major results on these materials have been presented at the end of the corresponding Chapters in which they are described in. The ZT_{max} of various thermoelectric materials investigated in the present thesis work are summarized in Fig. 6.1. Based on the matching $ZT_{\max}$, thermoelectric generators from following pairs have been fabricated:

(i) **Generators based on n-type PbTe and p-type TAGS alloys having nearly matching $\mathbf{ZT_{max}}$ at 730 K.** Low contact resistance thermolegs were fabricated using PbTe andTAGS-85 alloys with metallic shoes based on the concept of graded layers. In PbTe thermoleg, the sequence of the different layers was Ag disc/ Fe/PbTe+Fe/PbTe/PbTe+Fe/Fe/Ag disc. This sequence was selected based on the fact that Ag-Ag bonding can be easily made by diffusion bonding process. Since at high temperature Ag diffuses into PbTe, degradation of thermoelectric properties of PbTe takes place. Therefore, an interfacial Fe layer was introduced between Ag and PbTe. This is because Fe is immiscible with Ag at equilibrium i.e. they do not inter-diffuse. However, the negative aspect is that the CTE of PbTe is 23×10^{-6} K^{-1}and Fe is 12×10^{-6} K^{-1} at 25ºC. Therefore, hot-pressing of Ag/Fe/PbTe/Fe/Ag thermolegs leads to cracking at the Fe/PbTe interface and the thermolegs are easily broken. In order to solve this problem, a graded layer of a homogeneous material consisting of 50% Fe

+50% PbTe was inserted between Fe and PbTe, since the mixture has the intermediate value of CTE. Therefore, it solves the issue of CTE mismatch of Ag, Fe and PbTe. On the other hand, for TAGS-85 based thermolegs, a buffer layer of SnTe was used. Despite of having good match of CTE of SnTe and TAGS-85, the added advantage of SnTe layer is that it is also a p-type material which inhibits the diffusion of Ag into TAGS-85, which provide low contact resistance and good aging characteristics.

We have demonstrate 2p-n, 6p-n, 8p-n legs TEG. For a typical 2 p-n leg device, the average specific contact resistance was found to be $\leq 10\mu\Omega\text{-cm}^2$. For a hot end temperature of 500ºC and a temperature difference of 410ºC, two legs devices exhibited typical output power of ∼1.2W (at current of 17 A) with a working efficiency of 6%. The devices have been continuously operated for more than 12 months without any degradation.

(ii) **Generators based on p-type $TiSe_2$ and n-type $Cu_{0.11}TiSe_2$ having matching ZT_{max} at 650 K.** The ZT_{max} values for these materials were found to be 0.1 and 0.15, respectively. The efficiency of the generators was found to 0.1%, which is quite low. The reasons for low efficiency were found to be low *ZT* and high contact resistances. Despite of low efficiency, these generators are encouraging as they have selenides, which are alternate to very expensive tellurides.

(iii) **Generators based on n-type SiGe and p-type SiGe, both grown by melt-quench methods.** The ZT_{max} (at 1150 K) for n-type SiGe and p-type SiGe alloys was found to be respectively, ~0.12 and 0.5, which has been attributed to loss of dopants, phase segregation and grain growth. The generators yielded an power output of 0.2 W and an efficiency of 1.2% for 1 p-n leg device. The high contact resistance (3.25 mΩ-cm^2) is found one of the major factors for low efficiency.

In addition, as summarized in Fig. 6.1, various materials (either n-type or p-type) with record ZT_{max} has been obtained. These include:

(i) **n-type $PbTe_{0.5}Se_{0.5}$ shows *ZT* of 0.95 at 600 K**, which is attributed to the strong disorder in the crystal lattice due to atomic mass fluctuation. This disorder leads to increase in the point defects which scatter the majority charge carriers independent of energy, so the variation of the DOS at E increases, leading to a high α value. In addition, phonon scattering by defect states leads to a dramatic reduction of the κ. The increase in α and the reduction in the κ outweighs the increase in the ρ and thereby an increase in ZT is obtained.

(ii) **p-type $AgCrSe_2$ and $CuCrSe_2$ show *ZT* of 0.85 and 1 at 773 K**. These selenides have layered structure and are known to exhibit superionic conductor exhibiting the concept of phonon-liquid electron crystal. The strong disorders due to the presence Cu/Ag ions yield very low κ and high σ. In addition, The presence of various nanoscale amorphous regions apart from micro-scale features contribute to the lowering of κ_l.

(iii) **p-type $(AgCrSe_2)_{0.5}(CuCrSe_2)_{0.5}$ nanocomposites show *ZT* of 1.43 at 773 K.** In addition to the beneficial features of individual $AgCrSe_2$ and $CuCrSe_2$ for enhancement of *ZT*, the nanocomposites exhibits presence of natural all scale hierarchical architecture that reduces κ to extremely low values. The all scale hierarchical architecture consists of: (i) atomic scale disorder produced by Ag/Cu ions that scatter low mean free path phonons, (ii) nanoscale features and high angle grain boundaries between the nanosized grains of $CuCrSe_2$ and $AgCrSe_2$ that scatters mid wavelength phonons; and (iii) mesoscale $CuCrSe_2$ precipitates that scatter the higher mean free path phonons. These nanocomposites were found to be stable for prolonged periods.

(iv) **Mechanically alloyed n-type $Si_{80}Ge_{20}$ show record high *ZT* of 1.84 at 1073 K.** A large improvement in *ZT* of the mechanically alloyed n-type SiGe is a result of significantly low thermal conductivity k ~ 0.93 W/m-K (at 1073 K), which is attributed to the scattering of the spectrum of phonons by dislocations, nanoscale amorphous / crystalline features and grain boundaries introduced in the bulk during the process of synthesis.

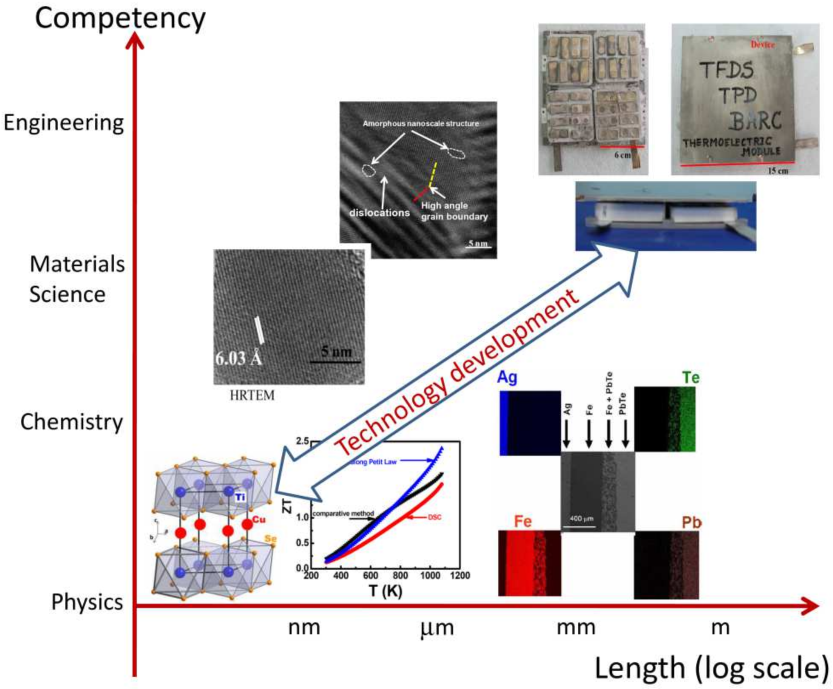

Fig. 6.2. Schematic representation of technology development of thermoelectric power generators requiring competence at multidisciplinary sciences at different length scales.

To sum up, the technology development of thermoelectric power generators requires competence at multidisciplinary sciences (i.e. physics, chemistry, materials science and engineering) at different length scales, as schematically shown in Fig. 6.2. To an extent, this thesis has been successful in demonstrating the indigenous development of thermoelectric generators with an efficiency of 6%. This thesis also opens up following work in the future:

- Synthesis of new n-type materials having compatible ZT of ~1.43 (at 773 K) that has been obtained for p-type $(AgCrSe_2)_{0.5}(CuCrSe_2)_{0.5}$ nanocomposites in this thesis work. One of the possibilities is to replace this material with TAGS-85 in PbTe/TAGS-85 generators. However, finding appropriate methodology for obtaining the low contact resistance would be a challenge.
- Synthesis of p-type $Si_{80}Ge_{20}$ using mechanical alloying process that has compatible ZT of 1.84 (at 1073 K) that has been obtained for mechanically alloyed n-type $Si_{80}Ge_{20}$. Of course, the challenge of making low contact resistance in SiGe based generators is another issue.
- PbTe/TAGS-85 thermoelectric generator is operable at 773 K, while SiGe operates at >1073 K. Therefore, in order to achieve higher efficiency a cascade device can be fabricated.

BIBLIOGRAPHY

---

[1] D M Rowe CRC Handbook on Thermoelectrics (Boca Raton, FL: CRC Press) (1996).

[2] D M Rowe and C M Bhandari *Modern Thermoelectrics* (London: Holt-S`aunders) (1983).

[3] C. Kittel *Introduction to Solid state Physics* (1996).

[4] N.W. Ascroft, N.D. Mermin *Solid State Physics.* Harcourt College Publishers (1976).

[5] T.Takeuchi, A. Yamamoto, K. Ogawa *MRS proceedings* (2011) 1314.

[6] A. Yamamoto, K. Ogawa ,T. Takeuchi *Materials Transactions* **52** (2011) 1539.

[7] Aldo V. da Rosa *Fundamentals of Renewable Energy Processes* (2008).

[8] T.J. Seebeck, Abh. Akad. Wiss. Berlin 1820-1821, 289 (1822)

[9] J.C. Peltier, *Ann. Chim.* **1**(1834) 371.

[10] D M Rowe CRC Handbook on Thermoelectrics (CRC Press) (1995).

[11] W. Thomson, Proc. R. Soc. Ed. 91 (1851).

[12] G. Nolas, J. Sharp, and H. Goldsmid. *Thermoelectrics: basic principles and new materials developments.* Springer, (2001).

[13] Antonio P. Gon¸calves , Claude Godart *Eur. Phys. J. B* **87** (2014) 1.

[14] E. Altenkirch, *Phys. Zeitschrift* **10** (1909) 560.

[15] E. Altenkirch *Phys. Zeitschrift* **12** (1911) 920.

[16] A.F. Ioffe, Semiconductor Thermoelements and Thermoelectric Cooling, Infosearch, London, 1957.

[17] J. R. Szczech, J. M. Higgins, S. Jin *J. Mater. Chem.* **21** (2011) 4037.

[18] J. R. Sootsman, D. Y. Chung, M. G. Kanatzidis *Angew. Chem. Int. Ed.* **48** (2009) 8616.

---

[19] A. Shakouri *Annu. Rev. Mater. Res.* **41** (2011) 399.

[20] N.F. Mott, H. Jones, The theory of the properties of metals and alloys, Dover Publication, New York, 1958.

[21] C. M. Jaworski, B. Wiendlocha, V. Jovovica and Joseph P. Heremans *Energy Environ. Sci.* **4** (2011) 4155.

[22] J.P. Hermans, B. Wiendlocha, A.M. Chamoire *Energy Environ. Sci.* **5** (2012) 5510.

[23] K. Ahn, M. K. Han, J. He, J. Androulakis, S. Ballikaya, Ctirad Uher, Vinayak P. Dravid, M. G. Kanatzidis *J. Am. Chem. Soc.* **132** (2010) 5227.

[24] M. Cutler, J. F. Leavy, R. L. Fitzpatrick *Phys. Rev.* **133** (1964) 1143.

[25] G.J.Snyder, E.S.Toberer *Nat. Mater.* **7** (2008) 105.

[26] H. Alam, S. Ramakrishna *Nano Ener.* **2** (2013) 190.

[27] M. Zebarjadi, K. Esfarjani, M. S. Dresselhauss, Z. F. Ren, G. Chen *Energy Environ. Sci.* **5** (2012) 5147.

[28] A.J.Minnich, M.S.Dresselhauss, Z.F.Ren, G.Chen *Energy Environ. Sci.* **2** (2009) 466.

[29] W. Liu, Q. Jie, H.S. Kim, Z. Ren *Acta Materialia* **87** (2015) 357.

[30] Y.L.Pei, Y. Liu *J. Alloys and Compounds* **514** (2012) 40.

[31] L. D. Zhao, H. J. Wu, S. Q. Hao, C. I. Wu, X. Y. Zhou, K. Biswas, J. Q. He, T. P. Hogan, C. Uher, C. Wolverton, V. P. Dravid ,M. G. Kanatzidis *Energy Environ. Sci.* **6** (2013) 3346.

[32] R. Tsu, W. E. Howard, L. Esaki *Phy. Rev.* **172** (1968) 779.

[33] R. Braunstkin, A. R. Moore, F. Herman *Phy. Rev.* **109** (1958) 695.

---

[34] Chao-Chun Wang, Dong-Sing Wuu, Shui-Yang Lien, Yang-Shih Lin, Chueh-Yang Liu, Chia-Hsum Hsu, and Chia-Fu Chen *Int. J. of photoenergy* **2012** (2012) 1.

[35] Zhi-Gang Chena, Guang Hana, Lei Yanga, Lina Chenga, Jin Zou *Progress in Natural Science: Materials International* **6** (2012) 535.

[36] D. Li, R.R. Sun, X.Y. Qin *Intermetallics* **19** (2011) 2002.

[37] S. Mohamed, E. Genk , H. H. Saber , T. Caillat *Ener. Conver. and Manag.***44** (2003) 1755.

[38] L.N. Vikhor , L.I. Anatychuk *Ener. Conver. and Manag* **50** (2009) 2366.

[39] Y.S. Kang, M. Niino, I. A. Nishida, .J. Yoshino *17th Int. conf. on Thermoelectrics* (1998) 429.

[40] J. Loffy *US patent US20090025770* A1 (2009) 1-49.

[41] G. Jeffrey Snyder , Tristan S. Ursell *Phy. Rev. Lett.* **91** (2003) 1.

[42] Shawna R. Brown, Susan M. Kauzlarich, Franck Gascoin, G. Jeffrey Snyder *Chem Mater.* **18** (2006) 1873.

[43] D. Ebling, M.Jaegle, M. Bartel, A. Jacquot, H. Bottner, *J. Electron. Mater.* **38** (2009) 1456.

[44] D. Ebling, K. Bartholome, M. Bartel, M.Jaegle, *J. Electron. Mater.* **39** (2010) 1376.

[45] L. D. Zhao, V. P. Dravid , M. G. Kanatzidis *Energy Environ. Sci.* **7** (2014) 251.

[46] J. He, M. G. Kanatzidis, V. P. Dravid *Mater. Today* **16** (2013) 166.

[47]J.P.Hermans, B. Wiendlocha, A.M. Chamoire *Energy Environ. Sci.* **5** (2012) 5510.

[48] Y. Pei, X. Shi, Aaron LaLonde, H. Wang, L. Chen & G. J. Snyder *Nature* **473** (2011) 66.

---

[49] Y. Pei, , H. Wang, G. J. Snyder *Adv. Mater.* **24** (2012) 6125.

[50] H. Wang, Y. Pei, A. D. LaLonde , G. Jeffery Snyder *Thermoelectric Nanomaterials,* Springer Series 3 in Materials Science 182, © Springer-Verlag Berlin Heidelberg 2013.

[51] H. Heinrich, K. Lischka, H. Sitter, M. Kriechbaum *Phys. Rev. Lett.* **35** (1975) 1107.

[52] H. Sitter, K. Lischka, H. Heinrich *Phys. Rev. B : Solid State* **16** (1977) 680.

[53] N.V. Kolomates, M.N. Vinogradova, L.M. Sysoeva *Semiconductors* **1** (1968) 1020.

[54] J. P. Heremans, V. Jovovic, E. S. Toberer, Ali Saramat, K. Kurosaki, A.Charoenphakdee, S. Yamanaka, G. J. Snyder *Science* **321** (2008) 554.

[55] C. M. Jaworski, V.Kulbachinskii, J. P. Heremans *Phys. Rev. B* **80** (2009) 2332014.

[56] M. D. Nielsen, E. M. Levin, C. M. Jaworski, K. Schmidt-Rohr, J. P. Heremans *Phys. Rev. B* **85** (2012) 045210.

[57] Q. Zhang, H.Wang, W.Liu, H. Wang, Bo Yu, Q. Zhang, Z. Tian, George Ni, S. Lee, K. Esfarjani, G. Chen, Z. Ren *Energy Environ. Sci.* **5** (2012) 5246.

[58] G.D. Mahan, J.O. Sofo, M. Bartkowiak *J. Appl. Phys.* **83** (1998) 4683.

[59] D. Vashaee, A.Shakouri *Phys. Rev. Lett*. **92** (2004) 106103.

[60] Rowe DM, G. Min. 13th Int. Conf. Thermoelectr., (1994), 339.

[61] T. H. Zou, X. Y. Qin, D. Li, B. J. Ren, G. L. Sun, Y. C. Dou, Y. Y. Li, L. L. Li, J. Zhang ,H. X. Xin *J. Appl. Phys.* 115 (2014) 053710.

[62] E. M. Levin , S. L. Bud'ko , K. Schmidt-Rohr *Adv. Funct. Mater.* **22**(2012) 2766.

[63] J. H. Lee, J. Wu, J. C. Grossman *Phys. Rev. Lett.* **104** (2010) 16602.

[64] B. Yu, M. Zebarjadi, H.Wang, K. Lukas, H. Wang, D.Wang, C. Opeil, M. Dresselhaus, G. Chen, Z. Ren *Nano Lett.* **12**, (2012), 2077.

---

[65] M. Zebarjadi, Giri Joshi, G. Zhu, B. Yu, A. Minnich, Y. Lan, X.Wang, M. Dresselhaus, Z. Ren, G. Chen *Nano Lett.* **11** (2011) 2225.

[66] J. H. Bahk, A. Shakouri *Appl. Phy. Lett.* **105** (2014) 052106.

[67] H.J. Goldsmid *Thermoelectric Refrigeration* Plenum Press New York 1964.

[68] G.D. Mahan Solid state Physics vol. **51** (Eds: H. Ehrenreich, F. Spaepen) Academic press Inc San Diego (1998) 81.

[69] H.J. Goldsmid *Introduction to Thermoelectricity* Springer Heidelberg 2009.

[70] Y.Pei , A.D. LaLonde , N. A. Heinz , X.Shi , S. Iwanaga , H.Wang , L.Chen , G. Jeffrey Snyder *Adv. Mater. 23* (2011) 5674.

[71] H.J. Goldsmid *Applications of thermoelectricity* METHUEN New York 1960.

[72] K. Biswas, J. He, Ivan. D. Blum, C.IWu, T.P. Hogan, D. N. Seidman, V. P. Dravid, M. G. Kanatzidis *Nature* **489** (2012) 414.

[73] L. M. Rogers , A. J. Crocker *J. Phys. D: Appl. Phys.* **4** (1971) 1016.

[74] L. Rogers , A. Crocker , *J. Phys. D: Appl. Phys.* **5**(1972) 1671.

[75] A. J. Crocker L. M. Rogers *J. Phys. Colloq.* **29** (1968) C4 129-132 .

[76] Y. Kulvitit , S. Rolland , R. Granger , C. M. Pelletier *J. Phy. Chem. Solids* **45** (1984) 977.

[77] G. S. Nolas, G. A. Slack, S. B. Schujman in Semiconductors and Semimetals, (Ed.: T. M. Tritt), Academic Press, San Diego **69** (2001) 255.

[78] C. Wood *Rep. Prog. Phys.* **51** (1988) 459.

[79] E. S. Toberer, P.Rauwel, S.Gariel, J. Taftøb G. Jeffrey Snyder *J. Mater. Chem.* **20** (2010) 9877.

---

[80] T. Caillat, J. -P. Fleurial, A. Borshchevsky *J. Phy. Chem. Solids* **58** *(*1997) 1119.

[81] C. Yu, T. J. Zhu, S. H. Yang, J. J. Shen, X. B. Zhao *Phys. Status Solidi RRL* **4** (2010) 212.

[82] E. S. Toberer, K. A. Sasaki, C. R. I. Chisholm, S. M. Haile, W. A. Goddard, G. J. Snyder *Phys. Status Solidi RRL* **1** (2007) 253.

[83] H. J. Kim, E. S. Bozin, S. M. Haile, G. J. Snyder , S. J. L. Billinge, *Phys. Rev. B* **75** (2007) 134103.

[84] B. Wolfing, C. Kloc, J. Teubner, E. Bucher *Phys. Rev. Lett.* **86** (2001) 4350.

[85] K. Biswas, J. He, Q. Zhang, G.Wang, C. Uher, V.P. Dravid , M. G. Kanatzidis *Nat. Chem.* **3** (2011) 160.

[86] G. S. Nolas, G. A. Slack, J. L. Cohn , S. B. Schujman *17th Int. conf. on Thermoelectrics* (1998) 294.

[87] W. Liu, Q. Jie, H.S. Kim, Z. Ren *Acta Mater.* **87** (2015) 357.

[88] A.Hill, E.R. Wallach *Acta Metall.* **37** (1989) 2425.

[89] Ian M. Watt, *The Principles and practice of electron microscopy*, Cambridge University Press, (1985).

[90] David B. William, C. Barry Carter, *Transmission Electron microscopy*, second edition, Springer, (2009).

[91] B. D. Cullity, *Elements of X-ray Diffraction*, second edition, Addison-Wesley (1978).

[92] K.W. Raymond, J.A. Corkill *J. Chem Educ.* 8 (1994) 204.

[93] D. Briggs, M.P. Seah, *Practical Surface Analysis by Auger and X-ray Photoelectron Spectroscopy*, Wiley (1983).

---

[94] J. F. Moulder, W.F. Stickle, P.E. Sobol, K. D. Bomben, *Handbook of X-ray Photoelectron Spectroscopy*, Physical electronics, USA, (1995).

[95] Wilhelm Melitz, Jian Shen, Andrew C. Kummel, Sangyeob Lee, *Surface Science Reports*, **66**(2011) 1-27.

[96] David Griffiths. *Introduction to Electrodynamics*. Prentice Hall, (1999).

[97] T.M. Tritt. *Thermal Conductivity: theory, properties, and applications*. Kluwer Academic/Plenum Publishers, (2004).

[98] Ana Paula F. Albers, Thomaz A.G. Restivo, Luciano Pagano, and Joo B. Baldo. *Thermochimica Acta*, **370** (2001) 111.

[99] M.A. Sheikh, S.C. Taylor, D.R. Hayhurst, and R. Taylor. *J. Phys. D: Appl. Phys* , **33(**2000) 1536.

[100] B. Hay, J.R. Filtz, J. Hameury, and L. Rongione. 15th *Symposium on Thermophysical Properties*, (2003) 1-20.

[101] K. A. Borup, J. de Boor, H.Wang, F. Drymiotis, F. Gascoin, X. Shi, L.Chen, M. I. Fedorov, E. Müller, Bo B. Iversena G. Jeffrey Snyder *Energy Environ. Sci*. **8** (2015) 423.

[102] M. Bukała, P. Sankowski, R. Buczko, P. Kacman *Nanoscale Res. Lett*. **6** (2011) 126.

[103] P. B.Pereira, I. Sergueev, S. Gorsse, J. Dadda, E.Mu¨ ller and R. P. Hermann *Phys. Status Solidi B* **250** (2013)1300.

[104] Y Chen, C M Jaworski, Y B Gao, H Wang, T J Zhu, G J Snyder,J P Heremans and X B Zhao *New Journal of Physics* **16** (2014) 013057.

---

[105] S. S. Kabalkina, L. F. Vereshchagin and N. R. Serebryanaya *Sov. Phy. Jetp* **24** (1967) 917.

[106] J. Davidow and Y. Gelbstein *J. Electron. Mater*. **42** (2013) 1542.

[107] R.F. Brebrik and R.S. Allgaier *J.Chem. Phys.* **32** (1960) 1826.

[108] R.F. Brebrik and E. Gubner *J.Chem. Phys.* **36** (1962) 1283.

[109] R.F. Brebrik Progress in Solid State Chemistry Vol. 3, Reiss, H., Ed., Pergamon Press, New York, 1966.

[110] R.F. Brebrik *J. Electron. Mater*. **6**(1977) 659.

[111] Y. Sato, M. Fujimoto and A. Kobayashi *Jpn. J. Appl. Phy*. **2** (1963) 688.

[112] M. Fujimoto and Y. Sato, *Jpn. J. Appl. Phy.* 5 (1966) 128.

[113] E.A. Skrabek *8th Intersociety Energy conversion Engineering conference*(1970) 15.

[114] V. Jovovic, J. P. Heremans *Phy. Rev. B* **77** (2008) 245204.

[115] R. S. Allgarer *Phy. Rev.* **111** (1958) 1029.

[116] H.J.GoldSmid, J.W. Sharp *J. Electron. Mater.* **28** (1999) 869.

[117] S.Yoneda, M. Kato , I. J. Ohsugi *J. Theo. App.Phy*. **7** (2013) 1.

[118] F.A. Leavitt, J.W. McCoy, P. Marudhachalam, M. Gaertner, Segmented thermoelectric module with bonded legs, *US patent* 2012/0103381 A1, 3rd May 2012.

[119] T. A. Keeler, Z. Salman, K. H. Chow, B. Heinrich, M. D. Hossian, B. Kardasz, R. F. Kiefl, S. R. Kreitzman, C. D. P. Levy, W. A. MacFarlane, O. Mosendz, T. J. Parolin, M. R. Pearson, and D. Wang *Phy. Rev. B* **77** (2008) 144429.

[120] J. Balogh, L.F. Kiss, A. Halbritter, Kezsmarki , G. Mihaly *Solid State Commun.* **122** (2009) 59.

---

[121] R. Gupta, M. Weisheit, H.U. Kerbs, P. Schaaf *Phy. Rev. B* **67** (2003) 074502.

[122] P. Vilars, A. Prince, H. Okamoto Handbook of Ternary Alloy Phase Diagrams (Materials Park, OH: ASM International) **8** (1995) 10753.

[123] N. Wang, D. West, J. Liu, J. Li, Q.Yan, B.L. Gu, S. B. Zhang, W. Duan *Phy. Rev. B* **89** (2014) 045142.

[124] G. Tan, L.D. Zhao F. Shi , J.W. Doak , S. H. Lo, H. Sun, C. Wolverton, V. P. Dravid, C. Uher, and M. G. Kanatzidis *J. Am. Chem. Soc.* **136** (2014) 7006.

[125] Y. Pei, X. Shi, A.D. Lalonde, H.Wang, L.Chen and G.J.Snyder, *Nature* **473** (2011) 1366.

[126] Y.I.Ravich, B.A.Efimova and I.A.Smirnov, *Semiconducting Lead Chalcogenides* (Plenum, 1970).

[127] G. T. Alekseeva , B. Efimova, L. M. Ostrovsk, O. S. Serebrya and M. Tsypin , *Sov. Phys. Semicond.* **4** (1971) 1122.

[128] J. Q. Li, S. P. Li, Q. B. Wang, L. Wang, F. S. Liu, W. Q . Ao, *J. Alloys Comp*. **509** (2011) 4516.

[129] N.M. Constantine, “Thermoelectric figure of merit of degenerate and non-degenerate semiconductors”, Mechanical Engineering Dissertations (2008).

[130] T.C. Holgate, S.Zhu, M.Zhou, S.Bangarigadu-Sanasy, H.Kleinke, J.He, T.M.Tritt, *J. Solid State Chem*.**197** (2013) 273.

[131] L.S. Krasavin, M.V. Spitsin, and A.N. Titov *Phys. Solid State* **39** (1997) 52.

[132] Y.S. Hor, R.J. Cava *Materials Research Bulletin* **44** (2009) 1375.

---

[133] M Sarma, A. R. Beal, S. Nulsen and R. H. Friend, *J. Phys. C: Solid State Physics* **15** (1982) 4367.

[134] . Morosan, H. W. Zandbergen, B. S. Dennis, J. W. G. Bos, Y. Onose, T. Klimczuk, A. P. Ramirez, N. P. Ong, R. J. Cava, *Nature Physics* **2** (2006) 544.

[135] H.J. Goldsmid, J.W. Sharp *J. Electronic Materials* **28** (1999) 869.

[136] H. Liu, X. Shi, F. Xu, L. Zhang, W. Zhang, L. Chen, Q. Li, C. Uher, T. Day, G. J. Snyder, *Nature Mater.* **11**(2012) 422.

[137] G. C. Tewari, M. Karppinen, A. K. Rastogi, *J. Solid State Chem.* **198 (**2013) 108.

[138] D. Srivastva, G. C. Tewari, M. Karppinen, R. M. Nieminen, *J. Phys.; Condens. Matter* **25 (**2013) 105504.

[139] F. M. R. Engelsman, G. A. Wiegers, F. Jellinek, B. Van Laar, *J. Solid State Chem.* **6 (**1973) 574-582.

[140] *High conductivity solid ionic conductor, recent trends and applications.* Ed. T. Takahashi, World Scientific, Singapore 1989, ISBN 9971-50-750-1.

[141] A. Vanderlee, G. A. Weigers, *J. Solid State Chem.* **82 (**1989) 216.

[142] B. A. Boukamp, G. A. Wiegers, *Solid State Ionics* **9-10 (**1983) 1193.

[143] S. Bathula, M. Jayasimhadri, N. Singh, A. K. Srivastava, J. Pulikkotil, A. Dhar, R. C. Budhani, *Appl. Phys. Lett.* **101** (2012) 213902.

[144] S. K. Bux, J-P Fleurial, R. B. Kaner, *Chem. Commun.***46** (2010) 831.

[145] Paz Vaqueiro, Anthony V. Powell, *J. Mater. Chem.* **20 (**2010**)** 9577.

[146] F. Gascoin, A. Maignan *Chem. Mater.* **23** (2011) 2510.

---

[147] S. N. Girard, J. He, X. Zhou, D. Shoemaker, C. M. Jaworski, C. Uher, V. P. Dravid, J. P. Heremans, M. G. Kanatzidis, *J. Am. Chem. Soc.* **133 (**2011**)** 16588.

[148] E. M. Levin, S. L. Bud'ko, K. Schmidt-Rohr, *Adv. Funct. Mater.* **22** (2012) 2766.

[149] G. J. Snyder, M. Christensen, M. Nishibori, T. Caillat, B. B. Iversen, *Nature Mater.* **3 (**2004) 458.

[150] E. S. Toberer, P. Rauwel, S. Gariel, J. Taftø, G. J. Snyder, *J. Mater. Chem.* **20 (**2010**)** 9877.

[151] G. M. Abramova, G. A. Petrakovskiy, A. N. Vtyurin, J. C. E. Rasch,b A. S. Krylov, J. V. Gerasimova, D. A. Velikanov, V. M. Boehm, V. Sokolov, *J. Raman Spectrosc.* **41 (**2010**)** 1775.

[152] A. Gagor, D. Gnida, A. Pietraszko, *Materials Chemistry and Physics* **146 (**2014**)** 283.

[153] G. Dennler, R. Chmielowski, S. Jacob, F. Capet, P. Roussel, S. Zastrow, K.Nielsch, I. Opahle, G. K. H. Madsen, *Adv. Energy Mater.* **4** (2014) 1301581.

[154] D. R. Brown, T. Day, T. Calliat, G. J. Snyder, *J. Electron. Mater.* **42 (**2013**)** 2014.

[155] M.C. Steele , F.D. Rosi *J. App. Phys.* **29** (1958) 1517.

[156] J.P. Dismukes, L. Ekstrom, E. F. Steigmeir, I. Kudman, D. S. Beers. *J. Appl. Phys.* **35** (1964) 2899.

[157] Jean-Pierre Fleurial and et al. *Proceedings of the Eighth Symposium on Space Nuclear Power Systems (*1991) 451.

[158] H. J. Goldsmid and A. W. Penn. *Phys.Lett. A* **27** (1968) 523.

[159] J.E. Parrot. *J. Phys. C.: Solid State Phys.*, **2** (1969) 147.

[160] C. M. Bhandari , D.M. Rowe . *J. Phys. C: Solid State Phys.* **11** (1978) 1787.

---

[161] D.M. Rowe, V.S. Shukla, N. Savvides *Nature* **290** (1981) 765.

[162] R. J. Baughman, G. L. McVay, R. A. Lefever *Mat. Res. Bull.* **9** (1974) 685.

[163] G. L. McVay, R. A. Lefever, R. J. Baughman *Mat. Res. Bull.* **9** (1974) 735.

[164] R. A. Lefever, G. L. McVay, R. J. Baughman *Mat. Res. Bull* **9** (1974) 863.

[165] D.M. Rowe R.W. Bunce. *J. Phys. D: Appl. Phys.* **10** (1977) 941.

[166] C. B. Vining *J. Appl. Phys.* **69** (1991) 4333.

[167] C. B. Vining *Proceedings of the Eighth Symposium on Space Nuclear Power Systems* (1991) 458.

[168] B.A. Cook *Proceedings of Intersociety Energy Conversion Engineering Conference* 2(1989) 693.

[169] D.W. Staub, SNAP 10A summary report, Atomics International Report NAA-SR-12073 (1967).

[170] J.P. Dismukes, L. Ekstrom, R.J. Paff. *J. Phys. Chem.k* **68** (1964) 3021.

[171] C.M. Bhandari, D.M. Rowe Contemp. Phy. **21** (1980) 219.

[172] Vadim Siklitsky. Silicon germanium. http://www.ioffe.rssi.ru, May 2012.

[173] B.A. Cook and et al. *Proceedings of Intersociety Energy Conversion Engineering Conference* **2** (1989) 693.

[174] B.A. Cook and et al *Proceedings of the Eighth Symposium on Space Nuclear Power Systems* (1991) 431.

[175] D.M. Rowe. *Thermoelectrics Handbook: Macro to Nano*. CRC Press, 2006.

[176] G.K. Williamson, W.H. Hall *Acta Metall.* **1** (1953) 23.

[177] R. Braunstein, A.R. Moore, F. Heraman *Phys. Rev.* **109** (1958) 695.

---

[178] Data for SiGe alloy samples used in the radioisotope thermoelectric generators (RTG) for NASA space flights were provided by Dr. Thierry Caillat from JPL.

[179] X. W. Wang, H. Lee, Y. C. Lan, G. H. Zhu, G. Joshi, D. Z. Wang, J. Yang, A. J. Muto, M. Y. Tang, J. Klatsky, S. Song, M. S. Dresselhaus, G. Chen and Z. F. Ren, *Appl. Phys. Lett*., **93** (1997) 193121.

[180] J. H. Son, M. W. Oh, B. S. Kim, S. D. Park, B. K. Min, M. H. Kim, H. W. Lee, *J. Alloys Comp*. **566** (2013) 168.

[181] G. Busch and O. Vogt Helv. *Phys. Acta* **33** (1960) 437.

[182] V.A. Johnson Progress in semiconductors, ed A.F. Gibson, Heywood, London, **1**(1956) 65.